# EXPERIMENTAL EVALUATION OF FLOW-STRUCTURE INTERACTION WITH ARTIFICIAL SEAGRASS

## RECOMMENDATIONS FOR RESTORATION AND FIELD APPLICATIONS

Von der Fakultät für Bauingenieurwesen und Geodäsie
der
Gottfried Wilhelm Leibniz Universität Hannover

zur Erlangung des Grades
Doktor der Ingenieurwissenschaften
Dr.-Ing.

genehmigte Dissertation

von

**Raúl Armando
Villanueva Granados**

geb. am 28.06.1990
in Tegucigalpa M.D.C., Honduras

2024

# Experimental Evaluation of Flow-Structure Interaction with Artificial Seagrass

## Recommendations for Restoration and Field Applications



Raúl Villanueva

2023

# SUMMARY

Coastal ecosystems are of extreme importance for the environment and human livelihoods based on their ecosystem services: they provide habitat for diverse fauna, supplying food, protection, and nursing grounds for a myriad of species; they provide a self-sustaining source of nourishment and income for the growing coastal communities; they sequester carbon more efficiently and in greater quantities than any land ecosystem; they trap sediments and reduce energy from waves, currents, and tides, thus protecting the coast and the inherent communities and habitats. Despite these services, coastal ecosystems have seen rapid decline over the past century, mostly due to the rapid human population expansion and the ensuing destructive infrastructure. One of the most affected ecosystems are seagrasses, which unfortunately do not receive the attention of more conspicuous ones such as coral reefs and mangrove forests. Nonetheless, recent research has shown that, although they only cover 0.2% of the ocean floor, seagrasses can sequester 10% of the ocean carbon (a.k.a. *blue carbon*), exceeding the rate of any land cover. Moreover, according to the United Nations (UN), half of the human population will be living near coastal areas by 2030, while already more than half of the population lives in urbanized areas, meaning more infrastructure, and hence more ecosystem destruction. This deadly trend has led to the disappearance of more than a third of the seagrass cover since the late 19$^{th}$ century.

To counter this, several restoration efforts have been initiated. Within this thesis, the emulation of seagrass ecosystem services is proposed and investigated as a restoration solution. Seagrasses facilitate their own growth by adapting to their surroundings, affecting the ambient hydrodynamics to promote their own survival. Reproducing this behavior through artificial structures in either virgin or former seagrass-covered habitats should then promote seagrass establishment and proliferation. In turn, the restored seagrass should provide these services itself, achieving a self sustaining habitat. Following this concept, a feasible solution was conceived: artificial seagrass (ASG) patches, comprising flexible shoots fixed to a likewise flexible natural geotextile. The ASG should be biodegradable so no harmful substances are introduced into the environment. Successful field deployment then requires lucid understanding of: a) the ecological provisions of seagrass occurrence and survival; b) the physical processes involved in flow-structure interaction; and c) the properties of biodegradable materials. While research on a suitable biodegradable yet flexible material for marine deployment ran parallel to this work, an interim solution was employed by testing plastics of different mechanical properties. These should serve as basis for the development of the final biodegradable product. ASG patches of different geometries were then tested in state-of-the-art, large-scale hydraulic facilities. The focus lied on the interaction between incident hydrodynamics and the submerged ASG, with the ecological provisions used as boundary and target conditions.

The experimental research presented here was subdivided into unidirectional and oscillatory

flow experiments, analyzing the mechanical response of ASG and the consequent effect on incident hydrodynamics. The results showed that flow needs to be developed within a meadow before maximum flow attenuation is reached, whereby a minimum length of one meter proved to be enough to reach full development. Flow attenuation then caters for shelter for growing seagrass. Attenuation was shown to be higher under unidirectional flow, with more than 50% flow reduction reached, but it also depends largely on incident flow velocity. Wave heights and in-canopy flow were also readily dampened by ASG, while allowing for enough circulation for nutrient transport, which in turn can foster growth. Furthermore, a discretely anchored base layer was shown to be susceptible to loads depending on the wave propagation direction and number of anchors. The flexibility of the ASG and underlying mat makes generalization of these results through computer models rather complicated. Nonetheless, current accepted models can be used to gain insight into the response to similar flexible mats. For now, safety factors could be employed to design prototypes to be tested in the field.

Alongside the results presented here, plenty of research has shown how geometric properties of submerged elements affect flow, with rigidity likewise playing an important role. Flexibility has continued to be the underbelly, making generalization of the processes all the more complicated. Further, the lack of field experiments and prototypes means that there is no real paradigm on field deployment of submerged flexible structures, and no appropriate approach to model submerged flexible vegetation is available. This ultimately means that no comprehensive guidelines for restoration exist, as only a few approaches are somewhat developed. Hence, the results presented here are intended to: i) expand the current knowledge regarding flow-structure interaction with fully flexible submerged elements; ii) provide a prototype which can be deployed in future field projects; iii) build a bridge between science, ecology and engineering to provide a sound, interdisciplinary solution contributing to climate change mitigation; and iv) provide an overview of the state-of-the-art in green engineering for practitioners and stakeholders to form the basis for restoration guidelines towards the well-being of coastal communities around the world.

**Keywords**: flow-vegetation interaction, artificial seagrass, ecosystem restoration, shelter, flume experiments, coastal ecosystem services

# Zusammenfassung

Küstenökosysteme sind aufgrund ihrer Ökosystemleistungen von äußerster Bedeutung für die Umwelt und den Lebensunterhalt des Menschen. Sie bieten Lebensraum für vielfältige Fauna, bieten Nahrung, Schutz und Brutstätten für eine Vielzahl von Arten. Sie stellen eine autarke Nahrungs- und Einkommensquelle für die wachsenden Küstengemeinden dar Sie binden Kohlenstoff effizienter und in größeren Mengen als jedes Landökosystem. Sie fangen Sedimente ein und reduzieren die Energie von Wellen, Strömungen und Gezeiten und schützen so die Küste und die damit verbundenen Gemeinschaften und Lebensräume. Trotz dieser Leistungen kam es im vergangenen Jahrhundert zu einem rapiden Rückgang der Küstenökosysteme, was vor allem auf die rasche Ausbreitung der menschlichen Bevölkerung und die daraus resultierende zerstörerische Infrastruktur zurückzuführen ist. Eines der am stärksten betroffenen Ökosysteme sind Seegräser, die leider nicht die Aufmerksamkeit auffälligerer Arten wie Korallenriffe und Mangrovenwälder erhalten. Dennoch haben neuere Untersuchungen gezeigt, dass Seegräser, obwohl sie nur 0,2% des Meeresbodens bedecken, 10% des Ozeankohlenstoffs (auch bekannt als *blauer Kohlenstoff*) binden können. Darüber hinaus wird laut der UN im Jahr 2030 die Hälfte der Menschheit in Küstennähe leben, während bereits mehr als die Hälfte der Bevölkerung in urbanisierten Gebieten lebt. Dies führt zu mehr Infrastruktur und damit mehr Ökosystemzerstörung. Dieser tödliche Trend hat seit dem späten 19. Jahrhundert zum Verschwinden von mehr als einem Drittel der Seegrasbedeckung geführt.

Um diesem Trend entgegenzuwirken, wurden mehrere Restaurierungsbemühungen eingeleitet. Im Rahmen dieser Arbeit wird die Nachahmung von Seegras-Ökosystemdienstleistungen als Wiederherstellungslösung vorgeschlagen und untersucht. Seegräser fördern ihr eigenes Wachstum, indem sie ihre Umgebung schützen, sich an sie anpassen, und so die Hydrodynamik der Umgebung beeinflussen, um ihr eigenes Überleben zu fördern. Die Nachahmung dieses Verhaltens durch künstliche Strukturen in unberührten oder ehemaligen Seegraslebensräumen sollte dann deren Etablierung und Verbreitung fördern. Im Gegenzug sollte das restaurierte Seegras diese Dienste selbst erbringen und so einen autarken wiederhergestellten Lebensraum schaffen. Diesem Konzept folgend wurde eine praktikable Lösung konzipiert: künstliche Seegrasflächen (KSG), bestehend aus flexiblen Blätter, die an einem ebenfalls flexiblen natürlichen Geotextil befestigt sind. Das ASG sollte biologisch abbaubar sein, damit keine Schadstoffe in die Umwelt gelangen. Daher erfordert ein erfolgreicher Feldeinsatz ein klares Verständnis von: a) den ökologischen Bedingungen des Vorkommens und Überlebens von Seegras; b) die physikalischen Prozesse, die an der Wechselwirkung zwischen Strömung und Struktur beteiligt sind; und c) die Eigenschaften biologisch abbaubarer Materialien. Während parallel zu dieser Arbeit an einem geeigneten biologisch abbaubaren und dennoch flexiblen Material für den Einsatz im Meer geforscht wurde, wurde als Zwischenlösung die Erprobung von Kunststoffen mit unterschiedlichen

mechanischen Eigenschaften eingesetzt. Diese sollen als Grundlage für die Entwicklung des biologisch abbaubaren Endprodukts dienen. Anschließend wurden ASG-Flächen unterschiedlicher Geometrie in hochmodernen hydraulischen Großanlagen getestet. Der Schwerpunkt lag auf der Wechselwirkung zwischen einfallender Hydrodynamik und dem untergetauchten KSG, wobei die ökologischen Gegebenheiten als Rand- und Zielbedingungen herangezogen wurden.

Die hier vorgestellte experimentelle Forschung wurde in unidirektionale und oszillierende Strömungsexperimente unterteilt. Die mechanische Reaktion von KSG und die daraus resultierenden Auswirkungen auf die einfallende Hydrodynamik wurde dann analysiert. Die Ergebnisse zeigten, dass innerhalb einer Wiese die Entwicklung der Strömung vollständig werden muss, bevor die maximale Strömungsdämpfung erreicht wird. Die Strömungsdämpfung bietet dann Schutz für wachsendes Seegras, wobei eine Mindestlänge von einem Meter ausreicht, um die volle Entwicklung zu erreichen. Die Dämpfung war bei unidirektionaler Strömung höher und erreichte mehr als 50%, hängt jedoch weitgehend von der einströmenden Strömungsgeschwindigkeit ab. Wellenhöhen und Strömungen innerhalb der Wiese wurden durch ASG ebenfalls leicht gedämpft und sorgten gleichzeitig für eine ausreichende Zirkulation für den Nährstofftransport, was wiederum das Wachstum fördern kann. Darüber hinaus ist eine diskret verankerte Grundschicht je nach Wellenausbreitungsrichtung und Anzahl der Anker Belastungen ausgesetzt. Die Flexibilität des ASG und der zugrunde liegenden Matte macht die Verallgemeinerung dieser Ergebnisse durch Computermodelle kompliziert. Dennoch können derzeit akzeptierte Modelle verwendet werden, um Einblicke in die Reaktion auf ähnliche flexible Matten zu gewinnen. Vorerst könnten Sicherheitsfaktoren genutzt werden, um Prototypen zu entwerfen, die im Feld getestet werden sollen.

Neben den hier vorgestellten Ergebnissen haben zahlreiche Untersuchungen gezeigt, wie sich geometrische Eigenschaften eingetauchter Elemente auf die Strömung auswirken, wobei auch die Steifigkeit eine wichtige Rolle spielt. Flexibilität ist nach wie vor der Nachteil, was die Verallgemeinerung der Prozesse umso komplizierter macht. Darüber hinaus bedeutet das Fehlen von Feldexperimenten und Prototypen, dass es kein wirkliches Paradigma für den Feldeinsatz von untergetauchten flexiblen Strukturen gibt und kein geeigneter Ansatz zur Modellierung untergetauchter flexibler Vegetation verfügbar ist. Dies führt letztlich dazu, dass keine umfassenden Leitlinien zur Restaurierung existieren, da nur wenige Ansätze einigermaßen entwickelt sind. Daher sollen die hier präsentierten Ergebnisse: i) das aktuelle Wissen über die Strömungs-Struktur-Interaktion bei vollständig flexiblen untergetauchten Elementen erweitern; ii) Bereitstellung eines Prototyps, der in zukünftigen Feldprojekten eingesetzt werden kann; iii) eine Brücke zwischen Wissenschaft, Ökologie und Technik schlagen, um eine solide, interdisziplinäre Lösung bereitzustellen, die zur Eindämmung des Klimawandels beiträgt; und iv) Bereitstellung eines Überblicks über den Stand der Technik im Bereich *Green Engineering* für Praktiker und Interessengruppen, um die Grundlage für Sanierungsrichtlinien zum Wohlergehen von Küstengemeinden auf der ganzen Welt zu bilden.

**Schlüsselwörter**: Hydrodynamik-Vegetation Wechselwirkungen, künstliches Seegras, Ökosystem Wiederherstellung, Schutzfläche, Kanal Experimente, Küstenökosystemdienstleistungen

# AUTHOR STATEMENT

As the author of this dissertation I declare that:

1. I read and followed the regulations for doctoral candidates at the Faculty of Civil Engineering and Geodetic Science, Leibniz University Hannover

2. this dissertation has been composed by me and is based on my own work unless specified by references or acknowledgements

3. I have no competing financial interests or gains that could have appeared to influence the work reported in this dissertation

4. the dissertation has not been submitted at another academic institution before

5. I have not previously applied for an exam as a doctoral candidate at another academic institution

This dissertation takes the form of a cumulative dissertation consisting of three peer reviewed first-authored articles accepted for publication in internationally recognized, high-impact scientific journals. The dissertation further builds upon additional co-authored studies consisting of published and unpublished research and experiments as well as a literature review within the framework of the SEAART project. The first-author articles comprise the main chapters of this dissertation (Chapters 2, 4, and 5). The corresponding article information and my concrete contribution to each are enumerated below (metrics extracted from the corresponding journals website and/or SJR in August 2023):

1. **Wake length of an artificial seagrass meadow: a study of shelter and its feasibility for restoration**

   | | |
   |---|---|
   | **Published in:** | *Journal of Ecohydraulics 7(1)* |
   | | CiteScore: 5.4 \| CiteScore Best Quartile: Q1 \| SJR 2022: 0.676 |
   | **DOI:** | doi.org/10.1080/24705357.2021.1938256 |
   | **Authors:** | R. Villanueva, M. Thom, J. Visscher, M. Paul, T. Schlurmann |
   | **Contribution:** | I conceptualized the test program with the support of J.V. and M.P., and conducted the physical model tests with the help of M.T.. I analyzed the test results, prepared the figures and graphs, and drafted the manuscript. M.P. and T.S. revised the manuscript and all authors approved for submission and subsequent publication. |

2. **Anchor forces on coir-based artificial seagrass mats: dependence on wave dynamics and their potential use in seagrass restoration**

   | | |
   |---|---|
   | **Published in:** | *Frontiers in Marine Science 9, 2022* |
   | | CiteScore: 5.2 \| SCImago Best Quartile: Q1 \| SJR 2022: 1.12 |
   | **DOI:** | doi.org/10.3389/fmars.2022.802343 |
   | **Authors:** | R. Villanueva, M. Paul, T. Schlurmann |
   | **Contribution:** | I conceptualized the test program with input from M.P.. I conducted the physical model tests, analyzed the test results, prepared the figures and graphs, and drafted the manuscript. M.P. and T.S. revised the manuscript and approved for submission and subsequent publication. |

3. **Wave dynamics alteration by discontinuous flexible mats of artificial seagrass can support seagrass restoration efforts**

   | | |
   |---|---|
   | **Published in:** | *Scientific Reports 13:19418* |
   | | SCImago Best Quartile: Q1 \| SJR 2022: 0.97 |
   | **DOI:** | 10.1038/s41598-023-46612-z |
   | **Authors:** | R. Villanueva, M. Paul, T. Schlurmann |
   | **Contribution:** | I conceptualized the test program with input from M.P.. I conducted the physical model tests, analyzed the test results, prepared the figures and graphs, and drafted the manuscript. M.P. and T.S. revised the manuscript and approved for submission and subsequent publication. |

The additional studies used to complement this dissertation are accessible through their corresponding DOIs and are listed below:

- **Using Artificial Seagrass for Promoting Positive Feedback Mechanisms in Seagrass Restoration**

  | | |
  |---|---|
  | **Published in:** | *Frontiers in Marine Science 8, 2021* |
  | **DOI:** | doi.org/10.3389/fmars.2021.546661 |
  | **Authors:** | J. Carus, C. Arndt, B. Schröder, M. Thom, R. Villanueva, M. Paul |
  | **Contribution:** | The paper was divided into subtopics: vegetation ecology, materials and engineering. I drafted the engineering part of the seagrass-flow interaction, including mechanical properties and implications. This was complemented by M.T.. All authors revised every topic independently and input knowledge accordingly to subsequently merge it for publication. |

- **Vertical biomass distribution drives flow through aquatic vegetation**

  | | |
  |---|---|
  | **Published in:** | *Proceedings of SCACR 2017 | TIB/UB Repository of LUH* |
  | **DOI:** | doi.org/10.15488/13254 |
  | **Authors:** | R. Villanueva, M. Paul, M. Vogt, T. Schlurmann |
  | **Contribution:** | M.P. and R.V conceptualized the test program. R.V., and M.V. conducted the physical model tests with support of M.P.. R.V. and M.V. analyzed the test results, prepared the figures and graphs. I drafted the manuscript. M.P. and T.S. revised the manuscript and approved for submission. |

- **Flow field and wake structure characteristics imposed by single seagrass blade surrogates**

  | | |
  |---|---|
  | **Published in:** | *Journal of Ecohydraulics 7(1)* |
  | **DOI:** | doi.org/10.1080/24705357.2021.1938253 |
  | **Authors:** | M. Taphorn, R. Villanueva, M. Paul, J. Visscher, T. Schlurmann |
  | **Contribution:** | I conceived the experiments. M.T. and R.V. conceptualized the test program. M.T. conducted the physical model tests with support of R.V.. R.V., M.P, and T.S. revised the manuscript and approved for submission and subsequent publication. |

# ACKNOWLEDGEMENTS

The journey I took to write this thesis started with a childhood dream: becoming a scientist. As I grew up, I understood I needed to study hard and, more importantly, look beyond the opportunities available locally. This led me down an unpredictable and wild path. What did I learn? Nothing in life can be planned. Life happens and you make the most of it. The people accompanying you along the way are more important than you can ever imagine. Here are my acknowledgments to those people; they helped me become who I am today.

First, I thank T. Schlurmann, my supervisor, and M. Paul, my co-supervisor, for believing in my work, the technical discussions, and the liberty of creativity. I am grateful for the opportunities I got at LuFI regarding travel and scientific exchange. I also thank Prof. T. Reusch, who kindly agreed to be the co-referent of this thesis, and the commission members for the insightful discussion during the examination. I thank the Leibniz University, my home for the best part of a decade, and the Graduate Academy of the University whose scholarship made my last publication possible. And I thank the Ministry of Science and Culture of the federal state of Lower Saxony whose sponsorship of the SeaArt project allowed me to pursue my PhD.

The rest of my LuFI colleagues accompanied me through a difficult road that most of them know all too well. I thank them for the moral support, the technical conversations, and the administrative help, but also for the good times at the institute and during our travels. I made some great friends along the way, relationships that transcend the institute's grounds. I also thank all the students whose theses supported this work, the *hiwis* who shoveled tons of sand with me and weaved artificial seagrass and helped build the complicated set-ups, and the workshop colleagues who helped bring my ideas to life.

Finally, this would not have been possible without the support of what I can only describe as the most important part of me: my family. As a Latin American, my concept of family is quite broad. My friends in Hannover became my family these past few years, as they heard and lived my ups and downs more than anyone else. Thank you guys, I love you all; you make me feel at home. I am thankful for the continued unconditional support of my parents, as well as that of my family in Honduras, who never stopped caring and asking for me and my progress. Your support meant the world to me. I am also thankful to my family in Europe: my sisters, who I am fortunate to have nearby; my cousins, who also make me feel at home abroad; the Premium WG and the Davi HG who experienced first-hand the writing process and all that came with it. Thank you all for being there along the journey and for your continued support.

Gracias mamá. Gracias papá. Gracias amigos y amigas. Gracias familia.

Raúl Villanueva

# CONTENTS

# LIST OF FIGURES

# LIST OF TABLES

# LIST OF SYMBOLS

## *Abbreviations and Acronyms*

| | | | | |
|---|---|---|---|---|
| ADV | Acoustic Doppler Velocimeter | | PHBV | Polyhydroxybutyratevalerate |
| ASG | Artificial Seagrass | | PIV | Particle Image Velocimetry |
| AV | Artificial Vegetation | | PP | Polypropylene |
| CC | Climate Change | | PVC | Polyvinyl Chloride |
| CM | Coir Mat | | RMS | Root Mean Square |
| Eco-DRR | Ecosystem-based Disaster Risk Reduction | | SLR | Sea Level Rise |
| | | | SNR | Signal-to-Noise Ratio |
| FoV | Field of View | | SSL | Seagrass-Sediment-Light Feedback |
| FT | Force/Torque Transducer – see recurring subscripts below | | TSA | Time-synchronous Signal Averaging |
| HDPE | High-Density Polyethylene | | UN | United Nations |
| IPCC | Intergovernmental Panel on Climate Change | | UNDRR | United Nations office for Disaster Risk Reduction |
| LSO | Light Sheet Optic | | UNISDR | (Now UNDRR) UN International Strategy for Disaster Reduction |
| NDC | Nationally Determined Contribution | | | |
| PA | Polyamide | | USS | Ultrasonic Sensor |
| PCL | Polycaprolactone | | VBD | Vertical Biomass Distribution |
| PE | Polyethylene | | WKS | Schneiderberg Wave Flume |
| PHA | Polyhydroxyalkanoate | | WR | wave run |

## *Variables and Constants*

| | | | | |
|---|---|---|---|---|
| $\alpha$ | fit coefficient of $F$ vs. $u$ (Chapter 4) – see recurring subscripts below | | | parameter |
| | | | $\beta$ | damping coefficient |
| | | | $\delta$ | mixing layer thickness |
| $\alpha_w$ | in-canopy flow attenuation | | $\eta$ | surface water level |

| | | | |
|---|---|---|---|
| $\kappa$ | von Kármán constant | $C_D$ | drag coefficient |
| $\lambda$ | wavelength | $C_f$ | friction coefficient |
| $\lambda_1$ | buoyancy to rigidity ratio for dynamic similarity | $c_g$ | wave group velocity |
| $\lambda_f$ | vegetation frontal area parameter | $C_M$ | inertia coefficient |
| | | $Ca$ | Cauchy number |
| $\lambda_p$ | vegetation plan area parameter | $D$ | depth to concrete flume bed (WKS) |
| $\nu$ | kinematic viscosity | $d$ | water depth |
| $\omega$ | wave angular frequency | $D_k$ | wake distance |
| $\phi$ | wave phase | $d_{50}$ | median sediment particle size |
| $\Pi$ | Cole's wake strength | | |
| $\rho$ | water density | $E$ | modulus of elasticity |
| $\rho_{\text{PA,PP}}$ | material density (subscript) | $E_w$ | wave energy density |
| | | $EI$ | flexural rigidity |
| $\tau_b, \tau_{b,w}$ | bed shear stress, wave-induced bed shear stress | $F$ | shear force – see recurring subscripts and superscripts below |
| $\theta$ | momentum thickness | $F_v$ | drag force on stem/vegetation |
| $\varepsilon_D$ | energy dissipation | $g$ | gravity constant |
| $\varphi$ | vegetation solid volume fraction | $H$ | wave height |
| $\xi$ | relative distance from wall in relation to shear | $h_c$ | canopy height/upright vegetation length |
| $a$ | frontal area per canopy volume | $h_r$ | reconfigured canopy height |
| | | $k$ | wave number |
| $A_\infty^{\text{rms}}$ | RMS free stream wave excursion length | $k_m$ | added mass |
| | | $k_r, k_i$ | real, imaginary components of wave number |
| $a_B$ | horizontal orbital wave amplitude near the bed | | |
| | | $k_s$ | equivalent sand roughness |
| $a_w$ | wave amplitude | $KC$ | Keulegan-Carpenter Number |
| $A_{ap}, A_f, A_r$ | corresponding area of anchor – see recurring subscripts below | $L$ | relative velocity between blade and water |
| $B$ | buoyancy ratio | $l_a$ | lever arm (distance) of measured forces |
| $b_v$ | width of vegetation | $L_d$ | drag length scale |

| | | | | |
|---|---|---|---|---|
| $l_e$ | effective length of vegetation | | $U$ | horizontal velocity component – see recurring subscripts and superscripts below |
| $L_m$ | length of the meadow parallel to flow | | $u, v, z$ | velocity components (case insensitive) – see recurring subscripts and superscripts below |
| $L_s$ | shear length scale | | | |
| $M$ | torque – see recurring subscripts and superscripts below | | $u_*$ | shear velocity |
| $N$ | areal density of vegetation | | $U_1$ | in-canopy current velocity |
| $n$ | Manning's roughness | | $U_2$ | above-canopy current velocity |
| $r_\alpha$ | ratio of $\alpha$ (front and rear) | | $U_b^{max}$ | near-bed maximum velocity |
| $r_a$ | wake attenuation ratio | | | |
| $R_k$ | reach of meadow influence along wake | | $U_i$ | instantaneous velocity |
| $Re, Re^{l_e}$ | Reynolds number, effective-length-based $Re$ | | $U_{h_r}$ | current velocity at canopy height |
| $S$ | vegetation shoot separation | | $x'$ | $x$-coordinate starting at leading edge of meadow (Chapter 2) |
| $S_k$ | shelter distance along wake | | | |
| $T$ | wave period | | $x, y, z$ | coordinate system |
| $t$ | time | | $X_D$ | initial adjustment length |
| $t_v$ | vegetation thickness | | $z_0$ | bed roughness length |
| $TKE$ | turbulent kinetic energy | | | |

### *Recurring superscripts and subscripts*

| | | | | |
|---|---|---|---|---|
| 0 | incident, i.e. at leading edge of meadow | | $c11$ | steady flow forcing model by Luhar and Nepf (2011) |
| $\infty$ | free stream/canopy-independent | | $f, r$ | front, rear (Chapter 4) |
| max | maximum value | | $fc, rc, mf$ | (for FT) front corner, rear corner, middle front |
| min | minimum value | | $k$ | along the wake (Chapter 2) |
| mod | modeled data | | | |
| obs | observed/measured data | | $M$ | calculated utilizing torque measurement (Chapter 4) |
| rms | RMS value | | $R$ | Resultant (multiple component, Chapter 4) |
| $c, C$ | current/flow-induced component | | | |
| | | | $w$ | wave-induced component |

| | | | | |
|---|---|---|---|---|
| $w16$ | wave forcing model by Luhar and Nepf (2016) | | | variable |
| | | $*$ | | non-dimensionalized value (Chapter 5) |
| $w19$ | wave forcing model by Lei and Nepf (2019a) | | | |
| | | overbar (e.g. $\overline{u}$) | | time average |
| $x, y, z$ | direction of measured | overhat (e.g. $\hat{u}$) | | canopy-integrated |

# CHAPTER 1

# INTRODUCTION

## 1.1  Background and Motivation

### 1.1.1 *Introduction*

The world population has grown exponentially over the past century, surpassing 8 billion people as of 2022 (UN, 2022). The resulting sudden increase in the demand for resources has created an unprecedented fast-growing stress on the environment. Albeit ubiquitous, this problem is especially evident in coastal areas, where almost a third of the world population currently lives (Reimann et al., 2023) –a figure projected to reach up to 2.9 billion by 2100 (Merkens et al., 2016). Coastal populations are vulnerable to extreme events such as storm surges, tsunamis, and sea level rise (SLR), which have been exacerbated by Climate Change (CC) in recent years (IPCC, 2019). This has prompted scientists and engineers to develop solutions to protect the increasing coastal population. In the past, these solutions were traditionally hard engineering structures (e.g. seawalls and dikes) that directly "block" incoming threats, usually disregarding any side effects on the environment and the livelihood of the populations that depend on it.

Recently, there has been a paradigm shift within the engineering community regarding coastal protection, where the role of the environment has been recognized as indispensable. Coastal ecosystems, viz., coral reefs, mangroves, and seagrasses, have been recognized to be essential for the protection and resilience of coastal regions (Guannel et al., 2016). As such, terms like "nature-based solutions", "ecosystem-based adaptation", and "building with nature" have taken the spotlight when it comes to modern coastal engineering, with guidelines such as *Building With Nature* (van Eekelen and Bouw, 2021) showing successful examples from all over the world. It has also been shown that hybrid solutions, i.e. hard and nature-based solutions combined, can help to improve current coastal engineering approaches in a sustainable manner (Schoonees et al., 2019). Coastal wetlands, i.e. the vegetated coastal ecosystems, have been shown to have an annual median storm protection value of \$447 billion, saving 4620 lives $yr^{-1}$ (Costanza et al., 2021). Further, the *Special Report on the Ocean and Cryosphere in a Changing Climate* (IPCC, 2019) identifies coastal wetlands as important players in our fight against CC, as these have been found to sequester 50% of the ocean-stored carbon –the so-called "blue carbon" –while occupying just 0.2% of the ocean surface (Duarte et al., 2013). This importance is strongly reflected in the inclusion of mangroves, seagrasses and salt marshes in the Nationally Determined Contributions (NDC) agreed upon during the Paris Agreement (UNFCCC, 2016), where 151 countries included at least one ecosystem in their NDCs and 71 countries included all of them (Herr and Landis, 2016).

The need to engineer better solutions to protect coastal wetlands and thus protect our livelihoods has therefore never been more critical. Nevertheless, these ecosystems are under threat not only from CC but also from anthropogenic stress. Seagrass meadows are particularly vulnerable to human activity, disappearing at a rate of 110 $km^2$ $yr^{-1}$ since 1980, hence negatively affecting the \$1.9 trillion $yr^{-1}$ they provide in ecosystem services (Waycott et al., 2009). This has prompted plenty of initiatives to promote seagrass recovery through restoration projects (Van Katwijk et al., 2009; van Katwijk et al., 2016). One such project is SEAART, a cooperation project aiming to promote the re-establishment of seagrass ecosystems through the use of biodegradable artificial meadows. The contents of this dissertation build on the engineering part of this project, seeking to understand the essential mechanisms that turn seagrasses into such efficient and essential ecosystem engineers.

**1**

The rest of this section builds upon a collaborative review where I substantially worked with the interdisciplinary team of SEAART to expose the motivation of the project (see Carus et al., 2021). The biological characteristics of seagrasses and the properties of prospective biodegradable materials were described by the ecologists and material scientists of the project, respectively, and are therefore only partially rephrased here for context. The hydro and morphodynamic interactions were drawn up by the engineers and are described in more detail in the subsequent chapters. The following subsections provide a background to the challenges seagrasses face, followed by a proposed alternative approach –a solution –for seagrass restoration, which was engineered and tested within the framework of this thesis. Section 1.2 then presents a synthesis of the main objectives of this dissertation and Section 1.3 an outline of the subsequent chapters, which describe and discuss the physical implications of the proposed solution in detail.

### 1.1.2 *The Importance of Seagrass and the Need for Restoration*

Seagrasses provide a myriad of ecosystem services (Reynolds et al., 2016) such as coastal protection (Ondiviela et al., 2014), nutrient cycling (McGlathery et al., 2007), and habitat disposition (Orth et al., 2006a; Serrano et al., 2023). These services boost biodiversity (Hemminga and Duarte, 2000) and human livelihoods (e.g. through fisheries, Beck et al., 2001). In addition, seagrasses have gained much attention in recent years as they have been proven to effectively sequester carbon (Duarte et al., 2005), positioning them at the forefront of nature-based solutions to mitigate CC under the banner of "Blue Carbon" (Herr and Landis, 2016; Nature Conservancy, 2021; van Zanten et al., 2023). Moreover, seagrasses have the ability not only to adapt to their environment but also to modify it to facilitate their own growth and that of other species (van der Heide et al., 2011), making them so-called ecosystem engineers (Bouma et al., 2005). They play an important role in coastal protection by increasing wave energy absorption (Paul and Amos, 2011) and stabilizing sediment (Christianen et al., 2013). Despite wide recognition of these services (e.g. Seddon et al., 2020), seagrasses have retreated massively, reaching a decline of 7% per year at the end of the last century (Waycott et al., 2009). They are thus under threat of disappearing in many locations worldwide (Unsworth et al., 2019; Short et al., 2011; Lotze et al., 2006). Moreover, global warming has diminished seagrass production in areas where it is still well established (Litsi-Mizan et al., 2023).

#### THREATS FOR SEAGRASS SEADOWS

The reasons for the worldwide decline of seagrass meadows include diseases, natural and anthropogenic disturbances and eutrophication (Orth et al., 2006a). In the 1930s, a pandemic caused by the slime-mold *Labyrinthula zosterae*, commonly known as the wasting disease, reduced the eelgrass *Zostera marina* stands dramatically (Cotton, 1933) and totally wiped out the subtidal *Z. marina* in the North Atlantic (Dolch et al., 2013). Natural disturbances, such as erosion, can lead to scouring around shoots and result in their dislodgement by hydrodynamic forcing (Infantes et al., 2011). This also leads to highly turbid water, which reduces light availability for photosynthesis. Short-term reductions in light availability may cause reversible stress (Collier et al., 2012), but minimum light requirements are often not met after vegetation cover has been lost. Moreover, burial of young plants has a significant impact on growth and survival (Cabaço et al., 2008), and can be caused by natural dune migration, burrowing, or settlement of suspended material.

In addition to natural threats, anthropogenic stress leads to the destruction and loss of seagrass meadows. These disturbances include mechanical destruction by anchoring vessels that can uproot large areas of seagrass (Abadie et al., 2016) and damage by underwater activities like dredging or shore nourishment campaigns that lead to enhanced turbidity and burial. Furthermore, the intake of nutrients and chemicals (e.g., herbicides) through input by rivers or sewage (Vitousek et al., 1997) directly affects seagrass health due to ammonium toxicity and nitrate inhibition through internal carbon limitation (Burkholder et al., 2007). Moreover, eutrophication promotes growth of phytoplankton, epiphytes, and macroalgae, leading to increased turbidity and shading of seagrass plants (Burkholder et al., 2007). These anthropogenic impacts are considered the major drivers of global seagrass loss (Duarte et al., 2005) and as long as they persist, seagrass restoration will continue to be deemed unsuccessful (Van Katwijk et al., 2009).

**RECOVERY OF SEAGRASS MEADOWS**

By reducing hydrodynamic energy through drag, seagrass meadows promote the settling of suspended sediment particles (Bouma et al., 2005), improving water clarity and quality (Short et al., 2007). Figure 1.1 shows a broad scheme of the effect of a seagrass meadow on the surrounding hydro and morphodynamics. The root and rhizome system of seagrasses stabilizes the trapped sediment even when above-ground biomass is low (Barbier et al., 2011). This positive feedback between seagrass and sediment suspension/deposition is called the seagrass sediment-light (SSL) feedback (Adams et al., 2016). While this feedback has a self-facilitative effect in intact seagrass meadows, it can also lead to bistability (Wilson and Agnew, 1992; Scheffer et al., 2009) with two alternative stable states: (i) a seagrass meadow with relatively clear water, and (ii) bare sediment beds with turbid water (van der Heide et al., 2007). Non-linearities in response to environmental drivers can lead such bistable systems to abruptly shift from one state into another by slight environmental changes (Carr et al., 2016). The resilience of bistable systems is thus low, meaning that after a significant disturbance, the systems cannot readily return to their previous state due to hysteresis –even if the disturbance has been eliminated (Scheffer et al., 2001). In exposed locations, the SSL feedback-induced bistability can render the natural recovery of seagrass meadows impossible (Carr et al., 2010). Prolonged high turbidity, for example, prevented the recovery of *Z. marina* in the Greifswalder Bodden in the Baltic Sea despite reductions in nutrient inputs over 15 years (Munkes, 2005).

Globally, many restoration projects try to re-establish seagrass meadows, with plenty of research on this aim (Paling et al., 2009; van Katwijk et al., 2016). A range of restoration guidelines combine the lessons learned from past restoration efforts (e.g. Campbell, 2002; Ganassin and Gibbs, 2008; Moksnes et al., 2016; van Katwijk et al., 2016). They all identify a variety of reasons for failure, one of the main being unsuitable site selection (van Katwijk et al., 2016). For example, high water and sediment movement at exposed sites inhibit transplant survival (Campbell, 2000); hence, low-energy areas are recommended for restoration schemes to improve restoration success rates (Orth et al., 1994). Nonetheless, given the right shelter, restored seagrass can thrive in high-energy environments, with established beds of seagrass in high-energy environments probably developing in adjacent low-energy areas or during calm periods, expanding once they were well established (Koch, 2001). At sites with high hydrodynamic energy, habitat enhancement strategies that promote
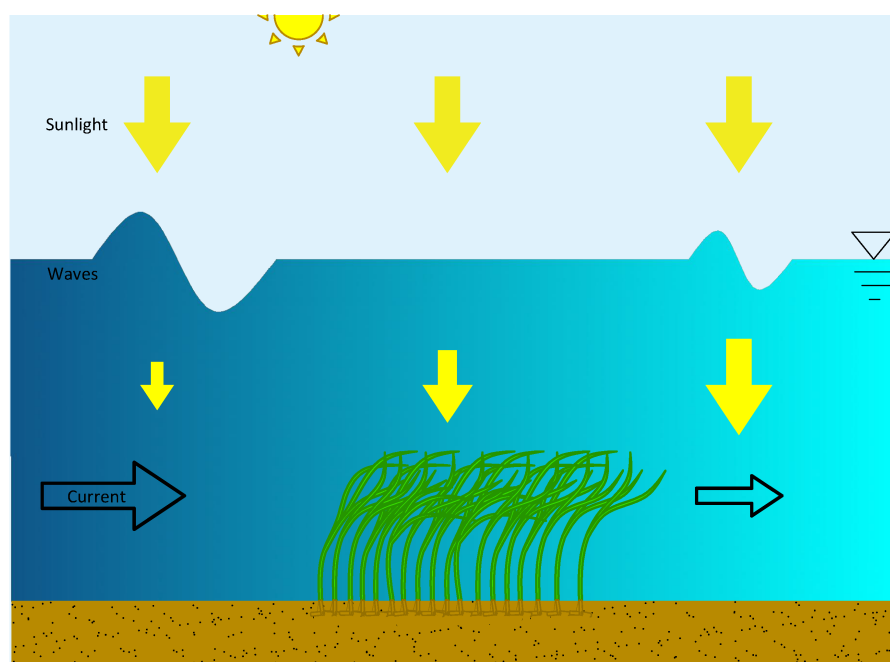
Figure 1.1: Qualitative scheme of the effect of seagrasses on their surroundings. This includes Seagrass-Sediment-Light Feedback (SSL), i.e. increasing sedimentation thus lowering turbidity (sunlight penetration); and reduction of hydrodynamic energy through flow and wave velocity attenuation (arrows and wave surface)

positive feedback mechanisms can thus increase restoration success. Therefore, within the SEAART project, we proposed creating an artificial seagrass (ASG) that mimics the SSL function of natural seagrass. Such ASG may provide a window of opportunity with respect to suitable hydrodynamic and light conditions, stabilizing sediment and allowing natural seagrass to either grow from seeds, take root after transplantation or expand existing meadows more easily.

### STATE-OF-THE-ART IN SEAGRASS RESTORATION

Restoration efforts provide a conceivable way to support the recolonization process and promote seagrass regrowth. Here, the self-facilitative effect of SSL feedback (Maxwell et al., 2017) plays a decisive role. Crossing a minimum threshold of reintroduced individuals and a minimum size of the transplantation area seem to be necessary to reduce turbidity from adjacent bare areas (van der Heide et al., 2007) and thus increase survival and population growth rate of transplanted seagrass (van Katwijk et al., 2016). However, large-scale transplantation is in most cases not feasible, so restoration may only be possible if clarity of the water column in a dedicated area is provided by other means, e.g., by the shelter of other species such as mussel beds (Bos and Van Katwijk, 2007). With many restoration approaches possible, there is no right or wrong method. Ultimately, the selection of the restoration method is going to depend highly on the selected site. Figure 1.2 shows a decision tree based on existing research to guide practitioners and help them select the most suitable restoration approach.
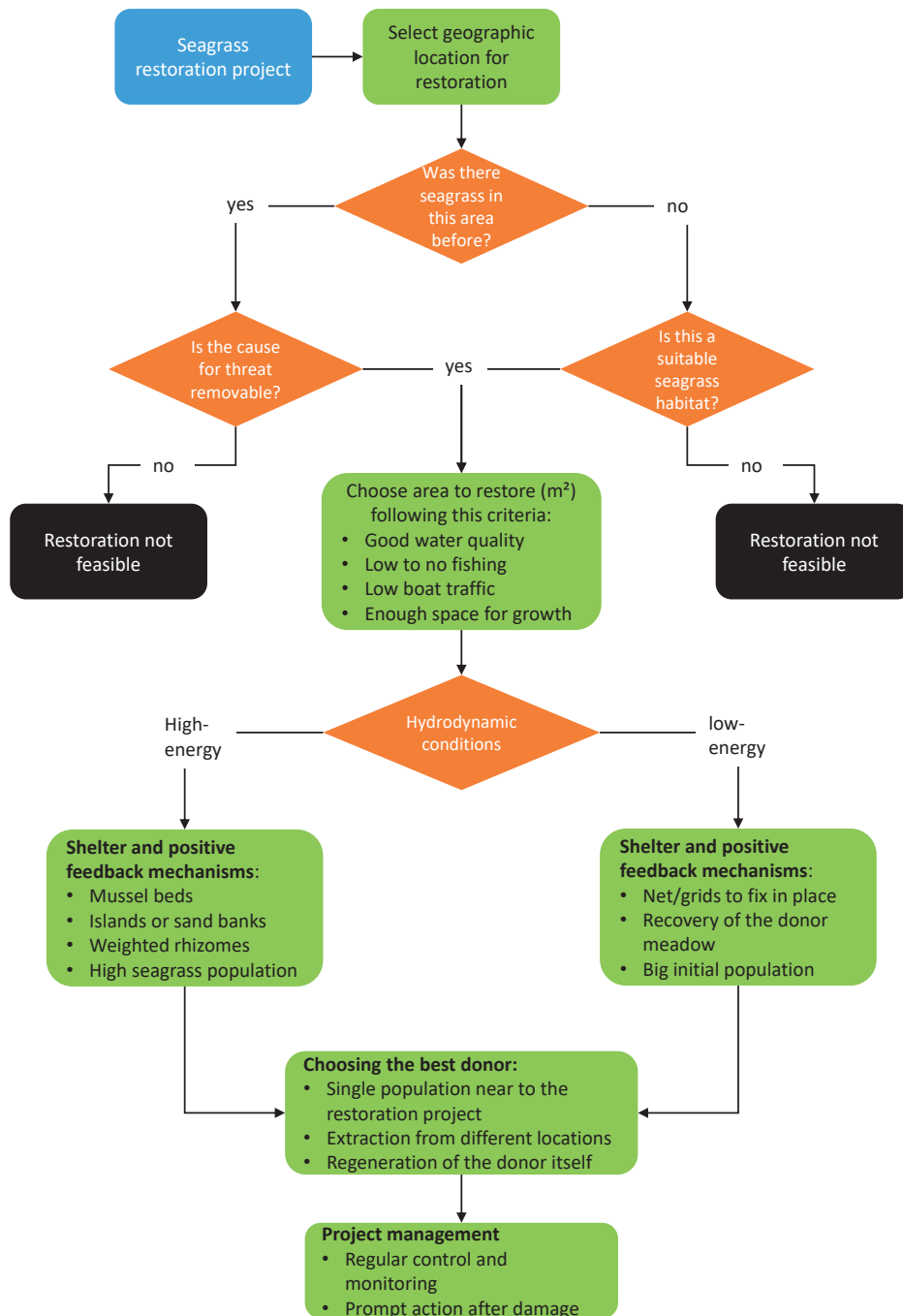
Figure 1.2: Decision tree concept for seagrass restoration.

**PROMOTING POSITIVE FEEDBACK MECHANISMS BY THE USE OF ARTIFICIAL STRUCTURES**

If natural protection structures are not present or cannot be introduced at the selected restoration site, alternative solutions and innovative approaches such as enclosures of ASG become necessary (van der Heide et al., 2007, Figure 1.2). Artificial structures promoting positive feedback mechanisms provide promising benefits for the restoration of natural seagrass by preventing transplants from being dislodged by incident hydrodynamics and foraging fauna (Campbell and Paling, 2003). They can either directly anchor the transplanted seedlings or stabilize the sediment

Table 1.1: Overview of existing restoration trials using artificial structures. Table adapted from (Carus et al., 2021)

| Species | Facilitation structure | Plant material | Success (yes/no) | Probable reason for failure | Drawback | References |
|---|---|---|---|---|---|---|
| *Potamogeton perfoliatus Stuckenia pectinata* | Natural beds of *Ruppia maritima* | Shoots | Depending on scale of restoration | Shading effect | Not universally present | Hengst et al. (2010) |
| *Zostera marina* | Natural mussel beds (*Mytilus edulis*) | Seedlings | Yes | – | Not universally present | Bos and Van Katwijk (2007) |
| *Amphibolis griffithii, Posidonia sinuosa* | Plastic garden mesh | Plugs | Yes | – | Plastic introduction | Van Keulen et al. (2003) |
| *Amphibolis Antarctica* | Sand-filled hessian bags | None* | Yes | – | Species-specific | Irving et al. (2010) |
| *Zostera marina* | Sand-filled hessian bags | Seeds | Yes | – | Low germination rate of seeds | Unsworth et al. (2019) |
| *Zostera marina* | Planting frames | Shoots | Yes | – | High losses if not thoroughly anchored, disturbance caused by the removal of the frames | Short et al. (2002); Leschen et al. (2010); Park and Lee (2007) |
| *Zostera marina* | Biodegradable grids | Shoots | Yes | – | High losses if not thoroughly anchored | Kidder et al. (2015) |
| *Zostera marina* | Holes drilled into shells | Shoots | Yes | – | Relatively time-consuming | Lee and Park (2008) |
| *Phyllospadix japonicas* | Underwater structure built of cement, sand and water | Shoots | Yes | – | Underwater structure stays in place | Park and Lee (2010) |
| *Cymodocea nodosa* | ASG to decrease herbivory-induced mortality | Seedlings | Yes | – | Plastic introduction | Tuya et al. (2017) |
| *Posidonia australis* | ASG with plastic leaves | Plugs | No | Storm damage | Plastic introduction | Campbell and Paling (2003) |
| *Zostera muelleri* | ASG with plastic leaves | Shoots | No | Shading effect, damage by wavering ASG leaves | Plastic introduction, colonization of ASG with epifauna and flora | Matheson et al. (2017) |

*Recruitment of existing seedlings.

surrounding the transplantation (e.g. Short et al., 2002; Park and Lee, 2007; Leschen et al., 2010). Table 1.1 provides an overview of restoration efforts using artificial structures.

Laboratory studies utilizing ASG to investigate the impact of submerged vegetation on the hydrodynamic regime (e.g. Nepf and Vivoni, 2000; Bouma et al., 2005) show that ASG mats promote positive feedback mechanisms by providing the sheltering capacity that is typically attributed to natural seagrass meadows. These mats consist of leaves fixed to a base layer, mimicking a natural meadow. Previous studies have shown that ASG can provide shelter for seagrass (Tuya et al., 2017). ASG mats could thus potentially help to restore seagrass where natural protection structures such as mussel beds are not feasible or where other restoration techniques have previously failed (Talbot et al., 2001). Ideally, this concept could substitute current labor and cost-intensive measures such as anchors on single shoots or weighted frames. Seagrass-like artificial structures have the advantage

that they integrate into the environment and use the natural feedback mechanisms to provide shelter (Adams et al., 2016). So far, ASG has mainly been used in other contexts, e.g., in offshore engineering, where it has found a commercial application in scour protection around pipelines, monopiles, and jackets (see discussion in Chapter 4), as it can significantly reduce flow and stabilize the sediment (Byers et al., 2006). ASG hence represents a promising tool for seagrass restoration.

### 1.1.3 *Artificial Seagrass: A Possible Solution?*

In a restoration context, ASG was attached around seagrass restoration plots to increase the long-term survival of the seedlings of the seagrass *Cymodocea nodosa* by decreasing herbivore-induced mortality (Tuya et al., 2017). Though beyond the intended purpose of the ASG, the authors stated that it probably modified small-scale hydrodynamics around the plots and thus reduced sediment transport. In a restoration experiment in Australia, ASG mats stabilized the sediment composition for transplants with significantly higher transplant survival and larger rhizome extension (Campbell and Paling, 2003). In another restoration test with ASG, eelgrass *Zostera muelleri* cover in intertidal plots with seagrass transplanted into ASG mats decreased after 24 months, presumably because of the strong shading caused by the ASG leaves (Matheson et al., 2017). Carus et al. (2020) showed through flume experiments that ASG can significantly reduce wave height and current velocity, thereby raising the flow velocity threshold which transplanted *Z. marina* shoots are able to withstand.

When considering ASG for restoration, the selection of the material is as important as the site selection. Commonly, ASG has consisted of conventional plastic, hence constituting an additional source of contamination (Andrady, 2011). Plastic becomes brittle and transforms into microplastic, which may in turn absorb organic pollutants and be consumed by marine organisms (Cole et al., 2011), ultimately ending on our table. The ASG mats described above were produced from durable materials intended to stay in place long-term, which makes them unsuitable for restoration efforts that seek to re-establish naturally vegetated ecosystems. The aim of all habitat enhancement should be to improve environmental conditions during the establishment, up to the point where the seagrass meadow itself can provide these ecosystem-engineering functions.

#### Fluid-Structure Interaction

The first challenge faced when implementing ASG to promote positive feedback mechanisms is correctly understanding fluid-structure interaction. Fluid mechanics, albeit highly complex, has been well developed within the engineering sciences, with well-known handbooks and guidelines such as *Open-Channel Hydraulics* (Chow, 1959), *Recommendations for Coastal Protection Structures (EAK)* (KFKI, 2020), and *EurOTop* (EurOTop, 2018) constituting a sound basis for applied engineering. However, interaction with other structures increases the complexity, introducing or enhancing effects such as friction, (viscous) layering, shear, turbulence, and vortex development. For rigid structures, fluid-structure interaction is relatively straightforward, as the structures comprise constant parameters that define their relation to the surrounding fluid in motion. As such, it has been possible to empirically develop formulations that generalize this interaction, e.g. unidirectional flow-to-wall interaction (e.g. the Law-of-the-wall and its many modifications, see Guo et al., 2005) and oscillatory flow around cylinders (e.g. the well-known Morison,

**1**

or MOJS, equation, Morison et al., 1950). At smaller scales, submerged vegetation has been commonly generalized through arrays of rigid cylinders, for which bulk coefficients (e.g. drag and inertia) and Morison-equation-based formulations are implemented (e.g. White and Nepf, 2007). These formulations have become standard practice in fluid-structure interaction with regard to submerged and emergent vegetation. Nevertheless, when structures become dynamic, i.e. flexible, the complexity increases in a spatial and temporal scale, with acceleration and inertia playing a more prominent role (Asano et al., 1992). Here, inherent rigidity and buoyancy come into play (Luhar and Nepf, 2011), and the interplay between the motion of the structure and the fluid becomes unsteady. This interaction is still poorly understood and validated models tend to be extremely sensitive to the input parameters. Further, model validation is highly dependent on the local conditions used for calibration.

**PROTOTYPE DESIGN**

A further challenge, of equal importance, with using ASG for restoration purposes is designing a climate-neutral prototype, i.e. with no negative impact on the environment, capable of providing the necessary shelter for growing seedlings. Prototype design thus implies the design of ASG leaves (e.g., material, buoyancy, stiffness, geometry) for optimal reduction of hydrodynamic forces (Vogel, 2020). While it is certainly appealing to design the ASG to mimic the exact properties of natural seagrass, it is of high importance to optimize the design to provide shelter more effectively without overshadowing regrowing seagrass (e.g. by modifications on the material mechanical properties or the geometry).

The selection of a suitable material for ASG is affected by the required intrinsic and technical characteristics (i.e. biodegradability and tensile strength). Moreover, the material should ideally integrate into the natural environment without any harmful consequences. Thus, introducing persistent plastics into marine environments has to be seen critically, and biodegradable materials should be considered for the construction of ASG. Employing biodegradable materials also prevents the disturbance of newly established seagrass because the structure does not need to be removed after successful re-establishment. Potential biodegradable ASG can be made of natural fibers, biodegradable plastic, or a combination of both, depending on the envisioned longevity. Pure cellulose fibers in the form of woven fabrics or filaments degrade very fast: for cotton and linen, a degradation time of 3–10 weeks was recorded (Dorée, 1920). Some compostable plastics, such as Polyhydroxyalkanoate (PHA), Polyhydroxybutyratevalerate (PHBV) and Polycaprolactone (PCL), have been shown to degrade under marine conditions (Narancic et al., 2018). For restoration, the material needs to be thoroughly tested beforehand under the conditions prevailing at the restoration site to assess its effect on the environment. Tests should include field trials and temperature changes to assess mechanical changes during degradation.

Geometrically, the ASG patch should be large enough to provide the shelter needed against hydrodynamic energy and erosion, but small enough to (a) be economically feasible; (b) not greatly disturb the natural environment (e.g., covering other habitats and reducing nutrient exchange between adjacent areas); and (c) provide enough space and light for seagrass to establish and expand beyond the ASG boundaries. The dimensions of the ASG providing this facilitation can be explored in physical experiments in a hydraulic laboratory facility (e.g., a wave flume or basin) with

systematic variation of specific parameters (e.g. wave height, wavelength, and distance between mats, see Chapters 3 and 5). The prototype meadow can vary in canopy height, leaf density, and meadow length as well as geometric and mechanical properties of individual stems to control sedimentation rates, reduction of hydrodynamic energy, and light availability (see Chapter 2). Spatially, the location of the re-establishing natural seagrass relative to the position of the ASG needs to be considered. Likewise, an effective spacing to facilitate re-establishment is needed. Potential arrangements include an integrated approach, where seagrass restoration takes place inside the ASG mats, whereby possible shading of the areas for seagrass recovery by the ASG should be minimized (Hengst et al., 2010). For primarily uni-directional flow (e.g. tidal areas), a stripe-like design could fulfill the task of sheltering the restoration areas without shading upcoming natural seagrass, whereby complex hydrodynamic conditions could require a checkerboard-like configuration.

Finally, the selected prototype should be anchored to the bed efficiently, ensuring that the ASG stays in place throughout its lifetime. Generally, restoration efforts were more successful when using some kind of anchoring keeping the transplanted seagrass in place (van Katwijk et al., 2016). Anchoring should be economically feasible and not affect the performance of the mats or hinder shelter in any way. The final mat and anchor design should seamlessly integrate to the environment and provide the highest possible restoration efficiency. A grid-like structure, for example, permits water to flow through and thus requires less anchoring than a closed structure, also lowering loads on the anchors (see Chapter 4). Proper ASG design will ultimately need detailed understanding of the processes affecting ASG to cost-effectively deal with this interaction in a favorable manner for seagrass.

## 1.2 Objectives of the Thesis

The overarching goal of seagrass restoration, as described above, is multifaceted with no general pathway to follow. To date, no general guidelines for seagrass restoration exist. This is because restoration success will depend greatly on many factors such as target vegetation (and its mechanical and biological properties), site and local environmental conditions, and the synergy with other organisms, including us humans and our deeply impactful presence. Therefore, literature reviews on different techniques (e.g. Ganassin and Gibbs, 2008; van Katwijk et al., 2016) and generalized guidelines based on pilot (mostly experimental) studies (Van Katwijk et al., 2009) are the only reference we have with regard to seagrass restoration. Site-specific guidelines are the closest we can get to sought-after standards for seagrass restoration, which is what practitioners and stakeholders consider if any approach is to be given proper funding and implemented on a large scale. An example of this was done by Sweden-based scientists, who published guidelines for seagrass restoration in Sweden (Moksnes et al., 2016). Of course, these guidelines only refer to methodologies applicable within Swedish coastal ecosystems. In a more general form, the removal of natural and anthropogenic disturbances is essential for it to be possible to even attempt restoration, as shown in Figure 1.2. But once restoration can be attempted, proper shelter of the seagrass to be restored takes the forefront, becoming a challenge that greatly depends on the in-situ hydrodynamic conditions. From an engineering perspective, this means that the flow-structure

*1*

| **Thesis Objectives** |
| :--- |
| *"The main objective of this dissertation is thus to understand how artificial seagrass (ASG) behaves under marine conditions and what its effects on local hydrodynamics are."* |

To achieve this, sub-objectives were set to improve the understanding and advance the state-of-the-art of:

- flow-vegetation interaction
- seagrass restoration techniques
- base-layer design and performance under marine conditions

In more general terms, this dissertation also intends to:

- inform practitioners on the feasibility of employing ASG mats for restoration
- build a bridge for interdisciplinary work between engineers, ecologists, and material scientists, which is needed for successful restoration attempts
- inform a more general public of the importance of seagrass and the need for restoration.

interaction needs to be well understood beforehand to be able to manipulate the local conditions and induce a seedling-friendly environment that can incite proper growth and proliferation.

The main objective of this dissertation is thus to understand how artificial seagrass (ASG) behaves under marine conditions and what its effects on local hydrodynamics are. To achieve this goal, it is imperative to primarily understand the concepts of fluid dynamics (e.g. unidirectional flow and wave dynamics), fluid-structure interaction, mechanics of flexible materials (i.e. static and dynamic properties), biomechanics (e.g. of natural geotextiles), and even organism interaction. The latter involves intense interdisciplinary work with biologists and ecologists, among others, as well as extensive field trials, which are conducted by experts in the field and a not described in detail here. To address this aim, the specific topics addressed in this thesis are:

(a) **Flow-structure interaction.** Submerged ASG shoots or leaves are subjected to loads exerted by the moving fluid. These loads cause the ASG to bend –or reconfigure –which affects drag on the ASG leaves but also the hydrodynamics surrounding a given meadow. Drag refers to the force exerted by the surface of the submerged vegetation on the moving water. This means that the extent of drag is greatly dependent on the geometric and mechanical properties of said leaves. Broader leaves, for example, exert more drag than thin ones. However, if the plant is rather stiff, meaning it has low flexibility, the areal contact and thus the resistance to flow increases (less reconfiguration), hence increasing drag. The greater the drag, the greater the attenuation of flow, meaning that hydrodynamic energy is more

readily reduced. Therefore, ASG affects its surrounding hydrodynamics depending on the mechanical properties. Flow-structure interaction is studied and described in detail here in the framework of physical experiments.

(b) **Artificial seagrass response to unidirectional flow.** In areas where submerged currents dominate, seagrasses are primarily exposed to unidirectional flow. If the main direction of the flow does not fluctuate much, then the loading will be constant in one direction. Changes in direction can occur as well, for example in tidal areas, where the ASG would experience cyclical changes of unidirectional flow, generally once or twice a day, depending on the geographic location. Rip currents and submerged ocean currents can also mean that the flow is mainly unidirectional. In this context, it is then important to understand the dependence between ASG and the incident hydrodynamic conditions. Furthermore, the flow within and in the wake of the meadow is going to be greatly affected by the meadow itself.

(c) **Artificial seagrass response to oscillatory flow.** As coastal ecosystems, seagrasses are mostly exposed to oscillatory flow, meaning that wave dynamics and its effect on ASG need to be investigated in detail. As mentioned before, the effect of the moving fluid on the ASG is largely dependent on the mechanical properties of the ASG. The nature of oscillatory flow means that loads on ASG are going to be cyclical in a smaller time scale than that of tidal areas, i.e. a frequency in the order of a few seconds. Drag is exerted on both sides of the ASG and, depending on how deep the ASG is set, may even incur drag directed towards the surface, as oscillatory flow is two-dimensional. Flow attenuation is then greater within the ASG meadow, with a lessened effect on its wake (with respect to the wave propagation direction) compared to unidirectional flow. However, the effect of the ASG on wave energy dissipation may have a greater extent but also depends greatly on the incident wave dynamics, i.e. incident wave heights and wave periods.

(d) **Blade dynamics of submerged vegetation.** Seagrass blades reconfigure depending on the incident hydrodynamics. The extent of this reconfiguration depends on the flow intensity, i.e. high or low-energy environments. The mechanical properties of the ASG can thus dictate its response to incident hydrodynamics. The stiffer the material (commonly expressed by means of the flexural rigidity), the less it bends with higher hydrodynamic input. The less it bends, the greater the orthogonal contact area with the incident flow, which in turn means greater drag. The greater the drag, the higher the attenuation of flow. Furthermore, changes in flexural rigidity within a single shoot or leaf can affect the behavior of the motion. For example, a weak base compared to the rigidity of the leaf will make it move like a cantilever. Extremely flexible leaves, on the other hand, will flow with the fluid, following its path and reconfiguring parallel to flow. The mechanics of these motions require different methods for calculation as the load distribution also changes depending on the position, which is a function of the incident load, i.e. the flow velocity.

(e) **Base layer prospects for artificial seagrass.** The ASG must be fixed to the bed in some way. Single-shoot transplantation techniques (see e.g. Zhou et al., 2014) can be labor intensive,

**1**

which would also be the case for artificial elements. An extrinsically manufactured mat of ASG may be the solution to this problem, thus easing installation. The mats, however, need to be placed while ensuring they stay in place. This means that they also need to resist the incident hydrodynamic conditions. The mats incur surface drag from the flow, but also from the drag transmitted by the artificial vegetation attached to it. It is therefore necessary to understand how this drag force is distributed within the anchoring system and how high it is expected to be. Knowing this, the proper anchoring system can be chosen to ensure longevity of the ASG mat. Nonetheless, the mat should share the biodegradable properties of the ASG to ensure the self-sustainability of the proposed solution.

(f) **Positive feedback mechanisms provided by artificial seagrass.** When thinking about restoration, the effect of ASG on incident hydrodynamics becomes a main driver for success. Attenuated wave energy may increase sedimentation, thus increasing light availability for growing seedlings. Moreover, the ASG protects these seedlings against uprooting and dislodgement. But the canopy is not the only area of interest. Proper restoration means that the vast areas of seagrass, which can be in the order of hectares, should benefit from ASG. Hence, the effect of the ASG goes beyond the meadow of artificial elements. Here, we focus on the shelter provided on the outer bound of the meadow, which will allow new seagrass to grow and extend the seagrass cover to an area greater than the ASG itself. The newly grown seagrass will in turn provide shelter for more seagrass, thus expanding the meadows and approaching large-scale restoration. For this, the shelter provided in the wake of the ASG is also studied and discussed here.

The topics described above correspond to the essence of this dissertation. These brief explanations are intended to provide a rough understanding of the concepts involved in flow-structure interaction and its relation to seagrass restoration. Focusing on these concepts, experiments were designed and carried out in different hydraulic facilities. Experimental data were analyzed and discussed in the context of restoration, and the results published in international peer-reviewed scientific journals with the goal of knowledge sharing and advancing the state-of-the-art in: i) flow-vegetation interaction; ii) seagrass restoration techniques; and iii) base-layer design and performance under marine conditions. Technical elucidations of these concepts are contained within the introduction of the corresponding chapters in this dissertation. The outline below (Section 1.3) provides an overview of the chapters where these topics are discussed. Thorough literature reviews, in-depth discussions, and contextualization with restoration are all part of each of the main chapters contained in this dissertation (Chapters 2, 4, and 5). Ultimately, beyond advancing the state-of-the-art of points i), ii), and iii) above, this dissertation should: 1) inform practitioners on the feasibility of employing ASG mats for restoration; 2) build a bridge for interdisciplinary work between engineers, ecologists, and material scientists, which is needed for successful restoration attempts with ASG; and 3) inform a more general public of the importance of seagrass and the need for restoration.

## 1.3 Thesis Outline

This research takes the form of a cumulative dissertation, thus building upon peer-reviewed studies that I drafted and either published in or submitted to international scientific journals in co-authorship with other scientists. In addition, other publications where I participated (as described above under Author Statement) were used to support the research presented here. The corresponding journals and publishers are indicated on the cover page of each of the chapters. The dissertation consists of a total of 7 chapters. The main chapters are Chapters 2, 4, and 5, which correspond to the first-authored peer-reviewed studies.

Chapter 2 focuses on ASG under unidirectional currents and the effect of meadow length (with respect to flow direction) on flow. Specifically, the wake structure of the flow behind ASG meadows of different lengths is discussed. State-of-the-art flow measurements provide high spatial resolution records of the flow behind ASG meadows at length scales not tested before in any laboratory. Finally, shelter effects are discussed as part of the positive feedback mechanisms provided by the meadow in the context of seagrass restoration under consideration of different incident flow velocities.

Chapter 3 complements the preceding chapter with additional unidirectional flow experiments in the same facility. Studies on the response of different materials to flow show how the stiffness of the material, together with its geometric characteristics, drive the flow response. This in turn provided the basis for the selection of a prototype ASG to be tested under oscillatory flow conditions –albeit not biodegradable yet, but providing target mechanical properties. In addition, the distribution of the biomass along artificial vegetation leaves is analyzed to broaden the picture depicted by the results of Chapter 2 to possible heterogeneous ASG choices.

Chapter 4 shifts the focus toward oscillatory flow. Before entering deeply into wave dynamics around ASG, the chosen base layer (i.e. the mat) needed to be analyzed and discussed. Chapter 4 thus focuses on the ASG base layer, starting with the material properties and performance under marine conditions of prospective biodegradable mats of different construction. Anchor distribution is also analyzed for the different mats, with different anchor number and positioning. Finally, a prototype ASG mat is selected for testing based on these experiments and tested against varying hydrodynamic conditions. The anchoring response of the (artificial) vegetated mats is measured and analyzed and ultimately discussed in the context of field-deployable mats and the minimum requirements these should fulfill if they are to be used to facilitate seagrass restoration.

Chapter 5 focuses on the flow dynamics around the ASG mats previously described. Water surface elevation and orbital velocities within the water column were analyzed to study the effect of ASG on wave height evolution and the velocity structure surrounding such mats, respectively. The wave energy dissipation was calculated based on the wave height evolution and velocity reduction and helped to assess the service provided by the ASG regarding the facilitation of the right conditions for seagrass growth. The experiments are insightful with regard to field measurements and pilot projects for restoration, as the sheer scale of the hydraulic facilities allows for testing on a prototype scale directly.

Chapter 6 briefly discusses the findings of the previous chapters under a more generalized context, providing a summary of what the results mean for future flow-vegetation interaction research, the mechanical properties of materials under marine conditions, and the forces that

*1*

may be expected from hydrodynamic loading not only on freely-moving submerged structures but also on the anchors supporting them. Furthermore, the implications of these findings with regard to seagrass restoration are also discussed. Facilitation through submerged structures and recommendations for pilot projects are given to help scientists as well as practitioners get a better understanding of the considerations to take when planning field experiments and ultimately restoration attempts. Finally, the shortcomings of the results presented here are given, which motivate the recommendations for future research, before the concluding remarks close this work.

# WAKE LENGTH OF AN ARTIFICIAL SEAGRASS MEADOW UNDER UNIDIRECTIONAL FLOW

## 2.1 Introduction

Submerged Aquatic Vegetation (SAV) is a part of coastal and estuarine ecosystems, which in turn are essential for both human and wildlife (Barbier et al., 2011). Their ability to alter their surroundings has granted them the title of ecosystem engineers (Koch, 2001; Bouma et al., 2005) and rendered them as an attractive supplement towards green engineering solutions for coastal protection (IPCC, 2019; James et al., 2019; Seddon et al., 2020). Among these ecosystems are seagrass meadows which provide important ecosystem services such as nutrient cycling (Unsworth et al., 2019) and coastal protection (Ondiviela et al., 2014). Despite this, they have sustained a worldwide loss of at least 29% of the total surveyed cover due to climate-related and direct anthropogenic stress (Duarte, 2002; Waycott et al., 2009). Therefore, seagrasses have been a focus of ecosystem restoration efforts through many studies and coastal ecosystem restoration projects over the past few decades (Fonseca et al., 1987; van Katwijk et al., 2000; van der Heide et al., 2007; Paling et al., 2009).

Van Katwijk et al. (2009; 2016) provide a comprehensive review of restoration efforts and present a guideline based on results from experiments and pilot studies. Several factors were identified that affect the success rate of seagrass reestablishment and survival, such as the biotic environment (Unsworth et al., 2015), effectiveness of the reproduction mechanisms (McMahon et al., 2014), light availability (Orth et al., 2006b; van der Heide et al., 2011) and hydrodynamic conditions (Fonseca and Bell, 1998); the two latter represented the most defining ones (van Katwijk et al., 2016). Loss of seagrass leads to enhanced hydrodynamic conditions which in turn hinders restoration efforts for re-establishment (van Katwijk et al., 2000; van der Heide et al., 2007). Seagrass survival studies analyzing seed dispersal and cloning (Orth et al., 1994; McMahon et al., 2014; Statton et al., 2017) commonly recognize the importance of shelter, i.e. areas protected by aquatic vegetation, coral reefs and other aquatic structures against high current and wave loading. This calls for restoration strategies that provide shelter to enhance natural protection for seagrass in its early stages.

One lesser-known restoration approach is the use of synthetic structures akin to actual seagrass, i.e. artificial seagrass (ASG), which can provide shelter to growing meadows. ASG can mimic the physical properties of real seagrass, thus emulating services such as providing habitat for fauna (Bell et al., 1985) and promote seagrass growth within a small area it encloses (Tuya et al., 2017) through reduction of hydrodynamic forcing. This characteristic of ASG has been exploited within physical experiments regarding seagrass research (e.g. Bouma et al., 2005). However, the use of ASG for restoration has not been sufficiently studied. Carus et al. (2021) provide an insight into the current stance regarding this approach and show that much research is still needed. In this study, we focus on the effectiveness of ASG at providing shelter to promote seagrass growth, the target species being *Zostera marina*. Pilot restoration projects generally choose wave-sheltered areas (e.g. by other ecosystems), as seagrasses prefer such conditions (Barbier et al., 2011). We, therefore, focus on the seagrass-flow interaction and test the effect of meadow length on incident current reduction.

### 2.1.1 *Shelter Definition*

Understanding the wake structure behind the seagrass meadow is essential for defining the shelter distance. Flow modulation in the wake of a meadow is a result of above-ground biomass (Paul, 2018) and suggests that the extent of shelter along the wake depends on meadow morphology and

**2**

the hydrodynamic conditions. However, a clear definition of shelter is not available in the literature for any specific meadow configuration. In the context of restoration, efficient shelter in the wake of ASG could be validated through the survival of seeds and seedlings deployed in and around the ASG. Shelter definition is complicated nonetheless, as it depends on the target species to protect. In general, flow velocity should be reduced to levels which the target species can resist. The shelter distance will in turn depend on the incident velocity and ASG meadow morphology. Early studies on established and robust *Z. marina* have shown a tolerance for currents ranging from 120–150 cm s$^{-1}$ (Fonseca et al., 1983). However, on growing SAV, Madsen et al. (2001) reported a beneficial range of current velocities as low as 0.02–0.06 cm s$^{-1}$, suggesting the current velocity around growing seagrasses should be drastically reduced. Koch et al. (2010) analyzed flow effects on seed movement of three different seagrass species and showed that velocities of about 10–25 cm s$^{-1}$, depending on sand grain size, allow for settlement and deposition. Orth et al. (1994) reported a critical bottom shear stress velocity of 0.7 cm s$^{-1}$ (corresponding to flow velocity of 8 cm s$^{-1}$) for *Z. marina* seeds. These values provide threshold velocities that should not be exceeded in order to ensure the survival of growing meadows.

The flow structure within canopies of model aquatic vegetation has been widely studied (e.g. Gambi et al., 1990; Fonseca et al., 1983; Nepf and Vivoni, 2000; Poggi et al., 2004). It has been shown that flow adjustment occurs along the meadow in the streamwise direction and depends on meadow morphology and hydraulic conditions (Chen et al., 2013). Further, wake effects have been analyzed by a handful of publications concentrating on flow structure characterization (Folkard, 2005; Lefebvre et al., 2010; Chen et al., 2012; Zong and Nepf, 2012; Hu et al., 2018). Most of these studies test flow velocities under 30 cm s$^{-1}$, utilizing Acoustic Doppler Velocimetry to build velocity profiles out of point measurements along the wake, with the furthest measurement usually ranging from 10—20 times the canopy height (for reconfigured flexible meadows). A comparison of studies and their respective initial model parameters, including this study, can be found in Table 2.1. Here, we characterize the flow structure behind submerged meadows of different lengths up to a distance 100 times the reconfigured canopy height. Thereafter, we estimate the shelter distance of ASG meadows of different lengths under high (> 30 cm s$^{-1}$) incident unidirectional currents based on flow velocity thresholds of 10, 20, and 30 cm s$^{-1}$. The shelter distance is then the horizontal distance behind the meadow up to which the velocity threshold is not exceeded. Meadow density and plant mechanical properties were not varied and are not further discussed here.

## 2.2 Experimental Set-up

The experiments were carried out in the circular track-flume at Ludwig-Franzius Institute of the University of Hanover, which comprises a width and a height of 1 m, respectively, with cement plastered walls and smoothed concrete floor (for a detailed flume description, see Goseberg et al., 2013). Flow is generated by 4 pumps with an installed capacity of 16 kW, able to generate constant currents of up to 0.8 m s$^{-1}$ in either direction. The recirculating flow passes through an 18-m-long horizontal and straight stretch, where model ASG was set up and the measurements were performed (Figure 2.1a). Flow straighteners were used to reduce swirls along the measuring area. At the center of the stretch, acrylic glass observation windows span along 3 m on both sides of the flume and

Table 2.1: Studies dealing with wake structure within the context of aquatic vegetation.

| Study | Device | Model Vegetation | Sub-mergence state | Water Depth [m] | Patch Length [m] | Patch Width [m] | Canopy height [m] $a$ | $b$ | Distance measured along wake [m] | ratio to $a$ | ratio to $b$ |
|---|---|---|---|---|---|---|---|---|---|---|---|
| Lefebvre et al. (2010) | ADV | Flexible* | Submerged | 0.40 | 0.50–2.25 | 0.15–0.30$^{\dagger}$ | 0.23–0.28 | 0.12–0.18 | 2.50 | 8.90–10.87 | 13.88–20.83 |
| Folkard (2005) | ADV | Flexible | Submerged | 0.35 | 1.00 | 0.90 | 0.50 | 0.175 | 2.40 | 4.80 | 13.71 |
| Zong and Nepf (2012) | ADV | Rigid | Emergent | 0.13 | 0.12–0.42 | 0.12–0.42 | 0.13 | - | 9.00 | 67.67 | - |
| Chen et al. (2013) | ADV | Rigid | Submerged | 0.14–0.28 | 1.50–4.80 | 1.20 | 0.07 | - | 0.50 | 7.14 | - |
| Chen et al. (2012) | ADV | Rigid | Emergent | 0.13 | 0.05–0.42 | 0.05–0.421‡ | 0.13 | - | 9.00 | 67.67 | - |
| Hu et al. (2018) | ADV | Flexible | Submerged | 0.14 | 0.1 | 0.10–0.40$^{\dagger}$ | 0.13–0.28 | 0.065–0.07 | 0.80 | 2.86–6.15 | 11.42–12.31 |
| This study | PIV | Flexible | Submerged | 0.40 | 1–3 | 1.00 | 0.2 | 0.072–0.097 | 8.40 | 42 | 86.6–116.7 |

*Used live vegetation; $^{\dagger}$ tested also (or $^{\ddagger}$ only) patches not spanning the full flume width. $a$: upright height, i.e., for flexible canopies, the extended leaf; $b$: average reconfigured height.

aluminum plates make up the bed (covering a recession of the bed otherwise used to test different bed materials).

A state-of-the-art stereoscopic Particle Image Velocimetry (PIV) system from LaVision GmbH was used here to measure 3D instantaneous velocities behind model ASG. Two CCD Imager ProSX 5MP-resolution cameras were located outside the flume on both sides, each looking through an observation window at an angle of 30° into the flume (Figure 2.1b). Image distortion caused by refraction was corrected through water-filled prisms whose outer planes were parallel to the viewing plane of the cameras. The viewing angle of the cameras also created a distortion which was corrected during image post-processing utilizing LaVision data acquisition and processing software Davis. The field of view (FoV) was formed within the illuminated area of a double-pulsed Nd:YAG laser expanded into a laser sheet parallel to the $x$-$z$ plane, located 55 cm from one of the walls. Polyamide-12 seeding material (density 1.06 g cm$^{-3}$ and diameter 50 $\mu$m) was used to visualize and measure flow velocity using PIV. Along the $x$-axis, the FoV was located in the center of the straight stretch following the window location (Figure 2.1a).

Throughout the experiments, the $x$-axis corresponded to the streamwise direction with $x = 0$ at the trailing edge of the ASG meadow, regardless of the length; the $y$-axis to the spanwise direction (perpendicular to flow and parallel to the bed); and the $z$-axis vertical along the water column, with $z = 0$ at the bed (Figure 2.1b). An additional reference point, $x'$, is given to mark the distance from the leading edge along the $x$-axis. The velocity components $u$, $v$ and $w$ correspond to the $x$, $y$ and $z$ directions, respectively. Throughout this chapter, the subscripts 0 and k indicate measurements at upstream and downstream positions, respectively. Each PIV measurement consisted of 500 dual-frame images taken at a frequency of 7 Hz ($\Delta t = 0.143$ s). A convergence analysis done for the instantaneous velocities as well as the resulting normal and shear stresses showed that 500 images sufficed for the purposes of this study, as these values were stable within that range. 3-Component

**2**
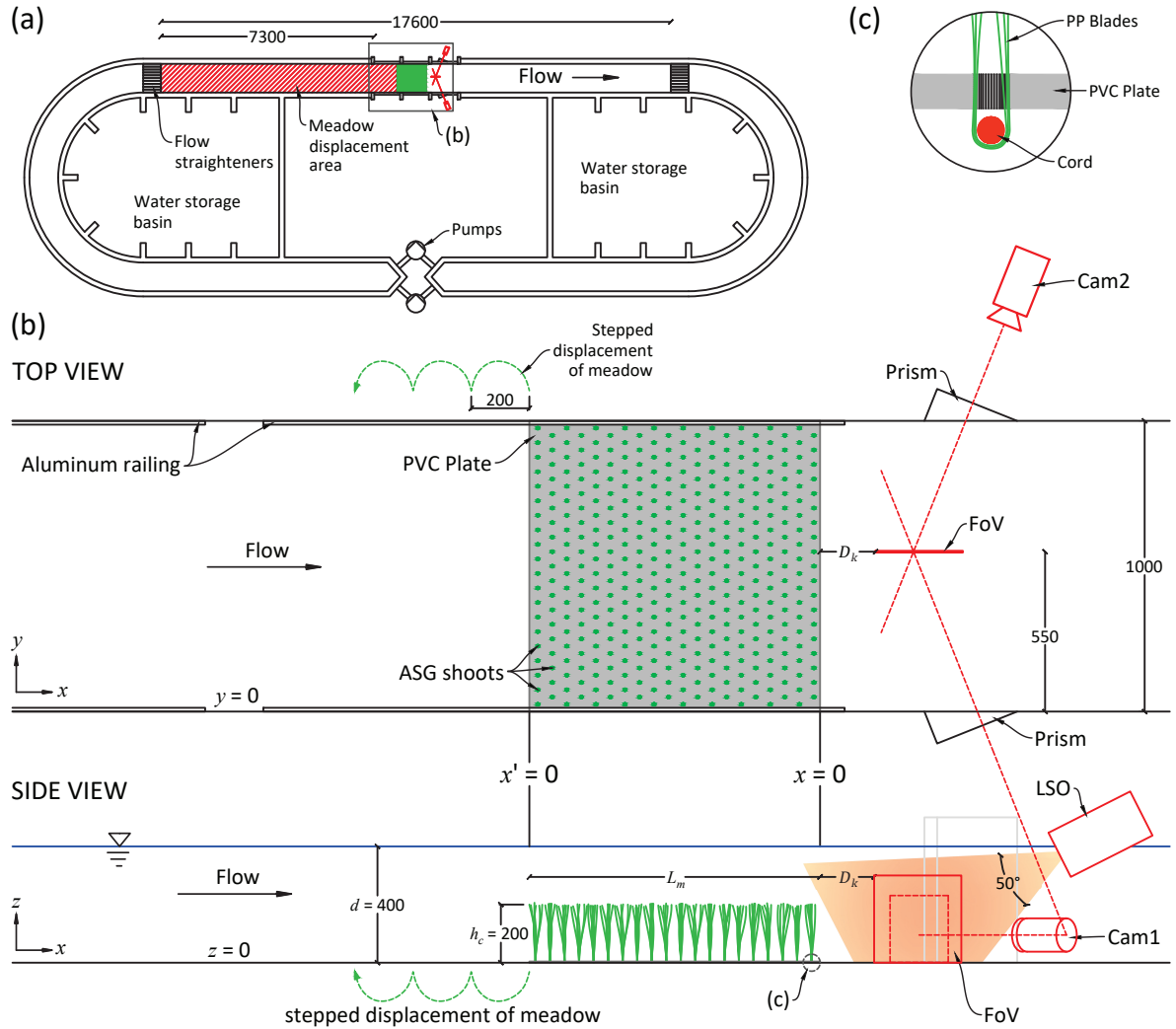


Figure 2.1: (a) Plan view of the recirculating flume. The diagonally hatched area indicates the section where the ASG meadows were displaced. (b) General set-up of stereoscopic PIV and cameras, with a 1-by-1-m ASG meadow. The dotted line within the FoV shows the effective (cropped) 200x230-mm window extracted from each measurement. $x$ and $x'$ measure distance along the $x$-axis with 0 at the trailing and leading edge of the meadow, respectively. (c) Detail of shoot construction. Cords ran normal to flow and aligned to the rows of perforations in the PVC plate. All dimensions in mm. LSO: Light Sheet Optic; FoV: Field of View; $L_m$: meadow length; $D_k$ wake distance; $h_c$: canopy height; and $d$: water depth.

$-u$, $v$ and $w$ –instantaneous velocity matrices (velocity fields) were produced for a 2D plane ($x$-$z$) with a size of 156x166 pixels. This corresponded to a size of 263x280 mm per dataset after image correction, which yielded a resolution of 1.6970 mm per pixel (in both $x$ and $z$-directions).

The water depth was kept constant at $d = 0.4$ m. The incident streamwise velocity is described as input velocity $u_0$ and corresponds to the bulk velocity measured in the flume at $z = 25$ cm, where no effect of the bed was observed. Control streamwise velocity measurements were done in the empty flume (no ASG) at different input velocities in order to calibrate the pumps and obtain control profiles to be contrasted with the velocities measured in the presence of ASG. The control average streamwise velocity profiles were used to calculate the shear velocity $u_*$ (Table 2.2) and Coles' wake strength $\Pi$ following the modified log-wake law (Equation 2.1, after Guo et al., 2005):

$$\frac{u_0 - u(z)}{u_*} = -\frac{1}{\kappa}\left(\ln\xi - 2\Pi\cos^2\frac{\pi\xi}{2} + \frac{1-\xi^3}{3}\right) \tag{2.1}$$

where $\xi$ is the relative distance from the wall and $\kappa = 0.41$ is the von Kármán constant.

In addition, measurements were also done directly in front of each meadow (FoV from $x' = -20$ cm to $x' = 0$) to obtain an upstream velocity field. Preliminary trials employing low streamwise velocities ranging from $u_0 < 1 - 30$ cm s$^{-1}$ behind a 1-by-1-m patch were done to assess the effect of the ASG on flow and thus select 3 input velocities to be further analyzed for shelter. Analysis of the streamwise velocity along the wake showed that flow velocity reduction was more obvious for input velocities $u_0 \geq 20$ cm s$^{-1}$. Nevertheless, a shelter effect could be seen for the whole range of input velocities, thus suggesting a significant service value for sheltering. As a result, higher input velocities of $u_0 = 30$, 45, and 60 cm s$^{-1}$ were chosen to investigate the full wake development and test the limits of shelter capabilities of the chosen configurations. For three different meadow lengths $L_m$, this provided a total of 9 different configurations to measure the wake flow. The channel Reynolds numbers, based on $u_0$ and channel geometry, ranged from 57500–115000.

### 2.2.1 *Artificial Seagrass (ASG) Meadows*

Regarding restoration, an efficient ASG meadow is one with a density small enough to provide space for seagrass to grow and that does not reduce light availability, i.e. through blockage of light by the seagrass blades (shadowing). Therefore, a low shoot density $N = 390$ shoots m$^{-2}$ (compared to nature, e.g. Ondiviela et al., 2014; Fonseca et al., 2019) was chosen. ASG meadows were then produced using 4-mm-thick PVC plates as a base and fixed to the bed by aluminum railings, which were also used to facilitate horizontal meadow displacement (Figure 2.1b). An alternating shoot placement pattern was chosen to avoid flow streams within the meadow, with a spacing $S = 5$ cm given by 5-mm perforations on the PVC plates. Each shoot consisted of 6 blades of polypropylene (PP; modulus of elasticity $E = 1.49x10^8$ Pa and density $\rho_{PP} = 0.9$ g cm$^{-3}$) of width $b_v = 5$ mm, thickness $t_v = 0.11$ mm and length $h_c = 200$ mm assembled by folding 3 strips in half over a thin cord, then passing both ends through a perforation (Figures 2.1c, 2.2). In this study, $h_c$ also represents the canopy height under no-flow condition, i.e. no blade reconfiguration. The dynamic similarity to real seagrass was tested using the buoyancy to rigidity ratio ($\lambda_1$ in Ghisalberti and Nepf, 2002), which yielded a value of 0.44 s$^2$ m$^{-1}$. This value is higher than the 0.055 s$^2$ m$^{-1}$ used by Ghisalberti and Nepf (2002), which best matched their target plant motion, due to the low $E$ and density of PP; however, field values may range from 0.001–1 s$^2$ m$^{-1}$ for different seagrasses (see Ghisalberti and Nepf, 2002, and references therein for a detailed description of this parameter). The frontal area per canopy volume (as described in Nepf, 2012a) was $a = b_v\Delta S^{-2} = 2$ m$^{-1}$ at the base (blades superposed) and 12 m$^{-1}$ at the top (all blades separated). For further calculations, $a$ was taken as the average value over $h_c$, i.e. $a = 7$ m$^{-1}$, which resulted in a solid volume fraction of $\varphi = at_v = 7.7x10-4$ (Nepf, 2012a). A total of three 1x1-m ASG mats were fabricated to produce 3 meadow lengths $L_m = 1$, 2 and 3 m, after which flow reduction should be distinguishable (Fonseca et al., 1982), covering the full width of the flume.

The flexibility of PP ASG blades leads to reconfiguration, resulting in a reconfigured canopy height $h_r$ varying with velocity. $h_r$ was determined manually by means of imagery taken during the
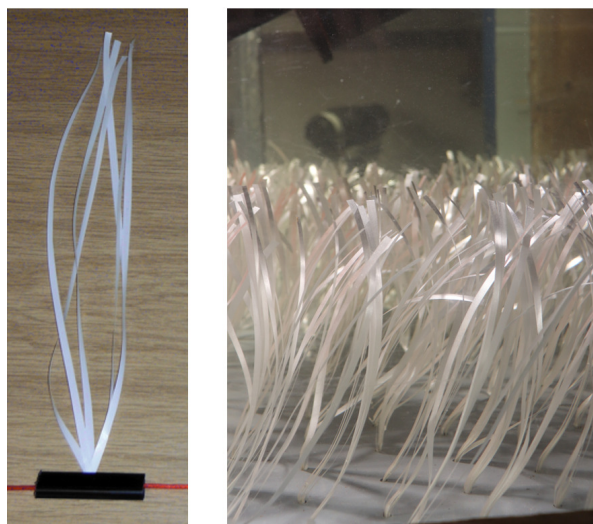
Figure 2.2: Model artificial seagrass (ASG) made of 3 strips of polypropylene (PP) bent in half and bound by a cord at the bottom. (left) 1 shoot; (right) submerged meadow.

experiments. A camera was fixed beside the flume directed orthogonally toward one of the windows. For the 2-m-long meadow, 2 photographs and a 160-s-long video of the meadow under the influence of flow at all 3 tested velocities were taken prior to the PIV measurement. This was repeated for each run for as long as the meadow was visible through the observation window. A tape measure aligned vertically on the window was used to read the meadow height in each photograph under each velocity, thus obtaining $h_r$ at 20-cm intervals from $x = 0$ to $x = 2$ m. The video was used to (qualitatively) observe plant sway and determine the plausibility of the taken tape measurement.

For the wake measurements, the ASG meadow was located upstream of the FoV. One FoV then corresponded to a flow field starting at a distance $D_k$ downstream of the meadow (Figure 2.1b). The entire meadow was progressively displaced opposite the direction of flow at 20-cm intervals, i.e. $D_k$ increased in 20-cm steps (overlap of around 5 cm between measurements) until it was no longer possible. Each step corresponded to one measurement and $x = 0$ moved synchronously with the ASG meadow so that the $x$ position of the FoV increased 1 step size per measurement. This resulted in 357 datasets for all tested configurations. The streamwise centered location of the observation windows (and FoV) meant that meadow displacement was limited to the half-distance of the flume. The length of the meadow itself also limited the maximum possible distance $D_k$ to be measured, such that the PIV measurements were carried out until $D_k = 840$, 740 and 640 cm along the wake for the 1, 2, and 3-m long meadows, respectively.

## 2.3 Data Analysis

### 2.3.1 *Flow Structure*

The PIV output matrices were imported into MATLAB to extract velocity vectors and analyze flow development along the wake of the meadow. A smaller window of 200x230 mm was cropped out of each step-wise measurement. Each dataset consisted of three sets (one for each velocity component) of 500 matrices representing 500 instantaneous velocity fields ($u$, $v$ and $w$) starting at

each given distance $D_k$ (Figure 2.1b) behind the meadow. Time-averaged statistics (mean, denoted by the overbar, i.e. $\overline{u}$, $\overline{v}$, and $\overline{w}$, and standard deviation) were calculated from the instantaneous velocity matrices. The fluctuating velocity components, denoted with a prime ($u'$, $v'$ and $w'$), were calculated by subtracting the mean from each instantaneous velocity. The computed fluctuating components were used to calculate Turbulent Kinetic Energy $TKE$ using Equation 2.2. However, it is important to note that the employed sample size (500 images) and frequency (7 Hz), both subject to experimental limitations, are both too low for realistic, reliable estimation of turbulence. Higher frequency fluctuations, for example, cannot be detected. The depiction made here intends to provide a qualitative evaluation of the turbulence distribution and tendency along the wake of the meadow and should not be taken as a full characterization of the $TKE$.

$$TKE = \frac{1}{2}\left(\overline{u'}^2 + \overline{v'}^2 + \overline{w'}^2\right) \tag{2.2}$$

The flow structure within the flume is affected by the meadow starting at the leading edge ($x' = 0$ m). The streamwise velocity decelerates with increasing $x'$ due to canopy drag, while the vertical velocity increases ($\overline{w} > 0$ m s$^{-1}$) starting at the leading edge as the flow is redirected upwards and decays with increasing $x'$ (Chen et al., 2013). $\overline{w}$ then reaches 0 at a distance described as the initial adjustment length $X_D$, which is a function of the canopy drag length scale $L_d$ and the drag coefficient $C_D$. $L_d$ has been adapted to aquatic canopies from analogies with surface vegetation interaction with atmospheric flows and is calculated as $L_d = 2(C_D a)^{-1}$ for $\varphi < 0.1$ (Nepf, 2012a). Further, a mixing layer develops along the streamwise direction (Ghisalberti and Nepf, 2002), therefore the flow structure at the trailing edge will vary for the different meadow lengths. Here, we characterize flow adjustment for the different test cases by comparing the mixing layer thickness, $\delta$, at the trailing edge of each meadow. $\delta$ depends on the velocity at the top of the canopy $U_{h_r}$, measured here at the trailing edge for each case; the flow velocity exiting the meadow $U_1$, measured here at the middle of the canopy layer, corresponding to the used $a$ and $\varphi$; and the velocity above the meadow, $U_2$, corresponding to the logarithmic profile (Equation 2.3, after Chen et al., 2013).

$$\delta = 2\left(\frac{\Delta U}{U_{h_r}}\right)L_s \tag{2.3}$$

In Equation 2.3, $\Delta U = U_2 - U_1$ and $L_s$ is the shear length scale, which depends on $C_D$. We calculated $C_D$ from the stem Reynolds number $Re$ and $\varphi$ using the empirical solution proposed by Tanino and Nepf (2008). Note that this empirical model was proposed after experiments with rigid cylinders as model vegetation. Here, we take flexibility into account by employing the reconfigured height $h_r$, as proposed by (Luhar and Nepf, 2011). We calculated $Re$ using the average measured near-bed flow velocity in front of the meadow up to half of $h_r$, i.e. $\overline{u}(0 < z < 0.5h_r)$ at $x' = -0.5h_c$, and the single stem width $b_v$. We then calculate $L_s$ and $X_D$ with Equations 2.4 and 2.5, respectively (Chen et al., 2013). The center of $\delta$ was then set at a distance $0.5\theta$ above $h_r$, where $\theta$ is the momentum thickness, as described by Ghisalberti and Nepf (2002).

$$\frac{L_s}{h_r} = 0.4(C_D a h_r)^{-1} \tag{2.4}$$

Table 2.2: Experimental parameters for each test case calculated based on the respective reconfigured height $h_r$ and solid volume fraction $\varphi = 0.00077$ and $a = 7$ m$^{-1}$. The attenuation ratio $r_a$ is given for $x = 0.5 h_c$.

| $u_0$ [cm s$^{-1}$] | $L_m$ [m] | $h_r$ [m] | $u*$ [m s$^{-1}$] | $U_1$ [m s$^{-1}$] | $U_2$ [m s$^{-1}$] | $U_{h_r}$ [m s$^{-1}$] | $Re$ [-] | $C_D$ [-] | $L_s/h_r$ [-] | $L_d$ [m] | $X_D$ [m] | $\delta$ [m] | $r_a(h_r)$ [-] |
|---|---|---|---|---|---|---|---|---|---|---|---|---|---|
| 30 | 1 | 0.097 | 0.023 | 0.025 | 0.355 | 0.262 | 1.06E+02 | 1.367 | 0.432 | 0.209 | 0.980 | 0.105 | 0.587 |
|    | 2 | 0.097 | 0.021 | 0.016 | 0.363 | 0.161 | 7.05E+01 | 1.592 | 0.371 | 0.179 | 0.936 | 0.154 | 0.745 |
|    | 3 | 0.097 | 0.024 | 0.027 | 0.378 | 0.167 | 1.15E+02 | 1.335 | 0.443 | 0.214 | 0.988 | 0.180 | 0.729 |
| 45 | 1 | 0.083 | 0.032 | 0.053 | 0.521 | 0.410 | 2.28E+02 | 1.132 | 0.606 | 0.252 | 0.954 | 0.115 | 0.469 |
|    | 2 | 0.083 | 0.033 | 0.035 | 0.522 | 0.265 | 1.49E+02 | 1.241 | 0.553 | 0.230 | 0.920 | 0.169 | 0.731 |
|    | 3 | 0.083 | 0.021 | 0.050 | 0.558 | 0.299 | 2.16E+02 | 1.144 | 0.600 | 0.250 | 0.950 | 0.170 | 0.650 |
| 60 | 1 | 0.072 | 0.038 | 0.060 | 0.666 | 0.504 | 2.61E+02 | 1.106 | 0.721 | 0.258 | 0.882 | 0.124 | 0.480 |
|    | 2 | 0.072 | 0.046 | 0.054 | 0.680 | 0.372 | 2.34E+02 | 1.127 | 0.708 | 0.254 | 0.875 | 0.170 | 0.695 |
|    | 3 | 0.072 | 0.023 | 0.069 | 0.713 | 0.364 | 2.97E+02 | 1.084 | 0.736 | 0.264 | 0.890 | 0.187 | 0.663 |

$$\frac{X_D}{L_d} = 1.5(1 + 2.3 C_D a h_r) \tag{2.5}$$

Finally, a simple quantification of the reduction of flow velocity, here described as attenuation ratio $r_a$, was done by integrating the area enclosed by the average streamwise velocity profiles ($\hat{u}$) up to $z = h_r$ utilizing Simpson's rule (Equation 2.6, newton-cotes quadrature rules) and the relative difference in flow velocity between upstream ($x' = -0.5 h_c$) and downstream ($x = 0.5 h_c$) using Equation 2.7. Note that $r_a$ provides a comparison between flow upstream and downstream for $0 < z < h_r$ and does not reflect changes along the whole water column or along the spanwise dimension. $r_a$ provides a simple quantification of the loss of velocity which, from continuity, can be seen in the upper part of the profile. A summary of all calculated parameters including hydraulic conditions for our test cases is given in Table 2.2.

$$\hat{u} = \int_0^{h_c} \overline{u}(z)\,dz = \frac{1}{6}\sum_{n=1}^{N}(z_{n+1} - z_n)\left[\overline{u}(z_n) + 4\overline{u}\left(\frac{z_n + z_{n+1}}{2}\right) + \overline{u}(z_{n+1})\right] \tag{2.6}$$

$$r_a = \frac{\hat{u}_0 - \hat{u}_k}{\hat{u}_0} \tag{2.7}$$

### 2.3.2 *Shelter Distance*

Vector stitching between datasets was applied to the calculated mean matrices to produce a full wake matrix for each configuration. The measured velocities were normalized by the corresponding input velocity. The positive effect of ASG on flow regarding shelter for restoration projects was interpreted and processed from the yielded data in two different ways: 1) the overall extent of the influence along the $x$-axis, which is defined here as the reach $R_k$, was obtained by calculating the difference between the upstream velocity field and the velocity fields at each step ($\Delta u$) whereby $R_k$ represents the distance behind the meadow at which initial conditions, i.e. $\Delta u = 0$ m s$^{-1}$ along the whole $z$-axis, were met; and 2) the span of continuous shelter provided by the meadow directly behind it along the $x$-axis, defined here as the shelter distance $S_k$, and determined for different threshold velocities chosen based on literature, as described below. Unfortunately, some

Table 2.3: Summary of shelter distance results. Reach of the impact of the meadow up to 90% ($R_{k,90}$) normalized by $h_c$; Slopes of $R_{k,90}$ and the tailing influence of the meadow normalized by $h_c$; and Shelter distance ($S_k$) normalized by $h_c$ for 3 incident velocities (denoted by the scalar subscript after $S_k$ given in cm s$^{-1}$). Missing values under $S_{k,90}$ correspond to an unreadable $S_k$ given that for $u_0 = 30$ cm s$^{-1}$, a threshold of likewise 30 cm s$^{-1}$ cannot be surpassed.

| $u_0$ | $L_m$ | $R_{k,90}/h_c$ | $R_{k,90}$ Slope | Tailing Slope | $S_{k,10}/h_c$ | $S_{k,20}/h_c$ | $S_{k,30}/h_c$ |
|---|---|---|---|---|---|---|---|
| [cm s$^{-1}$] | [m] | [-] | [-] | [-] | [-] | [-] | [-] |
| 30 | 1 | 17.69 | 0.021 | 0.011 | 3.65 | 12.20 | - |
| | 2 | 16.99 | 0.020 | 0.012 | 3.30 | 11.48 | - |
| | 3 | 17.16 | 0.018 | 0.013 | 2.63 | 10.43 | - |
| 45 | 1 | 15.99 | 0.025 | 0.008 | 0.90 | 2.50 | 9.35 |
| | 2 | 15.95 | 0.016 | 0.008 | 1.15 | 3.28 | 9.80 |
| | 3 | 17.16 | 0.025 | 0.010 | 0.95 | 3.00 | 8.85 |
| 60 | 1 | 12.33 | 0.028 | 0.012 | 0.00 | 1.08 | 3.18 |
| | 2 | 16.99 | 0.019 | 0.009 | 0.55 | 1.25 | 3.48 |
| | 3 | 15.12 | 0.028 | 0.006 | 0.00 | 1.28 | 3.25 |

PIV measurements showed inaccurate measurements near the bed due to high laser reflection. Considering this and that velocities near the bed are close to 0 due to bed friction, $S_k$ was set at the point along the $x$-axis where the mean velocity measured 3 cm above the bed exceeded the threshold velocity to be able to find a reliable and comparable value.

For $R_k$, $\Delta u$ was calculated and graphically stitched together, thus providing an overview of the incremental velocity changes induced in the wake. However, the velocity profile along the wake returns to normal conditions rather gradually, which complicates the identification of $R_k$ and $S_k$. The latter is additionally subject to ambiguity in its definition as literature values correspond to different species of seagrass and boundary settings, with field conditions playing an important role when dealing with restoration (van Katwijk et al., 2016). For the analysis, three different velocity thresholds were chosen: 10, 20 and 30 cm s$^{-1}$. The first value complies with literature based on seed dispersal and settling studies (e.g. Koch et al., 2010). The second is a practical value for restoration projects, given that seeds and seedlings should be, within this context, initially buried in the bed (van Katwijk et al., 2016). The third threshold serves as a reference for areas with higher current velocities. The resulting values of $R_{k,90}$ (further described in the results) and $S_k$ are given in Table 2.3.

## 2.4 Results

The control streamwise velocity profiles taken without the presence of ASG were compared with the upstream profiles ($x' = -0.5h_c$); this revealed no significant difference between these measurements. Figure 2.3 shows the profiles for $u_0 = 30$ cm s$^{-1}$, which were similar for all cases. Therefore, the effect of the meadow on flow was further characterized by the difference between downstream and upstream streamwise velocity, thus obtaining the calculated values of $r_a$ and $R_{k,90}$ presented in Tables 2.2 and 2.3, respectively.

Measurements of effective canopy height $h_r$ at 20 cm intervals revealed a gradual change in height depending on the position within the meadow (Figure 2.4), with the lowest heights ($5 - 6$ cm) along the first 20 cm. At 1 m ($x' = 5h_c$), a small peak was recorded for all cases, after which $h_r$

**2**
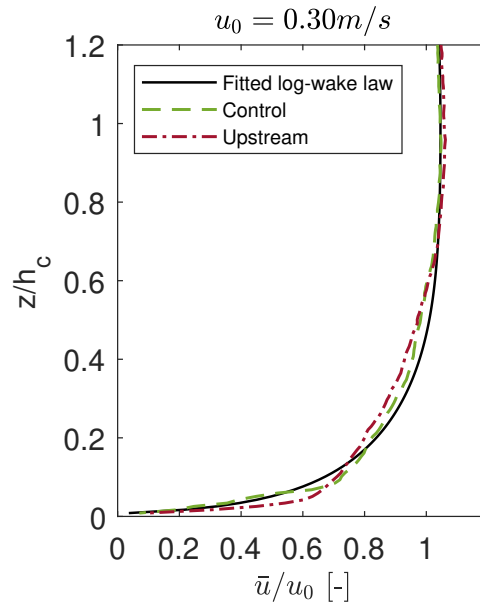


Figure 2.3: Comparison of the normalized control (no ASG) streamwise velocity profiles with those upstream ($x' = -0.5h_c$) of a 1-m meadow and the modified log-wake profile (Equation 2.1).

remained relatively constant for the next meter. The small peak could be caused by the transition between mats (1x1-m each), but this cannot be proven with our measurements. For the purpose of simplicity, an average $h_r$ was chosen to represent each input velocity $u_0$ based on the recorded heights from 1 to 2 m (Table 2.2).
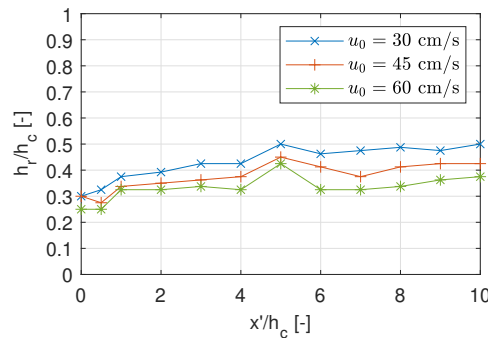


Figure 2.4: Evolution of effective canopy height $h_r$ for the 2-m meadow for different input velocities $u_0$. $x'$ is the distance from the leading edge of the canopy. Distances normalized by canopy height $h_c$.

### 2.4.1 *Streamwise Velocity and Turbulent Kinetic Energy Along the Wake*

The full wake vector field plots produced through matrix stitching showed a similar behavior among each other with regard to mean velocity $\overline{u}$ and $TKE$ along the wake, regardless of meadow length and input velocity (Figure 2.5 shows the resulting wake measurement for one test case). Three major characteristics could be discerned for all cases: i) a stark reduction of velocity in the area immediately behind the ASG meadow, especially up to $x/h_c = 5$ (i.e. 1 m) and quantified through $r_a$ (Table 2.2); ii) an acceleration of flow above the canopy; iii) an approach to upstream conditions with increasing $x$.
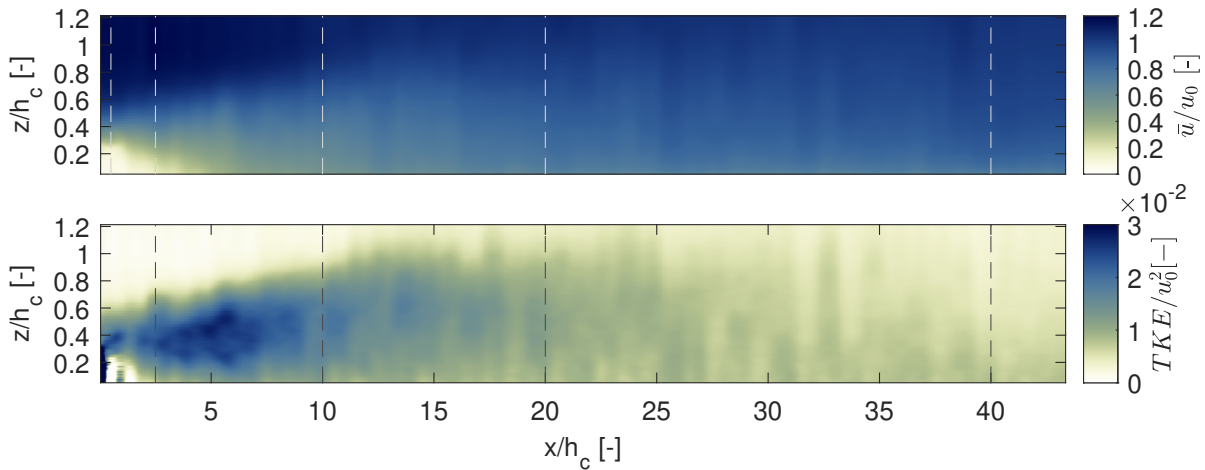
Figure 2.5: Mean streamwise velocity $\overline{u}$ (top) normalized by input velocity $u_0 = 30$ cm s$^{-1}$ and turbulent kinetic energy $TKE$ (bottom) normalized by $u_0^2$ along the full measured wake behind a 1-m ASG meadow. $x$ and $z$ are normalized by the canopy height $h_c$ and measure from the trailing edge of the meadow and the bed, respectively. The dashed lines mark the positions where profiles in Figures 2.6 and 2.8 are shown.

The attenuation ratio $r_a$ decreased with increasing velocity (Table 2.2). From $r_a$, attenuation is up to 70% at $x/h_c = 0.5$ for all input velocities. Interestingly, the meadow length $L_m$ appears to play a role in the interface between 1 and 2 m, showing an increase between 15–25% in attenuation for $1 < L_m < 2$ m, compared to a 1–8% difference for $2 < L_m < 3$ m. Furthermore, for all tested configurations, the first 50 cm ($x/h_c = 2.5$) show significant flow reduction, hence shelter capability (Figure 2.6). A complete return to upstream conditions was not observable for any of the test cases, despite measuring up to $x = 90h_r$. Nevertheless, the velocity profiles at the far end of the measurable area within the wake (Figure 2.6) are very close to initial conditions yielding an $r_a$ close to 1% for all configurations except two: $L_m = 2$ and 3 m for $u_0 = 60$ cm s$^{-1}$, which displayed a reduction of about 5%.

The wake structure analyzed here shows the development after different flow conditions. Initial adjustment ($X_D$) for all cases was 75–90 cm (Table 2.2). Note that $X_D$ and the corresponding calculated values in Table 2.2 are not normalized. Considering the mixing layer as well, full adjustment of flow is then reached when the Reynolds stress ($-\overline{u'w'}$) at $h_r$ is reached (Chen et al., 2013). Given that no measurements were done above the canopy, we compared the $-\overline{u'w'}(z = h_r)$ at the trailing edge of the canopy. For all cases, $-\overline{u'w'}$ increased with increasing meadow length, which means that a maximum $-\overline{u'w'}$ was not reached and flow in all cases is not fully developed. In natural canopies, this is also the case due to patchiness interrupting flow development (Rominger and Nepf, 2011). Chen et al. (2013) proved that flow development and the canopy layer velocity at the trailing edge are not a function of meadow length. The mixing layer thickness $\delta$, calculated utilizing Equation 2.3 at $x = 0.5h_c$, shows a similar behavior (Figure 2.7) as it increases with increasing meadow length, whereby the change is smaller between $L_m = 2$ and 3 m as between 1 and 2 m (this was also seen with the $TKE$). It is worth noting that although $\delta$ begins to stabilize after $x' = 2$ m, the log region of the velocity profile continues to increase. Furthermore, the mixing layer penetrates towards the bed for the highest input velocity when $L_m > 1$ m. In Figure 2.7, for $u_0 = 30$ cm s$^{-1}$ and $L_m = 3$ m, the FoV did not show a return to the log profile.

**2**
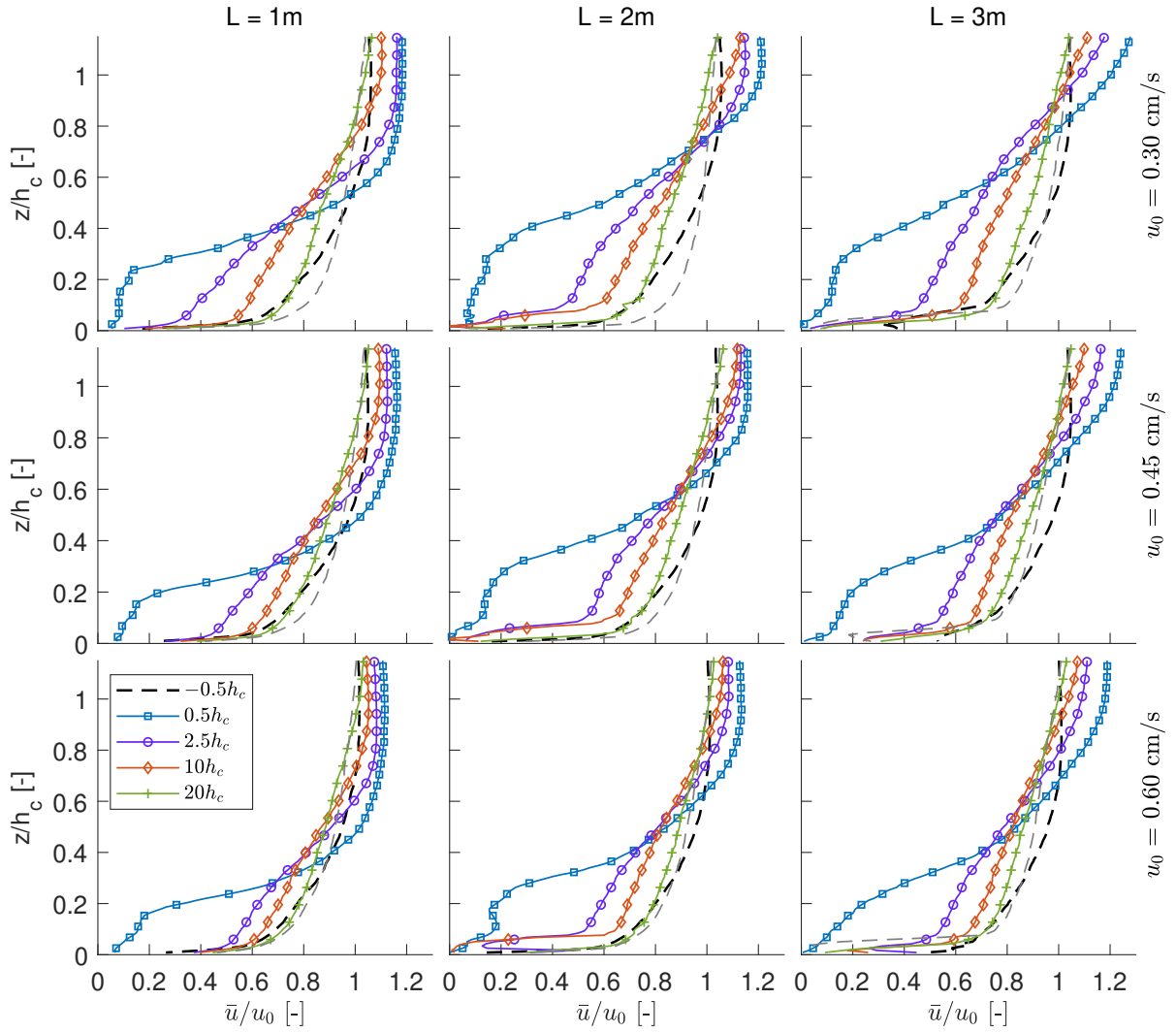


Figure 2.6: Profiles of mean streamwise velocity $\overline{u}$ at different positions in the wake of the meadow normalized by input velocity $u_0$. Subplot columns correspond to meadow lengths $L_m$ and rows to input velocities. The gray dashed profiles correspond to positions at the far end of the measurement length $D_k$, i.e. $x/h_c = 40, 35$ and 30 for $L_m = 1, 2$ and 3 m, respectively.

Similarly to $\overline{u}$, the magnitude of $TKE$ decreases further away from the meadow (Figure 2.8). In addition, the peak shifts upward (in $z$) with increasing $L_m$. We did a linear regression between the magnitude and $z$-position of the peak $TKE$ (at $x/h_c = 2.5$) and meadow length and input velocity. High correlations were found between the $TKE$ and $u_0$ and between the length and peak position ($R^2 = 0.93$ and $0.58$, respectively), and poor correlations between $TKE$ magnitude and $L_m$ and between peak position and $u_0$. This suggests that the position of peak turbulence is affected by meadow length, rather than upstream velocity, but $TKE$ can double in magnitude when doubling the velocity.

### 2.4.2 *Reach of Meadow Influence Along the Wake*

The resulting flow field after calculating $\Delta\overline{u}$ along the whole wake shows that the length of the flume did not suffice to find a full return to upstream conditions. Figure 2.9 shows one configuration
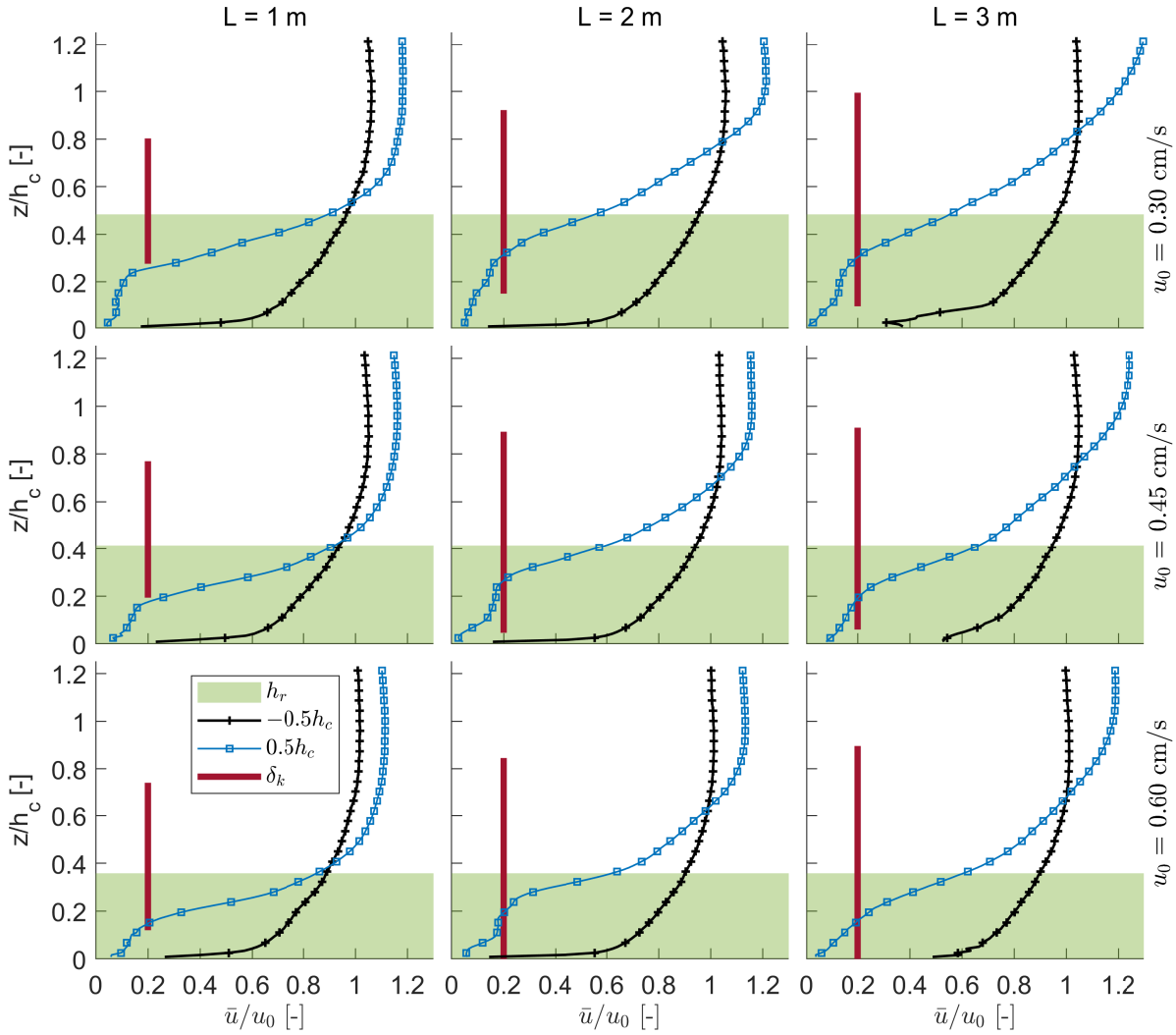
Figure 2.7: Mean streamwise velocity profile $\overline{u}$ normalized by input velocity $u_0$ at $x' = -0.5h_c$ and $x = 0.5h_c$. The mixing layer thickness $\delta$ is shown as a vertical bar. Subscript $k$ represents the wake. Subplot columns correspond to meadow lengths $L_m$ and rows to input velocities $u_0$. The shaded area represents the effective canopy height $h_r$.

whereby all other run combinations displayed similar behavior. Nonetheless, an upwelling trend can be discerned following $\Delta\overline{u}$ along the wake showing 2 different slopes: one representing the increased influence of the meadow, directly behind it (darker red areas in Figure 2.9) and a slightly less pronounced slope following the minor influence that tails (tailing slope) the meadow along the full measured wake (light red tailing zone). The slopes were calculated by isolating the areas of reduced velocity (see Table 2.3) –i.e. the darker areas, shown for all configurations in Figure 2.10 –and drawing a line through the center (for all cases, there is a distinctive transition zone between positive and negative values of $\Delta\overline{u}$ where $\Delta\overline{u} \approx 0$). It is worth noting that with increasing distance along the wake a slight increase in velocity just above the bed is initiated (Figures 2.6 and 2.9). We hypothesize that this is caused by secondary currents coming from lateral parts of the section injecting additional momentum and that the low-velocity zone for $x/h_c > 10$ is not influenced by the coherent structures. This would also explain the lack of difference between $L_m = 2$ and 3 m, but the present data is not of sufficient resolution to verify this hypothesis.
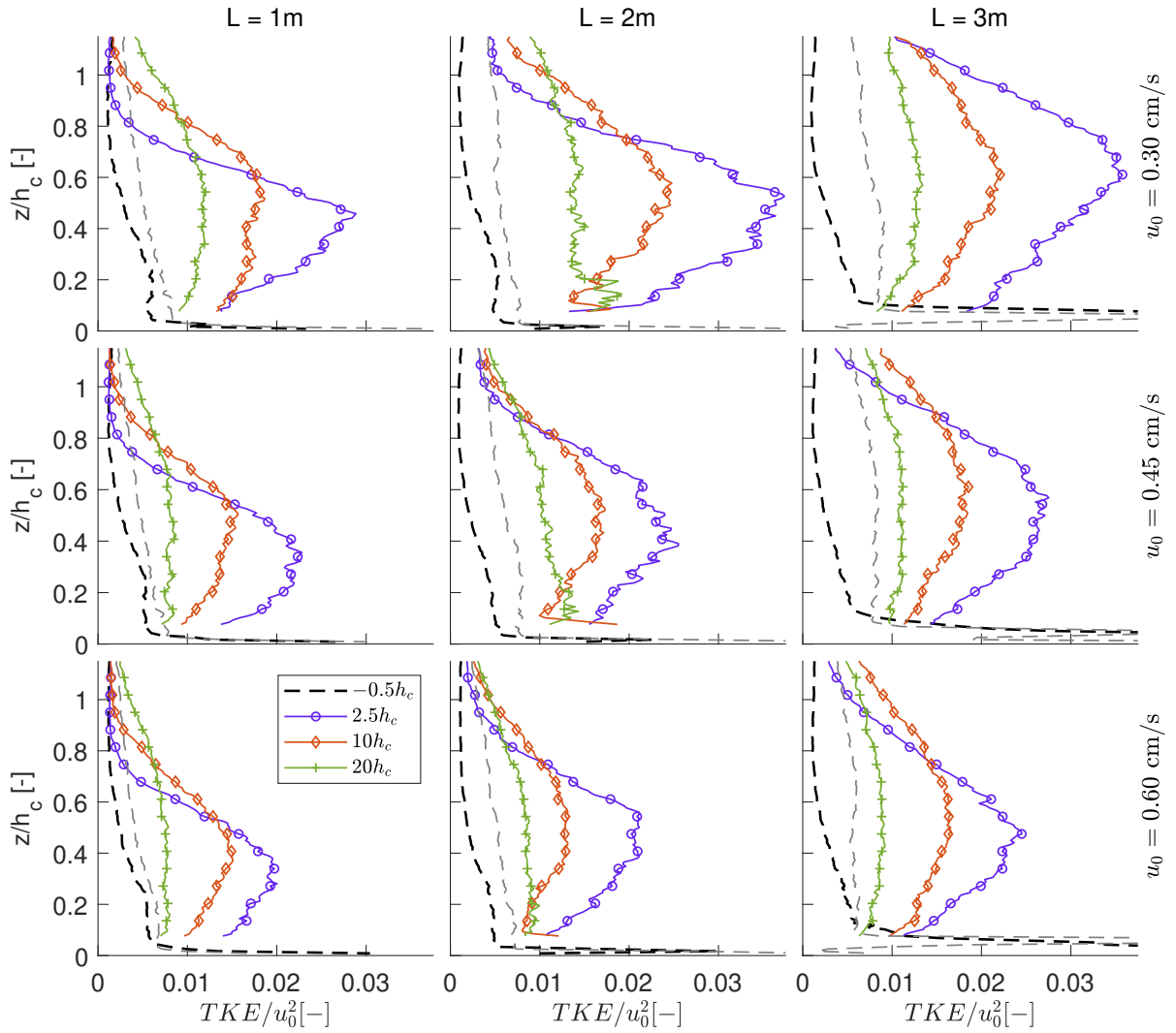
Figure 2.8: Profiles of turbulent kinetic energy $TKE$ normalized by the squared input velocity ($u_0^2$) at different positions in the wake of the meadow. Columns correspond to meadow lengths $L_m$ and rows to input velocities $u_0$. The gray dashed profiles show the positions at the far end of the measurement length $D_k$, i.e. $x/h_c = 40, 35,$ and $30$ for $L_m = 1, 2$ and $3$ m, respectively.
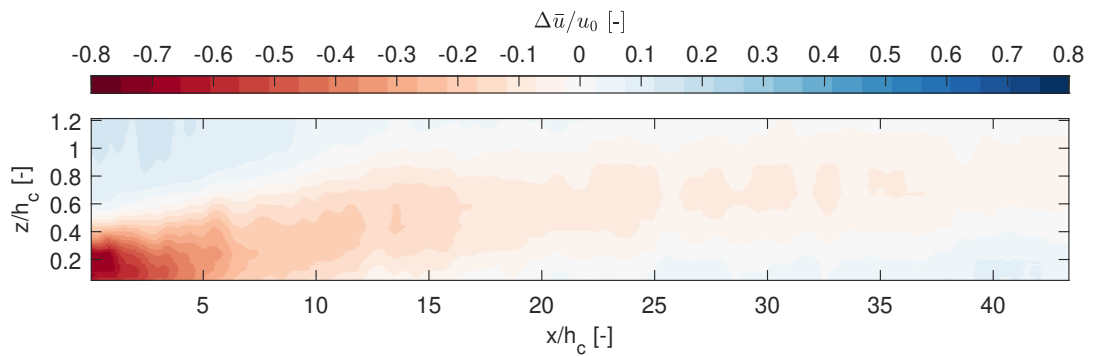


Figure 2.9: Differences in mean velocity ($\Delta \overline{u}$) along the wake of ASG normalized by incident velocity $u_0$ representing the reach ($R_k$) for $L_m = 1$ m and $u_0 = 30$ cm s$^{-1}$. $x$ and $z$ are normalized by the canopy height $h_c$ and measure from the trailing edge of the meadow and the bed, respectively.
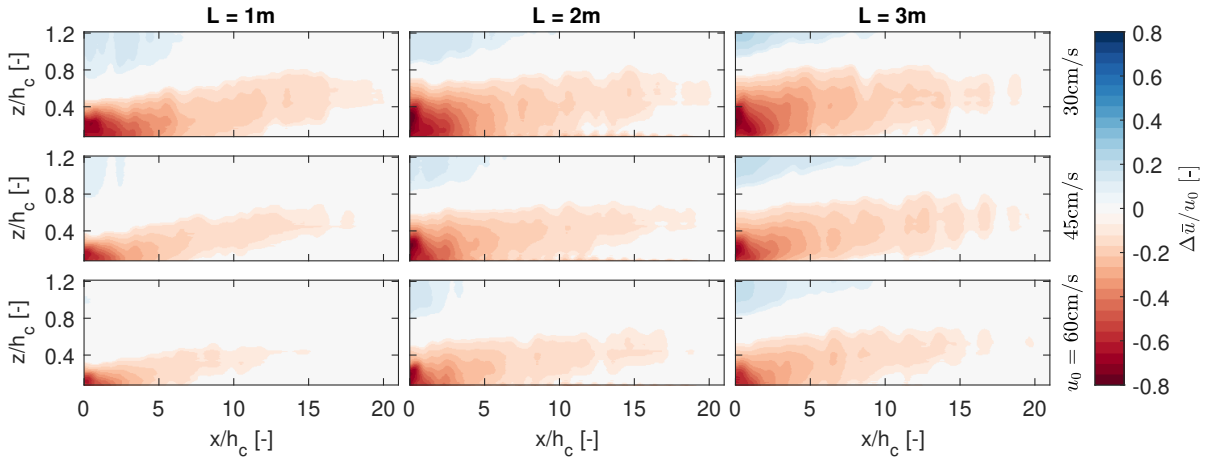
Figure 2.10: Contours of $\Delta\overline{u}$ up to 90% ($R_{k,90}$, i.e. reduction or increase above 10%) normalized by $u_0$. The $x$ and $z$-axes begin at the trailing edge of the ASG meadow and the bed, respectively, and are normalized by the canopy height $h_c$. $u_0$ differs by row and $L_m$ by column.

The tailing influence, i.e. the light red zone, observed in Figure 2.9 (which is similar in all cases, regardless of initial conditions) corresponds to the lowest values of $\Delta\overline{u}$. Therefore, to get a comparable quantity of $R_k$, a threshold of 90% was chosen, denominated $R_{k,90}$, such that all values portraying an absolute change in velocity less than 0.1 (10%) were set to 0 (Figure 2.10). The resulting $R_{k,90}$ values can be found in Table 2.3. Similar to the $r_a$ within the canopy layer, the extent of the influence does not vary greatly with varying $u_0$ or between $L_m = 2$ and 3 m, compared to $L_m = 1$ and 2 m. At 1 m length, the meadow loses influence with increasing velocity. However, there is a minimum difference in reach between a 2 and 3-m meadow. Velocity plays a major role in $R_{k,90}$ for the 1-m meadow which follows the flow adjustment characteristics discussed earlier.

Along the $z$-axis, distribution of the non-zero $\Delta\overline{u}$ at the trailing edge of the meadow varies similarly to $R_{k,90}$ and $h_r$ in that it increases with increasing $L_m$, decreases with increasing $u_0$, and shows a small variation between $L_m = 2$ and 3 m compared to that between $L_m = 1$ and 2 m. Like with the horizontal extent ($R_{k,90}$) velocity plays a more significant role at $L_m = 1$ m.

### 2.4.3 *Sheltering Distance*

Mean velocities above the chosen velocity thresholds were removed from the full wake in order to identify $S_k$ for each run under each respective threshold ($S_{k,10}$, $S_{k,20}$ and $S_{k,30}$, summarized in Table 2.3). Figure 2.11 shows $S_{k,20}$ for all run combinations, where it becomes obvious that the shelter area depends greatly on $u_0$. For an incident flow velocity of 30 cm s$^{-1}$, the ASG meadow is able to provide shelter, i.e. $\overline{u} < 20$ cm s$^{-1}$, up to $x/h_c = 12$ (240 cm). At an input velocity higher than 30 cm s$^{-1}$, the meadow loses most of its shelter capacity, irrespective of the meadow length. $S_k$ displays the same behavior for all thresholds (Table 2.3).

The lower velocity threshold of 10 cm s$^{-1}$ shows very low shelter distances of less than 25 cm ($x/h_c = 1.25$) for the input velocities higher than 30 cm s$^{-1}$ and only up to 75 cm ($x/h_c = 1.25$) for $u_0 = 30$ cm s$^{-1}$. On the other hand, a high-velocity threshold of 30 cm s$^{-1}$ shows longer shelter distances for every input velocity (not measurable for $u_0 = 30$ cm s$^{-1}$), being on average $x = 9.3h_c$ and $3.3h_c$ (186.6 and 66 cm) for $u_0 = 45$ and 60 cm s$^{-1}$, respectively.

**2**
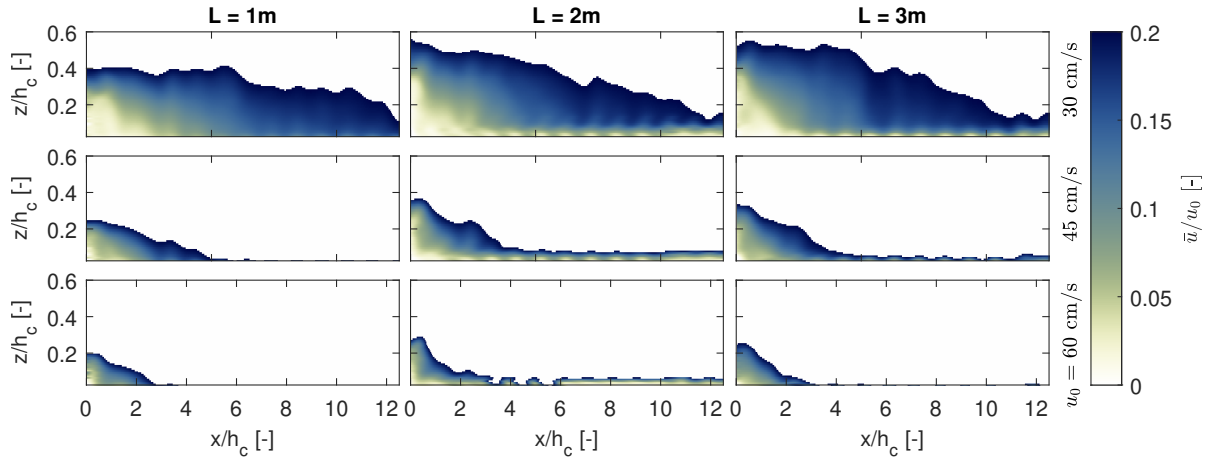


Figure 2.11: Flow fields along the wake for all configurations normalized by input velocity ($u_0$) showing the sheltered area for a threshold velocity of 20 cm s$^{-1}$. The white background represents an unsafe area for seagrass seeds and seedlings given the used velocity threshold. The $x$ and $z$-axes begin at the trailing edge of the ASG meadow and the bed, respectively, and are normalized by the canopy height $h_c$. $u_0$ varies by row and $L_m$ by column.

## 2.5 Discussion

The results suggest that the meadow has a marked effect on flow for all input velocities and meadow lengths. The meadow length $L_m$ played a smaller role after reaching 2 m. Despite testing velocities higher in comparison to all cited studies, the effect on flow along the wake was uniform for all meadow lengths. This suggests that meadow density may play a more important role. Fonseca et al. (2019) recently suggested that meadow density in naturally occurring meadows is not a result of flow velocity and likewise, meadow density does not affect flow reduction within a meadow. This, however, contrasts with other studies where density plays a major role in flow adjustment (see e.g. Chen et al., 2012; Zong and Nepf, 2012). Our study shows that even a highly porous and sparse meadow ($\varphi \ll 0.1$ and $a < 10$ m$^{-1}$) can effectively reduce flow velocity up to 70%. Furthermore, the model for rigid vegetation from Tanino and Nepf (2008), applied here for flexible vegetation utilizing the reconfigured height $h_r$, provided reliable results for the estimation of the drag coefficient (here $1.1 < C_D < 1.6$). We compared these results with assumptions from the literature, e.g. $C_D = 1.95$ tested by Luhar and Nepf (2011) and the more widely used assumption of $C_D = 1$ (Nepf, 2012b), obtaining similar results regarding the initial adjustment length $X_D$ (+10% for $C_D = 1$ and -10% for $C_D = 1.95$, on average), but lower boundary layer thickness $\delta$ (-25% on average) for the higher $C_D$. Increasing $\varphi$ had the same effect on $X_D$ and $\delta$, as $C_D$ increases as well (Tanino and Nepf, 2008), indicating that variations in meadow density, stem width and thickness play a more important role on flow adjustment compared to meadow length. Other studies suggest that reconfiguration, hence the flexibility of the material, plays an important role as well (Bouma et al., 2005; Luhar and Nepf, 2011; Fonseca et al., 2019). Fonseca et al. (1982) and Paul and Gillis (2015) present models of canopy height against incident flow velocity for *Zostera marina* and *Zostera noltii* meadows utilizing average measured canopy heights. Given the important role of the canopy height, a relationship between $h_r$ and the shelter distance $S_k$ was developed (Figure 2.12). The aforementioned studies, among others, tend to record and report an effective canopy height with a constant value depending on current velocity, regardless of meadow length. However, as seen in Figure 2.4, meadow length can
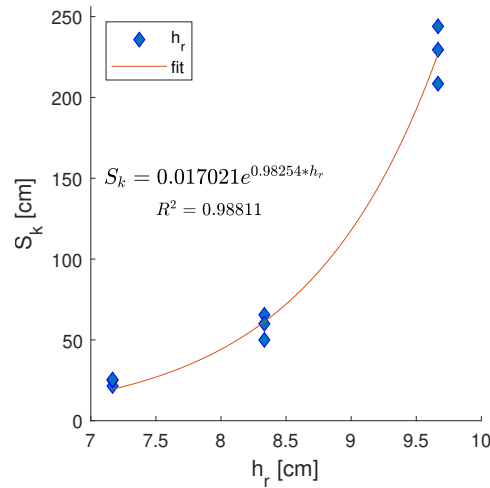
Figure 2.12: Relationship between effective canopy height $h_r$ and shelter distance $S_k$ along the wake. An exponential function of the form $y = b_1 e^{b_2 x}$ was fitted, yielding the given $R^2$. For the given fit coefficients, both parameters are to be given in cm.

affect the average effective canopy height along the meadow, suggesting that further studies should take this into account when measuring $h_r$.

As Figures 2.6–2.8 show, the velocity profile behind the meadow differs in its distribution along $z$ for the different meadow lengths. It is interesting to note that, up to our measured height, the profile transitions from a pure mixing layer profile at $L_m \leq 2$ m (e.g. Ghisalberti and Nepf, 2002) to a high-submergence-ratio hyperbolic tangent profile, as described by Nikora et al. (2013), at $L_m = 3$ m. The latter authors proposed a model that successfully predicts such vegetated flow profiles under fully developed flow by superposing canopy and boundary layer flow concepts, i.e. near-bed flow within the vegetation, the mixing layer and the boundary layer log and wake laws. Our profiles display a transition from the mixing layer profile to a profile including the boundary layer logarithmic profile when $L_m > 2$ m, which indicates that flow continues to develop even after a length of 2 m.

Flume experiments show *Z. marina* tolerance ranges between 5–100 cm s$^{-1}$ with maximum bending angles at velocities above 40 cm s$^{-1}$ (Fonseca et al., 1982). The results presented here confirm that after 40 cm s$^{-1}$ there are lower differences observed (here between 45 and 60 cm s$^{-1}$) compared with the lowest tested velocity of 30 cm s$^{-1}$, regardless of meadow length. Additionally, studies have shown that a 1-m meadow is enough to observe a reduction of flow (Fonseca et al., 1982; Lefebvre et al., 2010), which was confirmed here (Tables 2.2 and 2.3). Moreover, for restoration purposes, a 2-m meadow proved to be effective for sheltering and more feasible, given that the effect of the 3-m meadow was only slightly higher than that exhibited by the 2-m meadow.

Despite velocity being greatly reduced along the first few meters behind the meadow, turbulence increased, which could pose a problem for seeds and seedlings. As an example, Lefebvre et al. (2010) found that onset velocity for sediment motion behind a seagrass meadow was lower (< 20 cm s$^{-1}$) than for bare sand (20–23 cm s$^{-1}$), probably due to the increased turbulence, forming ripples up to a meter behind the meadow. This calls for further research on the velocity thresholds and their interaction with $TKE$. The high-resolution spatial measurement employed here allowed for

the recognition of an upward trend in changes in velocity along the wake. This trend can also be observed in the distribution of $TKE$ (Figure 2.8), suggesting that $TKE$ drives the wake structure behind a seagrass bed, whereby the meadow acts as an energy spreading filter on the whole water depth, despite the small $h_c/d$ ratio used here. As such, it contributes to the dispersion and upwelling of the incident current profile by the production of wake vortexes and a larger portion of turbulence to the flow field. The upwelling displayed two slopes –which could be separated at the 90%-reach of the influence of the meadow ($R_{k,90}$) –and an injection of momentum in the lower part for $x > 10h_c$ (Figures 2.6 and 2.8). The slope is greater between the trailing edge of the meadow and the $R_{k,90}$, but continues steadily positive along the rest of the measured stretch.

Our calculated shelter distance yielded values ranging from 2–25 times the reconfigured canopy height $h_r$ (or up to 10 times the canopy height $h_c$, Table 2.3), analogous to terrestrial studies, which have reported $2.5h_c$ for forest canopies (Detto et al., 2008). In aquatic canopies, Hu et al. (2018) demonstrated a strong correlation between eddy formation along the wake and sediment deposition. This, coupled with the shelter distance defined here for different threshold velocities, depending on target species to protect, could help improve the chances of success within restoration projects.

## 2.6 Conclusions

This study analyzed the effect of artificial seagrass (ASG) on flow, focusing on the wake structure and its development behind meadows of 3 different lengths under 3 different unidirectional current velocities. The meadows were of a constant shoot density of 390 shoots m$^{-2}$ and submergence ratio of 0.5 (under no-flow conditions). The objective was to analyze the shelter capacity of ASG given a certain shelter threshold velocity which can theoretically allow seeds and seedlings used in the framework of restoration projects to grow successfully.

We found that a meadow of length between 1 and 2 m parallel to the mean flow direction is enough to reduce flow velocity up to 70% (within the height covered by the ASG). The reduction obtained by larger meadows falls within a similar magnitude and is thus not proportional to the possible costs of assembling patches longer than 2 m. Nevertheless, a longer meadow can decrease bending and thus shift the turbulence peaks upwards, which is beneficial for settling seeds. Even a highly flexible ASG meadow with low density can provide shelter for seedlings up to 10 times the canopy height $h_c$ behind the meadow; nevertheless, a higher stiffness is recommended to reduce reconfiguration, which in turn could increase the shelter area. Furthermore, reconfiguration as a function of length needs to be better studied. Finally, regardless of length, density and incident velocity, an ASG meadow creates an upwelling reduction of flow which goes on par with the turbulence distribution. Further research is encouraged to describe the effects along the full water column. It is important to note that these results are for the specific chosen material and comparison with other materials would provide a better idea of the importance of meadow mechanical properties within the context of morphology and shelter.

**Chapter highlights**

- Shelter can be facilitated by submerged artificial vegetation along their wake when subject to unidirectional currents. Up to 70% reduction of flow was achieved for a low-density, highly flexible meadow resembling *Z. marina*.

- The shelter distance is inversely proportional to the incident hydrodynamic conditions, i.e. flow velocity.

- The shelter distance considering a threshold for survival of 20 cm s$^{-1}$ can be more than 10 times the canopy height for velocities up to 30 cm s$^{-1}$. However, higher velocities may reduce this distance to just above twice the canopy height.

- Reconfiguration of shoots affect the height of the shelter and the position of the shear layer along the water column. As reconfiguration depends not only on flow velocity but also on plant mechanical properties, the latter plays an essential role on flow adjustment both within an on the wake of the meadow.

- The length of the meadow relative to the wave propagation direction is only relevant within the first 1–2 m. After full flow development, the length of the meadow plays a less important role on flow reduction and thus on wake shelter.

- The effect of the meadow along its wake shows an upward trend which enhances turbulence and affects flow along the whole water column, regardless of the submergence ratio of the vegetation.

# PLANT MECHANICAL PROPERTIES: EFFECTS UNDER UNIDIRECTIONAL FLOW

This chapter presents a collection of results stemming from the following studies:

- *SCACR 2017 Proceedings*, Santander, Spain. R. Villanueva, M. Paul, M. Vogt, T. Schlurmann, 2017. **Vertical biomass distribution drives flow through aquatic vegetation**, CC BY 4.0 *Leibniz University Hannover.* Repository version can be found in: doi: 10.15488/13254

- *Journal of Ecohydraulics* 7:1, 58-70, M. Taphorn, R. Villanueva, M. Paul, J. Visscher, T. Schlurmann, 2021. **Flow field and wake structure characteristics imposed by single seagrass blade surrogates**, Copyright Taylor & Francis 2022, doi.org/10.1080/24705357.2021.1938253

Artificial seagrass (ASG) deployed in the field is going to be subject to many forces stemming from the unsteady hydrodynamic conditions. While Chapter 2 focuses on the wake of a homogeneous meadow under unidirectional flow, Chapters 4 and 5 test ASG under oscillatory flow. However, the variability and non-linearity of field conditions make generalization of results, such as the ones presented here, still a seemingly complex task. To approach an all-round overview of flow-vegetation interaction, this chapter aims to complement Chapter 2 with the description of additional unidirectional flow experiments –studies in which I took part within the conception and/or implementation. The experiments are described in less detail than the main studies (Chapters 2, 4, and 5) and the results only represent an overview of the presented studies. The description of these studies is meant to provide an insight into the role mechanical and geometric traits have in flow-vegetation interaction.

## 3.1 Introduction

With coastal zones becoming a hotspot for human populations, coastal defense measures have become extremely important in the engineering world. However, traditional measures and infrastructure affect the ecosystems drastically (Orth et al., 2006a). Therefore, these measures need to adapt by shifting the paradigm from gray infrastructure to nature-based solutions (Temmerman et al., 2013), whilst simultaneously boosting coastal ecosystem restoration efforts. Seagrasses correspond to one of these ecosystems, whose services can be used for coastal protection. For this, a sound understanding of the near-shore ocean processes around seagrasses is needed. Restoration and preservation of these ecosystems is thus important for the environment and human safety, which is why they have come forward on the scene of Ecological Solutions for Disaster Risk Reduction (Eco-DRR, as mentioned in the Sendai Framework for Disaster Risk Reduction, SFDRR, UNISDR, 2015).

Seagrasses reduce current velocities and wave energy within the surf zone (Koch et al., 2006; Paul et al., 2012). This in turn increases sedimentation, lowering turbidity and thus increasing light availability for the meadows. Causal relations and implications are an adaptation mechanism developed by seagrasses and other aquatic vegetation to ensure maximum light uptake and a stable ground (Koch, 2001). The flexibility of seagrasses is one of these adaptation mechanisms facilitating survival, where structural reconfiguration minimizes hydrodynamic loading (Luhar and Nepf, 2011), hence providing ideal conditions for growth. In addition, seagrasses adapt by reducing hydrodynamic loading to enhance sedimentation (Adams et al., 2016), adjusting to the local velocity by streamlining. Streamlining helps to reduce the hydrodynamic loading, thus not being ripped off their roots, and stimulate pollination (Gambi et al., 1990; Koch et al., 2006). Understanding the processes and driving forces that lead to structural reconfiguration and consequent energy dissipation is of vital importance for the evaluation of the system as a soft measure of coastal protection. Moreover, the conditions needed for adequate plant growth and survival also eventuate from these processes.

Following the objectives of this thesis (Section 1.2), biodegradable artificial structures should provide ideal conditions for seagrass growth. These elements compose the artificial seagrass (ASG) which, upon field deployment, should promote seagrass growth and incite restoration through flow

attenuation. The experiments described in Chapters 2, 4, and 5 deal with homogeneous meadows. However, a homogeneous meadow does not accurately represent what we would usually find in nature, which includes diverse species and extrinsic factors such as epiphytic cover (Barcelona et al., 2021), grazing fauna (Tanner et al., 2021) and extreme conditions, among others. A direct translation of results to field conditions is thus not possible.

To broaden the homogeneity of the results, different geometric and mechanical properties of ASG need to be considered as well. Villanueva et al. (2021) (Chapter 2) found that a highly flexible ASG can effectively alter the flow structure under unidirectional flow. For the ensuing experiments with waves (Villanueva et al., 2022, 2023, see Chapters 4 and 5), it was determined that the material needed to provide enhanced attenuation, as waves create a cyclical load which could be more degenerative for the thin polypropylene (PP) used by Villanueva et al. (2021). With this objective in mind, the choice of a new material was narrowed down to a surrogate comprising a different geometry, different mechanical properties, or both. Both approaches were taken into account, leading to two different sets of experiments: (1) experiments with varying leaf geometry to study the effect of the biomass distribution; and (2) experiments with single-stem ASG of varying materials, differentiated by their flexural rigidity $EI$. The following sections briefly describe the experiments done regarding (1) and (2), putting them into context with the aims and contents of this thesis.

## 3.2 Vertical Biomass Distribution Variations

With seagrass restoration in mind, the experiments portrayed in this thesis focus on one of the four major seagrass species found in Europe, i.e. *Zostera marina* (Ondiviela et al., 2014). The experiments shown in Chapter 2 comprised an ASG with no stem, but six leaves freely moving about a common pivot point, similar to natural *Z. marina*. Figure 3.1 shows examples of *Z. marina* found in the German North and Baltic Sea. But in reality, seagrasses, as all vegetation, vary widely in their geometry (Paul et al., 2014), which in turn dictates their response to the incident hydrodynamics. To take this into account, experiments regarding differences in geometry were carried out prior to the experiments described in Chapter 2. These had the aim of varying the cross-section of the chosen material (in this case polypropylene –PP) to represent variations in the vertical biomass distribution (VBD) of different seagrass species. PP was later proven to attenuate flow despite its low flexural rigidity of $EI < 1$ N mm$^2$ (Villanueva et al., 2021).

Like actual seagrasses, any surrogate exposed to currents will experience a force on each individual element. This is called the drag force, which is the consequence of inertial and viscous forces acting on the element by the moving fluid (Vogel, 2020). The surrogates then exert a resistance which can be directly related to the buoyancy and flexural rigidity of the element (Niklas, 1992; Fonseca and Koehl, 2006; Luhar and Nepf, 2011). These forces have been thoroughly studied and modeled empirically and analytically regarding the effects of vegetation, both artificial and natural, on coastal hydrodynamics(see e.g. Nepf and Vivoni, 2000; Ghisalberti and Nepf, 2009; Losada et al., 2016). Different studies prove how a form-specific vegetative element reduces current and orbital velocities and creates a dampening effect on waves and currents, whereby plant biomechanical properties and drag play an important role (Bouma et al., 2005; Paul et al., 2012). In this section, the focus is on assessing the effect of vertical biomass distribution (VBD) on hydrodynamics and
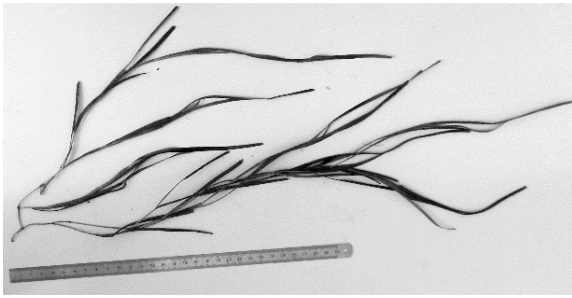
(a) Baltic Sea Specimen



(b) North Sea Specimen

Figure 3.1: *Z. marina* samples from the Baltic and North Sea.

the effectiveness of surrogates to mimic real seagrass.

### 3.2.1 *Methodology*

To investigate the effect of VBD, ASG was tested against a unidirectional current in a circular track-flume of 1 m width (for detailed information about the flume, see Chapter 2 and Goseberg et al., 2013; Schendel et al., 2016). ASG was tested under low-range currents of $u_0 = [0.05, 0.1, 0.2, 0.3]$ m s$^{-1}$), thus mimicking common found field conditions for seagrasses (Van Katwijk et al., 2009). As a *Z. marina* surrogate, polypropylene (PP) band, commonly known as gift ribbon ($\delta_{PP}$ = 0.45 g cm$^{-3}$) was used. PP has proven to be a suitable surrogate for experimentation due to its similar buoyant nature with respect to seagrasses (Bouma et al., 2005; Paul et al., 2016; Tuya et al., 2017). The shoot density was kept low compared to natural values (see e.g. Ondiviela et al., 2014), which can be described by Equation 3.1 (Nepf, 2012a), where $\lambda_f$ is the roughness density (also called the frontal area parameter), $a$ defines the frontal area per canopy volume and $h_r$ is the reconfigured canopy height. The upright height of the ASG was $h_c = 0.30$ m for all VBDs.

$$\lambda_f = \int_0^{h_r} a\mathrm{d}z = ah_r \tag{3.1}$$

Here, $\lambda_f = 0.1$ was kept constant to isolate the effects VBD on flow –i.e. shoot density, total biomass and blade length were kept constant. The distribution of biomass within a shoot was set to 3 variations: (a) biomass uniformly distributed along the length of the blades in each shoot (comparable to Chapter 2); (b) biomass concentrated along the upper half of the shoot and (c) biomass concentrated along the lower half. Table 3.1 shows the geometric characteristics of the variable ASG. Figure 3.2 shows the three different surrogates investigated.

The VBDs selected were related to different coastal vegetation found in nature: the seaweed *Fucus serratus* and cord-grass *Spartina anglica* whose biomechanical composition comprises high biomass concentration along the upper and lower parts of the plant, respectively (Bouma et al., 2005; Paul et al., 2014). The constant VBD assimilates the eelgrass *Z. marina*. Note, however, that these are idealized cases where all surrogates have the same mechanical properties. Natural seagrasses present different mechanical properties among each other. The surrogates were

Table 3.1: ASG parameters chosen for the different VBDs tested.

| shoot density [m$^{-2}$] | Biomass concentration | Blade length [cm] | Number of blades | upper width [mm] | lower width [mm] |
|---|---|---|---|---|---|
| | Constant | | 6 | 5 | 5 |
| 105 | Upper part | 30 | 2 | 25 | 5 |
| | Lower part | | 2 | 5 | 25 |
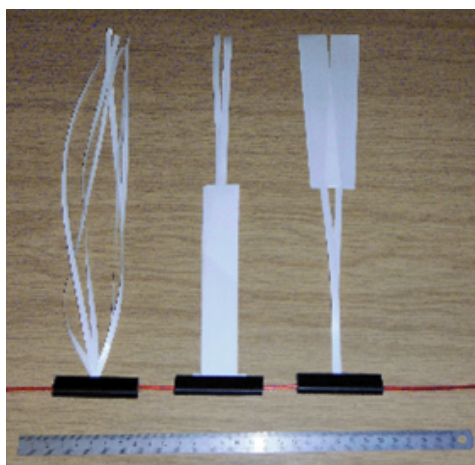


Figure 3.2: Different surrogates tested displaying the varying vertical biomass distributions (VBD).

differentiated using the flexural rigidity $EI$, where $E$ is Young's Modulus and $I$ is the second moment of inertia. $I$ is given by $(1/12)b_v t_v^3$ (with $b_v$ the width and $t_v$ the thickness, for a rectangular shape), suggesting that an increase in $t_v$ is exponentially more significant than increasing the width $b_v$ (perpendicular to the flow). Nonetheless, the VBD experiments within this section vary solely on the width, which turns the roughness density $\lambda_f$ into the decisive parameter. Section 3.3 then gives an insight into the variation of $EI$ and the cross-section of the surrogate.

**EXPERIMENTAL SET-UP**

The selected ASG variations were set up in two 1-by-1-m patches (Figure 3.3). A 40-cm gap separated both patches. The ASG shoots were placed with a constant separation $S = 10$ cm in both planar directions, alternating each row with a displacement of 5 cm to form a staggered formation to avoid preferential streams. For each measurement, the velocity was kept constant. Control measurements, i.e. without vegetation, were likewise done for all velocities. The horizontal flow velocity was measured utilizing a NORTEK Vectrino+ Acoustic Doppler Velocimeter (ADV) measuring at a 25 Hz. The velocities were measured at three points along $x$ (A, B, and C in Figure 3.3) and 10 points along $z$ at each $x$-location. This produced 3 profiles: A at 5 cm in front of the first meadow; B at 5 cm in front of the second meadow; and C at 25 cm behind the second meadow. A constant water height of $d = 0.60$ m at still water conditions was used. The ADV was mounted and displaced utilizing an automated process controller mounted atop the walls of the flume. Velocities were measured for 1 min at each point. The data from the ADV was processed using a low-pass filter with a 30% cut-off frequency. Additionally, the acceleration method (Goring and Nikora, 2002) was
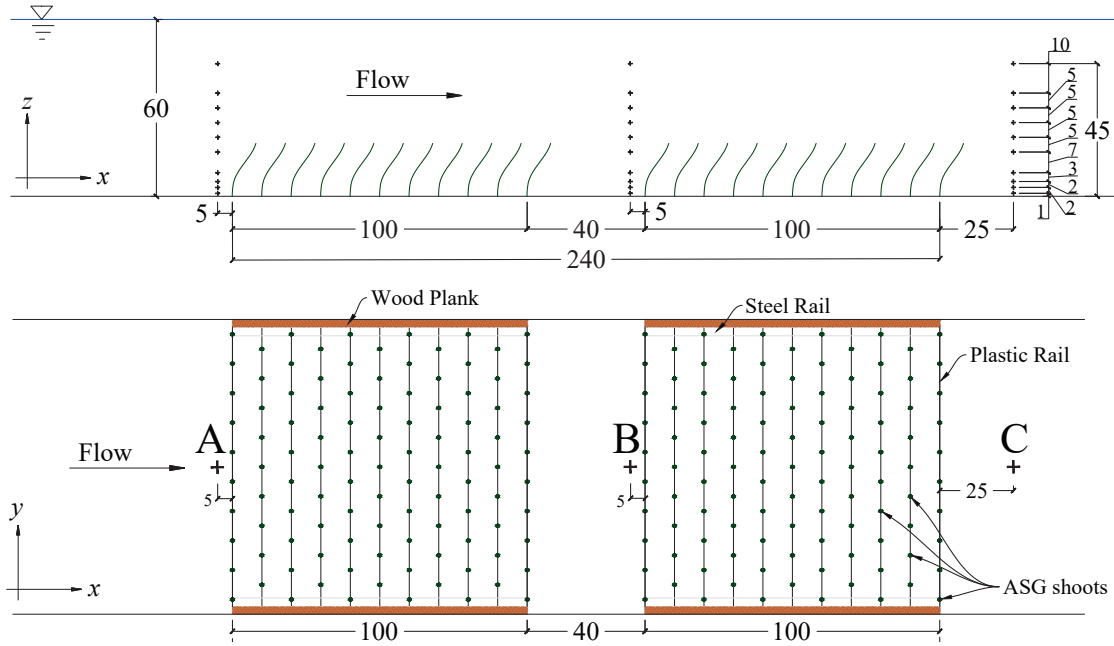
Figure 3.3: Experimental set-up used in the race track-flume, (top) side view and (bottom) top view. Crosses (+) mark the measurement points in the $z$ and $x$-directions. All units in mm.

used to filter the data.

To measure the reaction of the different ASG configurations to the incoming current, HD cameras were used to capture their movement under the different velocities. The flume features a 3-m window for model observation, which allowed for recording of the bending angles of the ASG through the use of a transparent raster (1x1 cm resolution). The plant position was then measured by reading the raster nodes. 10 measurements were recorded and averaged to obtain an idealized stable plant position under the given velocity, thus removing fluctuations caused by swaying. This resulted in the reconfigured height $h_r$ which depends on the incident flow velocity.

### 3.2.2 *Results and Discussion*

Initial data analysis shows an in-canopy flow reduction –or attenuation –while the above-canopy flow showed an increase compared to the reference case. This is caused by continuity following the in-canopy attenuation (e.g. Nepf and Vivoni, 2000; Bouma et al., 2005; Paul and Gillis, 2015). An inflection point that creates a shear layer above the canopy can be observed, which has been previously quantified as a function of the canopy density (Nepf, 2012a). Here, the chosen shoot density is classified as transitional (after Belcher et al., 2003) for a roughness density $\lambda_f \sim 0.1$, meaning that drag within the canopy, and not bed roughness, represents the driving factor for attenuation (Nepf, 2012a). Figure 3.4 shows the different velocity profiles measured at points A, B, and C for all tested VBDs and flow velocities.

The reduction in velocity is clear within the canopy layer, i.e. $z \leq h_r$. For the whole set of experiments, $12 \leq h_r \leq 20$ cm. While all VBDs reduced flow, the profile shape depended on the incident velocity and VBD. Behind the meadows, high velocities ($u_0 > 20$ cm s$^{-1}$) yielded a profile of the same shape as the reference case, meaning there is only element-scale turbulence present,

**3**
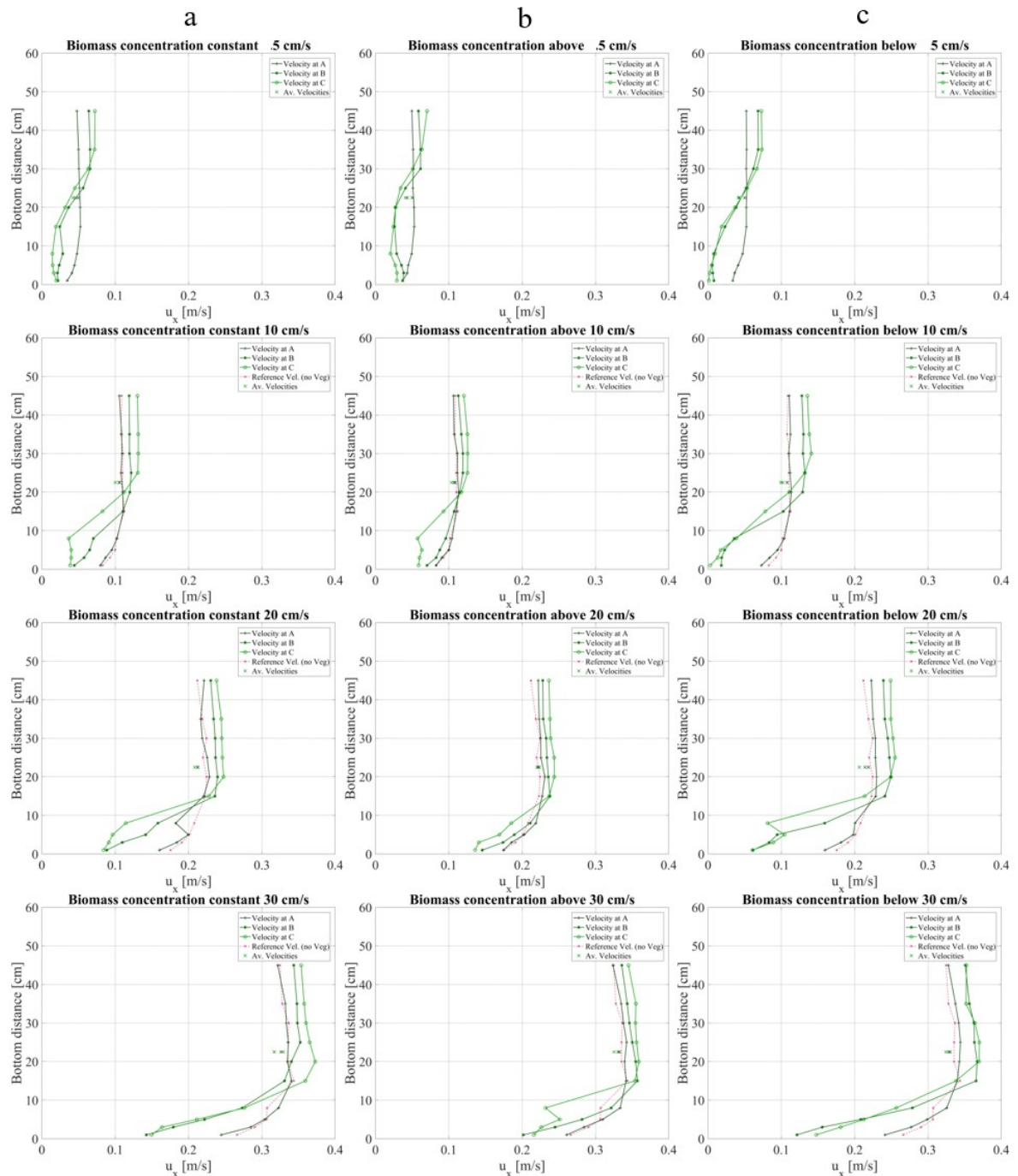


Figure 3.4: Velocity profiles at each measuring point —A, B and C —for each VBD: (a) constant, (b) above and (c) below; and each mean velocity by row: (1) 5 cm s$^{-1}$, (2) 10 cm s$^{-1}$, (3) 20 cm s$^{-1}$ and (4) 30 cm s$^{-1}$.

where bed drag –with some small contribution of vegetation drag –works as boundary layer (Nepf, 2012a). The same behavior was observed with $u_x = 20$ cm s$^{-1}$ at B and C for VBDs above and below and at B for VBD constant. At C, the inflection point appears and the profile showcases an S-shape created by the shear-like layer at the top of the canopy. For lower velocities, $h_r$ is close to $h_c$, yielding $\lambda_f \sim 0.1$. For comparison, $\lambda_f = 0.09$ the constant VBD. Note, however, that the shoot-like structure (no single element) means that $\lambda_f$ varies with respect to $z$ and the exact determination of the overall

Table 3.2: Average difference in $u_x$ [%] (at 20 cm s$^{-1}$) for canopy and above-canopy layers compared to the reference velocity.

| Biomass concentration | Position | Above-canopy | Within canopy |
|---|---|---|---|
| Constant | B | 9.04 | −24.5 |
| | C | 13.3 | −37.8 |
| Above | B | 7.28 | −5.61 |
| | C | 11.2 | −14.3 |
| Below | B | 13.05 | −30.28 |
| | C | 16.4 | −45.2 |

dominating roughness density for each setting is not straightforward. The differences in velocity profiles in Figure 3.4 show the dependence on both magnitude of velocity and in-canopy distance $x$ for the canopy to trigger an S-shaped curve on the profile, regardless of initial roughness density.

When focusing on the effect of VBD on velocity, its effect becomes clearer at B and C. Table 3.2 shows $z$-averaged values of the velocity above and within the canopy. In general, The VBD below caused the highest attenuation within the canopy; however, it also yielded the highest velocities above the canopy. A constant VBD achieved 80% of the attenuation reached by the VBD below. The VBD above yielded the smallest attenuation, especially for low velocities, reaching only 15% flow attenuation for the higher $u_0$. Moreover, for the lowest incident velocity ($u_0 = 5$ cm s$^{-1}$), the near-bed velocities were almost equal to the non-vegetated condition, especially after only 1 m of ASG. For a current flow of 20 cm s$^{-1}$, the average velocity above the canopy increased around 9–13% (Table 3.2), depending on the VBD, while attenuation within the canopy reached values above 30%. Note, however, that the average velocity for the whole water column varies less than 1%, following energy balance and continuity.

Stems on vegetation whose biomass is more spatially distributed upwards will reduce less flow than the leaves above, which causes this behavior. Koch et al. (2006) describes these differences regarding VBD and the effect on the velocity profile for real aquatic vegetation. A larger width means a larger $EI$, and hence a lower bending angle (Fonseca and Koehl, 2006). Streamlining therefore occurs less in the lower area and more in the upper for VBD below, thus yielding greater attenuation. For VBD above, the low flexural stiffness at the bottom increases bending drastically (i.e. lower $h_r$), keeping attenuation at a minimum. This was corroborated with the measured leaf position, as described in Section 3.2.1 (not shown here), where it could be observed, qualitatively, that the higher the bending angle, the lower the attenuation.

All VBDs showed enhanced attenuation after 2 m. This attenuation was lower than the one shown in Chapter 2, reaching up to 37.8% for $u_x = 20$ cm s$^{-1}$ and constant VBD. This is to be expected, however, as the velocity measurements are given for $x_i > h_c$, where $x_i$ is the position of the measurement behind the preceding meadow (i.e. B or C, Figure 3.3). In addition, the shoot density is half of that used in the experiments described in Chapter 2. The higher flow attenuation at C shows that attenuation increases with respect to $x$ within each canopy. Here, it is only possible to observe such behavior with the highest velocities (30 cm s$^{-1}$), where a horizontally layered behavior for the velocity field can be observed (see Figure 6 in Villanueva et al. 2017).

## 3.3 Surrogate Mechanical Properties

The design of a proper ASG is complicated, as several factors play an important role. First, the deployment location needs to be taken into account, which emulates as well the inherent hydrodynamic conditions. These conditions (and their respective extremes) will dictate how high the hydrodynamic load will be on the submerged structures. On the other hand, the effect of the ASG on hydrodynamics must also be considered, as successful restoration will depend on the hydrodynamic conditions facilitated by the ASG (Carus et al., 2021; Villanueva et al., 2021). The design of ASG must thus consider what the optimal properties to create the proper growth conditions are. These properties are flexural rigidity, buoyancy, and geometry (Taphorn et al., 2021).

To help improve ASG design, parallel experiments were envisioned to the ones presented in Chapter 2. These experiments were carried out and published by Taphorn et al. (2021), and are only briefly brought into context here. With the goal of bringing ASG design forward, the experiments were meant to expand the findings of Villanueva et al. (2021) into the mechanical and geometric variation of the ASG used. To achieve this, this study presents an in-depth analysis of the effect of single elements (stem-like) on unidirectional flow. Of course, the effect of a single element is not equal to that of a shoot or a meadow. When dealing with steady flow, a meadow and its effect on flow is usually represented with the bulk drag coefficient $C_D$ (see e.g. Nikora et al., 2013). This drag coefficient already takes into account the stem-to-stem interaction as it depends on the shoot density (Nepf, 1999). This becomes even more complex when dealing with flexible meadows, as is the case with all experiments detailed in this thesis.

To remove the effect of stem interaction within shoots or meadows, single elements were tested. This in turn helps to isolate the target parameters by testing elements of varying geometric and mechanical properties. The rest of this section is intended to provide a glimpse into this set of experiments, the idea behind them, and the main findings. These findings were the basis for the selection of a new kind of ASG to trial within the experiments with oscillatory flow (Chapters 4 and 5). The objective behind this was to optimize the material selection under the dogma: less material (single element) equals cheaper, simpler production and field installation. As the durability and rate of biodegradation is also affected by these properties (see Section 1.1.3), the ASG must last long enough to fulfill its goal: restoration facilitation.

### 3.3.1 *Methodology*

Previous studies have employed different materials as seagrass surrogates, such as polyethylene (PE) Vettori and Nikora (2018), Polypropylene (PP, Fonseca and Koehl, 2006), cable ties (Bouma et al., 2005), and even overhead foil (Okamoto et al., 2016). To analyze the effect of geometric and mechanical traits, different materials with varying geometry were chosen as seagrass surrogates (Table 3.3). The morphology of the surrogates was simplified and varied between each other by the cross-section, while the mechanical properties by the material composition. The mechanical properties can be characterized through the flexural rigidity $EI$. Table 3.3 shows the $EI$ of the different surrogates trialed. The modulus of elasticity $E$ was measured through bending and tensile tests done at a specialized laboratory ($EI_{\text{meas}}$). Literature values were used for comparison, yielding the $EI_{\text{calc}}$ shown in Table 3.3.

Table 3.3: Surrogate properties: material, modulus of elasticity ($E$), specific density ($\rho_s$), dimensions ($d_i$=inner diameter, $d_o$=outer diameter, $t_v$=thickness, and $b_v$=width), second moment of area $I$ (calculated). For the flexural rigidity $EI$, subscript "calc" indicates value calculated with literature values of $E$, "meas" with measured values through tensile and bending tests (see Taphorn et al., 2021). Table adapted from Taphorn et al. (2021) with the authorization of the author.

| Surr. | Material | $\rho_s$ [g cm$^3$] | Cross-section Shape | $d_i/d_o$; $t_v$ * $b_v$ [mm] | $I$ [mm$^4$] | $EI_{\text{calc}}$ [N mm$^{-2}$] | $EI_{\text{meas}}$ [N mm$^{-2}$] |
|---|---|---|---|---|---|---|---|
| A | Polyvinyl chloride | 1.38–1.55[a] | ▪ | 4*4 | 21.3 | 1000–3500[a] | 3310–3380 |
| B | Polyethylene | 0.92-0.95[a] | ◉ | 3/5 | 26.7 | 200–1400a | 78.8–99 |
| C | Silicone | 1–1.5[a] (0.64–0.96) | ◯ | 5/8.3 | 202.3 | 8-9[b] | 4.65–6.16 |
| D | Polyamide | 1.13[a] | ▯ | 1.36*4.8 | 1 | 1200[a] | 658–1020 |
| E | Silicone | 1–1.5[a] (0.75–1.12) | ◉ | 2/4 11.8 | 11.8 | 8–9[b] | 2.17–2.21 |
| F | Polypropylene | 0.9[a] | ▮ | 0.11*4.8 | 0.0005 | 1100–1300[a] | 149 |
| *Z. marina* | - | 0.7–0.9[c] | ▮ | (0.3–0.6)[d]* (2–10)[e] | 0.0045– 0.18 | 0.5–300[f] | - |

[a] Domininghaus (2013); [b] Henry (2014); [c] Luhar and Nepf (2011); [d] Paul and de los Santos (2019), [e] Larkum et al. (2006); Ondiviela et al. (2014); [f] Patterson et al. (2001); Ghisalberti and Nepf (2002)

The selected surrogates were tested under unidirectional flow. The experiments were carried out in the circular track flume of Ludwig Franzius Institute. The hydraulic facility is the same as the one explained in Chapter 2 and Section 3.2.1. Following the Experiments by Villanueva et al. (2021), the same PIV system was subsequently used to trial the ASG surrogates. The set-up of the system, i.e. the camera positioning, laser type and position, refraction-correction prisms, and data acquisition software, corresponded to the same set-up described in Chapter 2. See Villanueva et al. (2021) and Taphorn et al. (2021) for a detailed explanation of the PIV system, its calibration and relevant equipment, and the flume.

To isolate the differences between each of the materials chosen, single-stem surrogates were trialed. These were fixed to the bed, ensuring that their state at rest was vertical. This meant that, under water, the surrogate should stand upright, be it due to its inherent rigidity, its buoyancy, or both. The surrogates had a length of $h_c = 20$ cm and were fixed in the middle of the measurement stretch of the flume, with the cameras looking from both sides, providing the PIV stereoscopic image (Figure 3.5). Each measurement consisted of a specific surrogate with a specific input velocity $u_0$. 500 PIV images per measurement at a rate of 7 Hz were taken to measure the particle displacement in the immediate vicinity of the surrogate. This yielded a high-resolution 3-D velocity field time series of the area within the field of view (FoV).

The water depth $d$ was kept constant at 0.4 m. The surrogates were tested under constant flow velocities $u_0$ ranging from 0.014–0.3 m s$^{-1}$. Velocity profiles were extracted from the resulting velocity field at the following positions (with respect to $x = 0$ at the base of the surrogate, Figure 3.5): $x/h_c = [-0.1, 0.375, 0.75, 1]$. Trapezoidal numerical integration was then used to compare the velocities at each position with reference values (no ASG), yielding an attenuation ratio $AtR$ corresponding to the position, surrogate, and velocity trialed. Additionally, this study analyzed the occurrence of tip vortexes, and the consequent vortex generation and shedding frequency

**3**
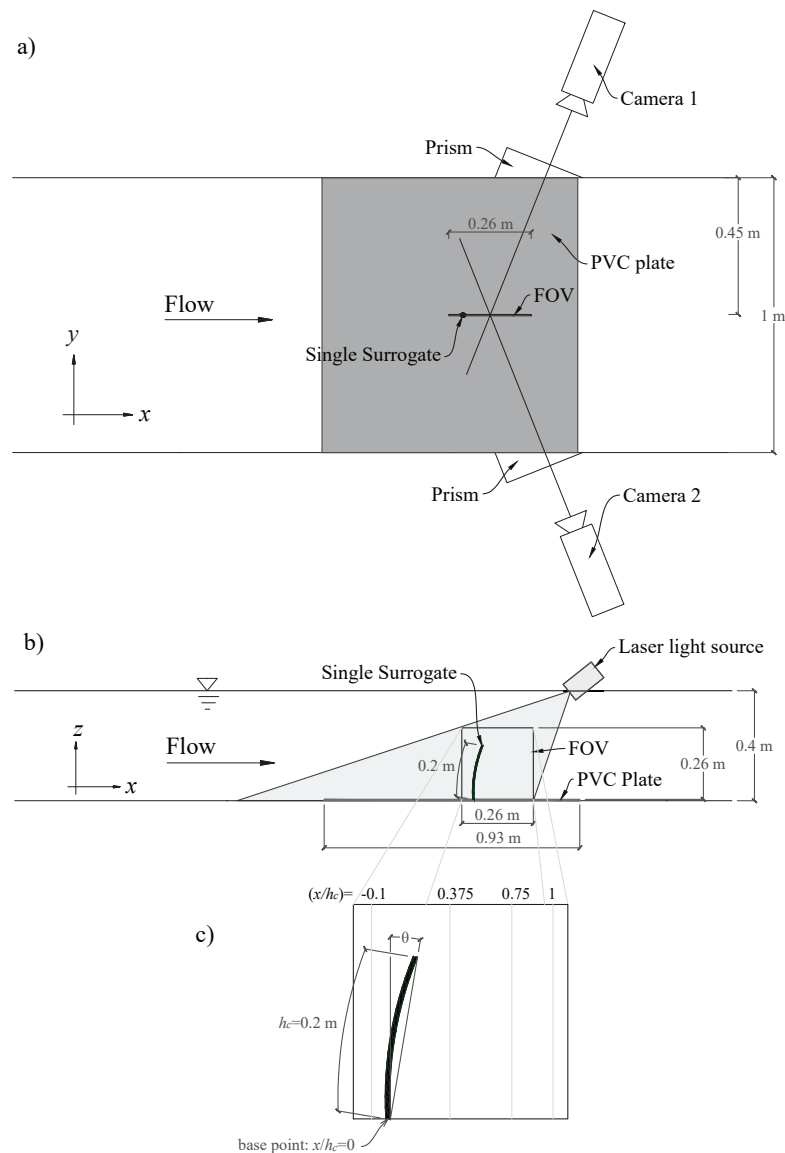


Figure 3.5: Experimental set-up of the single-element surrogate experiments. a) Top view; b) side view; c) example of the field of view (FoV) and initial inclination angle of a submerged surrogate. Figure adapted from Taphorn et al. (2021), reproduced with author authorization.

caused by the surrogate motion. Proper Orthogonal Decomposition (POD) was employed to analyze the $w$-component (out-of-plane velocity), yielding oscillating time series of $w$, which were then analyzed through Fast Fourier Transforms (FFT) to obtain the intrinsic frequencies. The dimensionless Strouhal Number was then calculated to represent the characteristic shedding frequencies of each surrogate. The analysis of vortexes and shedding frequencies is out of the scope of this thesis and is therefore not described further. However, the reader is incited to read more about this in Taphorn et al. (2021).
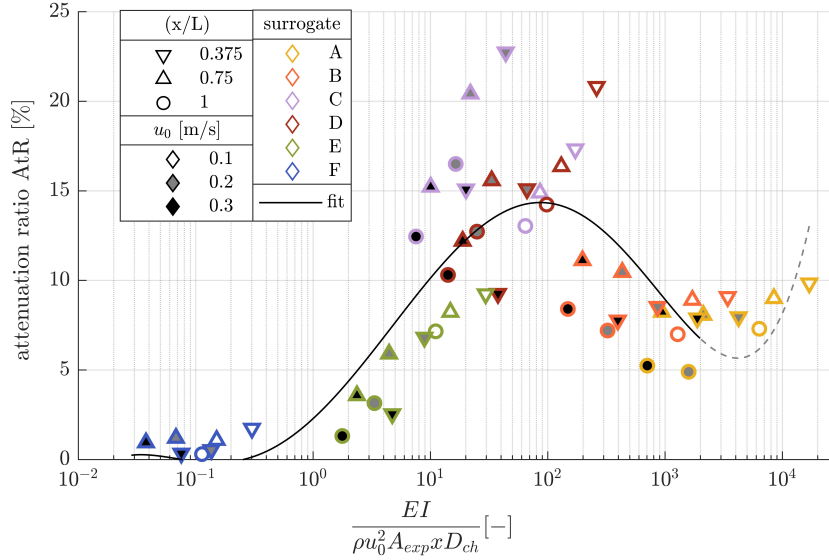
Figure 3.6: Attenuation ratio ($AtR$) as a function of the flexural rigidity $EI$ and material density $\rho_s$ for three position along the wake and $u_0 = [0.1, 0.2, 0.3]$ m s$^{-1}$. $EI$ is non-dimensionalized through the projected area exposed to flow ($A_{exp}$) and characteristic diameter $D_{ch}$. For values in the $x$-axis greater than $O(3)$, the results were expected to be an artifact of the experiments. The figure corresponds to Figure 6 in Taphorn et al. (2021), reproduced here with authorization of the author.

### 3.3.2 *Results and Discussion*

Experimentation showed that all surrogates bent in the direction of flow as a result of the exposure to a unidirectional current. Flow was attenuated to some extent by all surrogates, showing that single elements are also feasible structures to disrupt flow and further investigate their attenuation capacities. It was found that the rate of attenuation is a function of the mechanical properties of the material, the cross-section, the frontal dimensions, and the incident flow velocity.

Interestingly, the results showed that the highest flexural rigidity yielded an attenuation comparable to the lowest. For example, surrogate A (Table 3.3) yielded an attenuation ratio of 2–9%, comparable to surrogates F and E, which are the most flexible (i.e. lowest flexural rigidity). On the other hand, surrogates B, C, and D reached an attenuation of up to 38%. Moreover, the shape of the velocity profile behind the latter surrogates was effectively altered by the presence of the single elements, while for A, E, and F, it was seemingly unaffected. Surrogate A displayed no change in posture, regardless of incident velocity, while E and F were drastically bent in the direction of flow. This and the oscillating motion (swaying) initiated by flow around flexible elements suggest that the enhanced turbulence is responsible for the altered velocity profile and resulting attenuation.

The rate of flow attenuation provided by the specimens was a function of the incident velocities. This was especially true for the more flexible surrogates, i.e. $EI \leq 1200$ N mm$^2$. For surrogates B and C, on the other hand, the attenuation was higher for all flow velocities, showing a reduced dependence on the magnitude of the incident velocity. However, the distance behind the surrogate played a more important role, with surrogate C showing the maximum attenuation within the first 10 cm behind the element, while the other surrogates showed a more homogeneous attenuation along the wake for a distance up to one leaf length.

**3**

The different attenuation ratios of the different surrogates were first attributed to the different geometries. However, upon thorough analysis, a non-linear trend between the attenuation ratio of surrogates of the same cross-section (e.g.  B, C, and E) was observed, suggesting that $EI$, and not the geometry, governs the attenuation. The attenuation ratio was related to the flexural rigidity for the whole set of experiments, i.e. all input velocities, surrogates, and different distances behind the element (Figure 3.6). This relation showed an incremental trend for surrogates of non-dimensionalized flexural rigidity, i.e. $EI * (\rho_s u_0^2 A_{exp} x D_{ch})^{-1}$, less than 3x10$^2$. However, for the more rigid surrogates (A and B), a stable attenuation from 5–10% was observed regardless of incident velocity and distance behind the element.

To capture this behavior, an empirical relation to obtain the attenuation ratio was proposed through a 5$^{\text{th}}$-order polynomial equation: $AtR = 0.14\Gamma^5 - 0.58\Gamma^4 - 1.07\Gamma^3 + 3.3\Gamma^2 + 6.04\Gamma + 2.28$, where $\Gamma = \log[EI(\rho_s u_0^2 A_{exp} x D_{ch})^{-1}]$, $A_{exp}$ is the frontal area exposed to flow, given by $D_{ch} * h_r$. The relation provides a way to test different geometries and materials (given their flexural rigidity) based on their resulting attenuation. Special care is to be taken for $\Gamma > 3\text{x}10^2$, as the values of attenuation ratio do not follow the polynomial described above. More tests are thus needed to expand the range of validity or adjust the relation correspondingly.

## 3.4  Conclusions

This chapter focused on the influence of seagrass surrogates of varying geometries and mechanical properties on unidirectional flow. Two different experimental set-ups were presented, one testing highly flexible polypropylene surrogates with different width along the vertical axis, the other testing single surrogates of different cross-sectional area and flexural rigidity. These experiments should help quantify the effects of vertical areal distribution and the mechanical properties of materials to select an appropriate surrogate for seagrass used for field deployments.

The results showed that surrogates with a wider base are able to reduce flow better than those with wider upper halves, akin to wide leaves. Nonetheless, a constant width, even as small as 5 mm, produced a similar attenuating effect to the wider base, indicating that material can be saved by simply utilizing a constant distribution. Regarding geometry, wider cross-sections provided higher attenuation. However, the flexural rigidity proved to be more significant for effective attenuation, with a "sweet spot" found in medium flexural rigidities, i.e. not totally rigid that would not bend with flow, but also not highly flexible materials that lay flat under increased flow velocities.

These results provide the basis for future work with seagrass surrogates whose goal is to attenuate flow in a feasible way regarding field deployment. Chapters 4 and 5 make use of this contribution by changing the material tested under oscillatory flow. The ultimate goal of restoration can thus be optimized by selecting the right material based on its mechanical and geometric properties.

**3**

## Chapter highlights

- The vertical biomass distribution (VBD) affects flow within the water column, with concentration of biomass on the lower part of the canopy yielding greater attenuation.
- A VBD concentration above will induce less attenuation in the lower part, hence more erosion and increased velocities below the canopy top.
- A constant VBD will produce similar attenuation capacity as the surrogate with VBD concentrated in the lower part.
- Single-stem surrogates are able to reduce flow by themselves, proving that stem-to-stem interaction is not the only source of drag.
- The rate of flow attenuation induced by a single element perpendicular to flow is a function of its cross-sectional area.
- The flexural rigidity plays a more prominent role regarding flow attenuation, showcasing enhanced attenuation for medium rigidities.

# ANCHOR FORCES ON AN ARTIFICIAL SEAGRASS MAT UNDER WAVE LOADING

## 4.1 Introduction

Seagrasses are important globally spread coastal ecosystems that provide essential ecosystem services (Short et al., 2007). These services include habitat for fish, carbon sequestration (Barbier et al., 2011; Fourqurean et al., 2012), and reduction of hydrodynamic energy (Ondiviela et al., 2014). Despite these known services, almost a third of seagrass cover has been destroyed mostly due to human activity since records started during the late 19th century (Waycott et al., 2009). This has called for incentives to promote seagrass protection and restoration (Cullen-Unsworth and Unsworth, 2018) and to tackle the main challenges these ecosystems face (Unsworth et al., 2019). The UN Decade for Ecosystem Restoration highlights the need for immediate action, whereby new reports such as The Blue Guide to Coastal Resilience (Nature Conservancy, 2021), which provide guidelines for practitioners and stakeholders using nature-based solutions, include seagrasses as an essential ecosystem to be targeted for restoration.

A plethora of pilot seagrass restoration projects have tested different approaches; van Katwijk et al. (2016) provide a meta-analysis of more than 1700 trials, concluding that success, defined through seagrass survival, is mainly driven by the number of introduced seedlings and the site selected for restoration. Hydrodynamic conditions, i.e. incident wave heights and currents, also represent an important factor for survival (Barbier et al., 2011), such that shelter of seedlings plays an important role in restoration (Villanueva et al., 2021). To achieve shelter, artificial seagrass (ASG) mats can be deployed to minimize wave loading and currents in and around the desired restoration area, subsequently enhancing sedimentation and improving light availability (Carus et al., 2021). The ASG mats are composed of a base layer to which seagrass surrogates in the form of either flexible shoots or stems can be attached. Both components should ideally be made of biodegradable materials lest they become a source of microplastics whose proliferation and transport are enhanced by hydrodynamic loading (Kerpen et al., 2020) and represent a high risk to wildlife (Wright et al., 2013).

A candidate for the base layer to be used in seagrass restoration is coconut fiber –or coir. Coir-based geotextiles have gained popularity as a geoengineering solution as they provide high tensile strengths of up to 20 kN m$^{-1}$ (Subaida et al., 2008) while being biodegradable and hence less damaging to the environment. These geotextiles have been successfully applied for reforestation purposes –successfully prompting vegetation growth, improving soil stability, and protecting seedlings –as well as stabilization of riverbanks and sandy beaches, predominantly in Brazil, Indonesia, and India (see e.g. David et al., 2016). Admittedly, the tensile resistance of such geotextiles decreases with time due to degradation (Miller et al., 1998; Marques et al., 2014), yet they have proven to last for 2–5 years when used for soil stabilization and inland reforestation (Rickson, 2006). Experiments on tensile strength show 40% loss during the first half year and up to 80% after one year for reforestation under tropical conditions (Marques et al., 2014), and 77–90% after the third year for stream bank treatments (Miller et al., 1998).

Albeit scarce, examples of submerged ASG mats deployed in marine environments do exist; they focus on scour protection around pipelines and other structures, sediment and bed stabilization, habitat facilitation and even seagrass restoration (Ismail, 2003). On scour protection applications, one of the main problems commonly reported were anchors (Jones et al., 2006), whereby a popular

solution still used today is the one proposed almost half a century ago by Bakker et al. (1973): substrate-filled tubes that weigh down the mats. The authors advocate for weighted anchors, preferably flexible, to adapt to the changing environment and thus avoid failure, but also state that under extreme conditions pinned anchors may be needed. Jones et al. (2006) investigated the performance of ASG mats made by SSCS –a UK-based company focused on scour protection –and described the company-developed "Safe Anchor" which consists of a steel anchor buried at 1 m depth and connected to the mat by a high resistance strap. On seagrass restoration, Campbell and Paling (2003) used metal rods to anchor 1.5-by-1.5-m ASG mats to promote seagrass growth but did not measure the forces befalling the anchors. Bakker et al. (1973) reported an anchoring strength of about 1.5 kN for anchors pinned 0.5–1 m deep and state that "sufficient anchoring" is provided by anchoring tubes of 7–15 kg m$^{-2}$. However, none of these studies measured the actual forces occurring at the anchors under the local conditions. The anchors of flexible submerged mats lying on the seabed will experience oscillatory loads from the wave orbital motion and potentially increased loads caused by unidirectional currents (e.g. in tidal areas). The oscillatory motion is expected to create horizontal shear loads on the anchors caused by hydrodynamic drag and a lift force caused by both drag and buoyancy. The acting forces, however, will differ from other submerged anchors, such as those used for mooring lines, as these are affected by the water level fluctuations and movement along the whole water column (Peña et al., 2011). In addition, due to the flexibility of the mats, the distribution of forces will differ from the symmetrical force distribution given by the theory of plates and applied in construction and mechanics (e.g. anchor bolts and fastenings, see Mallée and Eligehausen, 2013).

To date, coir-geotextiles have not yet been employed permanently under marine conditions and their performance in such environments is largely unknown. Moreover, the forces occurring at the anchoring points of such mats have not been investigated. Thus, the aims of this study are: (i) compare the forces occurring at the anchoring points of coir-based geotextiles with differing structural composition; (ii) test the forces on a prototype ASG mat to be used in coastal areas for restoration purposes; and (iii) discuss the design criteria of candidate ASG mats to be used for restoration under real environmental conditions based on physical experiments (prototype scale to match material properties and wave-induced forces on ASG mats) and provide practical initial guidelines for future pilot studies. Finally, we derive a formula to determine the expected loading on anchors of ASG mats deployed in coastal areas depending on the local hydrodynamic conditions which can then be used as the basis for the conception of set-ups to be used in pilot projects.

## 4.2 Forces on an Artificial Seagrass Mat

### 4.2.1 *Drag Force*

Any submerged object in a marine environment will be subject to pressure and viscosity-induced forces –referred to as drag –and inertial forces caused by the mass acceleration of the fluid. These forces have been reliably represented by Morison-equation-based formulations where the forces are proportional to the square of the horizontal velocity ($F \sim u^2$), whereby generally, in the case of aquatic vegetation, plant movement and the inertial portion can be neglected (see e.g. Mendez and Losada, 2004; Losada et al., 2016), thus leaving the general form for drag force as:

$$F_x = \frac{1}{2}\rho C_D A u^2 \tag{4.1}$$

where the subscript $x$ represents the horizontal force component parallel to the main flow direction, $\rho$ is the water density, $C_D$ the drag coefficient, $A$ the characteristic area perpendicular to flow, and $u$ the flow velocity. Under wave conditions, this velocity $u$ is represented by the maximum horizontal wave orbital velocity, i.e. $u = U_w^{\max}$. $A$ will be given by the vegetation geometry orthogonal to flow, usually represented by the vegetation width $b_v$ and upright (stretched) height $h_c$.

A biodegradable ASG mat deployed for restoration would be composed of a flexible base layer and a set of flexible seagrass-like stems or shoots (Carus et al., 2021). The base layer lying on the seabed would be primarily subject to viscous drag driven by the so-called skin friction induced by an ambient current. This typical load case is commonly expressed by the bed shear stress $\tau_b$ which, for unidirectional flow, is analogously represented by means of the drag coefficient as $C_D = \tau_b/\rho u^2$ (Bricker et al., 2005). Under wave-induced loading, the skin friction represents a principal component of the wave-induced bed shear stress $\tau_{b,w}$ which in turn depends on the empirically derived friction coefficient $C_f$ (Pascolo et al., 2018), previously defined by Soulsby (1997) as:

$$C_f = 1.39\left(\frac{a_B}{z_0}\right)^{-0.52} \tag{4.2}$$

where $a_B$ is the horizontal orbital wave amplitude at the bed given by $a_B = uT/2\pi$, with $T$ the wave period; $z_0$ is the bed roughness length calculated as $z_0 = k_s/30$ with $k_s$ the equivalent sand roughness. The maximum wave-induced bed shear stress $\tau_{b,w}$ is then given by Equation 4.3. The subscript $w$ in Equation 4.3 and further equations in this chapter stands for waves.

$$\tau_{b,w} = \frac{1}{2}\rho C_f u^2 \tag{4.3}$$

The drag force on the ASG stems, on the other hand, is dominated by the pressure drag and is a function of the characteristic area normal to flow (Kobayashi et al., 1993; Mendez and Losada, 2004; Nepf, 2012a). To simplify the calculation of the drag force on flexible elements, Luhar and Nepf (2011) presented a model based on the effective blade length $l_e$ –i.e. the height of a single rigid stem whose drag matches that of a flexible stem of height $h_c$ (Equation 4.4). This model is based on the dimensionless parameters $B$ and $Ca$ (Equations 4.5 and 4.6) which correspond to the buoyancy term and the Cauchy Number, respectively, and represent the ratios of buoyancy and drag to the restoring forces due to stiffness.

$$l_{e,C} = h_c\left(1 - \frac{1 - 0.9Ca^{-1/3}}{1 + Ca^{-3/2}\left(8 + B^{3/2}\right)}\right) \tag{4.4}$$

$$B = \frac{\Delta\rho g b_v t_v h_c^3}{EI} \tag{4.5}$$

$$Ca = \frac{1}{2}\frac{\rho C_D b_v u^2 h_c^3}{EI} \tag{4.6}$$

where the subscript $C$ in $l_e$ represents the "current-only model", $\Delta\rho$ is the difference in density between water and the ASG, $t_v$ is the vegetation thickness, and $EI$ the flexural rigidity given by the modulus of elasticity $E$ and second moment of area $I$. The model was then applied to Equation 4.1 and successfully predicted the drag force on a single stem under unidirectional flow (Equation 4.7):

$$F_v = \frac{1}{2}\rho C_D b_v l_e u^2 \tag{4.7}$$

This formulation simplifies the calculation of the drag force on flexible elements using a single $C_D = 1.95$ for rigid cylinders (Vogel, 2020). Under this assumption, (Paul et al., 2016) further validated Equation 4.7 for varying regular and irregular wave conditions. The model was subsequently extended to consider wave-induced motion (Luhar and Nepf, 2016) where $l_e$ was found to depend on $Ca$ and the relative velocity between the stem and the oscillating water ($L$) given by the ratio $L = h_c/a_B$. The definition of $Ca$ changes for the extended model where it is given by $Ca_w = \rho b_v u^2 h_c^3/EI$, where the subscript $w$ represents the wave-extended model; $C_D$ is omitted due to its variation with the Keulegan-Carpenter Number ($KC = uT/b_v$), which gives the ratio between drag and inertial forces under wave-induced flow. $C_D$ is then only applied within the calculation of the modeled force (Equation 4.7) and is given by $C_{D,w} = \max(10KC^{-1/3}, 1.95)$ (Luhar and Nepf, 2016). Recalling that $u = U_w^{\max}$, the reconfigured height based on maximum forces caused by wave-induced flow is then given by:

$$l_{e,w} = b_1(Ca_w L)^{b_2} h_c \tag{4.8}$$

with $b_1 = 1.05 \pm 0.12$ and $b_2 = -0.03 \pm 0.08$ for $Ca_w L \leq 1$ and $b_1 = 0.65 \pm 0.07$ and $b_2 = -0.22 \pm 0.02$ for $1 < Ca_w L < 4000$. The inertial portion present in the right term of equation 20 in Luhar and Nepf (2016) can be neglected as at $U_w^{\max}$ the acceleration is equal to zero and $l_{e,w}$ can be used in Equation 4.7 with $C_{D,w}$ to obtain the modeled maximum forces under waves. Note that Equation 4.8 shows that the effective length is not dependent on $Ca_w L$ for $Ca_w L \leq 1$, which marks the limit at which the blade behaves like a rigid stem and the effective length approaches $h_c$. Lei and Nepf (2019b) expanded this model for a broader range of conditions, obtaining $b_1 = 0.94 \pm 0.06$ and $b_2 = -0.25 \pm 0.02$ for $0.3 < Ca_w L < 20000$. Other dimensionless parameters have been introduced in recent literature (e.g. Jacobsen et al., 2019) comparing the dimensionless ratio $CaL(KC^{-1})$ with $CaL$ and the typical hydrodynamic parameters $KC$ and the Reynolds number $Re$. Here, we focus on the stem-induced drag force which is a function of the material properties. As such, we further focus on $CaL$ and the resulting $l_e$ to characterize drag. Note that previously $Ca$ has been defined differently for unidirectional flow, pure wave, and combined waves and currents. While several studies define $Ca$ as $Ca_w$ mentioned above for pure wave conditions (Luhar and Nepf, 2016; Lei and Nepf, 2019b; van Veelen et al., 2021), Lei and Nepf (2019a) showed that $Ca$ given in Equation 4.6 is suitable for long waves ($L \ll 1$) as well as combined waves and currents.

### 4.2.2 *Anchor Forces*

The forces occurring at the anchors will depend on: (a) the size of the mat and corresponding skin friction represented by the bed shear stress (Equation 4.3), (b) the drag induced by the ASG

(Equation 4.7), and (c) the number of anchoring points per surface area. The latter aspect translates into a corresponding area which depends on the size of the mat. Here, we hypothesize that the force at the anchor of an ASG mat can be expressed as the sum of ASG and mat drag forces based on the characteristic area corresponding to the anchor (Equation 4.9).

$$F_{x,mod,ap} = F_v N A_{ap} + \tau_{b,w} A_{ap} = \frac{1}{2}\rho u^2 (C_D b_v l_e N + C_f) A_{ap} \tag{4.9}$$

with $N$ the shoot density per unit area. The subscript $ap$ stands for 'anchor position' which can be either $f$ for frontal or $r$ for rear anchor. Based on site-specific conditions (water depth, wave height and period, and the sediment composition) the expected maximum horizontal orbital velocity over the bed and $\tau_{b,w}$ (Equation 4.3) can be calculated. Finally, an estimation of the characteristic area for each anchor $A_{ap}$ (discussed in Section 4.4.1) can provide the expected drag force on the anchors using Equation 4.9.

## 4.3 Methodology

Laboratory experiments were carried out in the WKS (Schneiderberg Wave Flume) at Ludwig-Franzius-Institute in Hanover, Germany. The WKS is a 110-m long, 2.2-m wide, and 2-m deep wave flume equipped with a vertical paddle-type electric wave maker. The maximum paddle stroke is 1.8 m and its maximum wave height generation is 0.5 m. A 10.5-m-long, 10-cm-deep sand bed beginning 62.65 m away from the wave paddle (in idle position) was built (Figure 4.1). The sand consisted of a homogenously graded quartz sand of $d_{50}$ = 0.19 mm, particle density 2.65 g cm$^{-3}$ and bulk density 1.45 t m$^{-3}$. The sand bed was preceded by a 1:30 ramp made of 2.7-cm-thick plywood panels and a smaller 1:10 ramp was built out of gravel on the far end. A stepped aluminum artificial beach covered with thick industrial foam at the end of the flume was in place to increase wave absorption and minimize reflection. Additional plywood panels were installed covering the concrete bed of the flume along the full span of the sand bed to facilitate the mounting of anchors (Figure 4.2). The panels plus the layer of sand meant that the sand bed surface was 12.7 cm above the concrete flume bed.

The experimental set-up was divided into two sets of experiments: (1) experiments with three different coir mats without ASG for the purpose of testing different coir mesh combinations –from now on denominated CM; and (2) experiments with ASG using a coir mat as base layer to test the effect that the additional artificial vegetation has on anchor loading –from now on denominated AV. With regard to mat size and placement, sheltering and seagrass growth facilitation need to be considered. The dense coir-ASG combination covers the sand bed in such a way that actual seagrass could hardly grow within the mats. To circumvent this problem, a checkerboard-like configuration was envisioned (Carus et al., 2021), with alternating patches of ASG and bare sand, whereby shelter for growing seagrass is provided adjacent to the ASG and within the enclosed bare sand patches. A horizontally symmetrical patch of 2-by-2-m was chosen as prototype for testing the staggered configuration. All experiments were done at prototype scale so that scaling effects did not affect the results while facilitating transferability to field conditions. In all experiments, the mats were set, not buried, on the sand bed.
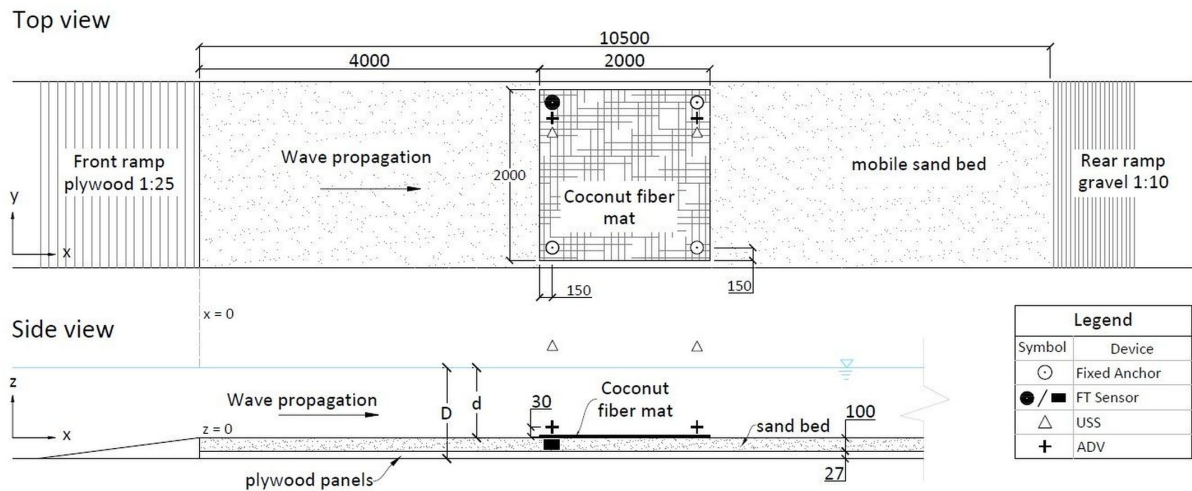
Figure 4.1: Top and side view of the experimental set-up section of the flume. The wave paddle is located at $x = -62.65$ m. $x = 0$ position shown by the gray dashed line joining both schemes. The experimental set-up shown corresponds to the coir mat experiments without artificial seagrass (one anchor set-up, see Section 4.3.2). The $z$-scale is exaggerated; all dimensions are given in mm. $d$ = water depth above the sand bed; $D$ = water depth above flume floor.

Although current loads may be high in tidal zones (Bouma et al., 2005), fully, perennially submerged areas are dominated by loads from orbital motion created by waves, whereby shallow, low-energetic (non-extreme wave loading and no wave breaking) areas are a reasonable choice for restoration projects (van Katwijk et al., 2016). We, therefore, aimed to produce nature-like conditions based on horizontal orbital velocities and investigated the load caused by near-bed velocities $u < 40$ cm s$^{-1}$ ($z = 3$ cm, Figure 4.1) which would represent a threshold value for growing seedlings and seeds (Fonseca et al., 1983; Koch et al., 2010). The incident wave conditions (regular, non-breaking waves only) were chosen accordingly by previously calculating the expected horizontal orbital velocities at the bed following linear wave theory. The chosen wave periods ranged from 1.5–5 s and wave heights from 2–33 cm, with 3 different depths for the AV series (Table 4.1). The input conditions yielded theoretically calculated velocities ranging from 0.03–0.38 m s$^{-1}$. The calculated velocities were only used during the experimental design phase, whereas for analysis, the measured velocities were used (Section 4.4). Control measurements with no coir or ASG mat were done for all chosen incident wave conditions (CM and AV) and device positions (Section 4.3.1) to directly assess the effect of the mats on anchor forces. For each experimental run (i.e. wave condition), sixty waves were generated employing a ramp time of 3 times the respective $T$. Throughout the experiments, the $x$, $y$, and $z$-directions corresponded to the wave propagation direction, the horizontal cross-section of the flume, and the vertical direction, respectively, with $x = 0$ at the start of the sand bed and $z = 0$ at the sand bed surface (Figure 4.1).

### 4.3.1 *Instrumentation*

To quantify the wave-induced forces on the anchoring points, we developed a sophisticated experimental set-up utilizing ATI Gamma IP68 Force/Torque transducers (FT) to measure the force acting on the anchors (see Figure 4.2 for device specifications). The FT were further calibrated with a manual force gauge (FMI-100B5) and known weights. Throughout this chapter, the forces at the

Table 4.1: Input parameters (depth *d*, wave height *H*, and wave period *T*) for experiments with coir-based mats and no artificial vegetation (CM) and experiments with artificial seagrass (AV).

**CM**

| run | 1 | 2 | 3 | 4 | 5 | 6 | 7 | 8 | 9 | 10 | 11 | 12 | 13 |
|---|---|---|---|---|---|---|---|---|---|---|---|---|---|
| $H$ [m] | 0.02 | 0.02 | 0.18 | 0.19 | 0.20 | 0.15 | 0.17 | 0.12 | 0.14 | 0.09 | 0.11 | 0.06 | 0.08 |
| $T$ [s] | 1.50 | 2.00 | 3.00 | 3.00 | 3.00 | 3.50 | 3.50 | 4.00 | 4.00 | 4.50 | 4.50 | 5.00 | 5.00 |

**AV**

| run | $H$ [m] | $T$ [s] | $d$ [m] | $u_{\text{meas}}$ [m s$^{-1}$] | $a_B$ [m] | $L$ [-] | $KC$ [-] | $Ca$ [-] | $C_D$ [-] | $CaL$ [-] | $l_{e,w16}$* [-] | $l_{e,w19}$* [-] |
|---|---|---|---|---|---|---|---|---|---|---|---|---|
| **1 Mat** | | | | | | | | | | | | |
| 1 | 0.11 | 2.00 | 0.50 | 0.18 | 0.06 | 4.64 | 74.04 | 3.08 | 2.41 | 13.08 | 0.37 | 0.50 |
| 2 | 0.06 | 3.00 | 0.50 | 0.12 | 0.06 | 4.70 | 74.35 | 1.40 | 2.41 | 5.84 | 0.44 | 0.61 |
| 3 | 0.19 | 4.00 | 0.50 | 0.43 | 0.27 | 0.92 | 359.36 | 17.55 | 1.95 | 15.88 | 0.35 | 0.47 |
| 4 | 0.11 | 5.00 | 0.50 | 0.23 | 0.18 | 1.39 | 238.26 | 4.97 | 1.95 | 6.74 | 0.43 | 0.58 |
| 5 | 0.22 | 2.00 | 0.63 | 0.29 | 0.09 | 2.74 | 120.78 | 7.98 | 2.03 | 21.34 | 0.33 | 0.44 |
| 6 | 0.11 | 3.00 | 0.63 | 0.19 | 0.09 | 2.76 | 119.83 | 3.48 | 2.03 | 9.41 | 0.40 | 0.54 |
| 7 | 0.06 | 4.00 | 0.63 | 0.09 | 0.06 | 4.55 | 72.89 | 0.73 | 2.40 | 3.22 | 0.50 | 0.70 |
| 8 | 0.22 | 5.00 | 0.63 | 0.38 | 0.30 | 0.85 | 394.07 | 13.72 | 1.95 | 11.14 | 0.38 | 0.52 |
| 9 | 0.33 | 2.00 | 0.83 | 0.28 | 0.09 | 2.80 | 117.53 | 7.49 | 2.04 | 20.77 | 0.33 | 0.44 |
| 10 | 0.22 | 3.00 | 0.83 | 0.32 | 0.15 | 1.63 | 202.30 | 9.87 | 1.95 | 15.89 | 0.35 | 0.47 |
| 11 | 0.11 | 4.00 | 0.83 | 0.20 | 0.13 | 1.95 | 169.38 | 3.91 | 1.95 | 7.48 | 0.42 | 0.57 |
| 12 | 0.06 | 5.00 | 0.83 | 0.08 | 0.07 | 3.84 | 87.01 | 0.67 | 2.27 | 2.46 | 0.53 | 0.75 |
| **2 Mats** | | | | | | | | | | | | |
| 1 | 0.11 | 2.00 | 0.50 | 0.15 | 0.05 | 5.35 | 63.00 | 2.20 | 2.53 | 11.13 | 0.38 | 0.52 |
| 2 | 0.06 | 3.00 | 0.50 | 0.14 | 0.07 | 3.94 | 88.80 | 1.99 | 2.27 | 6.97 | 0.43 | 0.58 |
| 3 | 0.19 | 4.00 | 0.50 | 0.46 | 0.29 | 0.87 | 379.98 | 19.65 | 1.95 | 16.79 | 0.35 | 0.46 |
| 4 | 0.11 | 5.00 | 0.50 | 0.26 | 0.20 | 1.24 | 267.27 | 6.23 | 1.95 | 7.56 | 0.42 | 0.57 |
| 5 | 0.22 | 2.00 | 0.63 | 0.26 | 0.08 | 3.10 | 107.08 | 6.28 | 2.11 | 18.92 | 0.34 | 0.45 |
| 6 | 0.11 | 3.00 | 0.63 | 0.21 | 0.10 | 2.51 | 134.11 | 4.44 | 2.01 | 10.53 | 0.39 | 0.52 |
| 7 | 0.06 | 4.00 | 0.63 | 0.10 | 0.06 | 4.07 | 82.64 | 0.94 | 2.31 | 3.65 | 0.49 | 0.68 |
| 8 | 0.22 | 5.00 | 0.63 | 0.35 | 0.28 | 0.91 | 360.99 | 11.34 | 1.95 | 10.21 | 0.39 | 0.53 |
| 9 | 0.33 | 2.00 | 0.83 | 0.27 | 0.08 | 3.00 | 111.21 | 6.80 | 2.09 | 19.65 | 0.34 | 0.45 |
| 10 | 0.22 | 3.00 | 0.83 | 0.34 | 0.16 | 1.56 | 212.43 | 10.93 | 1.95 | 16.68 | 0.35 | 0.47 |
| 11 | 0.11 | 4.00 | 0.83 | 0.16 | 0.10 | 2.41 | 136.71 | 2.54 | 1.97 | 6.04 | 0.44 | 0.60 |
| 12 | 0.06 | 5.00 | 0.83 | 0.07 | 0.05 | 5.07 | 70.94 | 0.47 | 2.46 | 2.01 | 0.56 | 0.80 |
| | | | | [13%] | [13%] | [14%] | [13%] | [25%] | [3%] | [13%] | [3%] | [3%] |

* values normalized by $h_c$. CM had a constant depth of $d = 0.50$ m. The measured maximum velocities and calculated hydraulic parameters are given for the AV experiments as well as the resulting effective length based on the wave extension models. Percentages in the last row indicate the average uncertainty of the calculated parameters.

**4**
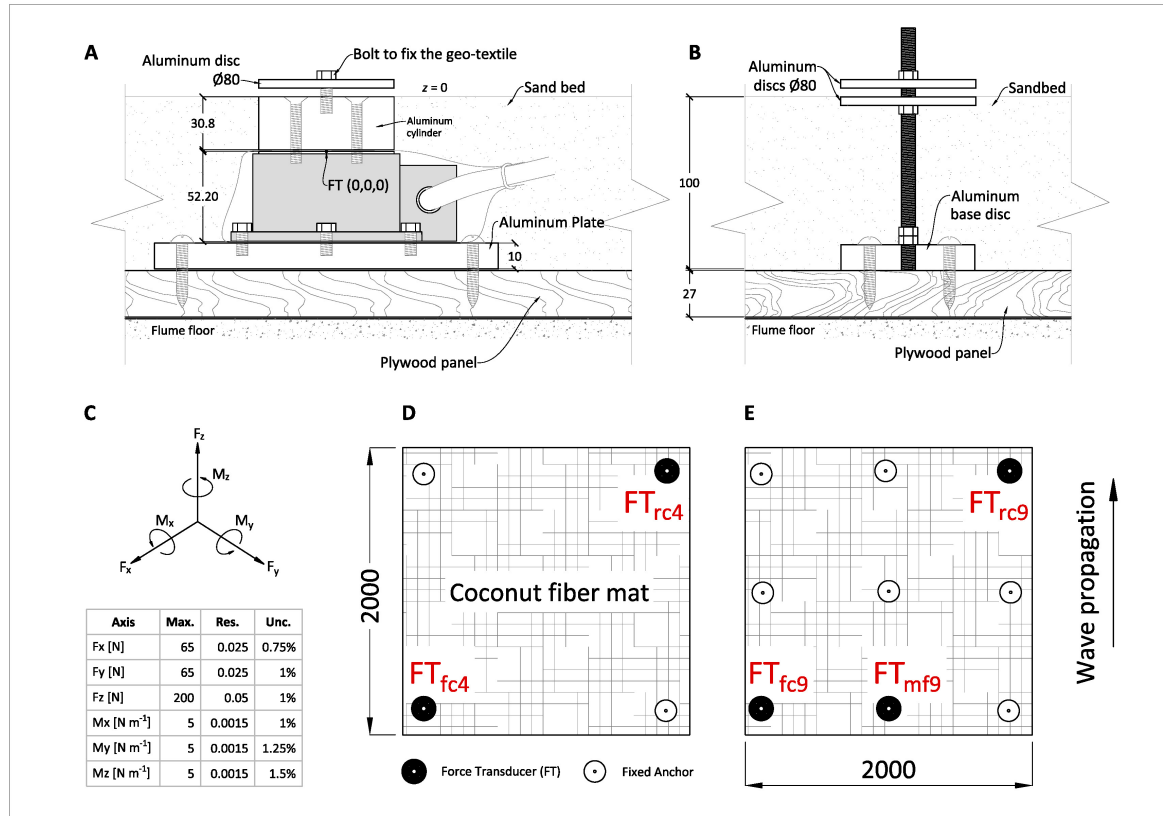


Figure 4.2: Anchor set-up and positions. (A) Force-Torque transducer (FT), shown in gray, and its mounting frame which includes a custom-made aluminum cylinder to make the transducer flush with the sand bed. (B) Fixed anchor construction. (C) Schematic of the 6 degrees of freedom of the FT measured at (0,0,0) shown in panel (A) and device specifications (Res = resolution; Max. = measuring range; Unc. = uncertainty given by manufacturer). The direction of the axes was set to match the coordinate system used in the flume. (D) 4-anchor mat configuration and position of the FT for measurements. (E) 9-anchor configuration with the different FT positions. Subscripts in panels (D,E) denote the specific anchor position and set-up as follows: f and r stand for front and rear, c and m for corner and middle, and 4 and 9 for the total number of anchors, respectively. Note that the indicated wave propagation direction for panels (D,E) is down to up. All dimensions are given in mm.

anchors are represented by $F$ and the torques by $M$, with a subscript indicating the direction. A custom-made 30.8-mm-long aluminum cylinder was fixed to the top of the transducer to set the anchor proxy flush with the sand bed ($z = 0$, Figure 4.2A). The offset created by the cylinder acts on the torque measurement of the FT, which was then accounted for during data post-processing. Nuts and aluminum discs were used to make sure that the coir mats did not come out of their anchoring point and that the full load went to the anchors. The fixed anchors, i.e. those without an FT, consisted of threads fixed to solid aluminum discs screwed into the plywood floor and additional discs to entrap the mat flush with the sand bed ($z = 0$, Figure 4.2B).

ULTRALAB Ultrasonic Sensors (USS) with a resolution of 0.2 mm were used to measure the water level fluctuations $\eta$ during the experiments and were installed over the sand bed. The position of the sensors varied depending on the set-up (sections 4.3.2 and 4.3.3). The USS and FT measured simultaneously through an HBM signal amplifier at a frequency of 100 Hz. Finally, wave orbital velocities were recorded simultaneously employing a trigger connected to the HBM and utilizing downward-looking NORTEK Vectrino+ Acoustic Doppler Velocimeters (ADV) measuring at 25 Hz

Table 4.2: Technical specifications of the coir mats used for the experiments.

| | Unit | CN700 (CM1) | Eromat 7H (CM2) | Eromat 75C (CM3) |
|---|---|---|---|---|
| Fabric type | - | flat coir fabric with coiled yam | Coir fiber | Coir fiber |
| Weight | [g m$^{-2}$] | 700 | 750 | 600 |
| Mesh width* | [mm] | 16 x 16 | 16 x 16 | 13 x 12 |
| Mesh material | - | - | PP-thread, UV-degradable | HDPE, UV-stabilized |
| Tensile strength° | [kN m$^{-1}$] | 14 (11)[+] | 1.11 (0.45)† | 11‡ |
| Elongation° | [%] | 19–24 | 26 (20)† | 20 (15)† |
| Longevity | [months] | - | 36–48 | 48 |
| Max. shear stress | [N m$^{-2}$] | - | 13.734 | 125 |
| roughness $n$ | [-] | - | 0.014 | - |

Source: Greenfix technical datasheets provided by SOILTEC GMBH. PP: Polypropylene; HDPE: High-density polyethylene. *CM1 is a woven net, size indicates average spacing between threads, both directions. For CM2 and CM3, mesh width refers to the synthetic reinforcement nets wrapping the coir. °Parenthesis indicates cross-sectional value. [+]DIN 53857. †D4595. ‡ISO-10319.
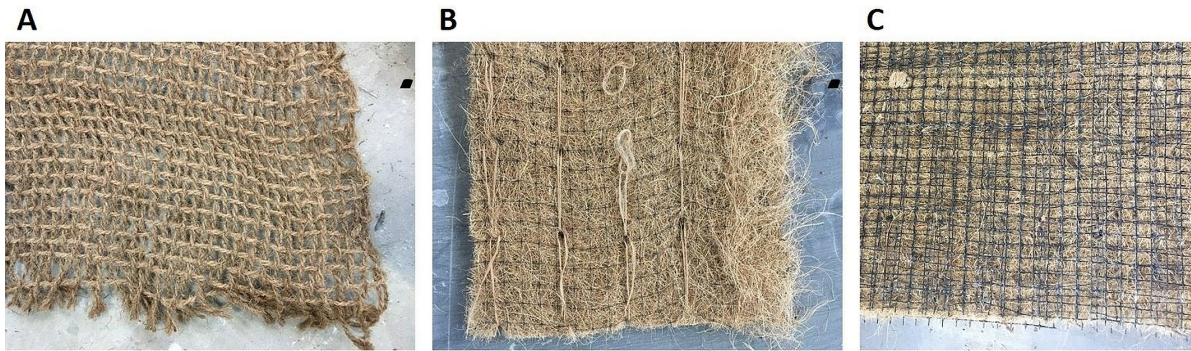


Figure 4.3: Coir mats used for testing without artificial seagrass. (A) CN700: Coir netting made of woven coir fiber (CM1), (B) Eromat 7H: Coir fiber encompassed by thin polypropylene (PP) (CM2). (C) Eromat 75C: Coir fiber encompassed by high-density polyethylene (HDPE) (CM3). An indication of size is given in Table 4.2

and 50 Hz for set-ups CM and AV, respectively. The $u$, $v$ and $w$ components of the measured velocities were respectively aligned with the $x$, $y$, and $z$ components of the set-up.

### 4.3.2 *Coir Mat Tests (CM)*

Three different types of coconut fiber mats (product: Greenfix, manufactured by SOILTEC GMBH) with no ASG were tested (Figure 4.3 and Table 4.2): (1) CN700 –a coir netting; (2) Eromat Type 7H –a coir fiber-mesh mat (weak polypropylene, PP, reinforcement); and (3) Eromat type 75C –a coir fiber-mesh mat (strong high-density polyethylene, HDPE, reinforcement) usually used for turf reinforcement. Throughout this chapter, the 3 mats are referenced by the number given above to identify specific mat experiments, e.g. CM1 corresponds to the coir netting (Figure 4.3A).

To match the envisioned checkerboard-like configuration at prototype scale, mats with a dimension of 2x2 m were used, meaning they covered most of the width of the channel (10-cm spacing between mat edge and flume wall at each side). Two anchor set-ups were used (Figure 4.2D,E): (i) 4-anchor set-up, one in each corner of the square mat; (ii) 9-anchor set-up, distributed in a 3-by-3-knot setting. For this set of experiments, a single FT sensor was available which was
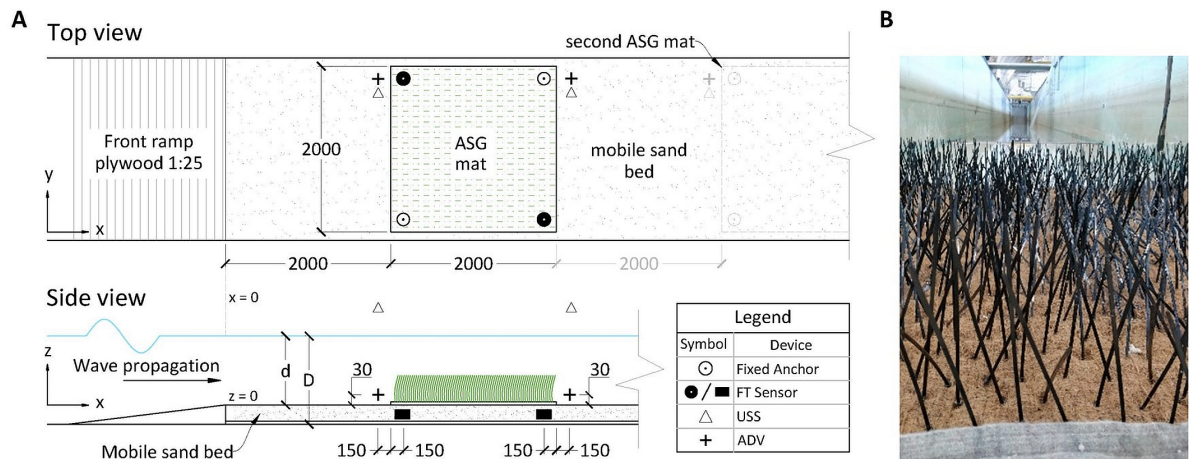
Figure 4.4: Schematic of the experimental set-up for ASG coir mats (1-mat set-up, 2$^{\text{nd}}$ mat shown dimmed). $z$-scale is exaggerated; all dimensions given in mm. (B) Close-up image of an ASG mat in the flume.

sequentially placed in different positions. Throughout this chapter, the frontal anchors refer to those affected first by incident waves (FT$_{fc4}$, FT$_{fc9}$ and FT$_{mf9}$, subscript $f$ for front, $c$ for corner, $m$ for middle, and the digit denoting the number of anchors in the set-up) and rear anchors those affected afterward (FT$_{rc4}$ and FT$_{rc9}$, subscript $r$ for rear). Two ADVs and two USS were aligned in the $y$-direction with the FT, with the ADVs measuring at a height of $z = 3$ cm (Figure 4.1). The aluminum discs of the anchors created a reflection that affected the ADV measurements, so ADVs were not placed directly above the anchors. We tested each mat type and anchor configuration with 13 different incoming regular wave conditions under a constant water depth $d = 0.5$ m (Table 4.1); each of these runs (i.e. each wave condition) was performed 3 times, once for each mat type, and repeated 5 times, once for each anchor position. This resulted in a total of 208 test runs (including a set of control runs performed without coir mats).

### 4.3.3 *Mat Tests with Artificial Vegetation (AV)*

The artificial vegetation was made of cable straps of width $b_v = 4.8$ mm, length of $h_c = 250$ mm and thickness $t_v = 1.36$ mm (Figure 4.4B), composed of polyamide (PA, density $\rho_{\text{PA}} = 1.13$ g cm$^{-3}$ and a flexural rigidity of $EI = 800$ N mm$^2$ Taphorn et al., 2021). A density of $N = 400$ shoots m$^{-2}$ was chosen, which results in a frontal area per canopy volume $a = 1.92$ m$^{-1}$ (Nepf, 2012a). The chosen shoot density and stem length is akin to those found in nature for strap-like seagrasses such as *Zostera marina* (e.g. Ondiviela et al., 2014). Albeit not biodegradable, PA was chosen based on the target mechanical properties of ASG used for restoration, which may potentially be used in the field (Bouma et al., 2005). Taphorn et al. (2021) proved that under unidirectional flow (in the absence of wave motion), a single-stem PA shoot, which was mechanically and geometrically identical to the one used in the present study, alters the incident velocity while displaying a flexible, plant-like motion. This motion is an essential parameter when studying structure-hydrodynamic interaction (Paul et al., 2016).

The CM series revealed that, under wave loading, the coir meshes tend to be torn apart from within due to the oscillatory motion. The coir netting (CM1) displayed the best stability under

wave loading, with threads basically intact after all runs. However, as PA is not positively buoyant, fixing the straps by tying them around the netting proved to be complicated even under laboratory conditions. Therefore, we produced a hybrid coir netting mesh by stacking the non-reinforced coir mesh (CM2) on top of the coir netting (CM1), the latter therefore serving as a kind of biodegradable reinforcement to the former. As the surface area remains unchanged and the contribution of the net proved to be minimal (Section 4.5.2), we do not expect a major difference between the drag contribution of the AV mat (excluding vegetation) and CM mats, the former being just a combination of two of the latter. Finally, to avoid that neither the fiber within the mesh nor single threads of the netting came apart during testing, an industrial sewing machine was used to seal the edges with a thin synthetic fabric; this proved to be highly effective as the mats had suffered no discernible damage by the end of the experiments and moreover seems practical under real conditions in the field.

The AV series was likewise done in prototype scale utilizing 2-by-2-m mats (Figure 4.4), where we tested the effects of having (a) one ASG mat and (b) two ASG mats with a bare sand bed gap of 2 m between them. The AV tests were done exclusively for the 4-anchor configuration. In addition, three different submergence ratios ($h_c/d$) were used, each with four varying wave conditions in order to meet the target horizontal orbital velocities above the bed (Table 4.1). Due to blade motion, the ADV sensors could not be placed within the mat. Therefore, orbital velocity profiles were measured around the mat(s) by deploying ADVs located 15 cm in front of and behind each mat –aligned in $x$ with the FT sensors (Figure 4.4A). The sensors were vertically displaced to measure at $z = [3, 10, 25, 35, 45]$ cm (with the last height only possible for the two higher $d$ used). The analysis of the velocity structure around the ASG and the gradual wave height decay in reference to propagation distance over the ASG mats was outside the scope of this chapter and is thus not further discussed here (see Chapter 5); nonetheless, the velocity profile measurements meant that each run was repeated 4-5 times (depending on $d$) thus yielding the corresponding number of repetitions for the AV force measurements. Previous research regarding wave-induced flow within and around seagrass meadows have decomposed flow into a mean current, mean oscillatory flow and the turbulent components (e.g. Luhar et al., 2010); here, however, we focus on measured bulk incident velocity affecting the anchors and refer to this as the orbital velocity within the entire chapter.

For AV, two FT were available (Figure 4.4) which allowed to simultaneously measure the induced forces at the frontal and rear anchors of propagating waves for all runs (FT$_{fc4}$ and FT$_{rc4}$ simultaneously, as depicted in Figure 4.2D). USS vertically aligned with the ADVs provided wave height measurements. For each test case, the experiments were thereafter repeated according to the number of mats and ADV vertical positions, including control measurements, resulting in a total of 168 runs with the conditions shown for AV in Table 4.1.

## 4.4 Data Analysis

All recorded data were processed utilizing MATLAB (Version R2020a). Water level fluctuations at the leading edge of the mat (or of the first mat for the 2-mat set-up) were extracted from the USS data. Autocorrelation was then used to calculate the period $T$ of the incoming waves by determining the

**4**

time-lag between correlation peaks, which was then compared with the calculated $T$ for control; the former did not deviate from the latter by more than 0.02 s, so we further used the measured $T$ for all corresponding calculations. 50 waves were then extracted from each of the time series produced by each Instrument. The USS and FT data were zeroed before each measurement and afterward detrended during post-processing to make sure only the fluctuations caused by wave propagation were considered. Non-linearity could be observed within the incident waves, especially for $T >$ 3 s, which resulted in analogous non-linear measurements from the FT and ADV measurements. Here, we focused on the measured incident velocity and corresponding measured forces, using the measured values in all calculations. Hence, these non-linearities are not further discussed in detail.

The output of the FT measurements corresponds to the shear forces in $x$ and $y$, the lift force in $z$, and the corresponding torques at the measuring point of the device (i.e. [0,0,0] in Figure 4.2A,C). The offset between the measuring point and acting forces caused by the buried position of the sensor was corrected during post-processing. The lift force $F_z$ could be directly taken from the measurements while the forces in $x$ and $y$ were a function of the torque in $y$ and $x$, respectively. Thus, for the forces directly at the anchor, $F_{x,M} = M_y/l_a$ and $F_{y,M} = M_x/l_a$, where $l_a$ is the lever arm and the subscript M depicts the forces calculated from the torque measurements. In order to derive the impact of the ASG mats on the anchor forces in all relevant directions, we subsequently subtracted the maximum measured forces of each run from the respective maximum measured control measurement; e.g. $F_x^{\max} = F_{x,M}^{\max}(\text{run}_i) - F_{x,cl}^{\max}(\text{run}_i)$, where the subscript $cl$ stands for the control measurement and the input variables are a function of the specific wave conditions ($\text{run}_i$).

A preliminary analysis of the forces occurring at the anchors revealed that the lift forces ($F_z$) were smaller in magnitude than the horizontal forces. In addition, the cross-sectional force $F_y$ was not negligible, indicating that, although particle motion is 2-dimensional, the forces at the anchors were 3-dimensional. This is because the anchors, located at the corners of the mats, experience forces directed towards the center of the mat as bed shear stress acts across its whole surface, i.e. in the $x$-$y$ plane (Figure 4.5). Here, we describe this horizontal force at the anchors through the resultant horizontal force, calculated from both relevant components (Equation 4.10) for each run for the complete time series, thus yielding a new time series of the resulting forces on the anchor. Finally, we calculated the respective direction of the resultant force in radians using the four-quadrant inverse tangent.

$$F_R(t) = \sqrt{F_x^2(t) + F_y^2(t)} \tag{4.10}$$

The ADV data were first curated by removing measurements not complying with threshold values of 15 dB for beam signal-to-noise ratio (SNR) and 70% for correlation (Sulaiman et al., 2013). The acceleration threshold method (Goring and Nikora, 2002) was then used to de-spike the data. The orbital velocity data presented here correspond to the measurements at $z = 3$ cm. Similarly, both ADV and FT data were filtered utilizing a 4th-order zero-phase digital filter to avoid peaks and outliers. After filtering, we calculated the average maxima and minima for all 50 waves within all data –i.e. water levels, horizontal and vertical orbital velocities, and all directions of forces and torques –through time-synchronous signal averaging (TSA). TSA provides a phase average of all waves as a function of sampling frequency and wave period. Here, the maxima and

minima corresponding to each run are represented by the maxima and minima of the resulting phase-averaged wave.

### 4.4.1 *Modeled Forces*

The expected forces on the anchors of an ASG mat were calculated for the AV series based on the wave-induced bed shear stress $\tau_{b,w}$ and the stem drag force $F_v$ (Equations 4.3 and 4.7, respectively). The measured incident velocity ($u_{\mathrm{max},f}$) and calculated $T$ were used to calculate $a_B$ and $KC$. $k_s$ was calculated from manning's $n$ given for the top mat (CM2, Table 4.2) using the relation $n \approx k_s^{1/6}/26$ (Marriott and Jayaratne, 2010) to then calculate $z_0$ and the friction coefficient $C_f$ utilizing Equation 4.2. $B$ and $Ca$ were calculated from the ASG mechanical and geometric properties and the measured maximum horizontal orbital velocities in the direction of wave propagation in front of the preceding mat ($u_{\mathrm{max},f}$). The chosen ASG is negatively buoyant with no marked effect on the drag force as the restoring forces due to stiffness certainly dominate, thus approaching a zero-buoyancy case (Luhar and Nepf, 2011) with $|B| = 0.16$. For the wave-induced model (using Equation 4.7 with Equation 4.8), the calculated modeled forces did not differ significantly when using either $Ca$ or $Ca_w$ ($R^2 = 0.99$ and RMSE=0.15 after linear regression); Equation 4.6 was thence further used for all calculations of $Ca$, yielding values ranging from 0.13–24.9 for the range of measured ($u_{\mathrm{max},f}$). For comparison, the range of $Ca$ of seagrasses can range from 0.16 for stiffer species up to 80000 for highly flexible ones (see table 1 in Lei and Nepf, 2019b, and references therein for further details on seagrass parameters). Furthermore, the measurements yielded the following ranges for the non-dimensional hydraulic parameters: $40 \leq KC < 400$; $1.95 \leq C_D \leq 2.95$; $0.66 < L < 8.45$; and $1.1 \leq CaL < 24.5$ (Table 4.1).

The modeled forces were calculated after both the approach under unidirectional flow proposed by Luhar and Nepf (2011), validated for waves by Paul et al. (2016), and the extended approach for wave-induced forces proposed by Luhar and Nepf (2016), including the further extension by Lei and Nepf (2019b) for a comparison of wave-based models. The application of both current-based and wave-based models was done to test the feasibility of using a flow-only-based model against the wave extension models when calculating anchor forces on a vegetated ASG mat. The flow-only model is easily applicable when only near-bed flow data is available for a specific site, whereas the wave extensions require knowledge of the governing sea state. For all models, $Ca$ was then given by Equation 4.6, while $C_D = 1.95$ for the unidirectional flow model and is a function of $KC$ for the wave-induced force model (Section 4.2). The corresponding effective length, $l_e$, was then calculated from Equations 4.4 and 4.8 and used in Equation 4.9 to calculate the forces at each anchor.

For the characteristic area $A_{ap}$, symmetry along the $y$ axis about the mid-flume ($x$-$z$ plane) was assumed so that only one frontal and one rear anchor were further analyzed (Figure 4.5). The force measurements for all test cases were then separated into frontal and rear anchor forces. Similarly, $A_{ap}$ was partitioned into a frontal ($A_f$) and rear ($A_r$) portion. Following a proportional relation between the force and the square of orbital velocity ($F \sim u^2$), a simple quadratic fitting approach ($y = \alpha x^2$) was tailored to capture this dependency by means of fitting the resulting $F_x$ vs. $u_{\mathrm{max}}$ plots for the frontal and rear anchor forces based on the frontal incident velocity, i.e. $u_{\mathrm{max},f}$. The ratio of the fitted coefficients ($\alpha$) was then taken as the relation between frontal and rear anchor forces.

**4**
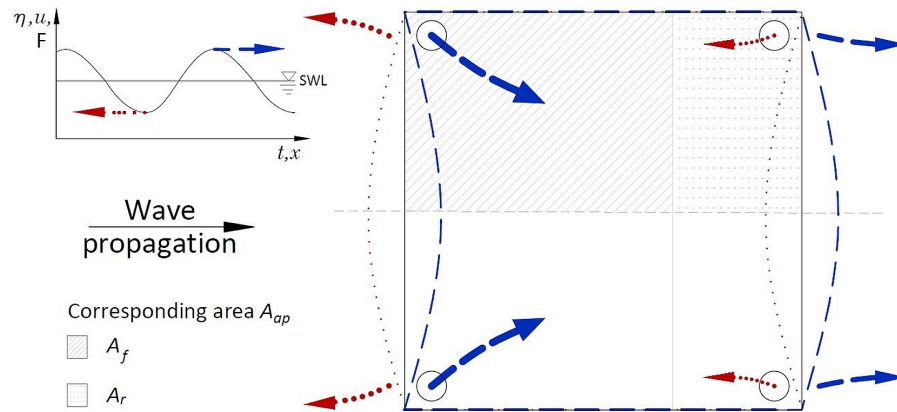


Figure 4.5: Qualitative scheme of the predominant directions of the resultant forces in the direction of wave propagation (blue dashed line) and opposite direction (red dotted line) for the 4-anchor configuration and respective (exaggerated) deformation of the mat with the corresponding area for each anchor (Aap) for the direction of wave propagation. The solid gray line denotes the original mat position. SWL = Still Water Level.

For simplicity, the ratio of forces was assumed analogous to the ratio of the corresponding length per unit width, i.e. $\alpha_f/\alpha_r = L_{m,f}/L_{m,r} = r_\alpha$, where $L_m$ is the length of the mat ($x$-direction) and is given by $L_m = L_{m,f} + L_{m,r}$. Finally, for our case using a mat of 2 m width, the equivalent area for the anchors on either side of the mat results in $A_f = L_{m,f}$ and $A_r = L_{m,r}$ for the frontal and rear anchors, respectively. $A_f$ can then be calculated as shown in Equation 4.11, after which $A_r = L_m$ - $L_{m,f}$.

$$A_f = L_{m,f} = \frac{L_m}{1 + \frac{1}{r_\alpha}} \tag{4.11}$$

## 4.5 Results

The control measurements showed that, for the range of velocities tested here, the horizontal forces at the anchors alone (no mat attached) were rather low ($F_x < 0.15$ N for velocities up to 30 cm s$^{-1}$). Results showing the resultant forces thus show the full measured force, i.e. no subtraction of the force measured from the control measurements. To compare measured anchor forces with modeled forces directly, the forces obtained from the control measurements were subtracted from the measured forces to obtain only the effect of the ASG and the coir mat.

### 4.5.1 *Force Components*

The velocity measurements for the AV series showed a minor difference in maximum measured horizontal velocities ($u_{\max}$) between the direction of wave propagation ($+x$) and the opposite direction ($-x$), the former being $10 \pm 3\%$ higher than the latter across all measurements. This indicates a non-linearity within the propagating waves where the maximum horizontal velocity at the crest is higher, but shorter in duration, than that at the trough and translates directly to the forces on the anchors (histograms in Figure 4.6). In Figure 4.6, the following measurements are presented: (A) CM2, $T = 1.5$ s and $H = 0.02$ m; (B) CM2, $T = 5$ s and $H = 0.08$ m; (C) 1 ASG Mat, $T = 2$ s and $H = 0.11$ m; and (D) 2 ASG Mats, $T = 4$ s and $H = 0.06$ m. Panels A and B show the CM configurations for 4 and 9 anchors (top and bottom, respectively). Panels C and D show the

vegetated runs (AV); note that in AV, the water level and particle velocity were not measured aligned with the anchors and are thus not shown. For the polar graphs, the magnitude is given by Equation 4.10 normalized by the maximum measured resultant force of the respective run, and the direction through the inverse tangent (direction of rear anchors $FT_{rc4}$ and $FT_{rc9}$ inverted to be aligned with the front). The force measurements exhibited differences in maximum forces for both directions depending on the anchor position. The $+x$ forces were 2–2.4 times higher than $-x$ forces at frontal anchors for CM, and about 1.67 times for AV. The rear anchor forces of CM tended to the opposite behavior with $-x$ forces slightly higher (1.05–1.15 times) than $+x$, whereas for AV rear anchors, the $+x$ force persisted as the dominant force showing symmetry to the front anchors (1.69 times the $-x$ forces). This ratio, however, lowered to 1.21 for the 2-mat configuration, suggesting an interaction between both ASG mats (see Section 4.5.3). Given the predominantly higher maximum velocities and forces measured in the direction of wave propagation, all further comparisons using $F_x$ and $u_{\mathrm{max}}$ refer to the $+x$ direction unless otherwise indicated.

The direction of the resultant forces calculated utilizing the inverse tangent showed that the forces were not parallel to the wave propagation direction (Figure 4.6). Frontal corner forces ($FT_{fc4}$ and $FT_{fc9}$) were directed towards the center of the mat, whereas the forces at rear corners ($FT_{rc4}$ and $FT_{rc9}$) differed depending on $u_{\mathrm{max}}$, with $F_R$ aligned with $x$ for low velocities (e.g. Figure 4.6C) and directed toward the center of the mat for higher $u_{\mathrm{max}}$. The maximum forces were in phase or only slightly off phase with the wave crest and $u_{\mathrm{max}}$ (time series in Figure 4.6), as reported by Paul et al. (2016). However, the average temporal distribution of the resultant force over one wave period displayed the opposite behavior, with the maximum forces in $+x$ direction generally corresponding to less than $0.25T$ and the forces in $-x$ dominating the rest of the time span of the wave period $T$ (histograms in Figure 4.6). At low $T$ ($<$ 3 s), the maximum lift forces were approximately $O(1)$ smaller than the maximum horizontal forces and were in antiphase with the surface water level $\eta$, meaning that $F_z$ was driven by the water column fluctuation and not buoyancy or lift (Figure 4.6A,C). Contrastingly, at $T > 3$ s (Figure 4.6B,D), the high horizontal forces occurring at the wave crest are brief, sudden, and act analog to the snap loads on mooring lines (e.g. Landmann et al., 2021). More importantly, the lift forces gain importance as they become comparable in magnitude to the horizontal forces; this, however, was only visible for AV, meaning that the lift force was mainly caused by drag on the ASG –recalling that this is a zero-buoyancy case. The irregularities with $u_{\mathrm{max}}$ seen in Figure 4.6B could be seen for several runs of CM and are attributed to the flapping of the highly flexible mats, especially CM2, around the edges.

The horizontally induced wave force increased with increasing $u_{\mathrm{max}}$. Higher wave heights $H$ produced higher shear velocities near the bed, as can be inferred from wave theory, whereas the wave period $T$ did not influence the value of $u_{\mathrm{max}}$ or $F_x$ linearly. Nevertheless, with longer $T$, and due to the small relative water depths ($H/d$), bed interaction caused stronger wave non-linearity, in which case the maximum forces and velocities could still be observed at the wave crests, but the anchor load exposure was predominantly at wave troughs (Figure 4.6).

A direct comparison of force components showed that anchor forces were dominated by shear and not by lift (Figure 4.7). For all tested set-ups, $F_x$ showed the highest values, with $F_y$ generally being slightly lower, yet in the same order of magnitude (Figure 4.8) –with the exception of $FT_{mf9}$,

**4**
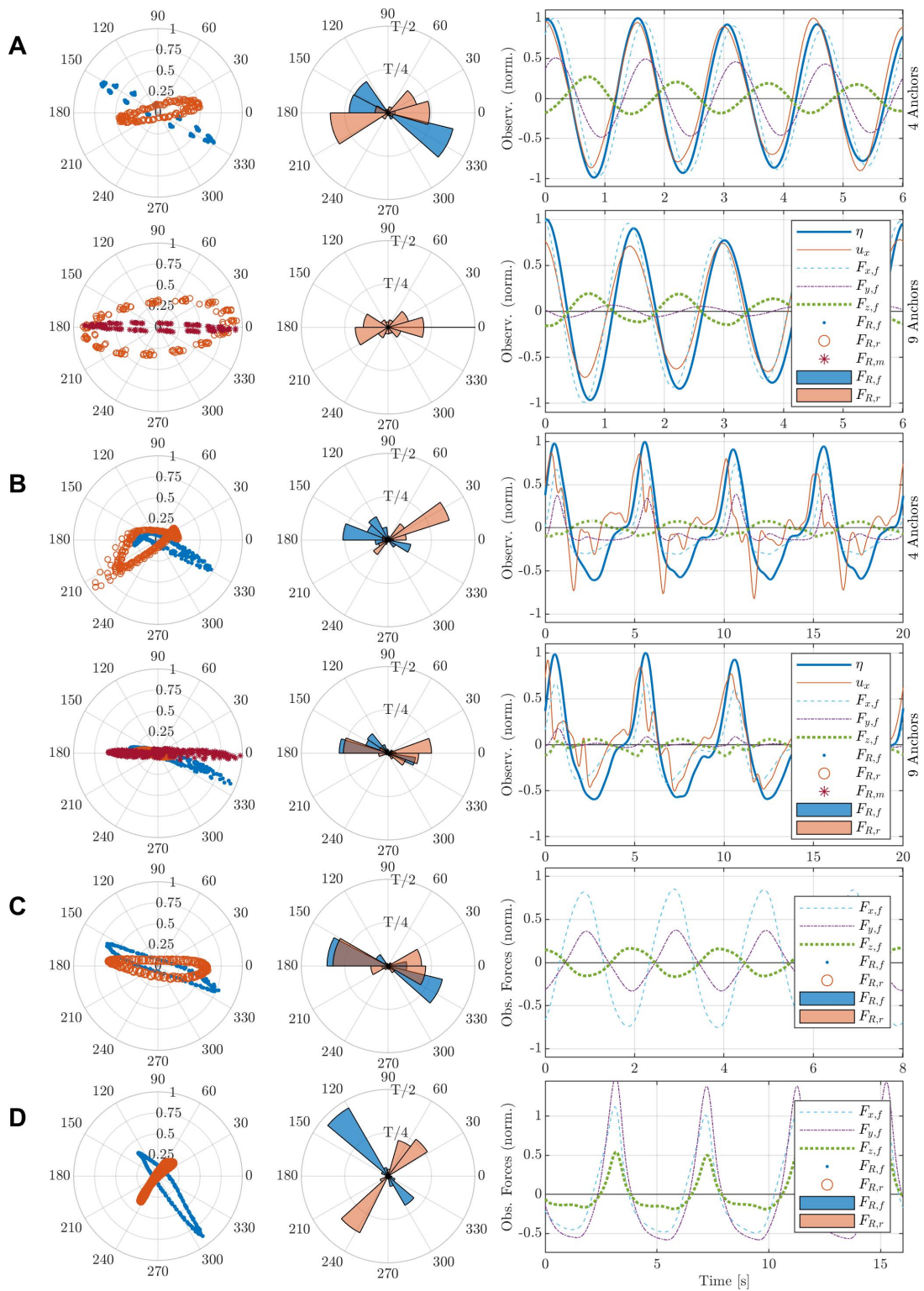


Figure 4.6: Observed and calculated resultant force at front and rear anchors. (Left) resultant force magnitude and direction; (center) histogram of average spatial distribution of forces at one anchor and the corresponding duration over one period. (right) time series of 4 waves for observed velocities, water level fluctuations, and forces. The legend within the time series refers to all subfigures within the respective panel, with subscripts $f$, $r$, and $m$ corresponding to front, rear, and middle-front anchors, respectively.

whose central position means that the $y$-direction forces cancel each other out (Section 4.5.2). This was especially true for the 4-anchor configurations showing that, under wave forcing, the mats pull the anchor towards the center of the mat (evident in Figures 4.5–4.8). At rear anchors, $F_y$ lost prominence, yielding values < 5 N (< 10 N) for all CM (AV) cases compared to forces up to 30 N (60 N) at the front in the $+x$ direction; hence, rear anchor forces in $+x$ were primarily one-dimensional. In the opposite direction ($-x$), the forces only increased marginally with $F_{y,r}$ < 7.5 N for both CM and AV. Similarly, $F_x$ showed values < 10 N for the $-x$ direction at the rear and < 15 N at the front for both CM and AV, demonstrating that the forces in the direction of wave propagation correspond to the dominant loads on the anchors.

### 4.5.2 *Forces on Coir Mats (CM)*

For all CM cases, the forces at the rear anchor were < 10 N and less than one-third of the corresponding forces at the front (< 30 N) for velocities over 0.1 m s$^{-1}$ (Figure 4.7). For the 9-anchor configuration, the middle-front anchor (FT$_{mf9}$) measured $F_x$ $O(1)$ higher than $F_y$, which was expected due to drag contribution from both sides of the anchor. However, the force measured did not amount to double that of the corner anchor (FT$_{fc9}$), as was originally expected (the corner anchor would be expected to take half of the load of that in the middle), with the quadratic fit coefficients showing that $F_{x,mf9} = 1.2F_{x,fc9}$ for both Eromats (CM2 and CM3). This shows that the outermost anchors incur in loads that do not correspond to a symmetric areal distribution with the neighboring anchor. Lift forces at all anchors were notably smaller than the shear forces with $F_z^{max} < 0.4F_x^{max}$ for all cases. CM1 and CM3 showed the highest $F_z$ contribution; however, it is worth noting that the former also displayed low horizontal forces (< 12 N) compared to the other 2 mats (Figure 4.9). The increased $F_z$ for CM3 is likely caused by the positive buoyancy of the HDPE mesh surrounding the coir.

For the 195 CM runs (all excluding control measurements), the resultant forces (Equation 4.10) did not exceed 30 N and were dominant at the frontal anchors (Figure 4.9). The 4-anchor configuration displayed the highest forces, up to 30 N, which were measured for both Eromats (CM2 and CM3). The woven net (CM1) measured forces lower than the other two mats by a factor of 3.3 (2.5) for the frontal (rear) anchors. Compared to the 9-anchor configuration, the frontal anchors measured an estimated 2 (4) times higher forces for CM2 (CM3); the rear anchor forces were in turn twice as high for both mats. For the netting, the measured forces did not vary in dependence on the number of anchors ($F_{R,f}$ < 15 N and $F_{R,r}$ < 5 N for all runs). CM2 –by construction the most flexible and unstable mat –displayed the highest forces at just over 30 N for the front corner with 4 anchors and above 20 N for the middle front with 9 anchors (Figure 4.9).

### 4.5.3 *Forces on Artificial Seagrass Mats (AV)*

#### MEASURED FORCES

The measured AV forces were above 2 times higher than the CM at high horizontal orbital velocities ($u \approx 0.4$ m s$^{-1}$) and up to 10 times higher at low velocities ($u \approx 0.1$ m s$^{-1}$), reaching values above 60 N (Figure 4.10). This demonstrates that the presence of the ASG had a marked impact on measured drag. Four to five force measurements (depending on $d$) were done per velocity measurement at
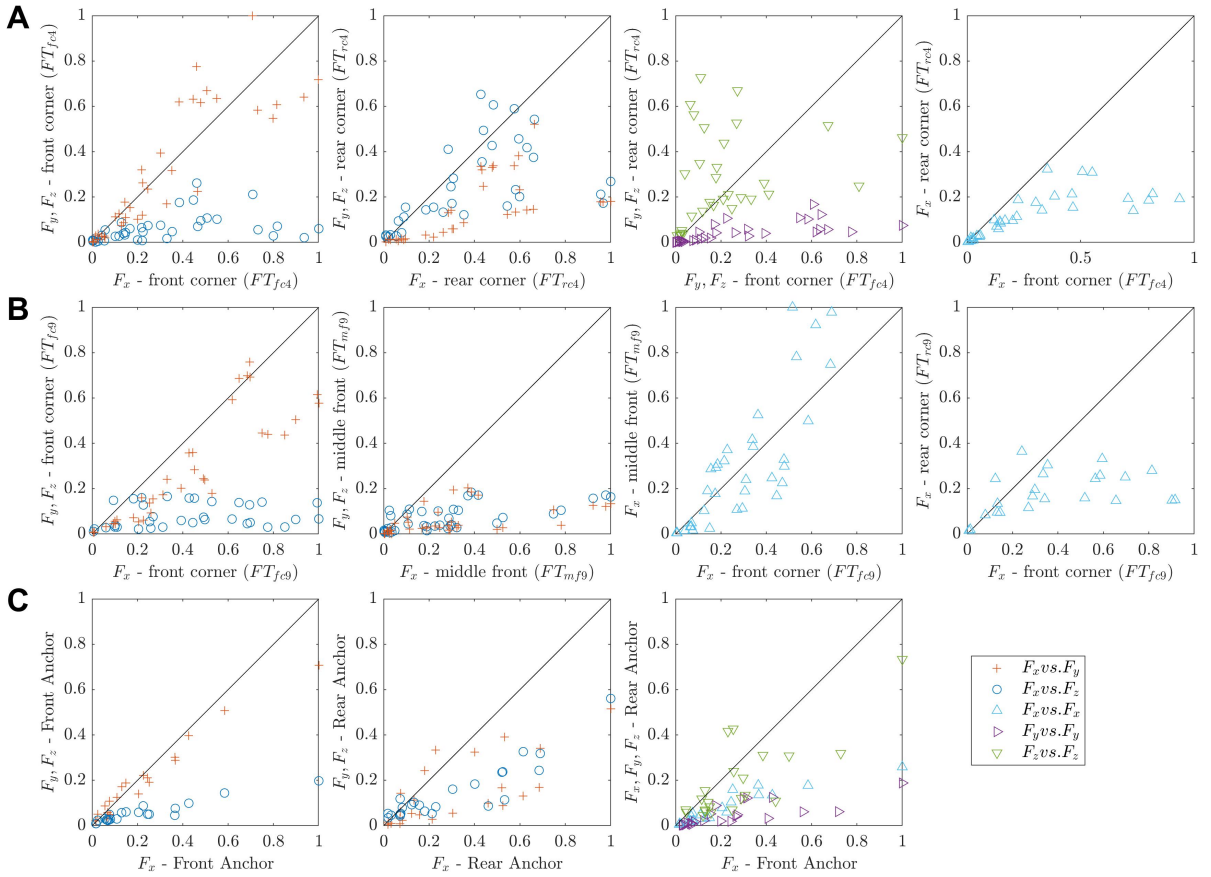
Figure 4.7: Force component (*x*, *y*, *z*) comparison for all runs depending on anchoring position (shown in the axis label). All forces are normalized by the maximum measured force. (A) 4-anchor configuration for non-vegetated mats (CM), showing the front (FT$_{fc4}$) and rear anchor (FT$_{rc4}$) forces. (B) 9-anchor configuration (CM), comparing components in the front corner (FT$_{fc9}$), middle-front (FT$_{mf9}$), and rear corner (FT$_{rc9}$) anchors. (C) front and rear anchor force comparison for the vegetated mat experiments (AV).

$z = 3$ cm resulting in the standard deviation denoted by the error bars in the figure. The rear anchor forces were lower than the frontal forces by a factor of about 2. A quadratic fit ($F_R = \alpha u_{\max}^2$) is shown for frontal and rear anchors yielding the R$^2$ and $\alpha$ coefficients shown in Figure 4.10.

The rear anchors did not display any change in dependence on the number of mats; in contrast, the front anchors experienced increased resultant forces to a factor of 1.4 based on quadratic fits (Figure 4.10) with the presence of a second mat. The forces for the 2-mat measurements ranged from 1.16 to 3.6 times the corresponding forces for the 1-mat measurement. Considering all measurements, the mean ratio of maximum resultant force measured for the 2-mat to 1-mat configuration was 1.77. Interestingly, despite this prevalent increase in horizontal forces in the presence of a second mat, the average ratio of maximum measured velocity over the bed $u(z = 0.03$ m) between both set-ups was $1.02 \pm 0.12$.

### MODELED FORCES

The bed shear stress $\tau_{b,w}$ depends on the wave friction factor $C_f$ and the horizontal orbital velocity $u$, where $C_f$ depends on $T$ and $a_B$. To be able to relate the $\tau_{b,w}$-induced forces with the flexible stem drag forces (Equation 4.7), we utilized the entirety of the measurements (CM and AV) to calculate the corresponding friction factors depending on the measured incident wave conditions. The
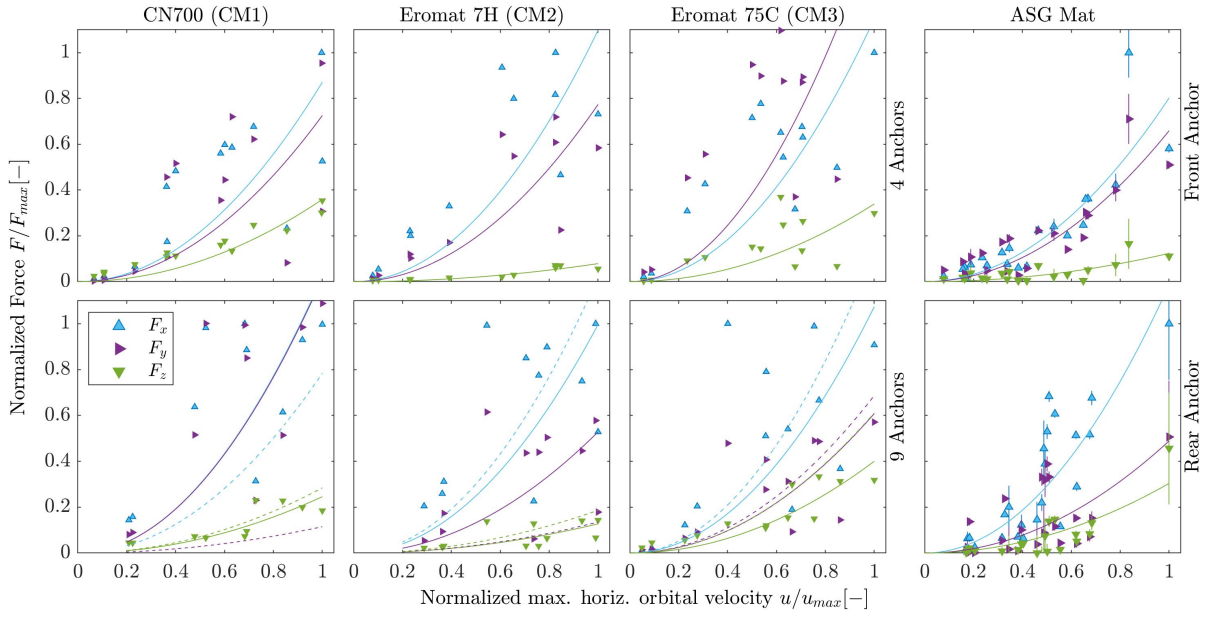
Figure 4.8: Force-velocity plots of maximum measured horizontal orbital velocities against the respective maximum measured shear and lift forces for all runs. All plots are normalized by the maximum value for the respective set-up. The 2 rightmost panels show the front and rear anchor of the ASG mat (AV). These comprised measurements with repetitions, thus resulting in the shown error bars, while the rest (CM) have no calculated uncertainty. The CM are exclusively for front anchors. Solid lines represent quadratic fits for comparison. Dashed lines in lower plots correspond to middle-front anchor (FT$_{mf9}$, markers omitted for clarity).
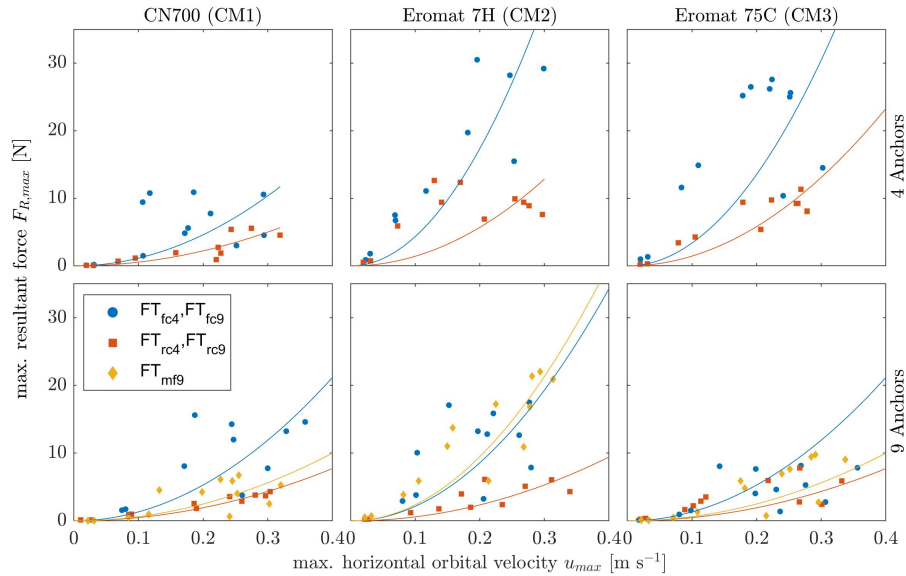


Figure 4.9: Resultant forces at all anchor positions for the experiments on coir mats (CM). Columns: mat type; rows: number of anchors. The subscripts in the legend indicate the anchor position of the measurement, with f = front, c = corner, m = middle, and 4 and 9 representing the number of anchors. A quadratic fit of form $F_R = \alpha u_{\max}^2$ is shown for reference, color-coded for the respective marker.

measured wave periods and maximum incident velocity for each run were then used to calculate $C_f$ (Figure 4.11A). An exponential fit of $C_f$ against $u_{\max}$ provided an equation for $C_f(u)$ (Equation 4.12), which was then used in Equation 4.9. $KC$ and $C_{D,w}$ for the wave extension model showed a linear dependency on the incident wave period (Figure 4.11B). $KC$ increased linearly with $u_{\max}$ at a
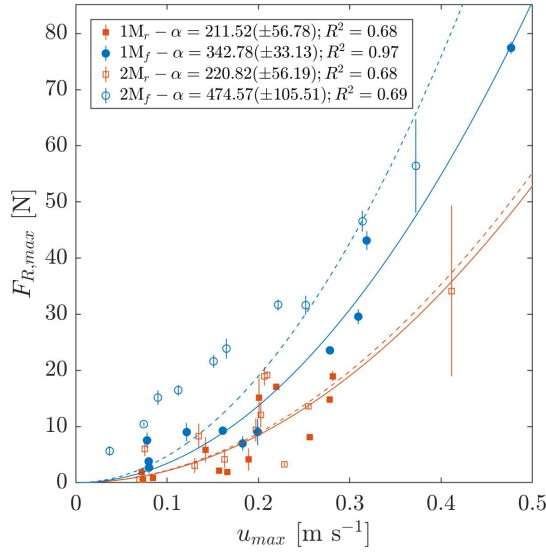
Figure 4.10: Mean maximum resultant forces $F_R$ measured at front and rear anchors (subscripts $f$ and $r$, respectively) of a 4-point anchored artificial seagrass mat. Filled markers correspond to the one-mat configuration (1M), void markers to the two-mat configuration (2M); error bars depict standard deviation (sample size $n = [4, 5]$). A quadratic fit of form $F_R = \alpha u_{\max}^2$ is shown for reference for each set of measurements with dashed lines representing 2M and solid lines 1M, respectively, color-coded according to the position $f$ and $r$. The values for $\alpha$ and coefficient of determination ($R^2$) are given beside the respective position in the legend. An additional fit for all front and all rear measurements (not plotted) yielded $\alpha = 384.12(\pm49.8)$; $R^2 = 0.82$ and $\alpha = 217.56(\pm36.71)$; $R^2 = 0.69$ for $f$ and $r$, respectively.

rate proportional to $T$, while $C_D$ reduced to 1.95 at a rate 3.2 times higher for $T = 5$ s compared to $T = 2$ s, and 2 times higher than $T = 3$ s (Figure 4.11B).

$$C_f(u) = (0.369 \pm 0.029)e^{(-72.6\pm7)u} + (0.063 \pm 0.009)e^{(-3.3\pm0.8)u} \tag{4.12}$$

The ratio of fitted coefficients for the measured frontal and rear horizontal forces ($F_x$) was $r_\alpha = 3.08 \pm 0.81$ (uncertainty propagated from the fit coefficients $\alpha_f$ and $\alpha_r$). Following Equation 4.11, $A_f = 1.51$ m$^2$ and $A_r = 0.49$ m$^2$. Equation 4.12 was then used to calculate $C_f$ after which Equation 4.9 returned the modeled forces for the rear and frontal anchors (Figure 4.12). The unidirectional flow ($c11$) and wave extension models ($w16$ and $w19$) captured the measured forces well with the modeled forces yielding an R$^2$ of 0.86 and 0.78 for the front and rear anchor forces, respectively for $c11$, and 0.91 and $> 0.73$ for both wave-based extensions. The models predicted forces at low velocities well, with $c11$ overestimating forces at velocities between 0.15 and 0.4 m s$^{-1}$ and $w19$ overestimating them at $u_{\max} > 0.4$ m s$^{-1}$. At the highest measured velocity, $c11$ and $w16$ predicted a similar force (3% deviation from each other at both anchor positions), which also agrees well with the corresponding measured force ($< 10\%$ deviation). $w19$, on the other hand, overpredicts the highest measured forces by a factor above 1.4. The forces modeled were dominated by the stem-based vegetation drag (Equation 4.7), with $F_v$ corresponding, on average, to $95 \pm 1.7\%$ of $F_{x,\text{mod},C}$ and $F_{v,w}$ to $93 \pm 1\%$ of $F_{x,\text{mod},w}$. The contribution of the bed shear stress in our calculated model was therefore marginal.

**A**

**B**
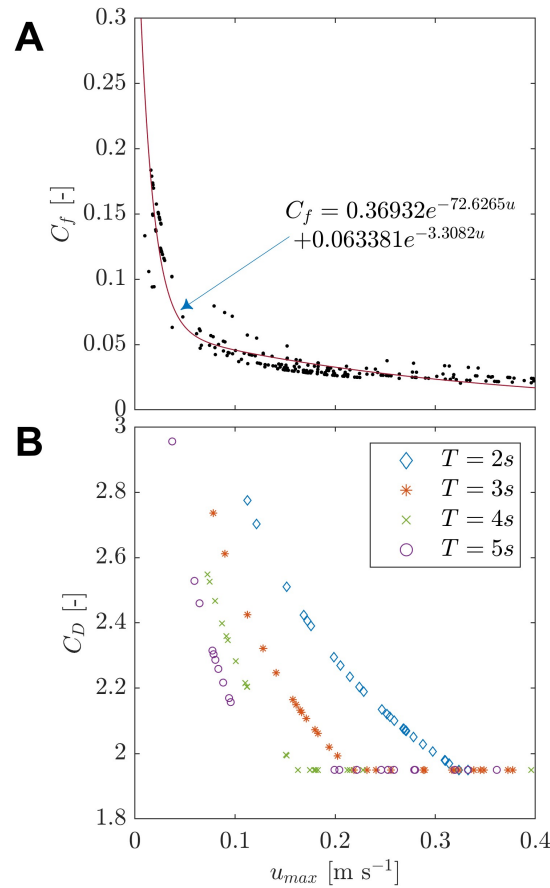
Figure 4.11: (A) Exponential fit ($R^2 = 0.92$, RMSE = 0.0147) for the calculation of the friction factor $C_f$ for all sets of waves trialed (with and without artificial seagrass). Uncertainty given in Equation 4.12. (B) $C_D$ calculated from $KC$ with $C_D = \max(10KC^{1/3}, 1.95)$ (Luhar and Nepf, 2016) as a function of the incident wave period $T$.

## 4.6 Discussion

### 4.6.1 *Wave-Induced Forces on Coir Mats*

Geotextile mats subject to marine hydrodynamics will experience cyclic forces that analogously transfer into the anchoring points. Our experiments demonstrate that the magnitude of these forces depends on the geometric and mechanical properties of the mats, the number of anchoring points, and the hydrodynamic conditions. More interestingly, our results show that the wave-induced force distribution is also affected by the anchor position relative to the direction of wave propagation, discernibly reflected in the difference in magnitude of the maximum forces measured between front and rear anchors.

Analogous to real vegetation, ASG increased drag forces under wave loading. The forces on anchors of ASG mats were considerably higher than for the bare mats. We can argue that the force surplus arises entirely from the surrogates; however, from CM, the forces coming from mats alone accounted for up to more than half of the measured forces with ASG, while the modeled vegetation drag could explain more than 90% of the measured force. Furthermore, the presence of a second ASG mat also affected the forces measured. One would expect the presence of a second mat to attenuate orbital velocities further, causing forces to sink. Surprisingly, our experiments showed the opposite behavior, with the measured forces increasing, on average, by a factor of 1.4
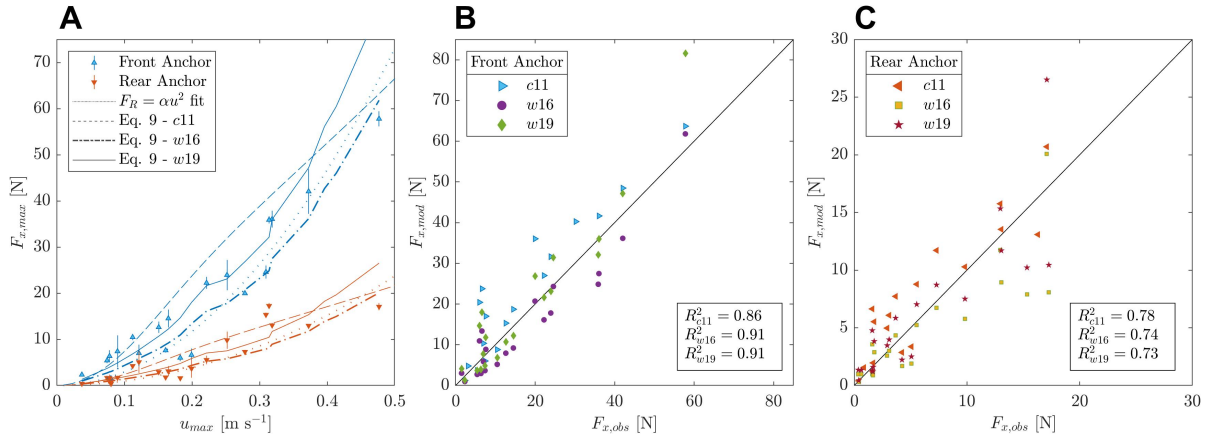
Figure 4.12: Measured (obs; using both 1 and 2-mat measurements) and modeled (mod) horizontal forces utilizing Equation 4.9 for the unidirectional flow forces model ($c11$) and wave-induced forces models ($c16$ and $c19$). (A) the maximum measured horizontal force and modeled forces as a function of the maximum horizontal orbital velocity $u_{\max}$. (B,C) show the plots of modeled versus observed forces depending on the anchor position. Note the different axis scales. Uncertainties of modeled forces and observations in panels (B,C) omitted for clarity.

while the measured orbital velocities did not vary significantly. A possible reason for this could be recirculating currents within the meadows. It has been shown that flexible meadows create a recirculating current with an in-meadow mean flow in the direction of wave propagation (Luhar et al., 2010; Pujol et al., 2013). Rigid meadows can enhance the recirculating current forming a strong in-meadow $+x$ current and above-meadow $-x$ current (Pujol et al., 2013). van Veelen et al. (2020) corroborated this for rigid vegetation, stating that these are up to 70% more effective at wave attenuation compared to flexible vegetation, with the flexible meadows showing little effect on recirculation. Our chosen vegetation, albeit falling under the category of flexible, has a higher rigidity than the fully flexible blades used in the cited studies, as can be inferred from the range of resulting $Ca$ (0.16–25). This may induce the generation of a current within the meadow. An interaction between both meadows would then enhance this current, which is plausible for waves with wavelength greater than the gap between the meadows. Furthermore, van Rooijen et al. (2020) showed a positive ($+x$) mean wave velocity at the leading edge of the meadow, with a low mean and predominantly negative ($-x$) velocity in front and behind the meadow. This mean negative velocity may be influenced by the presence of the second meadow and the generated mean current within both meadows, which may drive the higher forces experienced with 2 mats. Contrastingly, El Allaoui et al. (2016) showed that, for a meadow gap longer than twice the vegetation height (as is the case here), the wave velocities between the meadows rapidly return to the no-vegetation values. Although analogous to our velocity measurements, this does not explain the increase in measured force. Measurement of forces with a different number of mats and at all mats (instead of only the foremost) would be needed to further clarify this interaction and the governing mechanisms.

#### EFFECT OF MAT PROPERTIES

A mat comprising positively buoyant materials will sustain increased lift forces $F_z$ due to the acting buoyant force, as was observed with the HDPE-wrapped mat (CM3). Otherwise, the lift forces were observed to be less relevant compared to the shear forces. Furthermore, swaying (the back-and-forth movement of the mats under wave loading) was observed to increase both lift and

shear forces on the anchors, suggesting inertia (not taken into account here) may play a role for highly flexible mats. Mats of loose material (i.e. unwoven; here CM2 and CM3) showed a more prominent swaying motion than both CM1 and the AV mats which could be in part due to lower flow permissibility; i.e. the increased contact area on the closely packed fibers of CM2 and CM3 increase drag and friction, causing the mat to sway more. On the other hand, the AV mat, with a negatively buoyant ASG attached to it, was considerably heavier, which may reduce sway. Moreover, the increased forces may be accentuated by an underlying current created by a viscous sublayer between the mat and the bed generated during oscillatory motion, whereby a part of the water mass is redirected under the mat. Flow then separates into two domains, creating two opposite boundary layers and doubling the skin friction area (thus removing the 1/2 term in Equation 4.3).

The netting (CM1) –a woven coir fiber mat (Figure 4.3A) –logged the lowest forces which is likely due to its grid-like form; being a net, it does not cover the seabed homogeneously which translates into high flow permissibility, low drag and thus reduced sway. In our experiments, sway of CM1 was observed to be minimal. In addition, suspended sediment may deposit within the net thread spacing as these spaces correspond to no-flow zones, making the mat more prone to become buried due to water movement which may in turn increase stability. A buried mat –even if only partially –reduces the loading on the anchors significantly as the tensile strength of the soil and mat increases (Subaida et al., 2008). Burial was marginally observed during our experiments, but a prolonged field deployment could prove that such a structure would have a high burial rate.

CM2 and CM3 contained an extra reinforcement made of PP and HDPE, respectively. The reinforcement envelops the coir fiber to increase resistance as these were originally designed for erosion control and slope stabilization. Our results should thence provide a starting point for the design of natural mats reinforced with biodegradable materials ultimately having similar bulk mechanical properties as those shown in Table 4.2. Such materials could be polybutylene succinate (PBS) and polybutylene adipate-co-terephthalate (PBAT), which have been proven to have similar properties to PP and HDPE (Xu and Guo, 2010), or a combination of both (PBSAT), shown to be significantly similar to polyamide (Seonghun et al., 2020). These materials have been tested in the field to replace conventional fishing nets with biodegradable nets whose tensile strength is adequate for fishing while being a potential solution to ghost fishing (Grimaldo et al., 2018).

#### EFFECT OF THE NUMBER OF ANCHORS

The number of anchors played an important role by controlling both the freedom of movement of the mat and the corresponding area affecting each anchor. Here, going from a 4 to a 9-anchor configuration, the frontal and rear anchor forces were reduced by more than half for the unwoven fiber meshes, whilst the netting showed similar forces regardless of the number of anchors. This suggests that even with four anchors the drag force was not entirely transmitted to the nearest anchor but rather dissipated through thread elongation and friction between the bed and the mat.

The resultant forces were also observed to change in magnitude and direction depending on the number of anchors. A 4-anchor set-up resulted in a force normal to the wave propagation direction ($F_y$) comparable in magnitude to longitudinal forces ($F_x$). As Figures 4.5 and 4.6 show, the maximum forces are directed toward the center of the mat, with many cases reaching $F_y = F_x$. For a 9-anchor configuration, the orthogonal forces ($F_y$) on central anchors are present on both sides of the anchor

which means they cancel each other out. This would also be the case for any number of anchors set between the lateral edges of a mat of any width perpendicular to wave propagation, as long as the anchor separation is congruent. More anchors may reduce the forces each endures significantly, but can also increase the costs of installation, so this would depend on the needed resistance of the anchors based on field conditions.

**IMPORTANCE OF ANCHOR POSITION RELATIVE TO WAVE PROPAGATION DIRECTION**

For all cases (with and without ASG), front anchors showed higher forces than rear ones, thus showing that a major proportion of areal drag on a flexible mat falls upon the foremost anchors, simultaneously releasing stress on posterior ones (relative to the instantaneous orbital flow direction). Furthermore, maximum forces were predominantly higher in the wave propagation direction ($+x$) compared to its backward component ($-x$). These asymmetries may be attributed to bed interactions in shallow areas, which causes wave non-linearity (Figure 4.6). Higher but temporally shorter forces result from the analogous wave crests, whereas longer but weaker forces emanate at the trough. The more spontaneous $+x$ loads may be decisive regarding the design force of the anchors and the tensile strength of the mat. However, considering the longer-lasting $-x$ force, tensile fatigue on the mats could potentially become a major concern for the threads and fibers (Xu et al., 2014) while underwashing of the mats (and thus exposure of the anchors) could destabilize the mats and reduce anchoring strength (Bakker et al., 1973). Moreover, Stokes drift, i.e. mass transport in the direction of wave propagation, has been shown to be present within near-bed structures, which may also help explain the dominant $+x$ forces. Stokes drift has been shown to increase in the presence of submerged vegetation (Jacobsen, 2016) and other porous structures such as coral reefs (Webber and Huppert, 2021), which in turn is an essential mechanism for the healthy development of these ecosystems.

### 4.6.2 *Modeled Forces on Artificial Seagrass*

Many vegetation drag models deal with single-stem drag; similarly, we used the stem drag and shoot density to calculate the total drag created by an artificial meadow per unit bed area. Note that this simplification does not take into account the interaction between elements, which can have an effect on drag. Lima et al. (2007) calculated the total drag of a meadow based on single stems, the number of elements, and an adjustment coefficient to take these interactions into account. They stated that stem interaction leads to forces up to 4 times greater than single-stem calculations. Our experiments, however, did not corroborate this statement as the forces per unit area calculated based on single-stem drag closely matched the forces measured at the anchors without the need of an adjustment coefficient. However, it is worth noting that the forces calculated here use a $C_D \geq 1.95$ for all cases. Nepf (1999) found that $C_D$ decreased with increasing stem density as a result of stem-to-stem interaction, which may explain why, in these types of models, there is no need for an adjustment coefficient to include stem-to-stem interaction as suggested by Lima et al. (2007).

Notwithstanding, the model used here (Equation 4.9) proved to be capable of predicting the anchor forces reasonably well, regardless of the approach used. The stem drag model developed for unidirectional flow ($c11$) accounted for 95% of the forces modeled, while the wave-based model ($w16$) accounted for 93%. This renders the contribution of bed shear stress in our proposed

model almost negligible. The experimental results for CM showed that form drag also played a role in anchor forces, as the measured forces were higher than the calculated areal skin friction. Nonetheless, Carus et al. (2020) found that wave-induced bed shear stress was reduced due to the presence of ASG, which implies a low contribution of the friction drag compared to the form drag generated by the ASG. Furthermore, the swaying motion may call for the calculation of a relative velocity to calculate the $C_f$ ($u'' = u - u_{\mathrm{mat}}$, where $u''$ is the relative velocity and $u_{\mathrm{mat}}$ is the mat swaying velocity), whereby $C_f$, hence $\tau_{b,w}$, would be reduced even further. Mat motion was not measured here, so this relative velocity was not taken into account. The reduction of $\tau_{b,w}$ may explain why the modeled vegetation drag corresponded to such a high portion of the force measured at the anchor, undermining the contribution of the mats. Whilst the maximum calculated $\tau_{b,w}$ was 2 $\mathrm{N\,m^{-2}}$ for velocities of about $0.4\,\mathrm{m\,s^{-1}}$, the anchors of CM2 and CM3 registered forces up to $20\,\mathrm{N\,m^{-2}}$ within the same velocity range (assuming the same front-rear distribution of area $A_{ap}$ as calculated for AV). This denotes a higher contribution of form drag and dynamic loading (e.g. edge-flapping of the highly flexible mats) for the CM mats than just friction drag. Moreover, the characteristic area $A_{ap}$ used here, albeit a simplification, does not make the model less robust, as Equation 4.9 may also be implemented without $A_{ap}$ to obtain the force per unit area [$\mathrm{N\,m^{-2}}$] of meadow, which, for $2\,\mathrm{m^{-2}}$ (i.e. the sum of the front and rear anchor forces on one side of the mat), was accurately predicted here.

### 4.6.3 *Design Considerations and Implications for Restoration*

Previous approaches have shown that, for artificial seagrass mats used for erosion control, anchors buried 1 m deep utilizing hydraulic hammers are more than enough for any expected extreme load (Jones et al., 2006). However, these anchors may be expensive and cumbersome to install. Our experiments show that, for the range of near-bed velocities, the expected forces are not necessarily in the order of kN, so shallow anchoring or other techniques (e.g. sand tubes) may suffice as long as site selection follow guidelines for restoration (i.e. areas of low hydrodynamic forcing van Katwijk et al., 2016). Moreover, although increasing the number of anchors may reduce loads, it can increase costs. A four-anchor configuration may be enough for relatively small mats (e.g. 2x2 m, as done here) as long as the mat provides high flow permissibility and low buoyancy, and is thus not subject to increased swaying motion. Equation 4.9 can then provide an estimation of the expected maximum loads depending on the hydrodynamic conditions and ASG properties. As the direction of wave propagation can change periodically depending on the site, these maximum forces should be considered for all anchors. Additionally, a safety factor to account for extreme events can be implemented for field trials. A suitable safety factor will depend greatly on the anchor set-up and mat materials, as these, similar to mooring line design, will determine the rate of fatigue and ultimately failure of the system (Huang and Pan, 2010). Note, however, that in contrast to our findings, mooring line anchors suffer proportionally higher $F_z$ loads compared to shear, and are also subject to snap loads (i.e. abrupt, lagged loads arising from the near-surface oscillatory motion Landmann et al., 2021) which can be orders of magnitude higher than what we can expect for the mats.

Regarding field applications and restoration, our tests suggest that a woven fabric mat will

*4*

perform better due to higher flow permissibility and reduced anchor loading, with accelerated burial and facilitation of growth within the mat as positive feedbacks. A stable mat such as CM3 with an increased number of anchors (9-anchor configuration) also incurred lower forces at the anchors. Nevertheless, the geometrical properties of ASG need to be carefully chosen as these readily affect the intrinsic surrounding hydro and morphodynamics. Shoot density and canopy height proportionally affect sediment deposition and resuspension (Chen et al., 2007) which in turn affects seagrass growth and the subsequent survival stability (Adams et al., 2016). The stability of the materials likewise plays an important role, especially if biodegradable alternatives are set to be used. (Irving et al., 2014) reported that biodegradable jute bags with coarse weaving can facilitate seagrass growth, specifically *Amphibolis antarctica* in southern Australia, through increased sediment and seed fixation. In addition, (Wear et al., 2010) reported a drastic decrease in newly recruited seagrass 3 years after deployment due to degradation of the bags and wave loading, thus accentuating the need for biodegradability and temporal stability studies of ASG and mat candidates used for restoration. Moreover, field experiments are also needed as other environmental factors can affect anchor loading and mat performance. For example, the formation of biofilm and settlement of epiphytes on the ASG may have a marked effect, whereby some studies state that epiphytes reduce the drag coefficient (Hansen et al., 2014), while others found that epiphytes could increase drag up to 50% in macroalgae (Anderson and Martone, 2014). Ultimately, this study provides the basis to determine the expected anchor forces based on validated models of drag on marine vegetation. Moreover, the proposed formula can be applied with basic knowledge of field conditions and proposed materials for the ASG mats. Ultimately, restoration success will be achieved through field experiments. Valuable information to gather in future experiments includes the evaluation of the degradation times, burial rates and its effect on loads, changes in mechanical and chemical properties of the biodegradable materials, quantifying anchor fatigue, and assessing the lifetime of the ASG mats within the context of restoration.

## 4.7 Conclusions

This study was set up to understand the loading on the anchoring points of geotextile mats deployed under marine conditions. We measured forces on the anchors of coir-based geotextiles in a wave flume, testing coir mats of different construction and varying the number of anchors used to fix the mats to a mobile sand bed. We subsequently measured the forces on a mat covered in artificial seagrass (ASG) whose application in the field can be to provide shelter for growing seedlings during restoration projects. This should inform future pilot projects on the design considerations of biodegradable ASG mats to be deployed on the field.

Our results showed that the loading on each anchor will depend on (i) the hydrodynamic conditions, e.g. water depth, wave height, and wave period; (ii) the number of anchors set and the distance between them as well as their position relative to the wave propagation direction; and (iii) the mechanical composition and properties the mats. The hydrodynamic conditions are going to depend highly on the selected site for restoration. Sites with lower wave periods and higher wave heights may produce higher maximum loads, while longer wave periods will produce longer-lasting loads which may be detrimental to the mats and anchors. Further, the use of more anchors can

reduce the forces each anchor sustains; however, it is more important to choose a material that allows for through-flow, e.g. a net of woven coir fabric or any other grid-like structure. This would in turn reduce the number of anchors needed as the reduced oscillatory motion translates to reduced forcing. The forces on the anchors are dominated by the drag on the flexible ASG, which we tested empirically and compared to existing models for drag on single stems. The models, with the addition of a small contribution from bed friction, were able to provide reasonable estimates of the forces that are to be expected at the anchors based on the corresponding area for each anchor. Anchors facing incoming waves were found to take twice the load of the anchor further into the mat in the direction of wave propagation, after which the proportional corresponding area can be calculated. This proportion was found for a 2-m mat and needs to be investigated further in order to find a dimensionless value applicable to any mat length. Ultimately, knowing the target field conditions and the mechanical properties of the chosen ASG should then be enough to gain insights into the forces incurred by the anchors during deployment.

*4*

*4*

### Chapter highlights

- Loads on anchors deployed under marine conditions depend on mat and plant mechanical properties, incident hydrodynamics, and the number of anchors used.
- Loads are greater on anchors facing incoming waves and in the direction of wave propagation.
- Interaction between mats, e.g. fragmented canopies, may increase loads on the anchors of preceding mats.
- Bed shear stress and its corresponding drag are negligible in terms of anchor loading compared to vegetation drag.
- Forces on the anchors are 3-dimensional, with orthogonal forces (relative to wave propagation direction) capable of equaling longitudinal forces.
- Increased mat motion (e.g. sway) increases loads on anchors. Permeable mats (nets/grids) thus reduce loads as they reduce sway.

# CHAPTER 5

# WAVE DYNAMICS AROUND FLEXIBLE ANCHORED MATS OF ARTIFICIAL SEAGRASS

## 5.1 Introduction

Seagrass meadows have experienced great losses in recent decades, mostly due to human development (Duarte, 2002; Waycott et al., 2009). They represent important coastal ecosystems that provide services to the environment and to human populations (Seddon et al., 2020), including fish habitat, livelihood for coastal communities, and carbon sequestration (Duarte et al., 2013). Seagrasses alter their environment drastically by reducing wave energy and current velocity (Gambi et al., 1990), lowering turbidity by increasing sedimentation (van der Heide et al., 2011; Adams et al., 2016), and stabilizing the coastline by reducing erosion (James et al., 2019; Barcelona et al., 2021). This makes these ecosystems important actors in coastal protection schemes and priority targets in conservation and restoration within the contemporary key concept of nature-based solutions (Brodie et al., 2020; Rifai et al., 2022).

Several methods of seagrass restoration exist (see e.g. van Katwijk et al., 2016), with no go-to method unanimously considered the most efficient. Single-shoot transplantation techniques, for example, have been shown to be successful (e.g. Zhou et al., 2014), however, they can also be expensive and time-intensive. A widely accepted notion is that seagrasses provide themselves with the means of survival through positive feedback mechanisms (van der Heide et al., 2007). From an ecosystem engineering perspective, this means that seagrasses modify their local environmental dynamics, e.g. flow-induced energy flux and mass transport, in such a way that ensures survival and promotes further proliferation. Preliminarily, this can be externally achieved through shelter provided by other structures (Statton et al., 2017). Building on this, Carus et al. (2021) propose the use of biodegradable mats of artificial seagrass (ASG) to serve as shelter for real seagrass and thus promote growth. ASG would then provide the protection that spawning seedlings need by emulating seagrass coastal protection services.

The proposed mats must be anchored to the seabed as they undergo hydrodynamic loading. Considering the inherent costs of field applications, these anchors should be discrete (i.e. a fixed number of punctual anchors), while able to resist the highest expected hydrodynamic loads. Moreover, to adapt to the highly dynamic environment, both mats and ASG should be flexible; this flexibility, however, also means that their interaction with the surrounding environment is complex. The usage of flexible mats in the context of restoration makes sense in many ways, as these mats can be manufactured extrinsically and easily transported and deployed in the field. However, most understanding of flow-vegetation interaction focuses on shoots fixed to rigid, non-mobile base layers. As flow-vegetation interaction studies began to develop, the importance of flexibility of the plant was rapidly recognized. Asano et al. (1992) introduced the concept of relative velocity to account for the effect of plants swaying along with water particle motion. This swaying motion reduces drag, thus reducing flow attenuation. Other related concepts were then investigated, like the *monami* phenomenon (see e.g. Ghisalberti and Nepf, 2002) which also alters the velocity structure within and in the wake of a seagrass meadow. Similarly, a flexible mat means that the whole meadow can move along with particle motion, limited only by the amount of anchoring points used.

To date, other than scour protection studies with commercial motivation (see references in Chapter 4), there is no research regarding flexible, discretely anchored mats under marine

conditions. Moreover, current predictive models of flow-vegetation interaction have been validated for either idealized laboratory conditions (Lowe et al., 2005a; Luhar and Nepf, 2016) (i.e. fixed vegetation and uniformly anchored rigid base layers), or natural vegetation in the field (Bradley and Houser, 2009). The experiments described in this study revolved around the applicability of state-of-the-art flow-vegetation models to predict wave dynamics around flexible mats under oscillatory flow conditions. The loads undertaken by the anchoring points were investigated by Villanueva et al. (2022). Interestingly, the study found that about 95% of wave-induced drag on the flexible ASG mats could be explained by existing drag formulations based on meadow morphology and incident hydrodynamics. A similar effect may then be expected for both the velocity structure along the water column and the wave height evolution along the meadow. Specifically, we a) analyze the effect of flexible ASG, discretely anchored to a sand bed via a flexible base layer, on wave-induced flow velocities and wave propagation; b) compare this with the status quo of wave-vegetation interaction research; and c) discuss the suitability of currently accepted models applied to fully flexible anchored mats intended for field applications.

## 5.2 Theoretical Background

The interaction between submerged vegetation and hydrodynamics has been widely studied, with a great deal of focus given to unidirectional flow (Nepf and Vivoni, 2000; Neumeier and Ciavola, 2004; Folkard, 2005; Vettori and Nikora, 2020). Interest in submerged macrophytes and their effect on oscillatory flow, i.e. waves, gained momentum with the concept of energy dissipation (Dalrymple et al., 1984). It was noted that wave decay took place in areas where either changes in morphology were visible, or where submerged vegetation were present. It became clear that the latter have a complex interaction with hydrodynamics, partly observable through wave decay, but also penetrating the water column and affecting the velocity structure of the oscillatory (orbital) flow. Nevertheless, despite increased research surrounding this interaction, predictive methods to describe wave decay and oscillatory flow attenuation tend to be set-up-specific, hence delivering differing and even conflicting results. Table 5.A.1 (supplementary material at the end of this chapter) presents a summary of relevant studies applying different methodologies to investigate wave-vegetation interaction. With different target parameters, the obtained results and conclusions can vary greatly, even if the input conditions or the experimental set-up are similar.

### 5.2.1 *Wave Decay*

Wave decay has been calculated in many forms, whereby wave energy dissipation has predominantly been the starting point for any formulation. The energy dissipation formulation is based on the steady conservation of energy flux $\partial E_w c_g / \partial x = -\varepsilon_D$ (Mendez and Losada, 2004), where $E_w = (1/8)\rho g H^2$ is the energy density ($\rho$ is the water density, $g$ the gravitational constant and $H$ the wave height), $c_g$ is the group velocity, $x$ is the distance within the vegetation and $\varepsilon_D$ is the vegetation-induced rate of energy dissipation. Water waves propagating through submerged and emergent vegetation lose energy by performing work on the vegetation stems, which directly results in smaller wave heights (Dalrymple et al., 1984).

Based on bottom interaction, wave decay was considered to be exponential through the wave

decay ratio $H = H_0 \exp(-k_i x)$. The wave decay ratio is based on the real part of the complex wave number ($k = k_r - ik_i$) and calculated through the solution to the dispersion relation $\omega^2$ (see e.g. Kobayashi et al., 1993). However, for vegetated areas, a non-exponential wave decay was also proposed, with the following equation still widely used today (Dalrymple et al., 1984):

$$H(x) = \frac{H_0}{1 + \beta x} \tag{5.1}$$

where $H_0$ is the incident wave height at the leading edge of the meadow, $H$ is the wave height at distance $x$ from the leading edge and in the direction of wave propagation, and $\beta$ is the so-called damping coefficient. $\beta$ has been modified extensively from its original proposition by Dalrymple et al. (1984) depending on different boundary conditions, but can be expressed in general terms for flexible meadows through Equation 5.2:

$$\beta = \frac{4}{9\pi} C_D b_v N H_0 k \frac{\sinh^3 kl_e + 3\sinh kl_e}{(\sinh 2kd + 2kd)\sinh kd} \tag{5.2}$$

where $N$ is the shoot areal density, $b_v$ the plant width, $C_D$ the drag coefficient, $d$ the water depth and $l_e$ the vegetation effective length. $l_e$ refers to the upright length of a rigid meadow for which a flexible meadow of canopy height $h_c$ will exert an equivalent force on flow (see e.g. Luhar et al., 2010; Lei and Nepf, 2019b). This occurs due to reconfiguration of the plant caused by flow (steady or unsteady), such that the height of the meadow is no longer equal to $h_c$, but lower, which in turn reduces drag. Losada et al. (2016) extended the original formulation of Dalrymple et al. (1984) using the reconfigured meadow height instead of the upright length, successfully predicting decay within flexible canopies. This length, however, needs to be actively measured, which means more complicated set-ups, especially for field applications. The use of $l_e$ (Lei and Nepf, 2019b) allows for the implementation of the model for flexible canopies without the need to measure the actual plant reconfiguration.

Note that Equation 5.2 makes use of the drag coefficient $C_D$ and the geometric and spatial properties of the dissipating mechanism (submerged vegetation in this case). The selection of $C_D$ has been a topic of great debate regarding flow-vegetation interaction for decades. Boundary reflection (e.g. end of a flume in a laboratory), vegetation fields, and other morphological features cause modulation of waves so that in any particular scenario, $C_D$ needs to be calibrated through experimentation (Mendez and Losada, 2004). Nonetheless, the calibrated $C_D$ will still vary greatly depending on a myriad of factors, such as type and intensity of loading (pure waves vs. currents vs. a combination of both), plant flexibility and morphological characteristics, and whether plant motion is taken into account (Henry et al., 2015). Experimentally calibrated values have been commonly related either to the Reynolds Number ($Re = ub/\nu$, with $u$ the velocity, $\nu$ the kinematic viscosity, and $b$ the characteristic length) or the Keulegan-Carpenter Number ($KC = uT/b$, with $T$ the wave period), where the former focuses on the turbulent drag created by the plants and the latter on inertia. This makes $KC$ well suited for low-energy wave-dominated conditions and $Re$ better suited for turbulent dominated areas (see Hu et al., 2014; Ozeren et al., 2014; Chen et al., 2018, for comprehensive comparisons). Experimental calibration of $C_D$ based on $Re$ has been commonly given in general terms by:

$$C_D = n_1 + \left(\frac{n_2}{Re}\right)^{n_3} \tag{5.3}$$

where $n_i$ are constants that depend on the fitted experimental conditions. Notice, however, that the range of validity of $Re$ for any fitted case may vary depending on the trialed conditions (see e.g. Paul and Amos, 2011; Möller et al., 2014). Initially, values of 0.1–1 were considered appropriate based on the value for a rigid cylinder; nevertheless, the inclusion of vegetation motion (Asano et al., 1992) and the use of in-canopy velocities to calculate $Re$ (Lowe et al., 2005a) have led to a common use of values between 2–3, reaching up to $O(2)$ for low $Re$. Losada et al. (2016), on the other hand, used the top-of-canopy velocity to calculate $Re$, arguing that the use of in-canopy mean velocity is impractical due to the need to measure within the canopy. In addition, the authors utilized a variation of $Re$ implementing the effective blade length $l_e$ to include reconfiguration in the calibration of $C_D$:

$$Re^{l_e} = \frac{l_e U_w}{\nu} \tag{5.4}$$

Regarding calibration based on $KC$, Luhar and Nepf (2016) calculated $C_D$ based on the calibration for flat plates. This was validated for the application with flexible submerged vegetation under both unidirectional currents and oscillatory flow, leading to:

$$C_D = \max(10KC^{-\frac{1}{3}}, 1.95) \tag{5.5}$$

where, for the unidirectional limit, a minimum threshold of 1.95 was found to accurately describe drag induced by flexible blades. This formulation of $C_D$ based on $KC$ has been successfully applied to calculate drag forces on anchors under pure wave conditions (Villanueva et al., 2022) and wave damping under combined waves and currents (Schaefer and Nepf, 2022). Ozeren et al. (2014) showed the calculation of the bulk $C_D$ based on $KC$ fitting the data to the same form of Equation 5.3 for regular and irregular waves with model and real vegetation.

### 5.2.2 *Oscillatory Flow*

The velocity structure within the water column can be decomposed into three parts (e.g. Lowe et al., 2005a): steady flow, oscillatory or time-varying, and turbulent. The instantaneous velocity at an arbitrary point in space and time can then be written as:

$$U_i(z, t) = U_c(z) + U_w(z, t) + U'(z, t) \tag{5.6}$$

where $U_i$ is the instantaneous velocity, $U_c$ the steady flow component, $U_w$ the oscillatory component and $U'$ the turbulent component. The steady current $U_c$ observed under oscillatory flow was originally related to the mass transport velocity and solved analytically in terms of Stoke's Stream Function (Longuet-Higgins, 1953). Non-linearity of the oscillatory flow, caused in part by near-bed viscosity, can be captured through higher-order solutions such as those of Stoke's theory. This non-linearity means that the vertical and horizontal components of 2D wave motion are not 90° out of phase, as suggested by linear wave theory, resulting in a non-zero wave stress analogous

to the turbulent Reynolds stress (Luhar et al., 2010). Longuet-Higgins (1953) showed the analytical solution for mass transport velocity (here $U_c$) of a progressive wave both at the boundaries (not shown here) and at the interior of the water column (Equation 5.7) by solving the stream function. Equation 5.7 is valid for small values of mass transport velocity compared to the orbital velocity.

$$U_c = \frac{a^2 \omega k}{4 \sinh^2 kd} \left[ 2 \cosh \left( 2kd \left( \frac{z}{d} - 1 \right) \right) + 3 \right.$$
$$\left. + kd \sinh 2kd \left( 3 \left( \frac{z}{d} \right)^2 - 4 \left( \frac{z}{d} \right) + 1 \right) + 3 \left( \frac{\sinh 2kd}{2kd} + \frac{3}{2} \right) \left( \left( \frac{z}{d} \right)^2 - 1 \right) \right] \quad (5.7)$$

where $a$ is the wave amplitude, $\omega$ the wave angular frequency, and $z$ the height from the bed.

The oscillatory component of the velocity is more complex due to the cyclic nature of motion, where inertia plays an important role. Linear and higher order wave theories can predict these oscillatory velocities accurately; however, flow-vegetation interaction additionally requires: (1) an understanding of the geometric properties of the vegetation, given by the vegetation element frontal $\lambda_f$ and planar $\lambda_p$ proportion to the surface area:

$$\lambda_f = \frac{h_c b_v}{S^2} \quad (5.8a)$$

$$\lambda_p = \frac{b_v t_v}{S^2} \quad (5.8b)$$

where $S$ is the average separation between shoot central axes in both planar directions ($x$-$y$), and $t_v$ is the plant thickness; and (2) a scaling of these geometric properties with respect to the hydrodynamic environment, given by the canopy shear length scale $L_s$ and the drag length scale $L_d$ (Lowe et al., 2005a):

$$L_s = \frac{2h_c}{C_f} \quad (5.9a)$$

$$L_d = \frac{2h_c(1 - \lambda_p)}{C_D \lambda_f} \quad (5.9b)$$

where $C_f$ is the friction coefficient. Lowe et al. (2005a) proposed an analytical model to estimate flow within a canopy based on incident hydrodynamics and canopy geometric properties. The model balances the acceleration and force terms given by the set of Equations 5.8 and 5.9 and the oscillatory velocity $U_w$. They then developed a non-dimensionalized form of the model in terms of the wave orbital excursion $A_\infty^{\mathrm{rms}}$ to determine the relative magnitude of each of the terms:

$$\frac{\partial(\hat{U}_w^* - U_{\infty,w}^*)}{\partial t^*} = \frac{A_\infty^{\mathrm{rms}}}{L_s} |U_{\infty,w}^*| U_{\infty,w}^* - \frac{A_\infty^{\mathrm{rms}}}{L_d} |\hat{U}_w^*| \hat{U}_w^* - \frac{C_M \lambda_p}{1 - \lambda_p} \frac{\partial \hat{U}_w^*}{\partial t^*} \quad (5.10)$$

$$A_\infty^{\mathrm{rms}} = \frac{\hat{U}_{\infty,w}^{\mathrm{rms}}}{\omega} \quad (5.11)$$

where $C_M$ is the inertia coefficient, and $A_\infty^{\mathrm{rms}}$ is based on the root mean square free stream velocity $U_{\infty,w}^{\mathrm{rms}}$ (canopy unaffected). The asterisk (*) in Equation 5.10 indicates the velocity and time parameters non-dimensionalized through their product with $(U_{\infty,w}^{\mathrm{rms}})^{-1}$ and $\omega$, respectively. The over-hat represents the canopy-integrated values ($z = [0 : h_c]$). Lowe et al. (2005a) then proposed the attenuation of in-canopy oscillatory velocity as the ratio of canopy-averaged root mean square wave velocity and the corresponding free stream velocity:

$$\alpha_w = \frac{\hat{U}_w^{\mathrm{rms}}}{\hat{U}_{\infty,w}^{\mathrm{rms}}} \tag{5.12}$$

The dimensionless terms in Equation 5.10, i.e. $A_\infty^{\mathrm{rms}}/L_s$, $A_\infty^{\mathrm{rms}}/L_d$ and $C_M \lambda_p/(1 - \lambda_p)$, are of $O(1)$, whence the relative importance of each term is determined. Depending on the hydrodynamic conditions, $\alpha_w$ can be dominated by one or more of these terms, which can then reduce the solution to Equation 5.10 to disambiguate different flow conditions (Lowe et al., 2005a): canopy-independent ($\alpha_w = 1$), inertia-dominated ($\alpha_w = (1 - \lambda_p)/(1 + (C_M - 1)\lambda_p)$), general flow ($\alpha_w(A_\infty^{\mathrm{rms}}/L_s, A_\infty^{\mathrm{rms}}/L_d, C_M \lambda_p/(1 - \lambda_p))$), and unidirectional limit or current-dominated ($\alpha_w = \sqrt{L_d/L_s}$).

## 5.3 Methodology

To study the response of flexible mats of artificial seagrass in a marine environment, a series of experiments were carried out under controlled laboratory conditions. Initially, different mats and anchor configurations were tested, with mat mechanical performance, flow interaction, and the resulting loads on anchoring points scrutinized (Villanueva et al., 2022). Here, we focus on the velocity structure and wave height evolution. The compound set of experiments was carried out at the Schneiderberg Wave Flume (WKS) at Ludwig Franzius Institute of Leibniz University Hannover. The WKS is a large-scale wave flume with a length of 110 m, a width of 2.2 m, and a depth of 2 m. Waves are generated by an electrical paddle-type wave-maker with a maximum paddle stroke of 1.8 m and wave height generation of up to 0.5 m. This section provides a brief overview of the experimental set-up, focusing more deeply on the methodology used during analysis of aspects relevant to wave dynamic measurements. A more detailed description of the general set-up, including the wave flume and instrumentation, is given in Section 4.3.

Most flow-vegetation physical experiments are carried out in scaled-down form for practical reasons, with wave heights < 20 cm and periods < 2 s (Table 5.A.1). Here, the large scale of the flume allowed us to test prototype-sized mats (Carus et al., 2021), which provides insight into the potential hydrodynamic response of the mats under field conditions. Typical near-bed velocities found around seagrass-prone areas are usually lower than 0.5 m s$^{-1}$ (Fonseca and Bell, 1998; van Katwijk et al., 2000); consequently, velocities within this range were sought and input wave conditions selected by calculating the expected near-bed velocity based on linear wave theory. This resulted in wave periods from 2–5 s and wave heights up to 33 cm. Three different water depths were selected, leading to 12 different wave conditions (Table 5.1). Note that the near-bed velocities in Table 5.1 were used as estimates of the expected velocities, and are given only as reference. The true non-linear velocities were measured and are presented within the results. Further, to support

Table 5.1: Wave conditions tested for each wave run (WR).

| Parameter | | WR1 | WR2 | WR3 | WR4 | WR5 | WR6 | WR7 | WR8 | WR9 | WR10 | WR11 | WR12 |
|---|---|---|---|---|---|---|---|---|---|---|---|---|---|
| $T$ | [s] | 2 | 3 | 4 | 5 | 2 | 3 | 4 | 5 | 2 | 3 | 4 | 5 |
| $H$ | [m] | 0.11 | 0.06 | 0.19 | 0.11 | 0.22 | 0.11 | 0.06 | 0.22 | 0.33 | 0.22 | 0.11 | 0.06 |
| $d$ | [m] | 0.50 | 0.50 | 0.50 | 0.50 | 0.63 | 0.63 | 0.63 | 0.63 | 0.83 | 0.83 | 0.83 | 0.83 |
| $h_c/d$ | [-] | 0.5 | 0.5 | 0.5 | 0.5 | 0.4 | 0.4 | 0.4 | 0.4 | 0.30 | 0.30 | 0.30 | 0.30 |
| $\lambda$ | [m][*] | 4.44 | 7.09 | 9.66 | 12.19 | 4.75 | 7.69 | 10.53 | 13.31 | 5.15 | 8.54 | 11.77 | 14.95 |
| $U_b^{max}$ | [m s$^{-1}$][*] | 0.17 | 0.11 | 0.36 | 0.21 | 0.30 | 0.18 | 0.10 | 0.38 | 0.36 | 0.30 | 0.16 | 0.09 |

[*]expected values of wavelength $\lambda$ and the maximum horizontal orbital velocity 3 cm above the bed were calculated based on linear wave theory for reference.

the transmission of these conditions to other laboratory and field experiments, the dimensionless parameters $kd$ and Ursell Number ($U_R = H\lambda^2/d^3$, where $\lambda$ is the wavelength) are also given in Table 5.1. The tested wave trains consisted of 60 regular waves for each of the conditions tested.

### 5.3.1 *Experimental Set-up*

A mobile sand bed (homogeneously graded quartz of $d_{50} = 0.19$ mm, particle density of 2.65 g cm$^{-3}$, and bulk density of 1.45 t m$^{-3}$) was constructed on top of the concrete bed of the flume. The sand bed began 62.65 m from the idle paddle position, had a length of 10.5 m, a width equal to that of the flume, and a depth of 10 cm (Figure 5.1). 2.7 cm-thick plywood panels were installed below the sand bed to facilitate instrument and anchor mounting. The sand bed was preceded by a 1:30 plywood ramp and succeeded by a 1:10 gravel ramp. The far end of the flume was equipped with an artificial beach consisting of an aluminum stepped slope and industrial foam to enhance wave absorption. Within this study, the beginning of the sand bed was taken as $x = 0$; the $x$-axis ran parallel to the flume and was positive in the direction of wave propagation, the $y$-axis ran the cross-section with 0 at the right flume wall (with respect to the direction of wave propagation), and the $z$-axis along the vertical with 0 at the sand bed.

Prototype ASG mats were built to simulate mats that could be deployed in the field for restoration purposes (see Carus et al., 2021). For this, 2-by-2-m mats were built using rolls of coconut mesh of different compositions. Individual ASG stems were then fixed to this hybrid coconut mat to create a fully flexible ASG mat. Polyamide cable ties (PA, density $\rho_{PA} = 1.13$ g cm$^{-3}$ and flexural rigidity $EI_{PA} = 800$ N mm$^2$) of length $h_c = 250$ mm, width $b_v = 4.8$ mm, and thickness $t_v = 1.36$ mm were used as a seagrass surrogate. Density effects were not a focal point of this study, therefore, a constant shoot density of $N = 400$ m$^{-2}$ was chosen. This resulted in a separation between shoots of $S = 5$ cm and a frontal area per canopy volume of 1.92 m$^{-1}$ ($b_v/S^2$, Nepf, 2012a). The chosen ASG had low flexibility and the meadow density was kept low compared to real meadows to test the hydrodynamic effect of a stiffer, sparse meadow. Nonetheless, Taphorn et al. (2021) showed that PA reconfigured with hydrodynamic loading while simultaneously affecting the flow field around a single stem. The height of the strips was not varied during the experiments, therefore, the variation of depth resulted in different submergence ratios $h_c/d = [0.3, 0.4, 0.5]$ (Table 5.1).

To quantify wave decay, a total of 8 ULTRALAB Ultrasonic Sensors (USS) with a resolution of 0.2 mm were used to measure the water level fluctuations $\eta(t)$ at different positions along the $x$-axis
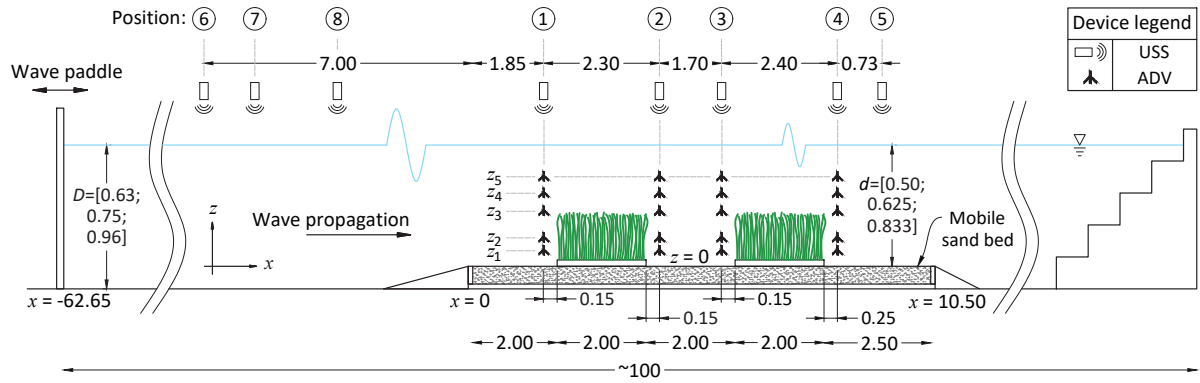
Figure 5.1: Schematic of the experimental set-up used for the experiments. $D$ = water depth to the concrete flume bed; $d$ = depth to sand bed. Shown are the device positions. USS = Ultrasonic Sensor; ADV = Acoustic Doppler Velocimeter. $z_i$ are the different ADV positions, where the 4 aligned ADVs were vertically displaced to the $i$ positions labeled, with $z_{1-5} = [3.3; 10.5; 25.7; 35.9; 45.7]$ [cm]. $z$-axis exaggerated by 4 times. All dimensions in meters.

**5**

(Figure 5.1). The positions of the devices are enumerated, starting with those over the sand bed, with positions 1–4 placed immediately in front and immediately behind the ASG mats to directly measure the effect of the mats on wave height evolution. Position 5 (corresponding to the last USS in $x$) was located 1.52 m before the end of the sand bed. Three USS were positioned in front of the sand bed as control points (positions 6–8) for the input wave conditions (Table 5.1), with positions 7 and 8 varying, depending on the wave condition used, to cover different points along one wavelength. An HBM signal amplifier bundled with the software CATMAN was used to synchronously measure water level fluctuations, pressure, and forces at a frequency of 100 Hz. Wave orbital velocities were recorded simultaneously by means of a trigger connected to the HBM. Four downward-looking NORTEK VECTRINO+ Acoustic Doppler Velocimeters (ADV) then measured the orbital velocities at 50 Hz. The $u$, $v$, and $w$ components of the measured velocities were respectively aligned with the $x$, $y$, and $z$ components of the set-up. Throughout this chapter, specific devices and their position will be referred to by the given acronym directly followed by the position number (e.g. ADV1 corresponds to the ADV at position 1, in front of the first ASG mat, Figure 5.1). The four ADVs were aligned in $z$ with each other and in $x$ with USS1–USS4, respectively.

For each wave run (WR), the 8 USS and 4 ADVs recorded simultaneously. To build the orbital velocity profiles, the ADVs were displaced vertically ($z_i$ in Figure 5.1) and the measurements repeated for the corresponding wave run. Finally, this was repeated for three different cases: 1) no vegetation, as control; 2) under the presence of 1 ASG mat, starting at $x = 2$ m; and 3) with 2 ASG mats with a 2-m gap between them. This resulted in a total of 168 wave run measurements.

### 5.3.2 *Data Processing and Analysis*

All recorded data were imported and processed in MATLAB (R2022a). Water level fluctuations for all USS data were standardized (mean = 0) around the still water level using the detrend function of MATLAB. The original time series was curated by removing the initial incoming and outgoing waves corresponding to the wave generator ramp time. Self-cross-correlation and a Fast Fourier Transform (FFT) were used to calculate the period $T$ of the incoming waves over the sand bed. The $T$ from the measurements did not vary from the input $T$ (Table 5.1) by more than 2%; therefore, from here on,

the listed input values are used for simplicity. Zero-up-crossing was used to identify the first full wave of the curated time series, after which 10 waves were extracted to obtain a time series with a length equal to $10T$. This was done to decrease the effect of wave reflection from the far end of the flume. The 10-wave time series window was then averaged into a single representative wave for the respective wave run using a phase averaging technique analog to that described by Lei and Nepf (2019a). The maximum and minimum values of $\eta(t)$ for each wave run were then calculated from the phase-averaged wave. Table 5.2 shows the measured wave heights at the leading edge ($H_0$) and the ratio $H/H_0$ for positions 2 and 4, i.e. just behind the first and second ASG mats.

The raw velocity data were preprocessed using the acceleration thresholding method (Goring and Nikora, 2002). As current models focus on the dominant velocity component, i.e. the horizontal component $u$, this study thenceforth focuses solely on this component. Figure 5.2 shows an example of data processing for one ADV within one wave run. To obtain a clear and homogeneous minimum and maximum value of the oscillating horizontal orbital velocity, a fourth-order zero-phase digital filter was utilized to remove any residual spikes in the data. Phase-averaging was used to find the maxima and minima of wave velocities ($U_w^{\max}$, $U_w^{\min}$) for each wave run. The resulting phase-averaged wave was then used to calculate the spatial phase-averaged steady current $U_c$ and the root mean square wave velocity $U_w^{\mathrm{rms}}$ utilizing Equations 5.13 and 5.14 (Table 5.2), respectively, with $\phi$ the phase (see Luhar et al., 2010).

$$U_c = \frac{1}{2\pi} \int_0^{2\pi} U_i(\phi) d\phi \tag{5.13}$$

$$U_w^{\mathrm{rms}} = \sqrt{\frac{1}{2\pi} \int_0^{2\pi} (U_i(\phi) - U_c)^2 d\phi} \tag{5.14}$$

Note that in Equation 5.14, $U_w^{\mathrm{rms}}$ represents the phase-averaged root mean square wave velocity, whereby recently, other authors have opted for the calculation of the wave velocity amplitude, obtained by multiplying the arguments within the square root by 2 (e.g. Zhang et al., 2018; Schaefer and Nepf, 2022). Here, the wave amplitude refers to the minimum and maximum of the measured phase averaged wave velocity ($U_w^{\min}$ and $U_w^{\max}$, respectively). $U_{\infty,w}^{\mathrm{rms}}$ was taken from the measurements at position 1 (leading edge of the meadow) utilizing the fitted velocity following Equation 5.15, with $b_1$ and $b_2$ as fit coefficients (see e.g. Pujol et al., 2013).

$$U_{\infty,w}^{\mathrm{rms}}(z) = b_1 \cdot \cosh b_2 z \tag{5.15}$$

To obtain comparable in-canopy root mean square velocities, the fitted profiles were integrated along the canopy layer:

$$\hat{U}_w^{\mathrm{rms}} = \frac{1}{h_c} \int_0^{h_c} U_w^{\mathrm{rms}} dz \tag{5.16a}$$

$$\hat{U}_{\infty,w}^{\mathrm{rms}} = \frac{1}{h_c} \int_0^{h_c} U_{\infty,w}^{\mathrm{rms}} dz \tag{5.16b}$$

Canopy flow attenuation $\alpha_w$ was then calculated utilizing Equation 5.12. Predicted values of
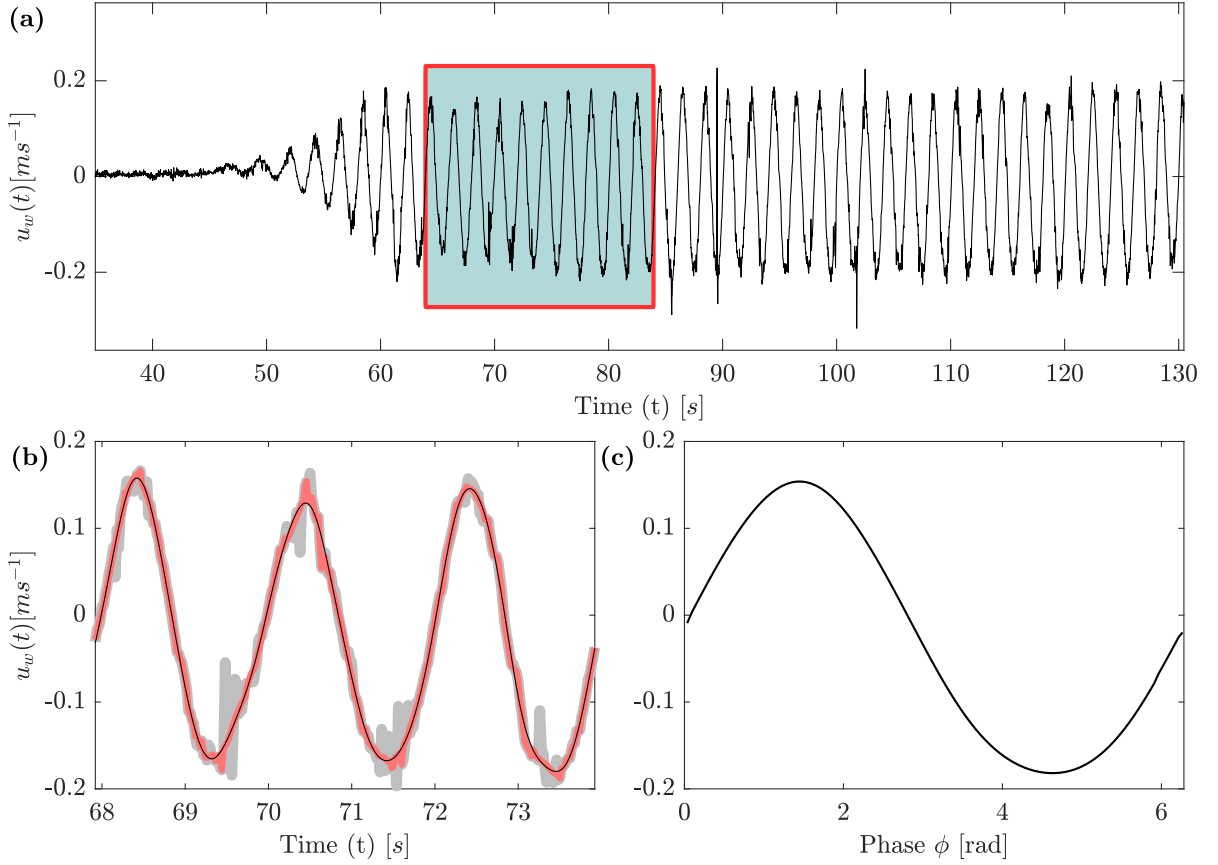
Figure 5.2: Processing of the orbital velocity time series for WR1, no artificial vegetation, ADV position 4 (see Figure 5.1 and Table 5.1). (a) shows the raw data record of the ADV with the 10-wave window that was extracted for post-processing. (b) shows a 3-wave window comparing the raw data (gray, thick line), the despiked data after Goring and Nikora (2002) (red, medium thick line), and the filtered data (thin, solid black line). (c) shows the resulting Phase Averaged wave calculated from the 10-wave window.

$\alpha_w$ were obtained by solving Equation 5.10, with Equation 5.11 used to calculate $A_\infty^{\mathrm{rms}}$. The friction coefficient $C_f$ was previously calculated by Villanueva et al. (2022) (see Chapter 4), with a general formulation as a function of $U_w$ obtained as a result (Equation 4.12), shown in simplified form below:

$$C_f = 0.369 e^{-72.6 U_w^{\mathrm{max}}} + 0.063 e^{-3.3 U_w^{\mathrm{max}}} \tag{5.17}$$

Note that previous studies have used a constant $C_f$ value of $O(-2)$ (commonly 0.01; Pujol et al., 2013). Finally, $C_M$ was obtained following $C_M = 1 + k_m$, where $k_m$ is the added mass and can be estimated as $k_m = b_v / t_v$ for rectangular cross-sectional shapes (Pujol et al., 2013). This resulted in a value of 4.53 for our experiments.

For the calculation of wave decay, the measured wave height of USS1 (leading edge of the first ASG mat) was used as $H_0$. The ratio of the average measured wave height to $H_0$ at each further position was then calculated. Equation 5.1 was fitted to the calculated $H/H_0$ ratios as a function of $x$ for cases with one and two ASG mats separately. $\beta$ was then obtained from the fit coefficient.

For a comparison with existing models, $Re$ was calculated through Equation 5.4 using the canopy-integrated velocities (Equation 5.16a). $l_e$ was calculated based on the scaling parameter

*CaL* (Luhar and Nepf, 2016), where *Ca* is the Cauchy Number and *L* the relative velocity between blade and water (for details see Chapter 4). $C_D$ was then calculated utilizing Equation 5.3 with $n_1 = 0.08$, $n_2 = 50000$ and $n_3 = 2.2$, as proposed by Losada et al. (2016) for pure wave conditions. Finally, Equation 5.18, a modification of Equation 5.2 proposed by Losada et al. (2016), was used to calculate $\beta$.

$$\beta = \frac{B_1 H_0}{B_2} \tag{5.18a}$$

$$B_1 = \frac{2}{3\pi}\rho C_D b_v N H_0 \left(\frac{gk}{2(\omega - U_c k)}\right)^3 \frac{\sinh^3 kl_e + 3\sinh kl_e}{(3k\cosh^3 kd)} \tag{5.18b}$$

$$B_2 = \left[\frac{\rho g}{8}\left(1 + \frac{2kh}{\sinh 2kh}\right)\left(\frac{g}{k}\tanh kh\right)^{\frac{1}{2}} + \frac{\rho g}{8}U_c\left(3 + \frac{4kh}{sinh2kh}\right)\right.$$
$$\left. + \frac{3\rho k}{8}U_c^2\left(\frac{g}{k}\coth kh\right)^{\frac{1}{2}}\right]\left[U_c + \frac{1}{2}\left(1 + \frac{2kh}{sinh2kh}\right)\left(\frac{g}{k}\tanh kh\right)^{\frac{1}{2}}\right] \tag{5.18c}$$

Equation 5.18a can be applied under wave-current conditions. $U_c$ was calculated utilizing Equation 5.7 (Table 5.2); note, however, that the lack of an additional, externally input steady current means that $U_c$ is orders of magnitude lower than $U_w$ and represents only the wave-induced underlying current. This reduces Equation 5.18a to a form analog to Equation 5.2. Nevertheless, the values of $\beta$ obtained with Equation 5.18 were higher than those of Equation 5.2 and were more comparable to the measured values.

## 5.4 Results

Table 5.2 shows the results of the measurements and the respective calculations described in Section 5.3. Measurements of WR3 ($H = 0.19$ m and $T = 4$ s) for both 1 and 2-mat configurations presented results that clearly indicated errors in measurements and were therefore omitted from the results presented below. The wave conditions chosen fell within the intermediate water regime, close to the transition to shallow water regime, following $0.003 \le d/gT^2 \le 0.08$.

Bed interaction and flume dimensions under the chosen wave conditions resulted in vertically asymmetric waves, most of which fell under the category of Stoke's second and third-order theory, and those with $T \ge 3$ s and $H > 0.1$ m transitioning to cnoidal waves. This asymmetry could be observed on the water level fluctuations $\eta$ and horizontal orbital velocities $U_w$. The measured $H$ thus represents the sum of the maxima and minima of the phase-averaged wave. For the orbital velocities, the rms-velocity $U_w^{\text{rms}}$ was used to obtain the results described below unless otherwise specified.

### 5.4.1 *Wave Decay*

Wave evolution for the control experiments (i.e. in the absence of ASG) showed that ramp-induced shoaling increased the wave height at USS1 (first position above the sand bed) relative to USS6 (pre-sand bed) by around 3%. Viscous dissipation caused by the walls and bed could also be observed through wave decay within the control experiments. The average rate of wave decay between USS positions 1 and 5 for all wave runs of the control experiments was 1.9±1.5% per meter.

Table 5.2: Calculated Parameters.

| | WR | $H_0$ [m] | $H_2/H_0$ [-] | $H_4/H_0$ [-] | $U_{c,1}$ [m s$^{-1}$] | $\hat{U}^{rms}_{\infty,w}$ [m s$^{-1}$] | $\hat{U}^{rms}_{w,2}$ [m s$^{-1}$] | $l_e/h_c$ [-] | $A^{rms}_{\infty}$ [m] | $\alpha_w$ [-] | $C_D$ [-] | $C_f$ [-] | $Re$ [-] | $KC$ [-] | $\beta$ [m$^{-1}$] |
|---|---|---|---|---|---|---|---|---|---|---|---|---|---|---|---|
| **1 Mat** | 1 | 0.09 | 0.96 | 0.96 | -3.70e-04 | 0.10 | 0.10 | 0.50 | 0.03 | 0.97 | 2.87 | 0.09 | 1.27e+04 | 42 | 0.008 |
| | 2 | 0.05 | 1.27 | 0.91 | 1.77e-05 | 0.07 | 0.05 | 0.61 | 0.03 | 0.79 | 2.87 | 0.08 | 1.04e+04 | 42 | -0.005 |
| | 4 | 0.11 | 0.12 | 1.22 | -1.80e-04 | 0.15 | 0.11 | 0.59 | 0.12 | 0.76 | 1.95 | 0.10 | 2.17e+04 | 154 | 0.060 |
| | 5 | 0.18 | 0.98 | 0.92 | 4.45e-05 | 0.21 | 0.19 | 0.44 | 0.07 | 0.91 | 2.26 | 0.12 | 2.28e+04 | 86 | 0.006 |
| | 6 | 0.11 | 0.85 | 0.86 | 1.14e-04 | 0.10 | 0.12 | 0.54 | 0.05 | 1.15 | 2.49 | 0.09 | 1.40e+04 | 65 | 0.013 |
| | 7 | 0.07 | 0.72 | 0.91 | -8.73e-05 | 0.06 | 0.07 | 0.71 | 0.04 | 1.27 | 2.77 | 0.08 | 9.96e+03 | 47 | 0.034 |
| | 8 | 0.20 | 0.93 | 1.14 | 4.29e-04 | 0.25 | 0.25 | 0.52 | 0.20 | 1.00 | 1.95 | 0.14 | 3.20e+04 | 257 | 0.035 |
| | 9 | 0.29 | 1.00 | 0.90 | 9.63e-04 | 0.24 | 0.20 | 0.44 | 0.08 | 0.84 | 2.15 | 0.14 | 2.69e+04 | 101 | 0.007 |
| | 10 | 0.23 | 0.94 | 0.87 | 2.43e-04 | 0.19 | 0.18 | 0.47 | 0.09 | 0.93 | 2.03 | 0.12 | 2.26e+04 | 119 | 0.006 |
| | 11 | 0.11 | 0.93 | 1.06 | -1.47e-04 | 0.10 | 0.09 | 0.57 | 0.06 | 0.93 | 2.29 | 0.09 | 1.43e+04 | 83 | 0.006 |
| | 12 | 0.05 | 0.90 | 0.97 | 7.60e-05 | 0.05 | 0.05 | 0.76 | 0.04 | 0.99 | 2.62 | 0.08 | 1.01e+04 | 55 | 0.008 |
| **2 Mats** | 1 | 0.09 | 0.94 | 0.88 | 2.16e-05 | 0.10 | 0.10 | 0.52 | 0.03 | 0.96 | 2.85 | 0.09 | 1.35e+04 | 43 | 0.020 |
| | 2 | 0.04 | 1.34 | 0.79 | 7.64e-05 | 0.09 | 0.06 | 0.59 | 0.04 | 0.68 | 2.61 | 0.09 | 1.32e+04 | 56 | -0.012 |
| | 4 | 0.12 | 0.09 | 1.08 | 2.60e-05 | 0.13 | 0.11 | 0.57 | 0.11 | 0.84 | 1.95 | 0.10 | 1.93e+04 | 140 | 0.040 |
| | 5 | 0.19 | 0.98 | 0.91 | 2.29e-04 | 0.20 | 0.18 | 0.45 | 0.06 | 0.90 | 2.29 | 0.12 | 2.27e+04 | 83 | 0.010 |
| | 6 | 0.10 | 0.96 | 0.93 | 5.24e-05 | 0.11 | 0.11 | 0.53 | 0.05 | 1.02 | 2.44 | 0.09 | 1.44e+04 | 68 | 0.012 |
| | 7 | 0.07 | 0.72 | 0.74 | -1.40e-05 | 0.05 | 0.08 | 0.69 | 0.03 | 1.45 | 2.80 | 0.08 | 9.35e+03 | 45 | 0.045 |
| | 8 | 0.20 | 0.87 | 0.11 | 1.60e-04 | 0.25 | 0.25 | 0.53 | 0.20 | 1.00 | 1.95 | 0.14 | 3.25e+04 | 255 | 0.060 |
| | 9 | 0.29 | 1.00 | 0.89 | 1.05e-03 | 0.24 | 0.21 | 0.45 | 0.08 | 0.85 | 2.15 | 0.14 | 2.72e+04 | 100 | 0.007 |
| | 10 | 0.20 | 1.10 | 1.17 | 3.96e-04 | 0.20 | 0.16 | 0.47 | 0.10 | 0.80 | 1.99 | 0.12 | 2.40e+04 | 128 | -0.012 |
| | 11 | 0.12 | 0.66 | 0.80 | 1.02e-04 | 0.08 | 0.12 | 0.60 | 0.05 | 1.57 | 2.50 | 0.08 | 1.16e+04 | 64 | 0.045 |
| | 12 | 0.06 | 0.53 | 1.07 | 1.06e-04 | 0.04 | 0.07 | 0.81 | 0.03 | 1.66 | 2.85 | 0.09 | 8.37e+03 | 43 | 0.016 |

$H_0$ represents the incident wave height, i.e. at the leading edge of the meadow (position 1, Figure 5.1). Non-zero numeric subscripts of $H$ and $U$ indicate the device position. WR3 was omitted due to anomalies in the measurements.

The incident wave heights from all measurements with ASG ranged from 5–31 cm in front of the sand bed (positions 6–7) and 4.5–29 cm at the leading edge of the first meadow (position 1). The ratio $H/H_0$ was close to unity at the positions in front of the sand bed, with a mean of 0.95±0.23 for all runs with ASG, while at positions above the sand bed, this lowered to 0.84–0.9±0.22 (positions 2–5). The rate of wave decay above the sand bed was 2.6±1.9% m$^{-1}$ under the presence of a single ASG mat, and 3.1±2.4% m$^{-1}$ when both ASG mats were present. The decay rate was highest between positions 1 and 2, at 5.6 and 7.2% m$^{-1}$ for 1 and 2 mats, respectively, suggesting that the first mat relative to the wave propagation direction has a more marked effect on wave decay.

Figure 5.3 shows the average wave height ratio evolution ($H/H_0$) along $x$ for six different runs segregating between one and two-mat-configurations. The average of ratios for all runs with ASG is presented to encompass all measurements. The damping coefficient $\beta$ was calculated by fitting Equation 5.1 to the wave height data, resulting in values ranging between -0.005–0.06 m$^{-1}$ and -0.012–0.06 m$^{-1}$ for 1 and 2-mat configurations, respectively (Table 5.2). The set of 1-mat experiments averaged $\beta = 0.0161 \pm 0.018$ m$^{-1}$, whereas for the 2-mat experiments $\beta = 0.021 \pm 0.023$ m$^{-1}$. As expected, the low shoot density $N$ coupled with the single-stem shoot trialed here resulted in a low wave decay; nonetheless, results show that a single ASG mat is enough to increase wave decay compared to the bare, non-vegetated areas in both control and ASG experiments (i.e. the gap). A second mat then enhanced wave decay, with $\beta$ for the 2-mat configuration being 30% higher on average than for the 1-mat configuration.

Although $\beta$ shows that wave decay is augmented by the mats, the variability of the values (Table 5.2) indicates that the input parameters have a meaningful effect on wave decay. Shoot and base layer morphology were not modified during the experiments; therefore, incident wave conditions
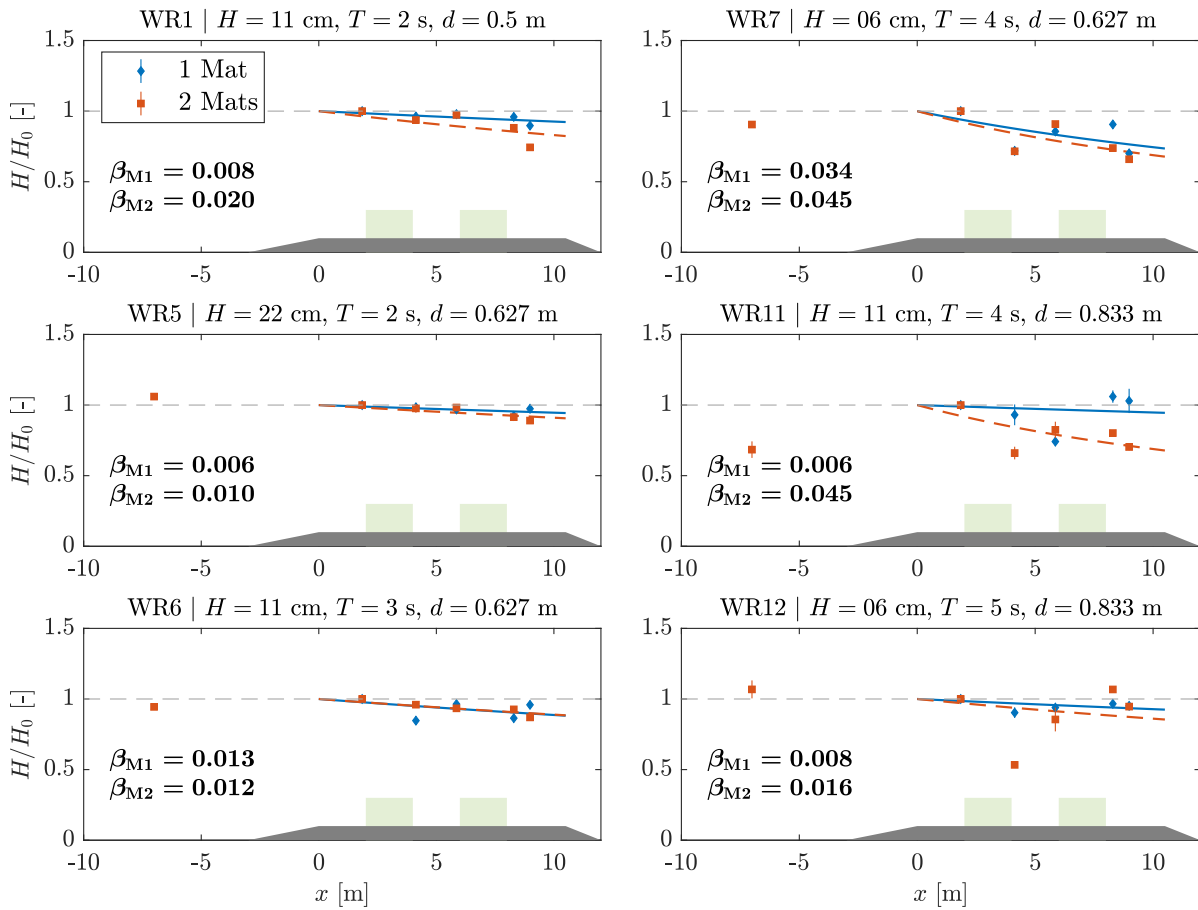
Figure 5.3: Wave Decay evolution for different wave runs. Data points show the average and standard deviation of $H/H_0$ for each USS over the sand bed and at position 6 in front of the sand bed. $H_0$ is taken from USS1 at the leading edge of the meadow. Fits follow Equation 5.1 with solid line representing runs with one mat (subscript M1) and dashed line runs with two mats (subscript M2). The corresponding resulting $\beta$ is given for each run. Shaded areas show ramp and ASG meadows (not to scale).

represent the governing variables. Analysis of the relationship between $\beta$ and the incident wave height ($H$ at position 1) showed no correlation for the wave conditions tested here. A simple linear regression between the water depth $d$ and $\beta$ also showed no significant correlation between both variables (p > 0.05). However, a light tendency of $\beta$ decreasing with increasing $d$ was observable, showing a low rate of change of -0.0048 per 10 cm of added water depth for the 1-mat experiments and -0.0019 dm$^{-1}$ for 2 mats. Regardless, the low rate and correlation indicate that the submergence ratios trialed here, i.e. $h_c/d = [0.3, 0.4, 0.5]$, had little effect on wave attenuation for the wave conditions trialed.

In contrast, analysis of the relation between the wave period $T$ and $\beta$ showed that the latter increased exponentially with increasing $T$. The relationship between $\beta$ and $T$ makes it obvious that $\beta$ is analogously sensitive to the wavelength $\lambda$ (4–14 m for this set of experiments). Figure 5.4 shows the change of $\beta$ with respect to $T$ for both mat configurations. An exponential fit for each set of experiments was done to showcase the effect of $T$ on wave decay, with the respective fits given in Equation set 5.19.
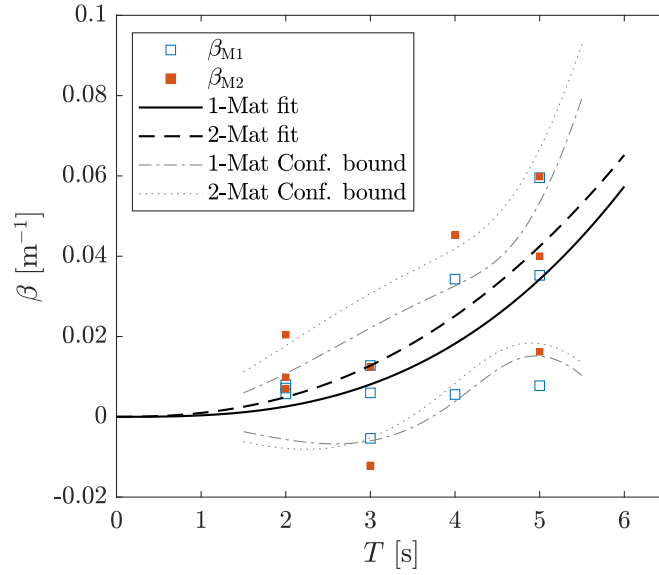
Figure 5.4: Damping coefficient $\beta$ plotted against the incident wave period $T$. Values shown for 1 and 2 ASG mats (M1 and M2, respectively). Lines show fit for each configuration (Equation 5.19) and the corresponding confidence bounds.

$$\beta_{M1} = 0.000361 T^{2.83} | R^2 = 0.44 \tag{5.19a}$$

$$\beta_{M2} = 0.000963 T^{2.35} | R^2 = 0.41 \tag{5.19b}$$

Note, however, that the variance of the fitted $\beta$ with respect to $T$ is still relatively high, with $R^2 < 0.5$ for both cases. The limited data and variability of the calculated $\beta$ produce fits with a high prediction variability within the confidence intervals, as shown in Figure 5.4. Therefore, it is important to keep in mind that although Equations (5.19a,b) may provide insight into an increasing damping coefficient with respect to $T$, this is explicitly valid for wave decay above meadows of similar geometric and mechanical characteristics and wave conditions to those trialed here, i.e. within the range $1 < T < 6$ s.

**MODELED DAMPING COEFFICIENT**

The calculation of $\beta$ requires an estimation of the drag coefficient $C_D$, which, for vegetated flow, has been commonly related to the Reynolds Number $Re$ and Keulegan-Carpenter Number $KC$. The range of canopy-integrated rms-velocities $\hat{U}_w^{\mathrm{rms}}$ measured here yielded values of $Re^{l_e}$ between 8300–32500 and $KC$ between 42–260. The ratio of effective length to upright canopy height ($l_e/h_c$) ranged between 0.44–0.81. Values of the stem-based $Re$ (i.e. based on $b_v$) were $O(1)$ lower, ranging between 200–1200. The calculation of $C_D$ following Equation 5.5 yielded values between 1.95–2.96 (mean = 2.4).

Figure 5.5 shows $C_D$ plotted as a function of $Re^{l_e}$. Results from other studies with different experimentally fitted $C_D = f(Re)$ following Equation 5.3 are shown for comparison. For the present set of experiments, the corresponding fit is shown resulting in the coefficients shown in Equation 5.20 ($R^2 = 0.79$). Additionally, a fit with the stem-based $Re$ is also plotted. The different results show how sensitive $C_D$ is to the choice of characteristic length and input velocity, directly reflected in the
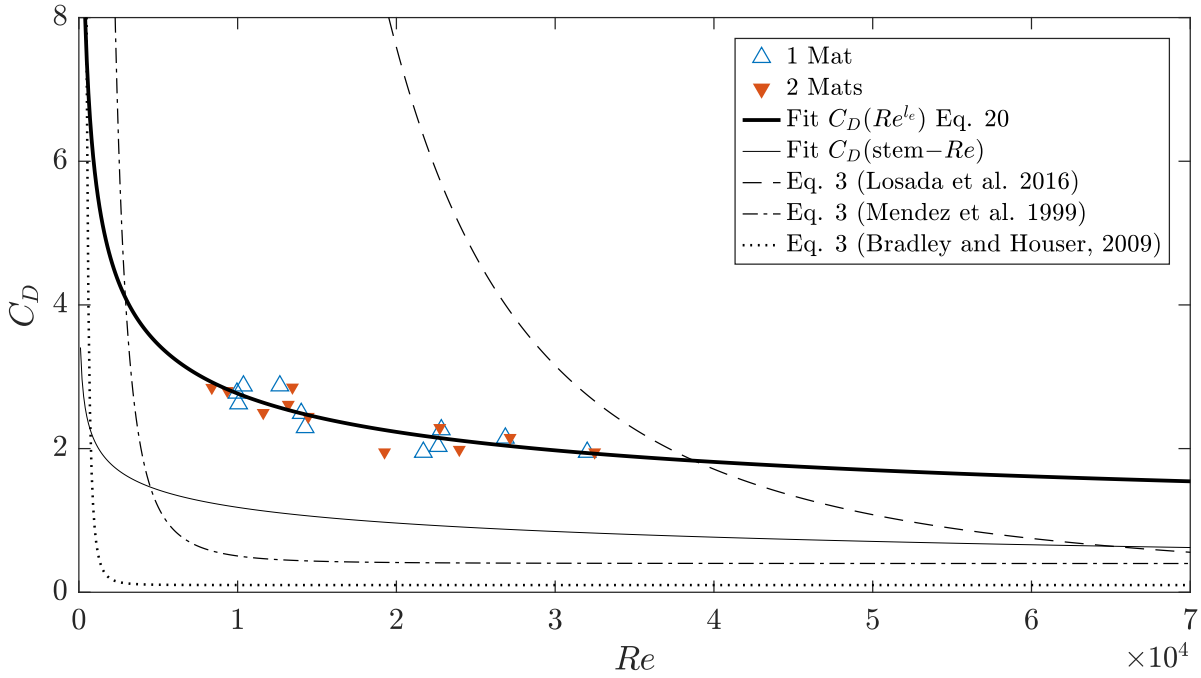
Figure 5.5: Drag coefficients (Equation 5.5) as function of $Re^{l_e}$ (Equation 5.4) and resulting fit (Thick solid line, Equation 5.20). Thin solid line shows the fit for $C_D$ as a function of the stem-$Re$. Results of Equation 5.3 using the coefficients found by Losada et al. (2016) ($n_1 = 0.08, n_2 = 50000$, and $n_3 = 2.2$), Méndez et al. (1999) ($n_1 = 0.40, n_2 = 4600$, and $n_3 = 2.9$), and Bradley and Houser (2009) ($n_1 = 0.1, n_2 = 925$, and $n_3 = 3.16$) are given for comparison.

variation of the scale of $Re$.

$$C_D = 0.31 + \left(\frac{127000}{Re^{l_e}}\right)^{0.35} \tag{5.20}$$

The modeled damping coefficient $\beta_{mod}$ was then calculated based on $C_D$ (Equation 5.5) following Equation 5.2. Figure 5.6 shows the comparison between the modeled values and the values obtained from measurements ($\beta_{obs}$). A linear fit between modeled values and measurements showed that the model underestimates the damping coefficient by 52% (based on the slope of the linear fit, no intercept). A comparison with modified forms of Equation 5.2 are also shown in Figure 5.6: Equation 5.18 (after Losada et al., 2016) overestimated $\beta_{obs}$, with $\beta_{mod} = 1.15(\pm 0.32)\beta_{obs}$, while a further modification by Lei and Nepf (2019b) (discussed later) yielded $\beta_{mod} = 1.30(\pm 0.21)\beta_{obs}$. Both models underestimated $\beta_{obs}$ for wave runs with the longest periods, i.e. $T = 5$ s, and wave heights above 0.1 m. A similar pattern was observable with the model after the original formulation (Equation 5.2), where a 1:1 comparison between modeled and measured values showed that the $\beta_{mod}$ underpredicts $\beta_{obs}$ for all but one of the wave runs with $T \geq 4$ s.

### 5.4.2 *Velocity Structure*

The maximum measured orbital velocities $U_w^{\max}$ increased proportionally with the increase of $H$, as is expected from wave theory, with no correlation to either $T$ or $d$ found for the range of conditions trialed. Comparison of $U_w^{\max}$ with the maximum velocities measured in the opposite direction (i.e. $U_w^{\min}$) showed that the non-zero net momentum transport in the direction of wave propagation (i.e. Stoke's Drift) was present regardless of the number of mats (0, 1 or 2) and
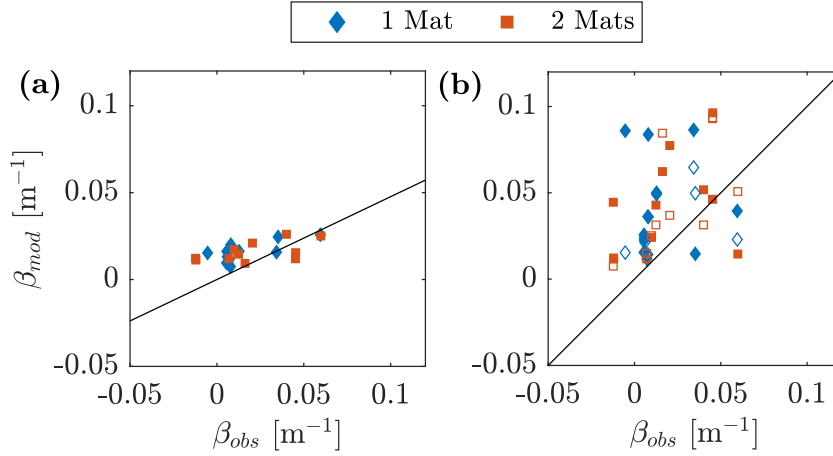
Figure 5.6: Predicted (subscript *mod*) versus measured (subscript *obs*) wave damping coefficient $\beta$. (a) $\beta$ modeled after Equation 5.2. Solid line represents a linear fit with intercept at (0,0). (b) comparison with results form Equation 5.18 (after Losada et al., 2016). Solid line represents 1:1 line. Hollow markers represent the results from the model of Lei and Nepf (2019b) for comparison.

ADV position (1–4). The ASG thence did not alter the overall mass transport in the direction of wave propagation, demonstrated by the ratio $U_w^{\max}/|U_w^{\min}|$, which, averaging for each set of measurements, yielded $1.34 \pm 0.22$ for the control experiments, and $1.36 \pm 0.19$ and $1.37 \pm 0.23$ for the one and two-mat-configurations, respectively. Figure 5.7a shows the range of $U_w$ at each ADV position for WR1 ($H = 0.11$ m, $T = 2$ s), whereby the aforementioned asymmetry becomes greater for higher $T$ as non-linearity effects intensify. The canopy-integrated velocities ranged from 0.35–0.53 m s$^{-1}$ for M0, 0.34–0.48 m s$^{-1}$ for M1, and 0.33–0.46 m s$^{-1}$ for M2 ($|\hat{U}_w^{\min}| : \hat{U}_w^{\max}$). The highest velocities in the direction of wave propagation were measured exiting the meadows, i.e. at positions 2 and 4, while in the opposite direction, the highest velocities were at position 1, i.e. exiting the first meadow at the leading edge. Overall, WR8 ($H = 0.22$ m, $T = 5$ s, and $d = 0.63$ m) recorded the highest velocities.

Figure 5.7b shows the steady flow component of the velocity measurements ($U_c(z)$) calculated utilizing Equation 5.13. With no external current input, $U_c(z)$ was expected to be close to zero. For purely oscillatory conditions, however, a non-zero current has been shown to occur (see e.g. Luhar et al., 2010). The magnitude of $U_c(z)$ was predominantly within the range of $O(-4)$ and $O(-5)$, with a few values reaching $O(-3)$. The highest values were observed for the M0 experiments, though the near-bed velocities of both ASG experiments likewise reached $O(-3)$. At the leading edge of the meadow (position 1), a peak in the positive direction could be observed within the first 10 cm along $z$ for WR2, 5, 9, and 10. The theoretical model (Equation 5.7, after Longuet-Higgins, 1953) predicted values in the same order of magnitude as the measurements for the lowest energy runs (i.e. $H < 0.1$ m). However, neither the shape of the profile nor the highest magnitudes were captured well by the model which overestimated $U_c(z)$ for $H > 0.2$ m by up to $O(1)$.

The lowest panel of Figure 5.7 shows the profiles of rms-velocities $U_w^{\mathrm{rms}}(z)$, whose canopy-integrated values $\hat{U}_w^{\mathrm{rms}}$ (Equation 5.16) ranged from 0.04–0.29 m s$^{-1}$ for M0, and from 0.04–0.25 m s$^{-1}$ for M1 and M2. The maximum value was consistent at all ADV positions for M1, but lowered to 0.22 m s$^{-1}$ for M2 at position 4, showing a reduction of $\hat{U}_w^{\mathrm{rms}}$ along $x$. The dashed
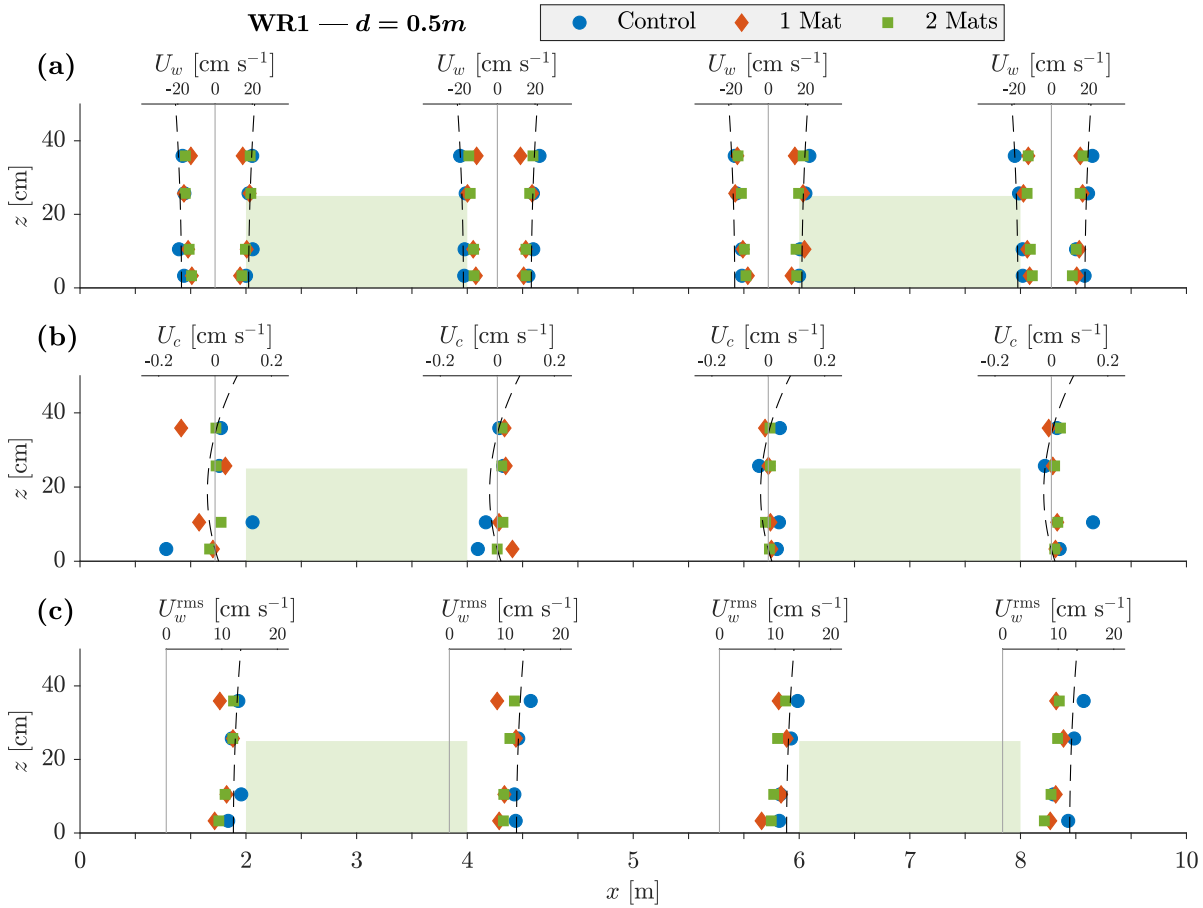
Figure 5.7: Velocity Structure for WR1 ($H$ = 0.11 m, $T$ = 2 s). Profiles show $x$-$z$ position of ADV measurements. Data points show measured values for control (no ASG mats), 1-mat, and 2-mat experiments. (a) fully measured wave velocity excursion showing maxima ($U_w^{\text{max}}$) and minima ($U_w^{\text{min}}$); dashed fitted line shows theoretical profile following Equation 5.15. (b) Steady current component of flow $U_c$ calculated from measurements using Equation 5.13; dashed line represents Equation 5.7. (c) Root mean square velocity calculated from measurements and phase-averaged using Equation 5.14; fitted line from Equation 5.15. Shaded areas show ASG at full height $h_c$.

line in Figure 5.7c was fitted using Equation 5.15 as a function of $z$ at position 1 and is thence shown at each further $x$-position for reference. $U_w^{\text{rms}}(z)$ was observed to decrease with increasing distance from the leading edge of the front meadow. Furthermore, as the measured velocities increased, the changes along $x$ became more conspicuous. To better visualize the effect of the meadows on $U_w^{\text{rms}}$, the percentage change in velocity relative to position 1 was calculated and is shown in Figure 5.8. The velocity profiles show that the vegetation induces skimming flow, which is the result of discontinuity in the drag force and mass balance along the meadow. Skimming flow has been shown for wind profiles around urban canopies (Coceal and Belcher, 2004) and submerged vegetation as a function of wave conditions (Maza et al., 2012).

Analogous to the information given by $H/H_0$, the percentage change shown in Figure 5.8 shows the evolution of $U_w^{\text{rms}}$ along $x$ with respect to the value at position 1, i.e. $U_{\infty,w}^{\text{rms}}$, calculated as $[(U_w^{\text{rms}}(x,z)/U_{\infty,w}^{\text{rms}}(x,z))-1]*100$. Negative values represent velocity reduction, while positive values indicate an increase. The values are averaged from all wave runs, with the deviations depicted by vertical bars. The deviation was relatively low for most of the positions ($f(x,z)$), ranging between 8–20%, except for measurements of M2 at position 2, where the reduction deviated by an average of
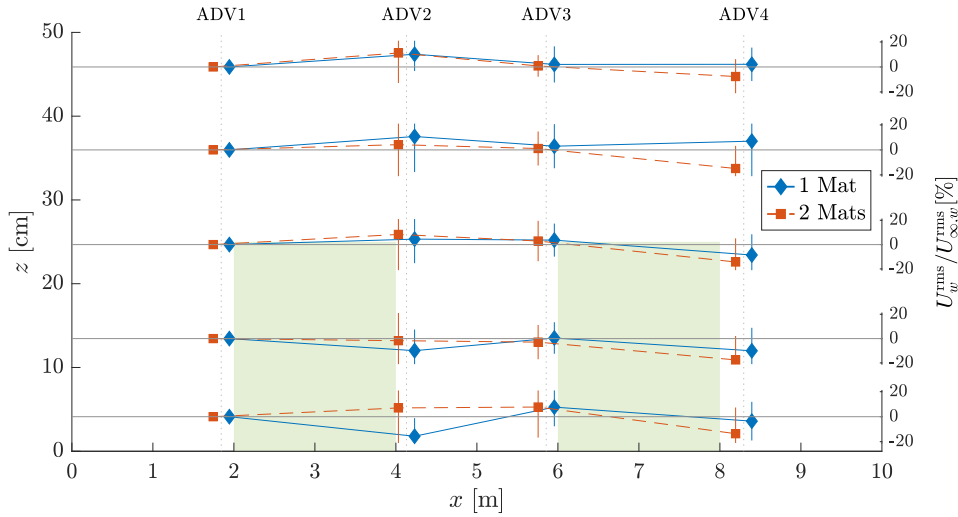
Figure 5.8: Percentage change in $U_w^{\mathrm{rms}}$ with respect to measurements at the leading edge of the meadow (position 1). The average percentage change of all wave runs is shown. Vertical bars at each point represent standard deviation. Markers deviate slightly from ADV position axes for clarity. Shaded areas show ASG at full height $h_c$.

30% at all $z$ measurements. Deviations higher than 20% were also measured at $z_4 = 35.9$ cm at all $x$-positions for M1, and just over 20% at $z_1 = 3.3$ cm for M2 at positions 3 and 4. The reduction of $U_w^{\mathrm{rms}}$ along $x$ ranged from 2–17.5% and was more prominent directly behind the ASG mats. Increases in $U_w^{\mathrm{rms}}$ ranged from 0.5–11%, with the highest values ($\geq 10\%$) in the region above the meadow ($z_4, z_5$), which indicates an increase in velocity resulting from the presence of ASG. There was also an increase (7–7.7%) in the near-bed velocities within the gap between both ASG mats, i.e. positions 2 and 3, whereas with 1 mat, the same value (7%) was observed at position 3, but rather increasing from a reduction ($-15.6\%$) at position 2. With increasing distance behind the first mat, $U_w^{\mathrm{rms}}$ decreased again, regardless of mat configuration. However, the second mat enhanced this reduction, which was additionally accentuated by the proximity to the bed, with M2 reducing 10, 7.5, and 5.7% more than M1 for $z_1$, $z_2$, and $z_3$, respectively. This tendency to increase after the first mat and gradually reduce as waves go through the second mat was observed along the full transect for M2. For M1, the velocities sink directly behind the ASG mat and subsequently set up immediately afterward, a behavior that is only prominently observed within the canopy height. Above the canopy, the velocities for M1 remain on average relatively stable.

The flow attenuation parameter $\alpha_w$ is analogous to the percentage change shown in Figure 5.8, depicting the evolution of $\hat{U}_w^{\mathrm{rms}}$. Table 5.2 shows $\alpha_w$ calculated between positions 1 and 2. However, like $U_w^{\mathrm{rms}}$, $\alpha_w$ displayed variation along $x$. Increases in $\hat{U}_w^{\mathrm{rms}}(x)$ were recorded, which led to $\alpha_w > 1$, indicating flow enhancement instead of attenuation. The variability exhibited by the spread of the velocity data (Figure 5.8) and $\alpha_w$ indicates that the incident wave conditions greatly alter the velocity structure, especially since no vegetation parameters were modified during experimentation. To assess the effect of the hydrodynamic input parameters, $\alpha_w$ was calculated at each position along $x$ with respect to $\hat{U}_{\infty,w}^{\mathrm{rms}}$, subsequently plotting against the different instances of $H$, $T$, and $d$ separately (Figure 5.9). Within the uncertainties, the calculated values of $\alpha_w(x)$ generally did not show a clear trend toward gain or fall depending on the incident hydrodynamic parameters. An exception can be observed for the averaged values with the addition of a second
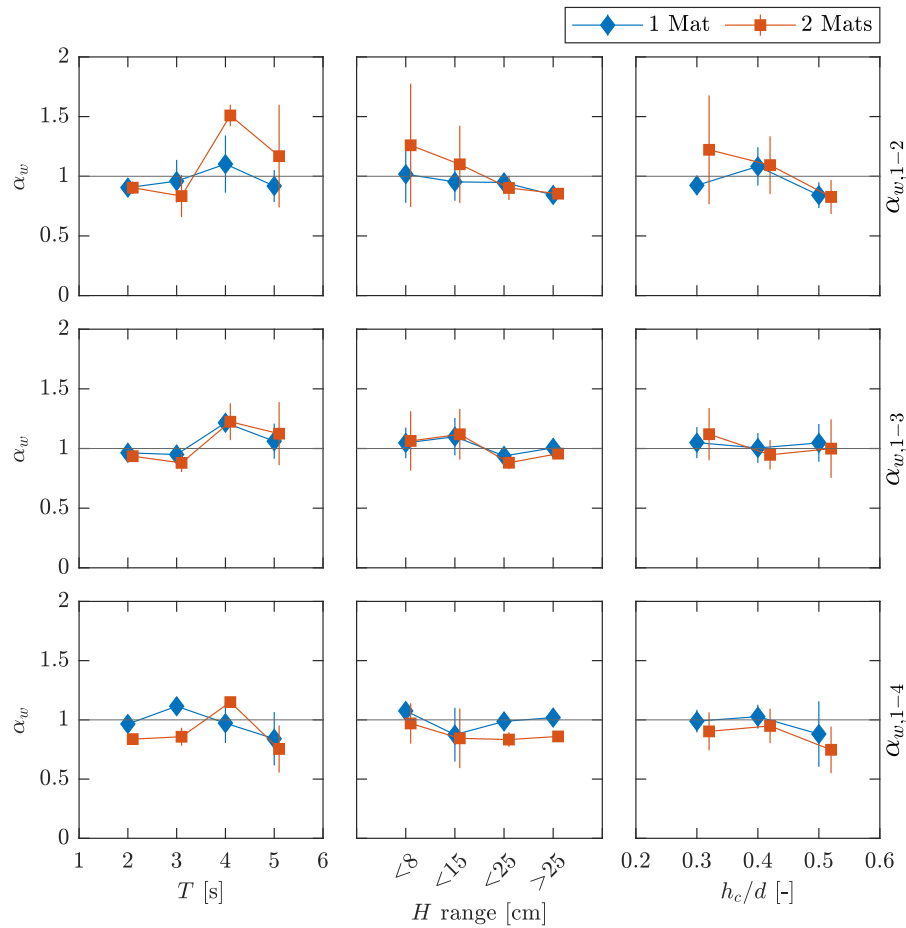
Figure 5.9: Variation of the flow attenuation parameter $\alpha_w$ depending on the hydrodynamic parameters and the position of measurement: wave height $H$, wave period $T$, and water depth $d$ shown in columns 1, 2, and 3, respectively. Position of $\alpha_w$ shown by rows (subscripts on the right indicate position). Deviation of measurement given by vertical bars. $H$ is shown for a range of measured wave heights.

mat, especially between positions 1 and 2. However, the second mat increased the uncertainties by up to 40%. Taking these averages, it can be seen that for the 2-mat configuration, $\alpha_w$ decreases with increasing $H$, going from 1.26±0.52 to 0.90±0.1 for waves >15 cm, indicating that higher waves, thus higher velocities, are more readily attenuated. Similar behavior to that described between $\beta$ and $d$ was observed between $\alpha_w$ and $d$, where, sorting by submergence ratio $h_c/d$, $\alpha_w$ increased from 0.83±0.14 for $h_c/d = 0.5$ to 1.22±0.46 for $h_c/d = 0.3$ (2 mats), denoting less attenuation for increased depths (i.e. decreased submergence ratio). The wave period, on the other hand, showed less attenuation, i.e. higher $\alpha_w$, as it increased, going from 0.90±0.05 for $T = 2$ s to 1.17±0.43 for $T = 5$ s. These tendencies were less reflected as the distance along $x$ increased, with the differences between 1 and 2 mats becoming less obvious.

**MODELED FLOW ATTENUATION**

Figure 5.10 shows the empirical values of $\alpha_w$ plotted against the ratio $A_\infty^{\text{rms}}/S$ along with the solution to the model in Equation 5.10. The wave conditions and vegetation characteristics trialed here led to a range of $A_\infty^{\text{rms}}$ from 3–22 cm for M0 and 3.2–20 cm for M1 and M2. With a constant shoot separation $S = 5$ cm, this resulted in the range of $A_\infty^{\text{rms}}/S$ of roughly 0.6–4. This range of $A_\infty^{\text{rms}}/S$
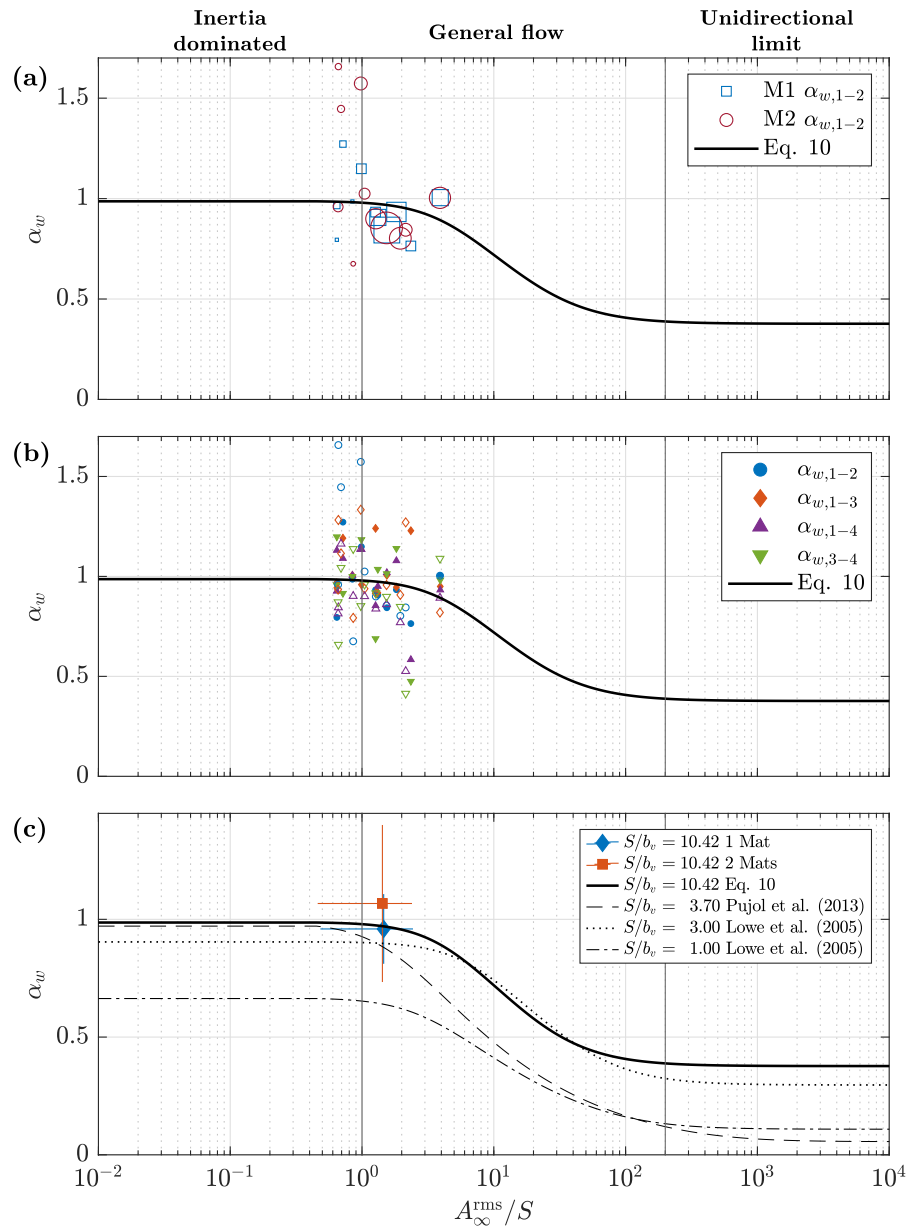
Figure 5.10: Canopy flow attenuation parameter $\alpha_w$ as a function of the ratio of wave orbital excursion and stem separation $A_\infty^{\mathrm{rms}}/S$. Solid line represents solution to Equation 5.10. (a) $\alpha_w$ between positions 1 and 2. Size of Markers qualitatively show the range of wave heights measured. (b) $\alpha_w$ at all positions (denoted by subscripts). Hollow markers represent 2-mat experiments. (c) Comparison of the solution to Equation 5.10 for different studies with varying plant characteristics. Mean and error of $\alpha_{w,1-2}$ shown for reference.

puts the conditions trialed here at the interface between the general flow and inertia-dominated regimes (Lowe et al., 2005a). The wide spread of $\alpha_w$ discussed above makes it obvious that the model (Equation 5.10) does not agree with a wide range of the conditions trialed here. Figure 5.10a shows $\alpha_w$ between positions 1 and 2 distinguished by the number of mats and the measured wave height, together with the solution to Equation 5.10. It can be seen that the model generally performs better for greater wave heights ($H > 0.15$ m), with lower wave heights both over and underpredicting $\alpha_w$. As before, this was accentuated for M2.

Figure 5.10b shows $\alpha_w$ at all positions. The differentiation between 1 and 2 mats reveals that

over and underprediction by the model is more likely to occur under the presence of a second mat, with only 36% of the M2 runs falling within $\pm 10\%$ of the modeled $\alpha_w$ compared to 55% for M1. Figure 5.10c shows the solution to Equation 5.10 from studies with different input hydrodynamic conditions and vegetation parameters for comparison with the present set of experiments. For reference, the average value of the set of wave runs for M1 and M2 are shown, where it can be observed that although the set of experiments agrees well with the model for the average (especially for 1 mat), the uncertainty is high for varying hydrodynamic conditions.

## 5.5 Discussion

### 5.5.1 *Wave Dynamics Around Flexible ASG Mats*

The velocity profiles showed the presence of a wave-induced current whose profile $U_c(z)$ was modified by the flexible ASG mats. For rigid surrogates, it has been shown how $U_c(z)$ shifts direction at canopy interfaces (i.e. canopy top and meadow edges, van Rooijen et al., 2020), while a return current, essential for nutrient circulation within the meadow, has been observed for flexible vegetation (Luhar et al., 2010). Here, these behaviors were only observed at certain interfaces, yet not as a common occurrence. Nonetheless, like previous studies (Pujol et al., 2013), the profiles of $U_c(z)$ around flexible vegetation are of similar form to non-vegetated conditions. This is because $N$ was too low to properly modify the wave-induced current, which easily penetrated into the canopy.

The control experiments showed that the measured wave decay encompassed energy loss not only due to vegetation but also static continuous losses, i.e. losses due to wall and bed friction. The choice of $H_0$ in Equation 5.1 is thus not inconsequential. Further, previous studies (Mendez and Losada, 2004; Luhar et al., 2010) emphasize the assumption that energy dissipation and the ensuing wave decay stem mostly from drag-induced forces caused by vegetation, whereby the current paradigm sets $H_0$ as the incident $H$ (leading edge of meadow). Hence, neither the non-vegetated wave height nor the effect of continuous losses along $x$ is taken into account. For comparison, $\beta$ calculated based on $H$ of the control experiments (M0) at each position (effectively removing continuous losses) ranged from 0–0.03 m$^{-1}$, or half the range presented above ($-0.01 < \beta < 0.06$ m$^{-1}$). Moreover, if we take $H_0$ as the incident $H$ of M0, $\beta$ ranges from -0.01–0.13, demonstrating an additional effect of the ASG compared to non-vegetated areas. These differences are particularly important when intending to apply empirical models developed under laboratory conditions to field applications.

With a low shoot density, a flexible base layer, and single-stem flexible shoots, the measurements indicate that a sparse, fully flexible canopy is able to dissipate energy. This in turn could promote seagrass growth (Carus et al., 2021). The degree of attenuation is clearly dependent on vegetation properties and incident hydrodynamic conditions and can vary greatly between set-ups. For example, Losada et al. (2016) obtained a range of $0.02 \leq \beta \leq 0.32$ m$^{-1}$ ($O(1)$ higher than this study) for experiments with circular patches of *S. anglica* and *P. maritima* of varying rigidity, whereby, compared to this study, density was up to 3 times higher, $h_c/d \geq 0.5$ (including emergent conditions), and $1.7 \leq T \leq 2.2$ s (see Table 5.A.1). Here, $\beta < 0$ for 3 wave runs (all with $T = 3$ s, Table 5.2), which result from $H/H_0 > 1$ at certain positions. Flow attenuation displayed a similar behavior ($\alpha_w > 1$), indicating increased flow around the meadows. The wave setup and enhanced

flow were certainly initiated by the obstructing structure, i.e. ASG, but could be boosted by mat motion. Furthermore, the interaction between the oscillatory flow and the meadow at position 1 could lead to an increase of $\hat{U}_w^{\mathrm{rms}}$ with respect to $\hat{U}_{\infty,w}^{\mathrm{rms}}$. Of course, this has not been observed as a common phenomenon in other experimental studies, which suggests that the increased mat flexibility and added mat motion may be responsible for the reduced attenuation.

Moreover, with measurements taken at canopy interfaces, the measured $U_w$ is affected by a vegetated side and a non-vegetated side. The effect of the bare side is particularly evident within the gap hydrodynamics, where, within the canopy height, in-gap measured velocities varied depending on whether a second mat was present further downstream. The evolution of $U_w^{\mathrm{rms}}/U_{\infty,w}^{\mathrm{rms}}$ shown in Figure 5.8 shows how, with one mat, the attenuation of flow was enhanced directly behind the mat, and velocities increase rapidly before steering toward a steadily attenuated flow downstream. With 2 mats, however, the first mat does not have the same attenuating effect per meter but rather presents a shift of the attenuated velocities toward the end of the second meadow. This suggests that the 2 mats behave as a single meadow, with the highest attenuation at the trailing edge. Furthermore, skimming flow becomes apparent at the canopy interfaces, gradually attenuating flow further down the wave propagation direction (Stratigaki et al., 2011). Savio et al. (2023) showed for aligned patches that skimming flow develops roughly at gap width equal to patch length, consistent with the measurements here. On the other hand, a similar study on gap hydrodynamics (El Allaoui et al., 2016) found that wave velocities were reduced after the first meadow and returned to pre-vegetated conditions for gaps longer than $2h_c$. This was not corroborated here (gap length: $8h_c$) as $U_w^{\mathrm{rms}}$ showed no attenuation within the gap, but further down the meadows.

Perhaps an interesting outcome to discuss with regard to wave decay and flow attenuation is the relationship between both. Figure 5.11 shows the relation between $H/H_0$ and $\hat{U}_w^{\mathrm{rms}}/\hat{U}_{\infty,w}^{\mathrm{rms}}$ for the complete set of experiments (all positions). A linear fit was done for the set of 66 points (4 outliers removed due to unlikelihood). Figure 5.11 shows that measurements with higher wave attenuation (i.e. lower $H/H_0$) yielded lower flow attenuation (higher $\alpha_w$), while higher flow attenuation resulted in lower wave attenuation. In general terms, this suggests that as velocities around the meadows are more actively reduced, wave heights are less reduced with respect to the incidence. This is consistent with Lowe et al. (2007), who found that the rate of wave dissipation increases with increasing flow through the meadow, i.e. higher $\alpha_w$. Therefore, as flow penetrates more readily into the meadow, wave heights are more actively reduced.

**EFFECT OF INCIDENT HYDRODYNAMIC CONDITIONS**

Studies have shown that wave energy dissipation can vary depending on the wave period (Paul and Amos, 2011), higher submergence ratios $h_c/d$ lead to higher wave attenuation (Losada et al., 2016; Stratigaki et al., 2011), and vegetation geometric characteristics (e.g. $\lambda_f, \lambda_p$) play an essential role (Paul et al., 2012). Here, other than the variation of $h_c/d$, the constant vegetation traits remained independent of the fluctuating hydrodynamics. The high variability exhibited by the results thus indicates that the hydrodynamic conditions greatly affect wave and flow attenuation. Previous studies have shown that the rate of energy dissipation is highly dependent on $T$ (Lowe et al., 2007; Bradley and Houser, 2009; Manca et al., 2012), with shorter wave periods yielding higher wave attenuation and longer periods higher in-canopy flow attenuation. The relationship between $H/H_0$
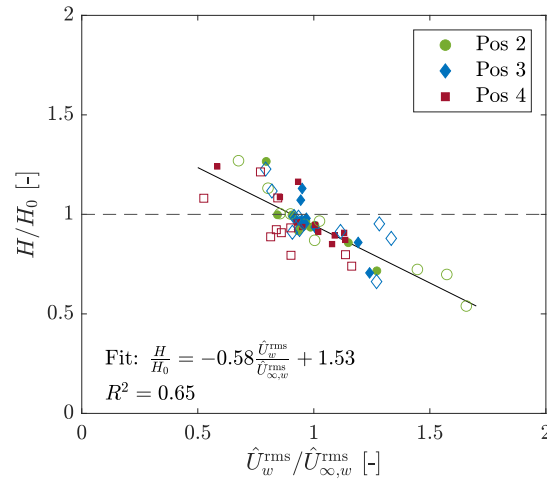
Figure 5.11: Relation between wave evolution $H/H_0$ and flow attenuation $\hat{U}_w^{\mathrm{rms}}/\hat{U}_{\infty,w}^{\mathrm{rms}}$ at all positions (Pos) relative to position 1. Hollow markers indicate 2-mat configuration. Solid line represents linear fit.

and $\alpha_w$ shown in Figure 5.11 corroborates this inverse behavior. However, as shown in Figure 5.9, for $T \geq 3$ s and $h_c/d \leq 0.4$, $\alpha_w$ was enhanced within the gap of the 2-mat configuration compared to the 1-mat configuration, suggesting that flow enhancement is a result of the gap. This was also reflected with $h_c/d$, where $\alpha_w$ decreased for increasing $h_c/d$ at position 2, indicating that flow within the gap becomes proportionally lower as the meadow takes more of the water column. Moreover, connecting $h_c/d$ and $T$, the measurements indicate that flow penetrates more easily into the canopy for longer wave periods as the submergence ratio decreases. The inconsistency within the results suggests that the effect of the gap on flow varies with $T$ and $h_c/d$. Lara et al. (2012) found that while turbulent diffusion was enhanced by heterogeneous meadows (i.e. with gaps), flow velocities were not enhanced by meadow patchiness. Moreover, Paul et al. (2012) argued that $\lambda_f$ and $\lambda_p$ are more important than a varying submergence ratio stemming from varying $d$, which, for $h_c/d \leq 0.4$, was also observed here. For storm conditions, Möller et al. (2014) found that marshes attenuated waves regardless of the variable water depth. In-depth gap hydrodynamic studies are necessary to couple the effect of the gap with interchanging submergence ratios and varying hydrodynamic conditions.

### 5.5.2 *Predictive Models of wave and flow attenuation*

The experiments demonstrated that the flexible ASG mats attenuate waves and flow similarly to conventional (fixed) meadows, i.e. behavior and parameter sensibility are established comparably. However, the attenuation magnitude was generally lower than predictive models would suggest, with uncertainties increasing as a function of incident hydrodynamic conditions. As analytical models are generally validated experimentally to support the range of empirical values obtained, most models are also sensitive to input variability. Recent wave attenuation models based on the original model (Dalrymple et al., 1984) thus further incorporate intrinsic conditions such as measured in-canopy flow and plant motion. van Veelen et al. (2021) extended the model to account for vegetation flexibility and motion by including blade excursion during wave loading; they validated it for regular waves with small $A_\infty$ over cylindrical, flexible, and near-stiff vegetation, and performed well applied to real salt marshes of different stiffness (*P. maritima,*

*S. anglica* and *E. athericus*). Further, following the findings of Lowe et al. (2007), Lei and Nepf (2019b) extended Equation 5.2 by factoring in flow attenuation, thus incorporating the effect of vegetation on in-canopy flow; they also incorporated $l_e$ to account for plant motion and consequent drag reduction (similar to Losada et al. 2016), obtaining a modified Equation 5.2 as $\beta = (2/9\pi)C_D b_v N k H_0 \alpha_w^3 (J_1/J_2)$, where $J_1 = 9\sinh(kl_e) + \sinh(3kl_e)$ and $J_2 = \sinh kd(\sinh(2kd) + 2kd)$. Modified forms of Equation 5.2 (Losada et al., 2016; Lei and Nepf, 2019b) yielded values of $\beta$ of the same order of magnitude as those observed here, while Equation 5.2 largely underestimated them (Figure 5.6). It is not surprising that the modified formulations improved the results; however, it is interesting to note that both approaches underestimated the damping coefficient for longer-period waves. With both models empirically validated for $T < 2$ s, it becomes clear that future models should focus on longer-period waves, as such conditions also lead to higher flow attenuation (Lowe et al., 2007) and are more likely to dominate field conditions (Koch et al., 2006; Bradley and Houser, 2009). Note that shorter wave periods lead to more flow through the canopy, leading to $\lim_{T\to 0} \alpha_w = 1$, which reduces the equation described above to Equation 5.2.

The measurements yielded a wide range of $\alpha_w$, suggesting that Equation 5.10 is not applicable to flexible ASG mats. However, it is important to remember that $\alpha_w$ measured here corresponds to the ratio at the edges of the meadows and not the in-canopy flow (measured through a clearing, Lowe et al. 2005a). Knowing this, it is expected to have higher values of $\alpha_w$ than in-canopy measurements would yield. However, as the results show, $\alpha_w$ was both over and underestimated by the model, depending on wave run and position. This leads us back to the sensitivity with regard to input conditions and the role of the gap in patch-to-patch hydrodynamics. Even though the results suggest that the model should not be used to determine the flow attenuation expected by similar flexible mats, the resulting average from the ensemble of measurements indicates that for a general range of conditions, the model can provide proper insight into the effect of the canopy. Special care should still be taken regarding gap hydrodynamics, which was shown to be unstable.

Model results proved to be sensitive to the choice of input parameters, such as $C_D$, $C_f$, and $C_M$, the characteristic lengths (e.g. $b_v$, $h_c$, and $l_e$), and the resulting dimensionless quantities describing flow patterns (e.g. $Re$ and $KC$). Table 5.A.1 lists several studies that have investigated different parameters, proposing ways to calculate them depending on target conditions. Ultimately, it is important to know how a model was validated to determine which parameters are more relevant and what input they need for their calculation. For the present experiments, canopy-integrated rms-velocities were used as the characteristic velocity. The use of in-canopy velocities provides an estimation of $C_D$ which better represents vegetation-induced drag as this may also vary along $z$. This is especially true for higher frequency conditions beyond the shallow water regime, as the oscillatory velocity becomes more sensitive to $z$ and the velocity at the canopy top may thus greatly differ from near-bed velocities. Note that rms-velocities are lower than the maximum velocity $U_w^{\max}$, meaning that dependent parameters will be proportionally lower. However, $U_w^{\max}$ does not dominate the range of velocities in a temporal scale within a given period (see Villanueva et al. 2022), especially as the frequency decreases. Thus, a better representation of the time-averaged $Re$ or $KC$ is given by the representative rms-velocity.

### 5.5.3 *Implications for Field Applications*

The conditions trialed corresponded to a wide range of wave heights, periods, and depths to mimic the wide range of conditions that can be found in the field (Koch et al., 2006). This yielded a high variability within the resulting attenuation coefficients (i.e. $\beta$ and $\alpha_w$) and associated parameters (e.g. $C_D$ and $Re$), making it difficult to assess the suitability of a single model to predict any specific effect that a field-deployed ASG mat may have on its surrounding hydrodynamics. The flexible nature of the discretely anchored mats provides higher freedom of movement (sway) than typically fixed meadows used for experimentation. For the tested mats under 2D wave excursion, Villanueva et al. (2022) showed how the forces on the anchors are effective in all 3 dimensions. Moreover, it is important to remember that field and laboratory conditions can differ greatly. Losses due to viscous dissipation from flume walls and reflection effects are not present in the field, whereas external factors such as organism interaction with the (artificial) vegetation and the spatiotemporal variability of the field conditions can render empirical models very limited in their application.

Nevertheless, the results showed that flexible ASG mats affect both wave evolution and the velocity structure along the water column, with predictive models yielding estimates adequate in magnitude for the average of a wide range of conditions. Insight into expected wave and flow attenuation can be obtained as long as flow-vegetation interaction is considered; i.e. plant flexibility and canopy-affected flow. Fragmented canopies, however, will affect the hydrodynamics and thus decrease model accuracy. While current models may provide helpful insight into the effect of single continuous meadows on local hydrodynamics, more research into the effect of fragmented canopies as well as the interaction with random waves and waves plus current should be investigated to provide more accurate predictions of the effect of mats deployed in the field on local hydrodynamics. Furthermore, mat sway should be measured in future experiments to incorporate its effect on the velocity structure in and around a meadow.

The attenuation of waves and oscillatory flow by the ASG mats indicates that they could help to promote seagrass growth. This is especially true for the 2-mat configuration, which showed increased attenuation and a single-meadow behavior when observing flow modulation. However, the enhanced gap hydrodynamics also suggest that shelter within the gap is reduced, hence settling of seedlings may be challenging. As measurements behind the second mat showed enhanced attenuation, this may be a phenomenon exclusive to the first gap (relative to the main wave propagation direction) for fragmented canopies with more than two patches. Moreover, as wave frequency decreases and flow tends to the uni-directional limit ($T \rightarrow \infty$, e.g. in tidal areas) shelter is provided in the wake of seagrass meadows (Chapter 2) so that the dominating wave conditions play an important role. Based on these results, we suggest that field experiments with artificial seagrass should employ mats that also allow for seagrass to grow within the ASG, not only aiming for in-gap growth based on wave shelter. Furthermore, for a wide range of conditions and single meadow interaction, results showed that the models can provide insight into the expected attenuation effects of the meadow, as long as uncertainties are also cross-examined and informed. Seagrass reestablishment efforts using ASG can thus be supported by existing flow-vegetation-interaction models by providing faithful magnitude projections of the effect of anchored mats in the field.

## 5.6 Conclusions

Experiments were carried out in a large-scale flume to test the effect of discretely anchored flexible mats of artificial seagrass (ASG) on wave evolution and flow structure. Such mats are intended to be deployed in the field to promote seagrass growth, sheltering seedlings from harsh conditions where otherwise they would not be able to thrive. To help design these mats, an accurate understanding of their effect on the surrounding hydrodynamics is needed.  For this purpose, 2x2-m mats were tested under varying hydrodynamic conditions. Furthermore, as several models of flow-vegetation interaction have been developed, the experiments aimed to test their suitability to predict the effect of the mats under varying hydrodynamic conditions.

The experiments showed that the flexible mats are generally able to attenuate waves and flow. This was enhanced when a second mat was added behind the first one, with a 2-m gap between them. The attenuation of flow and waves was higher behind the second mat. However, the presence of the second mat also induced flow enhancement within the gap between both mats. Further, it was found that less flow attenuation, i.e. more flow through the canopy, leads to increased wave height reduction. Models of flow-structure interaction were not able to capture the effect of the mats for the whole range of conditions. The models were unstable regarding gap hydrodynamics. however, for a wide range of conditions and single meadow interaction, the models can provide good insight into the expected attenuation effects of the meadow. More research on gap hydrodynamics and the effect of mat flexibility on flow structure is needed to determine their role in inconsistent model results.

# SUPPLEMENTARY MATERIAL

## 5.A  Studies of Wave-Vegetation Interaction

The evolution of research on wave-vegetation interaction focused on wave dynamics can be separated into studies dealing solely with wave attenuation and those focusing on the velocity structure. Originally, a Morison-based formula was used to calculate wave decay. This was related to the energy density of the waves and the loss of energy reflected wave decay (Dalrymple et al., 1984). The loss of energy was expressed exponentially through the imaginary wave number $k_i$ by relating the forces exerted by vegetation on flow. Linearization of this formulation led to the well-known damping coefficient $\beta$, used to calculate wave evolution as a function of the meadow length, i.e. wave decay. Wave decay is sometimes denoted as $K_v(x)$, where $K_v = 1/(1 + \beta x)$, and $x$ is the distance within the meadow following the direction of wave propagation.

With time, flow oscillation and its effect on aquatic vegetation, which is usually flexible, was considered (Asano et al., 1992). Sway was taken into account through the relative velocity between the plant and the surrounding instantaneous flow component. This reduced drag, and thus wave damping. Calibration through the drag coefficient $C_D$ thus began to vary. Chen et al. (2018) and Henry et al. (2015) provide a comprehensive overview and analysis of different $C_D$ formulations based on either $Re$ or $KC$. Furthermore, the characterization of $Re$ and $\beta$ using $l_e$ became important (Luhar et al., 2010; Losada et al., 2016), as reconfiguration modifies vegetation effects on flow. The considerations mentioned above are necessary to take into account plant traits to determine their effect on the velocity structure accurately.

Other studies focused on the changes in in-canopy velocities to describe vegetation-induced wave attenuation. Newer studies (e.g. Lei and Nepf, 2019b; Zhang et al., 2021) have incorporated separate drag calculations for the stem and blades of a plant shoot. Interaction among leaves has also been largely neglected. Zhang et al. (2021) include this from previous studies through a so-called sheltering coefficient.

Table 5.A.1 shows a summary of relevant studies, ordered chronologically, to show the differences between experimental capacities, hydrodynamic conditions trialed, vegetation characteristics, and the main focus of the studies.

Table 5.A.1: Summary of wave-vegetation interaction studies

| Study | Focus[b] | Exp. facility | Flume dim. ($l$[m]x$b$[m]) | Waves tested | Wave Height $H$[cm] | Wave Period $T$[s] | Flow vel.[c] [cms$^{-1}$] | Vegetation[d] | Shoot density [m$^{-2}$] | Water Depth $d$[m] | Patch dim. ($l$[m]x$b$[m]) | Canopy Height $h_c$[m] | Summary[a] |
|---|---|---|---|---|---|---|---|---|---|---|---|---|---|
| Asano et al. (1992)[e] | WD | flume | 27x0.5 | regular | 5.6–12 | 0.71–2 | - | Artificial Kelp (f) | 1100/1490 | 0.45/0.52 | 8x0.5 | 0.25 | $C_D = O(1)$, calib. based on $k_i$, $u_r$ |
| Fonseca and Cahalan (1992) | WD | flume | 6.10x0.23 | regular | 1–20 | 0.6–3 | - | live(4 species) | 750–2870[g] | 0.06–0.19[g] | 1x0.23 | 0.17–0.41[g] | %-change of $E_w(x)$ as $f(d)$. Up to 40% reduction from seagrass |
| Dubi (1995) | WD | flume | 33x1 | regular + random | 4.5–17 | 1.26–4.42 | - | artificial (f) *L. hyperborea* | 1200 | 0.4–1 | 9.3x0.5[h] | 0.2 | $k_i$ governed by $T$, sensitive to $d$, $N$ |
| Méndez et al. (1999)[e] | VS/ WD | flume | see [e] | regular + random | see [e] | see [e] | - | artificial kelp (f) | see [e] | see [e] | see [e] | see [e] | $Re$-based $C_D$ for sway/no sway (Eq. 5.3). Reflection significant. $H/H_0$ func. of drag forces, veg. parameters |
| Mendez and Losada (2004)[e] | WD | flume | see [e] | random, breaking + non-breaking + shoaling | see [e] | see [e] | - | artificial kelp (f) | see [e] | see [e] | see [e] | see [e] | $\beta$ model: $KC$-based $C_D$ (form: $C_D = exp(n_1 KC_{l_r})/KC_{l_r}^{n_2}$, $KC_{l_r} = KC$ factored by $l_r$. No sway/reflection) |
| Lowe et al. (2005a) | VS | flume | 12x1.2 | regular | - | 1–3 | 2–5.3 | cylinders (r) | 100/ 44/25 | 0.43 | 1.8x1.2 | 0.1 | $\alpha_w$ decreases with increasing $A_\infty$ |
| Lowe et al. (2007) | VS/ WD | field | - | random | - | 2–25 (7.8 peak) | - | cylinders (r) | 64 | 1.5–1.8 | 2.4x1.2 | 0.1 | $\varepsilon = f(A_\infty)$, increases with increasing $\alpha_w$. $C_D$ scales as $C_D \lambda_f \alpha_w^3$ |
| Bradley and Houser (2009) | WD | field | - | random | 7–9 | ~1–100 (0<freq[Hz]<1) | - | live *T. testudinum* | 1100 | 1 | 43.3xInf | 0.25– 0.30 | $k_i = f(T, E)$. New $C_D$ based on $Re$ (Eq. 5.3), $KC$ (form $C_D = n_1 KC^{n_2}$) |
| Luhar et al. (2010) | VS | flume | 24x0.38 | regular | 1.6–10.6 | 0.9–2 | - | artificial (f) *Z. marina* | 300–1800 | 0.16–0.39 | 5x0.38 | 0.13 | mean current within canopy $f(A_\infty, x)$, attenuation characterized by $\alpha_w$ |

Table 5.A.1 Summary of wave-vegetation interaction studies (continued)

| Study | Focus[b] | Exp. facility | Flume dim. ($l$[m]x$b$[m]) | Waves tested | Wave Height $H$[cm] | Wave Period $T$[s] | Flow vel.[c] [cms$^{-1}$] | Vegetation[d] | Shoot density [m$^{-2}$] | Water Depth $d$[m] | Patch dim. ($l$[m]x$b$[m]) | Canopy Height $h_c$[m] | Summary[a] |
|---|---|---|---|---|---|---|---|---|---|---|---|---|---|
| Stratigaki et al. (2011) | VS/ WD | flume | 100x3 | regular | 39–43 | 2.3/3/ 3.5/4 | - | artificial (f) *P. oceanica* | 180/360 | 1.10/1.30/ 1.70 | 10.7x3 | 0.55 | measured $H(x)/H_0$. Higher N, $h_c/d$ = higher $H$ reduction. $u$ increases at canopy top |
| Paul et al. (2012) | WD | race-track flume | 17.55x0.6 | regular + current | 10 | 1 | 10 | artificial (f,r) *Z. noltii* | 500–8000 | 0.3 | 3x0.6 | 0.10/ 0.15/ 0.30 | measured $H(x)/H_0$ varying $h_c$, N, EI. Wave attenuation is $f(\lambda_f, \lambda_p, N)$. Current reduces wave attenuation |
| Pujol et al. (2013) | VS | flume | 6x0.5 | regular | - | 0.714/ 1/1.25 | - | cylinders (r), artif. (f) *P. Oceanica* | 128/640/ 1280 | 0.3 | 2.5x0.5 | 0.14 | Vel. attenuation characterized by $\alpha_w$. Vel. profile, wave-induced current dependent on $h_c/d$ |
| Möller et al. (2014) | WD | flume | 300x5 | regular + random | 0.1–0.9 | 1.5–6.2 | - | real *Puccinellia, Elymus* | 1225 | 2 | 39.44x5 | 220/ 700[g] | Re-based $C_D$ formulation (Eq. 5.3) for regular, random waves |
| Hu et al. (2014) | WD | flume | 40x0.8 | regular + current | 4–20 | 1–2.5 | 0–30 | wooden rods (r) | 62/ 139/ 556 | 0.25/ 0.5 | 6x0.8 | 0.36 | Re-based $C_D$ for combined waves+current fitted from $\beta$. $U_c/U_w$ determine decay contribution of current |
| Ozeren et al. (2014) | WD | flume | 20.6x0.69 | regular + random | 3–15 | 0.7–2 | - | birch dowel (r), foam-cords (f) and real (2 species) | 156/ 350/ 623/ 545/ 2857 | 0.5–0.7 | 3.66 | 0.48– 1.03 | $C_D$ calc. based on exp. fitted $\beta$. Re, KC-based $C_D$ formulations given (Eq. 5.3) |
| Losada et al. (2016)[f] | WD | 3D wave basin | 30x44 | regular + random + current | 12–20 | 1.2–2.2 | 30 | live *P. maritima* and *S. anglica* | 430 (*S.a.*)/ 877–1389 (*P.m.*) | 0.4/ 0.6 | 6[j] | 0.28/ 0.47 | Re-based formulation of $C_D$ (Eq. 5.3) for varying wave+current conditions |
| El Allaoui et al. (2016) | VS | flume | 6x0.5 | regular | - | 0.833 | - | PE (f) | 320/1280 | 0.3 | 0.84x0.5[i] | 0.14 | $U_w$, $U'$ increase within gap, reduce for gap width $< 2h_c$ with N found to be important for shelter |

Table 5.A.1 Summary of wave-vegetation interaction studies (continued)

| Study | Focus[b] | Exp. facility | Flume dim. ($l$[m]x$b$[m]) | Waves tested | Wave Height $H$[cm] | Wave Period $T$[s] | Flow vel.[c] [cms$^{-1}$] | Vegetation[d] | Shoot density [m$^{-2}$] | Water Depth $d$[m] | Patch dim. ($l$[m]x$b$[m]) | Canopy Height $h_c$[m] | Summary[a] |
|---|---|---|---|---|---|---|---|---|---|---|---|---|---|
| Luhar et al. (2017) | WD | flume | 24x0.38 | regular | 1.8–11.2 | 0.8–2 | - | PE (f) around 2-cm dowel | 300-1800 | 0.16–0.39 | 0.5x0.38 | 0.13 | $\beta$ better predicted by $l_e$, which depends on $CaL$. Link used to calculate ratio of bare bed and vegetated $H$ |
| Abdolahpour et al. (2018) | VS | flume | 50x1.2 | regular | - | 5–9 | - | birch dowels (r), artif. (f) *P. australis* | 400–3000 | 0.76 | 3–9x1.2 | 0.15/ 0.3 | Vertical mixing quantified. Flexibility decreases shear, thus mixing, but increases wake velocities |
| Zhang et al. (2018) | VS | flume | 24x0.38 | regular | 2–8.4 | 1/ 2 | - | artificial (f) *Z. marina* and *V. americana* | 280/ 600/ 820/ 1370 | 0.4–0.45 | 2/7x0.38 | 0.14 | $TKE$ is dependent on $A_\infty$ and $S$, can be proportionally linked to $\Delta E$ (formulation proposed) |
| Chen et al. (2018)[k] | WD | flume | see[e] | regular + current | see[e] | see[e] | see[e] | wooden rods (r) | see[e] | see[e] | see[e] | see[e] | Obtaining $C_D$ from force measurements vs. calibration through $\beta$. $KC$-based formulation of $C_D$ (form $C_D = n_1 KC^{n_2} + n_3$). |
| Lei and Nepf (2019b) | WD | flume | 24x0.38 | regular | 1.6–10 | 1/ 1.4/ 2 | - | low-density PE (f) ($t_v$ varies) | single blade + 280–1370 | 0.28 | 5x0.38 | 0.03/ 0.05/ 0.1/ 0.15 | $\beta$ calibration based on $l_e$ scaling law (obtained from single blade exp.), good agreement for range of lab, field applications |
| van Veelen et al. (2020) | VS/ WD | flume | 30.7x0.8 | regular | 10–20 | 1.4–2 | - | bamboo dowel (r) and silicon (f) | 1111 | 0.3–0.6 | 1.5x0.8 | 0.30 | $KC$-based $C_D$ from fitted $\beta$ (form $C_D = (n_1/KC)^{n_2} + n_3$), improved using in-canopy velocities |

Table 5.A.1 Summary of wave-vegetation interaction studies (continued)

| Study | Focus[b] | Exp. facility | Flume dim. ($l$[m]x$b$[m]) | Waves tested | Wave Height $H$[cm] | Wave Period $T$[s] | Flow vel.[c] [cms$^{-1}$] | Vegetation[d] | Shoot density [m$^{-2}$] | Water Depth $d$[m] | Patch dim. ($l$[m]x$b$[m]) | Canopy Height $h_c$[m] | Summary[a] |
|---|---|---|---|---|---|---|---|---|---|---|---|---|---|
| van Rooijen et al. (2020) | VS | flume | 35x1.2 | regular | 9–21 | 2–5 | - | dowels (r) | 3100 | 0.75 | 2.5x1.2 | 0.30 | force-derived $C_D$ applied to develop numerical model of vertical distribution of $U_i$ in and above canopy |
| Zhang et al. (2021) | WD | flume | 24x0.38 | regular | 2–8.2 | 1.1/ 1.4/ 2 | - | artif. *S. alterniflora* (f) | 280 | 0.18–0.45 | 4x0.38 | 0.30 | validation of modified $\beta$ based on scaling law $CaL$ to account for differing morphological characteristics of single shoots |
| Schaefer and Nepf (2022) | WD | flume | 24x0.38 | regular | 0(pure current)–8.2 | 2 | 2.7–10 | artif. *Z. marina* low-density PE (f) | 950 | 0.27/ 0.45 | 6.1x0.38 | 0.136 | new $\beta$ formulation for wave-current conditions based on $l_e$. $l_e$ function of in-canopy velocity $U_1$ ($\neq U_c$) |

[a]refers to main outcome and approach taken, with $E_w$=energy density; $\varepsilon$=rate of energy dissipation (calculated based on forces); $k_i$=exponential decay coefficient; $\beta$=damping coefficient based on the linearized height evolution $H/H_0$; $\alpha_w$=in-canopy flow attenuation based on the canopy flow formulation (Equation 5.10); $A_\infty$= wave excursion; $u_r$=relative velocity between plants and flow; $l_r$=reconfigured length due to flow; $TKE$=Turbulent Kinetic Energy. Other variables found in text/nomenclature. [b]VS: Velocity Structure; WD: Wave Decay [c]for experiments with waves plus current [d](f): flexible, (r): rigid, PE=Polyethylene [e]experimental data from Asano et al. (1988) for regular and Dubi (1995) for irregular [f]details on experimental set-up in Lara et al. (2016) and Maza et al. (2015) [g]species dependent [h]flume partitioned [i]with cross-sectional gaps [j]circular patch of vegetation [k]experimental data from Hu et al. (2014)

*5*

### Chapter highlights

- Orbital velocities around ASG mats were reduced by up to 16%. Although this reduction is clearly lower than for unidirectional currents (see Chapter 2), enhanced mixing may be beneficial for growing vegetation with regard to nutrient disposition.

- The presence of the second mat reduced orbital velocities more than when a single 2-by-2-m-mat was present.

- Velocities within the gap were enhanced, as were the velocities above the meadows, rendering the space within the meadows the most sheltered under oscillatory flow conditions.

- Flow-structure interaction models can provide an idea of flow attenuation within the ASG based on plant mechanical properties. Nonetheless, the flexible mats and the gap between them increased uncertainties greatly, so the use of these models is not an advisable benchmark for flexible mat performance.

- The ASG mats enhanced wave decay, especially with 2 mats present. However, current wave decay models overestimate wave decay for these fully flexible mats, especially for higher frequency (shorter wave periods) waves.

# GENERAL DISCUSSION & CONCLUSIONS

# 6.1 Preamble

The main objective of this thesis was to gain insight into how artificial seagrass (ASG) behaves under marine conditions and what its effect on local hydrodynamics is. The gained knowledge from literature was experimentally tested to assess the performance of ASG as a method for shelter facilitation to promote seagrass growth and support restoration projects.

To this purpose, on-shore fluid dynamics, i.e. in coastal areas, were reviewed and the interaction between submerged structures and said dynamics was analyzed. Flow-vegetation interaction was considered regarding both unidirectional and oscillatory flow –currents and waves, respectively. The conditions arising from this interaction were then put into the context of seagrass survival and restoration facilitation. Here, the use of flexible materials increased the complexity of the experimental procedures and analyses described in the previous chapters. Ultimately, flexible mats of ASG were proposed and tested under controlled conditions to kick-start the development of alternative seagrass restoration techniques. These techniques can assist scientists and engineers in the further development of sustainable solutions, and support practitioners with the implementation of innovative ways toward successful seagrass restoration.

Section 6.1.1 provides a summarized overview of the main findings of the experiments. This summary can be utilized as a starting point for scientists, engineers, or end-users working in the field, who wish to understand and further study flow-vegetation interaction, replicate and expand the experiments, or start field trials. Section 6.2 then goes into detail regarding the results of the experiments presented above and their interpretation with respect to flow-vegetation interaction. Further, the results are put into the context of ASG design. Finally, Section 6.3 presents some recommendations based on the findings, as well as some shortcomings of this work to be considered when planning further investigation.

### 6.1.1 *Summary for practitioners*

The laboratory experiments yielded results that can be used in field experiments to assess the performance of ASG. The results presented in Chapters 2–5 are subject to the boundary conditions trialed in each set of experiments. This means that the results cannot be generalized. Instead, they should be expanded and combined with a wider range of boundary conditions before a paradigm that can lead to concrete guidelines can be conceived. Nonetheless, for the range of conditions trialed here, the results present a sound starting point for field applications with ASG of similar composition. In general, hydraulic experiments with artificial seagrass (ASG) will depend on the input parameters, which include on the one side the hydraulic boundary conditions (e.g. water depth and wave and flow characteristics), and on the other hand the mechanical and geometric properties of the submerged structure. When dealing with submerged vegetation, their geometric characteristics will represent the spatial obstacle affecting flow, while the mechanical properties will dictate the restoring forces which will directly affect attenuation and energy loss. Figure 6.1.1 shows a simplified overview of the input and output parameters that need to be considered for experimentation and modeling. The dimensionless hydrodynamic coefficients are a result of the input conditions and will in turn affect the output. This means that they directly affect the resulting surrounding hydrodynamics. Furthermore, being dimensionless parameters, they can
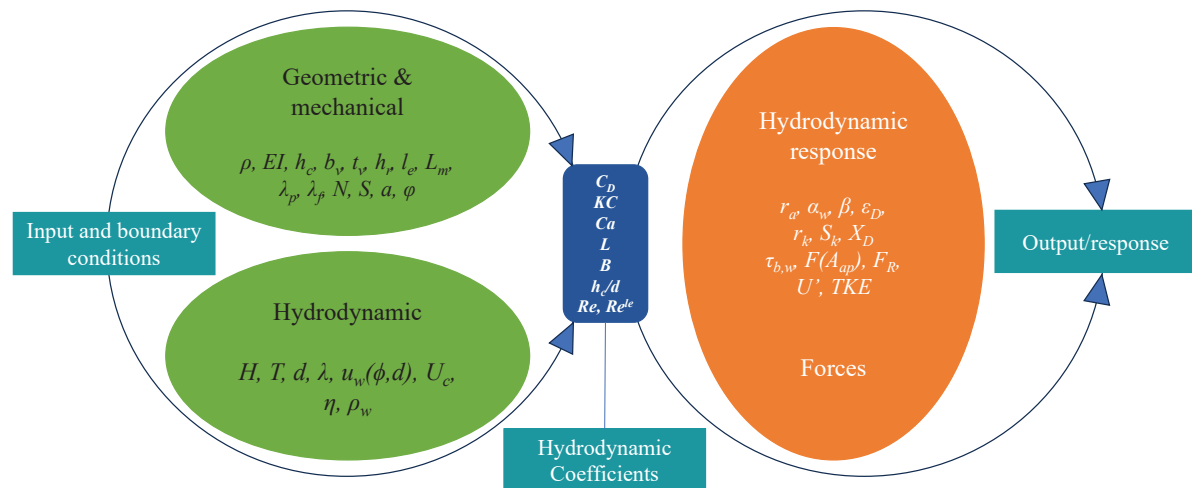
Figure 6.1.1: Input and output parameters and the intrinsic hydrodynamic coefficients that govern flow-vegetation interaction.

**6**

better characterize a wide range of input, and therefore output, conditions, turning them into the governing parameters of flow-vegetation interaction.

To aid in the conception of new experiments based on the results presented in this thesis (Chapters 2, 4, and 5), the most relevant input conditions and resulting hydrodynamic coefficients are summarized in Table 6.1.1. The range of values that were trialed are given for reference for future trials and should help to choose the desired initial conditions. These can be either used to start planning further flume or field experiments of similar conditions or to look for complementary conditions to expand the results found here.

Note that the main difference between the experiments described here lied on the ASG chosen. While the results on unidirectional flow refer to an extremely flexible ASG (flexural rigidity $EI$ = 0.075 N mm$^2$), the oscillatory flow experiments apply to a much stiffer ASG of $EI$ = 800 N mm$^2$. Despite this difference, the more flexible ASG proved to be effective in attenuating flow and thus providing shelter for prospective seedlings. Table 6.1.2 shows a summary of the main parameters that reflect the attenuating effect of the ASG under unidirectional and oscillatory flow. The flexible ASG was able to reduce flow by up to 70% ($r_a$) under unidirectional conditions. Under oscillatory flow, ASG had a less pronounced effect on flow attenuation in the immediate wake of the meadow (up to 16%). However, with mixing being an important part of nutrient cycling (Luhar et al., 2010), one does not aim for extreme attenuation within the context of restoration. It is also important to note the effect of flow development ($X_D$), which will dictate the minimum length a meadow should have to provide maximum attenuation. With the effect of the meadow seen at more than 100 times the reconfigured canopy height $h_r$, it is safe to say that, under unidirectional flow, ASG has a marked impact on the wake flow. A 90% come-back to non-vegetated conditions can be expected up to 18 times the canopy height $h_c$, whereby shelter can reach >10 times the $h_c$ for thresholds velocities of 20 cm s$^{-1}$. Further, under oscillatory flow conditions, the attenuation of in-canopy flow and wave height provided by the single-stem ASG also proves that effective, easy-to-produce-and-deploy

Table 6.1.1: Range of input and boundary conditions trialed in the experiments presented in Chapters 2, 4, and 5 as well as the range of resulting hydrodynamic coefficients.

| Parameter | | uni-directional flow range | Oscillatory flow range |
|---|---|---|---|
| $C_D$ | [-] | 1.08–1.6 | 1.95–2.95 |
| $Re_{\text{channel}}$ | [-] | 57500–115000 | - |
| $Re$ | [-] | 70–300 | 200–1200 |
| $Ca$ | [-] | $\leq 0.1$ | 0.13–24.9 |
| $KC$ | [-] | - | 40–400 |
| $u_0$ | [m s$^{-1}$] | 0.01–0.60 | 0.07–0.46 |
| $d$ | [m] | 0.4 | 0.5–0.83 |
| $L_m$ | [m] | [1,2,3] | [1,2] with gap |
| $N$ | [shoots m$^{-2}$] | 390 | 400 |
| $a$ | [m$^{-1}$] | 2 | 1.92 |
| $h_c$ | [m] | 0.2 | 0.25 |
| $EI$ | [N mm$^2$] | 0.075 | 800 |
| $X_D$ | [m] | 0.88–0.98 | - |

ASG mats can be developed. Ultimately, for further experiments, the ranges of the hydrodynamic coefficients ($C_D, Re, KC$, etc.) can be replicated for a myriad of hydrodynamic conditions to improve the models shown here.

Ultimately, field experiments will introduce a higher non-linearity to the models, which may produce conflicting results. Moreover, further input conditions caused by extreme weather conditions and extrinsic factors such as epiphytes may affect the hydrodynamic interaction greatly. For example, it has been found recently that the epiphytic content of the seagrass correlates directly with sediment capture, which is also a source of nutrients for this precious ecosystem (Barcelona et al., 2023). The design of ASG mats for restoration should include these factors, based on sound field experimentation, to develop solutions for better success. An interdisciplinary workflow is also needed, where the experience of ecologists regarding the few successful seagrass restoration projects (e.g. Orth et al., 2020) is coupled with ASG mat design. To assist future restoration projects, the following sections provide a more detailed summary of the results of the experiments presented

Table 6.1.2: Summary of the observed effect of the parameters presented in Table 6.1.1.

| Parameter | | Range | flow condition | Comment |
|---|---|---|---|---|
| $r_a$ | [%] | 47–75 | unidirectional | negligible change between 2 and 3 m o f meadow |
| $\Delta r_a(L_m = [1,2])$ | [%] | 16–26 | unidirectional | |
| $\Delta r_a(L_m = [2,3])$ | [%] | 1.6–8 | unidirectional | |
| $R_{k,90}$ | [m] | 16–18$h_c$ | unidirectional | regardless of flow velocity, except for 60 cm s$^{-1}$ at $L_m = 1$ m |
| $S_{k,20}$ | [m] | 10.43–12.20$h_c$ | unidirectional | for $u_0 = 30$ cm s$^{-1}$ |
| | [m] | 2.50–3.28$h_c$ | unidirectional | for $u_0 = 45$ cm s$^{-1}$ |
| | [m] | 1.08–1.28$h_c$ | unidirectional | for $u_0 = 60$ cm s$^{-1}$ |
| $F_R$ | [N] | $\leq 60$ | oscillatory | for velocities $\leq 40$ cm s$^{-1}$ |
| $r_a$ | [%] | 0–24 | oscillatory | represented by $\alpha_w$ |
| $\beta$ | [m$^{-1}$] | $\leq 0.06$ | oscillatory | |

here and recommendations for ASG mat design based on these results.

## 6.2 Artificial Seagrass for Restoration

The use of ASG for restoration has been motivated in Chapter 1, along with open questions about its performance and suitability. Here, performance and suitability were derived from laboratory experiments. Note that, although laboratory experiments are economically and time-wise more feasible than field experiments, they are still complex and time-consuming. This is especially true for the prototype-scale experiments shown here, which led to limitations regarding measurement resolution and the variation of parameters such as vegetation areal density and meadow materials. This means that results cannot be generalized for all seagrass species and more research is needed to achieve this. Nevertheless, the experiments yielded high-quality data that led to valuable quantitative interpretations of the performance of ASG mats under various flow conditions. The focus here was then to assess the ASG mat performance through: a) its mechanical response to hydrodynamics; and b) its effect on its surrounding hydrodynamic environment. The former is important for mat design (see Section 6.2.2) while the latter dictates how effective a mat can be for restoration purposes.

Within the context of restoration, *shelter* is the keyword, as it is the target ecosystem service that ASG should provide to facilitate natural seagrass regrowth. Based on the effect of the different materials, meadow morphology, and incident hydrodynamic conditions tested, the potential of ASG can be brought to the spotlight as a possible restoration solution. Successful sheltering results in re-population by natural seagrass, which in turn will enhance the existing services of ASG and expand on them. For example, seagrasses provide shelter not only through their leaf cover but also through escarpment formation when they erode and expose the peat beneath (Serrano et al., 2023); they also adapt to the local conditions and stabilize sediment more efficiently through their rhizomes (Barbier et al., 2011). Nonetheless, shelter will also depend on the local predominant conditions. Under uni-directional currents, flow attenuation was observed to be up to 70%, whereas, under pure wave conditions, only 16% of the peak velocity was reduced. However, even though oscillatory flow reduction is clearly lower than for unidirectional currents, enhanced mixing may be beneficial for growing vegetation with regard to nutrient disposition (Thomas and Cornelisen, 2003; Lowe et al., 2005b). Moreover, enhanced mixing can also be seen within the water column along the wake of an ASG meadow under current-dominated conditions (see Chapter 2), which may also benefit adjacent ecosystems. For these reasons, site selection for ASG deployment is of extreme importance (see Section 6.2.2). This also concerns the re-established meadows as seagrasses adapt to their surroundings and the ecosystem services they provide can vary depending on the local conditions (Hardison et al., 2023).

It is important to remember that the definition of shelter is still rather subjective. The thresholds shown here cover a wide variety of literature-based values for different species (see Koch et al., 2010), but ultimately, shelter will depend on the ability of the ASG meadow to attenuate flow under current-dominated conditions, and dissipate energy under wave-dominated ones. Here, the shelter distance considering a threshold for survival of 20 cm s$^{-1}$ can be more than 10 times the canopy height for velocities up to 30 cm s$^{-1}$; however, higher velocities may reduce this distance to just

above twice the canopy height. Reconfiguration then becomes another key term, which depends on the mechanical properties of the material selected. Shoot reconfiguration will determine the position of the shear layer created above the canopy interface, which will in turn determine the distance from the bed where we can consider shelter is being provided by the meadow. The shelter distance (in *x*) and the shelter height (in *z*) thence create the shelter area behind any given ASG meadow and corresponds to the area where seedlings can grow and the meadow can re-establish. Reconfiguration has even been shown to control the carbon absorption rates of seagrass meadows along with patch size relative to the width of the test section (Matsumura et al., 2022). However, the effects of the patch size still need more research, as flume dimensions usually introduce limitations that can only be overcome through field trials.

Patch size research will become even more important when beginning field trials as the boundary conditions predominant in wave and current flumes are not present anymore. Likewise, patchiness and its potential benefits and deficiencies will determine the most efficient patch size and distribution. Flume experiments show that low-density patches enhance nutrient uptake (high-density ones drive transport out of the meadow) (Adhitya et al., 2014) and that staggered patch configurations will further enhance hydrodynamic resistance (Savio et al., 2023). These results advocate the use of the checkerboard configuration proposed in Chapter 1 (see also Carus et al., 2021), whereby gap hydrodynamics also take a lead role which needs to be further researched. The results discussed in Chapter 5 showed that the presence of a second mat may reduce the overall near-bed velocities, but the velocities within the gap are still higher than those immediately adjacent to the meadows. This renders the area *within* the meadows as the most suitable for seagrass regrowth. This is of course true for wave-dominated conditions, as unidirectional flow conditions showed enhanced shelter along the wake. Note, however, that tidal flow means that sheltered wake areas will alternate back and forth in symphony with the tidal frequency. This again supports the use of several patches in a staggered configuration, creating protected wakes in all directions. Finally, for in-canopy shelter, it is important to note that the swaying motion of the mat may inhibit seagrass fixation, for which reason base layer design and anchoring play an important role under purely wave-dominated conditions (see Section 6.2.3).

### 6.2.1 *Fluid-Structure Interaction*

The results of the experiments described here portray a clear image of the sensibility of known models to the mechanical and geometric properties of (artificial) seagrass meadows. Depending on the target location, marine conditions may differ greatly, from mainly unidirectional flow to purely oscillatory flow. It is important to know how the ASG will behave under both possible predominant conditions. In addition, the effects of the geometric and mechanical properties of the seagrass meadows are equally important. As shown here, meadow characteristics such as meadow length and plant geometry affect the local hydrodynamics. Moreover, density has been shown to influence erosion and organic carbon concentration based on the incident hydrodynamics (Egea et al., 2023). The cited study demonstrated that erosion led to a release of dissolved organic carbon regardless of the predominant conditions (unidirectional or oscillatory flow).

The co-dependent study of Taphorn et al. (2021) showed how, apart from the incident

hydrodynamic conditions, the attenuating effect of different materials on flow is determined mainly by the modulus of elasticity (affecting the flexural rigidity), the buoyancy and the cross-sectional dimension. For vegetation (or any submerged flexible artificial structure intended to resemble aquatic vegetation), the geometry is rarely constant or symmetrical. Stems and leaves differ in mechanical composition and thus also their response to flow (Paul et al., 2014). Wider vegetation will have a greater area of resistance, which will affect the velocity structure near the bed. However, the penetration depth of the logarithmic velocity profile (as in non-vegetated conditions) will depend on the rigidity and not on its perpendicular breadth. Therefore, effects along the water column will be correlated to the length of the vegetation and their rigidity. For vegetation with wide leaves above a more rigid stem, flow attenuation will be poor due to streamlining of the leaves, and preferential flow pathways both above the canopy and near the bed will form.

With aquatic vegetation, be it artificial or natural, we not only have a single blade or stem but also a conglomerate of shoots that make up the meadow. Therefore, it is important to take the effect of the full meadow into consideration. The width of the meadow was not varied here and is considered infinite. The length along the main flow direction was varied to observe its effects on the flow structure. In addition, the submergence ratio of the meadow may also affect flow, as described in Chapter 5. Koken and Constantinescu (2023) showed how, although the adjustment length did not change with varying submergence ratios, the flow structure was affected greatly, with drag force even decreasing at the leading edge for increasing submergence ratios. From the experiments shown here, the flow structure was generally different for unidirectional and oscillatory flow. Both flow types are thus discussed separately below.

### UNIDIRECTIONAL FLOW

The length of the meadow in $x$ proved to be an important parameter just within the first 2 m relative to the main flow direction. Within this distance, a reduction of up to 70% of the flow velocity could be measured, meaning that even a low shoot density and highly flexible ASG can attenuate flow to a great extent. This was true regardless of the plant geometry and incident conditions, which can be attributed to the development length within the meadow (Chen et al., 2013). This means that, for meadows longer than about 2 m, the attenuation of flow and the velocity profile can be expected to be relatively constant. This also means that the wake structure immediately behind a meadow will not differ greatly in relation to the meadow length.

When analyzing the wake further from a meadow, the effect of the meadow on flow can be measured for a distance a full order of magnitude higher than the blade length of the ASG. The effect can be characterized by the magnitude of the changes in velocity compared to upstream conditions. Here, flow velocity takes a more important role, such that the velocity reduction behind any given meadow will be inversely proportional to the incident velocity. This can be defined in terms of shelter distance if a reference threshold value is selected and will determine the shelter capacity of a meadow with respect to a given seagrass species (see below).

Moreover, the ASG increases turbidity and onsets vertical mixing. Though this has been shown within a submerged meadow (Abdolahpour et al., 2018), the experiments shown here exhibited mixing along the wake as well. This is clearly discernible through an upward trend of the form of the velocity profile and the turbulence distribution. We hypothesized that this effect spreads through

the full water column, though we were not able to measure near-surface velocities, so this could not be corroborated.

**OSCILLATORY FLOW**

Oscillatory flow generates a different synergy with aquatic vegetation, as drag forces on the leaves become mainly 2-dimensional. Under oscillatory flow, flow penetrates more easily into the canopy than under unidirectional flow conditions (Lowe et al., 2005a). This in turn means that mass transport within the meadow is of higher magnitude. Furthermore, mass transport occurs with net positive bias in the direction of wave propagation (Longuet-Higgins, 1953), so loads, erosion, and nutrient transport will be of more significance in this direction.

Orbital velocities around ASG mats were reduced by up to 16%, showing that orbital velocities are not attenuated to the extent of unidirectional flow. The oscillatory nature of flow increases inertia, which inhibits the attenuation capacity of the ASG. Therefore, for oscillatory flow, stiffer materials may help increase the attenuation. This can also be reflected in the wave-damping effects of the meadow, though mechanical changes to the ASG were not done here so this is not discussed further. The wake structure behind the meadows shows a gradual return to upstream conditions, which was much closer to the meadow in comparison to the purely unidirectional flow experiments.

The oscillatory flow also ignited 2-dimensional drag, i.e. the vegetation drag had significance in both the $x$ and $z$ directions. This was particularly visible through the load test on the anchors. Moreover, if point anchors are used, the vegetation drag on flow acts within an area, meaning that a corresponding area of the ASG mat loads the anchor. This in turn further turns the drag forcing from 2-D to 3-D. Furthermore, the presence of a second mat can reduce orbital velocities more than when a single mat is present, as was shown here for the 2-by-2-m mats. However, velocities within the gap were enhanced, as were the velocities above the meadows, rendering the highest flow attenuation to be within the meadow.

### 6.2.2 *Surrogate Design Considerations*

When designing a surrogate vegetation to be deployed under marine conditions it is imperative to first answer some questions: 1) what is the purpose of the surrogate? 2) where is the surrogate going to be deployed? The answer to both questions will help to envisage surrogate candidates that suit their future purpose. As mentioned in Chapter 4, ASG can be used for several purposes, so its mechanical and morphological properties will vary correspondingly. Here, with restoration as the main motivation, the first question is already answered and will ensure that the ASG mimics the characteristics of the target seagrass in such a way that most ecosystem services can be incipiently provided by the ASG. The ASG should then be able to secure environmental shelter for either growing seedlings or seeds and the safe settling of the latter. In addition, it will have to allow for nutrient cycling, light availability, and seed transport for the sexual reproduction of the plants. Almost simultaneously, question 2 –site selection –comes into play as the local hydrodynamic and environmental conditions will dictate which natural and anthropogenic disturbances need to be overcome (see Section 1.1.2). The answers to both questions will then be the building blocks for an appropriate design of ASG used for restoration.

From the experimental results in Chapter 2 we can conclude that shelter along the wake is up

to four times more efficient under unidirectional currents, meaning that tidal areas may benefit from dense ASG mats that create protected wakes. This would mean denser meadows should be constructed. On the other hand, when waves dominate the hydrodynamic conditions, shelter becomes more important within the meadow. Here, a dense meadow would inhibit seagrass growth through increased shading (Matheson et al., 2017). Once the site conditions have been determined, a target sheltering method and the corresponding mechanical properties of the material may be chosen. The results of Taphorn et al. (2021) demonstrated we can control how much resistance to flow we would like to have from a certain surrogate depending on the chosen material. Even a highly flexible material reduces flow on its wake. However, spatially speaking, the extent of the reduction will depend on the deflection as well, which is also controlled by the surrogate stiffness. For this reason, a stiffer material will provide more shelter along the wake. Moreover, if the conditions are dominated by unidirectional flow, then a more flexible but denser canopy can also be suitable, as this will provide shelter and trap more sediment, thus clearing the water column and increasing light availability. Furthermore, to counteract the poor nutrient cycling a dense meadow may induce, the surrogate can be constructed of different materials simultaneously, changing the Vertical Biomass Distribution (VBD) to create preferential pathways along $z$ (Chapter 3). A rigid stem with a more flexible leaf-like blade will affect the governing parameters ($EI$, $B$ and the cross-sectional area), modifying the response of the surrogate to flow and thus its effect on flow.

Under wave-dominated conditions, flow penetrates more readily into the canopy and shelter along the wake is not as effective as under unidirectional flow. Here, a stiffer ASG that provides flow resistance but can be sparser will allow for light to penetrate the substrate and reach growing seedlings. This will allow natural seagrass to (re)establish within the ASG and expand outwards. Orbital velocity reduction and wave dissipation by ASG will only increase as the seagrass reproduces and expands. Further, the ASG mats enhance wave decay, especially with more than one mat present. However, current wave decay models will likely overestimate wave decay for fully flexible mats, especially for higher frequency waves (shorter wave periods). For the design of the ASG with respect to predominant hydrodynamic conditions, flow-structure interaction models can provide an idea of flow attenuation within the ASG based on plant mechanical properties. Nonetheless, the flexible mats and the gap between them may increase uncertainties greatly, so use of these models is not an advisable benchmark for flexible mat performance. It is important to remember that no model can generalize for all types of flexible vegetation. The models developed or described here build on the specific conditions trialed during experimentation, subject to several limitations. Nonetheless, they provide a starting point that can be used to gain insight into the expected effect of a similar ASG, and then expand it through further flume experiments or even field trials.

Finally, it is worth noting that this whole discussion is based on the ASG tested in the experiments described in the previous chapters. The results were discussed along with previous models which also build upon a variety of surrogates. Most previous experiments, including the ones presented here, were done utilizing synthetic materials, mostly made of plastic. New forms of quality control are used to detect and inform about the presence of microplastics in our everyday lives. Pervez et al. (2023) showed through 3 indices of beach quality how microplastic pollution is worryingly high in eastern Asian beaches, a problem that is sadly far from localized. Moreover,

Molin et al. (2023) suggests that microplastic leaching may affect respiration and photosynthesis of seagrass, though their experiments show a good level of resilience from *Z. marina*. Nevertheless, microplastics have made their way to every corner of the world and our lives, being even detected in the air of the northern Atlantic (Goßmann et al., 2023), suggesting that a believed sink (or rather collector, i.e. the ocean) of microplastic pollution can become a source. Hence, the advancement of new biodegradable materials needs to be progressed through intense interdisciplinary work with material scientists. This will help to avoid introducing new sources of plastic pollution into the coastal environment and cement ASG as a sustainable alternative for seagrass restoration.

### 6.2.3 *Base layer Design*

The first consideration that comes into mind regarding mat design is the dimensions it should have. Here, the incident hydrodynamic conditions take priority. Remembering that for unidirectional flow the initial flow adjustment needs to be considered, we also know that for all trials and per most literature, a meadow length of 2 m can ensure full flow development or at least be close enough to it. After full flow development, the length of the meadow plays a less important role in flow reduction and thus in wake shelter. If waves dominate, the length of the meadow becomes even less important, as the interaction between adjacent mats and the gap hydrodynamics take a leading role. The mats trialed here were 2 m long and proved to attenuate both the orbital velocities and the wave heights. This may also be linked to the orbital wave excursion, which depends on the wave period (Lowe et al., 2005a, 2007). Longer wave periods signify longer wave excursions which, if longer than the meadow length, may diminish the effect of the meadow. This was not tested here, so it is encouraged for future experiments. For the design, and considering the purpose of the ASG mat, namely restoration, a 2-m mat (square) will be transportable and easy to deploy. This can be upscaled to cover larger areas but within the practicality regarding transport and installation.

After the base layer dimensions have been chosen, the question of anchoring arises. The loads on anchors deployed under marine conditions will depend on mat and ASG mechanical properties, incident hydrodynamics, and the number of anchors used. It is thus important to assess the maximum possible hydrodynamic loads based on the local environmental conditions and historic and probabilistic data. Although sand-filled tubes may be used for robust and continuous anchoring of the mats, these will affect the sediment transport in and out of the ASG mats. In addition, they may also be cumbersome to transport in terms of weight. In any case, the effect of weight-based anchoring should be studied further in the context of ASG mats deployed for restoration before they are selected as the most effective option. On the other hand, we have the point anchors trialed and discussed here. With them, it is important to know that the drag forces are going to be more concentrated than with continuous anchoring.

During base layer design, we note that bed shear stress and its corresponding drag is negligible in terms of anchor loading compared to vegetation drag. The vegetation material design (Section 6.2.2) is thus more critical regarding load calculation. The base layer, on the other hand, should be resistant enough not to rupture under hydrodynamic loading. Furthermore, it should resist fatigue from the cyclic motion of oscillatory flow. Even under unidirectional flow, vortex shedding (Taphorn et al., 2021) and coherent motion such as *monami* (Ackerman and Okubo, 1993) may create a cyclic

loading that can lead to base layer fatigue. Woven base layers made out of natural geotextiles may provide the flexibility and biodegradability required here, while at the same time resisting the aforementioned hurdles. Moreover, the permeability of the base layer may be important to allow for burial of the mat. Burial will stabilize the mat (Subaida et al., 2008), reducing loads as they reduce sway, and may thus facilitate the growth of seedlings within the ASG mat. This is especially important when purely wave conditions dominate, as shelter in the wake is not particularly high.

Regarding anchor design, it is important to note what the main flow direction is. In unidirectional flow, loads would be constant along the meadow after the flow has developed fully, so the calculation of the maximum loads may be straightforward. For wave conditions, however, the interaction with other mats may play a role. It was observed that the first mat experienced higher forces than the second one for a 2-mat configuration with a gap between them. A bigger set-up with a continuous array of ASG mats should provide insight into the inter-mat effects. More importantly, the anchors facing incoming waves sustain the highest loads, so this becomes a critical value to consider. Moreover, forces were shown to be greater in the direction of wave propagation. This means that the mats placed at the edge of any cluster of mats would have the critical loads from incoming waves and need to be designed accordingly. Adding to the critical load calculation is the sway of the mat, which was speculated here to contribute to the loads. Specific measurements of sway are needed to corroborate this. Finally, wave motion results in 3-dimensional loads on the anchors, with orthogonal forces (relative to wave propagation direction) capable of equaling longitudinal forces, such that both the surrogates, the base layer, and the anchors need to be able to endure the constant or cyclic loads in all directions. Ultimately, base layer design should be harmonious with surrogate design to create ASG mats that can promote seagrass re-establishment efficiently and eventually disappear without leaving any harmful mark on the environment.

## 6.3 Outlook and Recommendations

This thesis offers a glimpse of the potential of ASG mats for ecosystem restoration applications. The results presented here should be the foundation for field research on practical and feasible options for restoration support. Firstly, the proposed and tested models should be expanded by validating them under different initial and boundary conditions. This would help to address the shortcomings of the results, which mainly arose from laboratory and time-related limitations. Nonetheless, there is still much room for progress; the list in the box below briefly describes the drawbacks that need to be addressed in future research and projects. While fluid-structure interaction reaches maturity, the biodegradability of materials under marine conditions and their performance in the field is still unfledged. Therefore, more research in this area is encouraged along with rigorous interdisciplinary work with material scientists and ecologists.

Further research on ASG can be coupled with research surrounding natural vegetation and field experiments. Advancements in vegetation modeling can be implemented to flexible ASG mats as more robust models are developed. Lopez-Arias et al. (2023) show that fluid-vegetation interaction can be modeled more robustly utilizing plant parameters (in this case salt marshes) instead of relying on calibrated parameters such as the drag coefficient. This will increase the range of applicability of models, thus providing more possibilities to test different ASG configurations that

**Drawbacks to address following the results of this dissertation**

*"... there is still much room for progress"*

- The effects of the ASG meadow shoot density on shelter coupled with the mechanical properties of different materials.
- Measurement of the velocity structure along the full water column to asses the distribution above the meadow and along the wake (e.g. to identify the extent of the upward trend which was not measurable here).
- Use of different materials for base layer, including different levels of flexibility.
- Quantification of base layer motion, i.e. sway, and its effect on the known attenuation effect of the ASG mat.
- Supplement the hydrodynamic conditions by trialing various irregular and sea state conditions, producing results closer to reality.
- Pilot projects in the field to establish the performance of ASG mats in terms of shelter for seagrass, biodegradation rates, sediment stabilization, and general ecosystem support.

**6**

can later be evaluated in the field. Ultimately, ASG could find applications beyond restoration. Erosion control (as discussed in Chapter 5) could be extended to use environmentally-friendly ASG that could promote vegetation growth around pipelines and other submerged infrastructure, which would in turn continue providing this service after the biodegradable ASG has disappeared. Furthermore, ASG in the field will probably find further interactions that are not possible to test in laboratories as organisms create a symbiosis with the submerged structures. Fauna can benefit from shelter as well, meaning in turn that ASG can turn into feeding grounds for larger animals. Different kinds of vegetation may also exploit the shelter and grow. This symbiosis may be beneficial but also detrimental for both the ASG and the growing restoring seagrass. These positive and negative feedback mechanisms need to be investigated to assess the real potential of ASG.

Nevertheless, the use of ASG for restoration has been demonstrated to be feasible. ASG, just as any other vegetation surrogates, can help not only to restore degraded ecosystems but also to battle climate change. Submerged aquatic vegetation can sequester large amounts of carbon (Duarte et al., 2005; Lei et al., 2023), the so-called blue-carbon, and help to diminish the impact of seal level rise in estuaries and other coastal areas (Taylor-Burns et al., 2023). Further, the shelter provided by ASG can be analogous to other structures such as artificial coral reefs, which have also been used for ecosystem restoration (Harris, 2009; Polak and Shashar, 2013; Tran et al., 2019). Artificial corals consist of comparatively large structures, constructed of different composites, meaning they can be expensive and cumbersome to install, so a synergetic relationship between different artificial structures could be beneficial for large-scale ecosystem restoration projects. The

implementation of ASG has the potential to be rudimentary and inexpensive, making it feasible for worldwide applications. But first, this potential has to be cemented in the catalog of restoration support structures. Regardless, ASG has helped to advance the understanding of fluid-vegetation interaction. The coupling of this with ecosystem restoration also bridges the work of different disciplines, promoting and exploiting interdisciplinarity, which should be common practice in our battle to mitigate and adapt to climate change.

## 6.4 Conclusions

Seagrasses have been shown to be essential for the environment, the climate, and our livelihoods. Despite their importance, they have been disappearing at a rapid pace, especially during the past century. Restoration approaches have been taking momentum, with some alternatives more successful than others. To support this momentum, a relatively new approach has been proposed, namely the use of artificial seagrass (ASG) to introduce the ecosystem services of seagrasses and thus promote its (re)establishment. However, to be able to apply this solution, its efficacy needs to be indisputably recognized. For that, the processes behind the presence of ASG in the marine environment need to be well understood. This dissertation presented a series of laboratory experiments and analyses of the physical processes involved with fluid dynamics and flexible, artificial vegetation. Different materials and incident hydrodynamic conditions were trialed to finally be able to engineer a suitable ASG mat that can be trialed in the field.

ASG represents a promising option for seagrass restoration by creating suitable hydrodynamic and light conditions and stabilizing sediment for seagrass establishment. ASG supports seagrass when habitat conditions are too harsh for seagrass meadows to re-establish themselves. Here, with this positive feedback as a central objective, ASG was tested under controlled laboratory conditions. Different materials and incident hydrodynamic conditions that generalize the expected loads under marine conditions were trialed. It was shown that the flexibility of the materials complicates the predictability of forces using state-of-the-art research on fluid dynamics and fluid-structure interaction. Nonetheless, it was also shown that considering the hydrodynamic response of the vegetation, the agreement between current models is reliable enough to provide an accurate estimation of the maximum hydrodynamic loads expected. This helps to design the needed resistance of the anchoring and base layer used and establish the mechanical properties (stiffness and density) the artificial meadow should possess. Further, it was also shown that the wake of a meadow is well protected, even for extremely flexible ASG, under current-dominated conditions, and that flow attenuation within the meadow should be prioritized simultaneously with light availability and base layer permeability under pure wave conditions. These results inform scientists in different disciplines about the characteristics that ASG should have to obtain positive results with regard to shelter for growing seedlings. Further, it was shown that the specific material of both the surrogate itself as well as its base layer are extremely important to control the extent of attenuation of flow achieved. The attenuation can translate into shelter, which will in turn promote seagrass re-establishment. The degree of protection needed will depend on the local hydrodynamic conditions and the inherent resilience of the target seagrass species to be restored.

While the general facilitating effect of ASG has been extensively proven through laboratory

studies on flow-vegetation interaction, field applications have been limited to small-scale pilot projects with no transmittable results. To test the potential of ASG in habitat restoration, large-scale field trials are required. Furthermore, a variety of locations and therefore conditions should be tested to be able to generalize the results. Ultimately, ASG can be applied in co-action with other solutions to provide benefits beyond shelter for restoration, such as structural protection, extended feeding and mating grounds, and coastal protection through energy dissipation. Still, more studies are needed to overcome the uncertainties associated with this promising approach. Field trials should be generalized after an extensive multidisciplinary laboratory campaign that brings models of fluid-structure interaction under marine conditions to robust and reliable levels. Finally, field trials can provide extra insight into the impacts of external factors that are not present in the laboratory, such as sunlight exposure, grazing by fauna, microbial growth, and more.

# BIBLIOGRAPHY

Abadie, A., Lejeune, P., Pergent, G., and Gobert, S. (2016). From mechanical to chemical impact of anchoring in seagrasses: the premises of anthropogenic patch generation in *Posidonia oceanica* meadows. *Marine pollution bulletin*, 109(1):61–71.

Abdolahpour, M., Ghisalberti, M., McMahon, K., and Lavery, P. S. (2018). The impact of flexibility on flow, turbulence, and vertical mixing in coastal canopies. *Limnology and Oceanography*, 63(6):2777–2792.

Ackerman, J. and Okubo, A. (1993). Reduced mixing in a marine macrophyte canopy. *Functional Ecology*, pages 305–309.

Adams, M. P., Hovey, R. K., Hipsey, M. R., Bruce, L. C., Ghisalberti, M., Lowe, R. J., Gruber, R. K., Ruiz-Montoya, L., Maxwell, P. S., Callaghan, D. P., et al. (2016). Feedback between sediment and light for seagrass: Where is it important? *Limnology and Oceanography*, 61(6):1937–1955.

Adhitya, A., Bouma, T., Folkard, A., Van Katwijk, M., Callaghan, D., De Iongh, H., and Herman, P. (2014). Comparison of the influence of patch-scale and meadow-scale characteristics on flow within seagrass meadows: a flume study. *Marine Ecology Progress Series*, 516:49–59.

Anderson, L. M. and Martone, P. T. (2014). Biomechanical consequences of epiphytism in intertidal macroalgae. *Journal of Experimental Biology*, 217(7):1167–1174.

Andrady, A. L. (2011). Microplastics in the marine environment. *Marine pollution bulletin*, 62(8):1596–1605.

Asano, T., Deguchi, H., and Kobayashi, N. (1992). Interaction between water waves and vegetation. In *Coastal Engineering 1992*, pages 2709–2723. ASCE.

Asano, T., Tsutsui, S., and Sakai, T. (1988). Wave damping characteristics due to seaweed. In *Proc. 35th Conf. on Coastal Engrg., 1988*.

Bakker, I. W., Bax, J., Grootenboer, D., and Tutuarima, I. W. (1973). Artificial seaweed coastal and submarine-pipeline protection studies with stretched polypropylene foam strands. *La Houille Blanche*, (8):661–676.

Barbier, E. B., Hacker, S. D., Kennedy, C., Koch, E. W., Stier, A. C., and Silliman, B. R. (2011). The value of estuarine and coastal ecosystem services. *Ecological monographs*, 81(2):169–193.

Barcelona, A., Colomer, J., Serra, T., Cossa, D., and Infantes, E. (2023). The role epiphytes play in particle capture of seagrass canopies. *Marine Environmental Research*, page 106238.

Barcelona, A., Oldham, C., Colomer, J., Garcia-Orellana, J., and Serra, T. (2021). Particle capture by seagrass canopies under an oscillatory flow. *Coastal Engineering*, 169:103972.

Beck, M. W., Heck, K. L., Able, K. W., Childers, D. L., Eggleston, D. B., Gillanders, B. M., Halpern, B., Hays, C. G., Hoshino, K., Minello, T. J., et al. (2001). The identification, conservation, and management of estuarine and marine nurseries for fish and invertebrates: a better understanding of the habitats that serve as nurseries for marine species and the factors that create site-specific variability in nursery quality will improve conservation and management of these areas. *Bioscience*, 51(8):633–641.

Belcher, S., Jerram, N., and Hunt, J. (2003). Adjustment of a turbulent boundary layer to a canopy of roughness elements. *Journal of Fluid Mechanics*, 488:369–398.

Bell, J. D., Steffe, A. S., and Westoby, M. (1985). Artificial seagrass: how useful is it for field experiments on fish and macroinvertebrates? *Journal of Experimental Marine Biology and Ecology*, 90(2):171–177.

Bos, A. R. and Van Katwijk, M. M. (2007). Planting density, hydrodynamic exposure and mussel beds affect survival of transplanted intertidal eelgrass. *Marine Ecology Progress Series*, 336:121–129.

Bouma, T., De Vries, M., Low, E., Peralta, G., Tánczos, I. v., van de Koppel, J., and Herman, P. M. J. (2005). Trade-offs related to ecosystem engineering: A case study on stiffness of emerging macrophytes. *Ecology*, 86(8):2187–2199.

Bradley, K. and Houser, C. (2009). Relative velocity of seagrass blades: Implications for wave attenuation in low-energy environments. *Journal of Geophysical Research: Earth Surface*, 114(F1).

Bricker, J. D., Inagaki, S., and Monismith, S. G. (2005). Bed drag coefficient variability under wind waves in a tidal estuary. *Journal of Hydraulic Engineering*, 131(6):497–508.

Brodie, G., Holland, E., Antoine De Ramon, N., Soapi, K., and Hills, J. (2020). Seagrasses and seagrass habitats in pacific small island developing states: Potential loss of benefits via human disturbance and climate change. *Marine Pollution Bulletin*, 160:111573.

Burkholder, J. M., Tomasko, D. A., and Touchette, B. W. (2007). Seagrasses and eutrophication. *Journal of experimental marine biology and ecology*, 350(1-2):46–72.

Byers, J. E., Cuddington, K., Jones, C. G., Talley, T. S., Hastings, A., Lambrinos, J. G., Crooks, J. A., and Wilson, W. G. (2006). Using ecosystem engineers to restore ecological systems. *Trends in ecology & evolution*, 21(9):493–500.

Cabaço, S., Santos, R., and Duarte, C. M. (2008). The impact of sediment burial and erosion on seagrasses: a review. *Estuarine, Coastal and Shelf Science*, 79(3):354–366.

Campbell, M. (2000). A decision-based framework to increase seagrass transplantation success. *Biol. Mar. Medit*, 7(2):336–341.

Campbell, M. L. (2002). Getting the foundation right: a scientifically based management framework to aid in the planning and implementation of seagrass transplant efforts. *Bulletin of Marine Science*, 71(3):1405–1414.

Campbell, M. L. and Paling, E. I. (2003). Evaluating vegetative transplant success in *Posidonia australis*: a field trial with habitat enhancement. *Marine Pollution Bulletin*, 46(7):828–834.

Carr, J., D'odorico, P., McGlathery, K., and Wiberg, P. (2010). Stability and bistability of seagrass ecosystems in shallow coastal lagoons: Role of feedbacks with sediment resuspension and light attenuation. *Journal of Geophysical Research: Biogeosciences*, 115(G3).

Carr, J. A., D'Odorico, P., McGlathery, K. J., and Wiberg, P. L. (2016). Spatially explicit feedbacks between seagrass meadow structure, sediment and light: Habitat suitability for seagrass growth. *Advances in Water Resources*, 93:315–325.

Carus, J., Arndt, C., Bouma, T., Schröder, B., and Paul, M. (2020). Effect of artificial seagrass on hydrodynamic thresholds for the early establishment of *Zostera marina*. *Journal of Ecohydraulics*, 7(1):17–27.

Carus, J., Arndt, C., Schröder, B., Thom, M., Villanueva, R., and Paul, M. (2021). Using artificial seagrass for promoting positive feedback mechanisms in seagrass restoration. *Frontiers in Marine Science*, page 993.

Chen, H., Ni, Y., Li, Y., Liu, F., Ou, S., Su, M., Peng, Y., Hu, Z., Uijttewaal, W., and Suzuki, T. (2018). Deriving vegetation drag coefficients in combined wave-current flows by calibration and direct measurement methods. *Advances in water resources*, 122:217–227.

Chen, S.-N., Sanford, L. P., Koch, E. W., Shi, F., and North, E. W. (2007). A nearshore model to investigate the effects of seagrass bed geometry on wave attenuation and suspended sediment transport. *Estuaries and Coasts*, 30:296–310.

Chen, Z., Jiang, C., and Nepf, H. (2013). Flow adjustment at the leading edge of a submerged aquatic canopy. *Water Resources Research*, 49(9):5537–5551.

Chen, Z., Ortiz, A., Zong, L., and Nepf, H. (2012). The wake structure behind a porous obstruction and its implications for deposition near a finite patch of emergent vegetation. *Water Resources Research*, 48(9).

Chow, V. T. (1959). *Open-channel Hydraulics*. McGraw-Hill civil engineering series. Blackburn Press.

Christianen, M. J., van Belzen, J., Herman, P. M., van Katwijk, M. M., Lamers, L. P., van Leent, P. J., and Bouma, T. J. (2013). Low-canopy seagrass beds still provide important coastal protection services. *PloS one*, 8(5):e62413.

Coceal, O. and Belcher, S. E. (2004). A canopy model of mean winds through urban areas. *Quarterly Journal of the Royal Meteorological Society*, 130(599):1349–1372.

Cole, M., Lindeque, P., Halsband, C., and Galloway, T. S. (2011). Microplastics as contaminants in the marine environment: a review. *Marine pollution bulletin*, 62(12):2588–2597.

Collier, C., Waycott, M., and McKenzie, L. (2012). Light thresholds derived from seagrass loss in the coastal zone of the northern great barrier reef, australia. *Ecological Indicators*, 23:211–219.

Costanza, R., Anderson, S. J., Sutton, P., Mulder, K., Mulder, O., Kubiszewski, I., Wang, X., Liu, X., Pérez-Maqueo, O., Martinez, M. L., et al. (2021). The global value of coastal wetlands for storm protection. *Global environmental change*, 70:102328.

Cotton, A. (1933). Disappearance of *Zostera marina*. *Nature*, 132(3329):277–277.

Cullen-Unsworth, L. C. and Unsworth, R. (2018). A call for seagrass protection. *Science*, 361(6401):446–448.

Dalrymple, R. A., Kirby, J. T., and Hwang, P. A. (1984). Wave diffraction due to areas of energy dissipation. *Journal of waterway, port, coastal, and ocean engineering*, 110(1):67–79.

David, C. G., Schulz, N., and Schlurmann, T. (2016). *Assessing the application potential of selected ecosystem-based, low-regret coastal protection measures*. Springer.

Detto, M., Katul, G. G., Siqueira, M., Juang, J.-Y., and Stoy, P. (2008). The structure of turbulence near a tall forest edge: The backward-facing step flow analogy revisited. *Ecological Applications*, 18(6):1420–1435.

Dolch, T., Buschbaum, C., and Reise, K. (2013). Persisting intertidal seagrass beds in the northern wadden sea since the 1930s. *Journal of Sea Research*, 82:134–141.

Dominghaus, D.-I. H. (2013). *Kunststoffe: Eigenschaften und Anwendungen*. Springer-Verlag.

Dorée, C. (1920). The action of sea water on cotton and other textile fibres. *Biochemical Journal*, 14(6):709.

Duarte, C. M. (2002). The future of seagrass meadows. *Environmental conservation*, 29(2):192–206.

Duarte, C. M., Losada, I. J., Hendriks, I. E., Mazarrasa, I., and Marbà, N. (2013). The role of coastal plant communities for climate change mitigation and adaptation. *Nature climate change*, 3(11):961–968.

Duarte, C. M., Middelburg, J. J., and Caraco, N. (2005). Major role of marine vegetation on the oceanic carbon cycle. *Biogeosciences*, 2(1):1–8.

Dubi, A. (1995). *Damping of water waves by submerged vegetation: a case study on Laminaria hyperborea.* PhD thesis, Thesis, Department of Structural Engineering, The Norwegian Institute of Technology, Trondheim, Norway.

Egea, L., Infantes, E., and Jiménez-Ramos, R. (2023). Loss of poc and doc on seagrass sediments by hydrodynamics. *Science of The Total Environment*, page 165976.

El Allaoui, N., Serra, T., Colomer, J., Soler, M., Casamitjana, X., and Oldham, C. (2016). Interactions between fragmented seagrass canopies and the local hydrodynamics. *PLoS One*, 11(5):e0156264.

EurOTop (2018). *Manual on wave overtopping of sea defences and related structures: An overtopping manual largely based on European research, but for worldwide application.* Van der Meer, J.W., Allsop, N.W.H., Bruce, T., De Rouck, J., Kortenhaus, A., Pullen, T., Schüttrumpf, H., Troch, P. and Zanuttigh.

Folkard, A. M. (2005). Hydrodynamics of model *Posidonia oceanica* patches in shallow water. *Limnology and oceanography*, 50(5):1592–1600.

Fonseca, M., Fisher, J., Zieman, J., and Thayer, G. (1982). Influence of the seagrass, *Zostera marina L.*, on current flow. *Estuarine, Coastal and Shelf Science*, 15(4):351–364.

Fonseca, M. S. and Bell, S. S. (1998). Influence of physical setting on seagrass landscapes near beaufort, north carolina, usa. *Marine Ecology Progress Series*, 171:109–121.

Fonseca, M. S. and Cahalan, J. A. (1992). A preliminary evaluation of wave attenuation by four species of seagrass. *Estuarine, Coastal and Shelf Science*, 35(6):565–576.

Fonseca, M. S., Fourqurean, J. W., and Koehl, M. (2019). Effect of seagrass on current speed: importance of flexibility vs. shoot density. *Frontiers in Marine Science*, 6:376.

Fonseca, M. S. and Koehl, M. (2006). Flow in seagrass canopies: the influence of patch width. *Estuarine, Coastal and Shelf Science*, 67(1-2):1–9.

Fonseca, M. S., Thayer, G. W., and Kenworthy, W. J. (1987). The use of ecological data in the implementation and management of seagrass restorations. *Fla. Mar. Res. Publ*, 42:175–187.

Fonseca, M. S., Zieman, J. C., Thayer, G. W., and Fisher, J. S. (1983). The role of current velocity in structuring eelgrass (*Zostera marina L.*) meadows. *Estuarine, Coastal and Shelf Science*, 17(4):367–380.

Fourqurean, J. W., Duarte, C. M., Kennedy, H., Marbà, N., Holmer, M., Mateo, M. A., Apostolaki, E. T., Kendrick, G. A., Krause-Jensen, D., McGlathery, K. J., et al. (2012). Seagrass ecosystems as a globally significant carbon stock. *Nature geoscience*, 5(7):505–509.

Gambi, M. C., Nowell, A. R., and Jumars, P. A. (1990). Flume observations on flow dynamics in *Zostera marina* (eelgrass) beds. *Marine ecology progress series*, pages 159–169.

Ganassin, C. and Gibbs, P. J. (2008). *A review of seagrass planting as a means of habitat compensation following loss of seagrass meadow.* CiteSeer, Australia: NSW Department of Primary Industries.

Ghisalberti, M. and Nepf, H. (2009). Shallow flows over a permeable medium: the hydrodynamics of submerged aquatic canopies. *Transport in porous media*, 78:309–326.

Ghisalberti, M. and Nepf, H. M. (2002). Mixing layers and coherent structures in vegetated aquatic flows. *Journal of Geophysical Research: Oceans*, 107(C2):3–1.

Goring, D. G. and Nikora, V. I. (2002). Despiking acoustic doppler velocimeter data. *Journal of hydraulic engineering*, 128(1):117–126.

Goseberg, N., Wurpts, A., and Schlurmann, T. (2013). Laboratory-scale generation of tsunami and long waves. *Coastal Engineering*, 79:57–74.

Goßmann, I., Herzke, D., Held, A., Schulz, J., Nikiforov, V., Georgi, C., Evangeliou, N., Eckhardt, S., Gerdts, G., Wurl, O., et al. (2023). Occurrence and backtracking of microplastic mass loads including tire wear particles in northern atlantic air. *Nature Communications*, 14(1):3707.

Grimaldo, E., Herrmann, B., Vollstad, J., Su, B., Moe Føre, H., Larsen, R. B., and Tatone, I. (2018). Fishing efficiency of biodegradable pbsat gillnets and conventional nylon gillnets used in norwegian cod (*Gadus morhua*) and saithe (*Pollachius virens*) fisheries. *ICES Journal of Marine Science*, 75(6):2245–2256.

Guannel, G., Arkema, K., Ruggiero, P., and Verutes, G. (2016). The power of three: coral reefs, seagrasses and mangroves protect coastal regions and increase their resilience. *PloS one*, 11(7):e0158094.

Guo, J., Julien, P. Y., and Meroney, R. N. (2005). Modified log-wake law for zero-pressure-gradient turbulent boundary layers. *Journal of Hydraulic Research*, 43(4):421–430.

Hansen, A. T., Hondzo, M., Sheng, J., and Sadowsky, M. J. (2014). Microscale measurements reveal contrasting effects of photosynthesis and epiphytes on frictional drag on the surfaces of filamentous algae. *Freshwater biology*, 59(2):312–324.

Hardison, S. B., McGlathery, K. J., and Castorani, M. C. (2023). Effects of seagrass restoration on coastal fish abundance and diversity. *Conservation Biology*.

Harris, L. E. (2009). Artificial reefs for ecosystem restoration and coastal erosion protection with aquaculture and recreational amenities. *Reef Journal*, 1(1):235–246.

Hemminga, M. A. and Duarte, C. M. (2000). *Seagrass ecology.* Cambridge University Press.

Hengst, A., Melton, J., and Murray, L. (2010). Estuarine restoration of submersed aquatic vegetation: the nursery bed effect. *Restoration Ecology*, 18(4):605–614.

Henry, P.-Y., Myrhaug, D., and Aberle, J. (2015). Drag forces on aquatic plants in nonlinear random waves plus current. *Estuarine, Coastal and Shelf Science*, 165:10–24.

Henry, P.-Y. T. (2014). Bending properties of a macroalga: Adaptation of peirce's cantilever test for in situ measurements of laminaria digitata (laminariaceae). *American journal of botany*, 101(6):1050–1055.

Herr, D. and Landis, E. (2016). Coastal blue carbon ecosystems. Opportunities for Nationally Determined Contributions. Policy brief.

Hu, Z., Lei, J., Liu, C., and Nepf, H. (2018). Wake structure and sediment deposition behind models of submerged vegetation with and without flexible leaves. *Advances in Water Resources*, 118:28–38.

Hu, Z., Suzuki, T., Zitman, T., Uittewaal, W., and Stive, M. (2014). Laboratory study on wave dissipation by vegetation in combined current–wave flow. *Coastal Engineering*, 88:131–142.

Huang, C.-C. and Pan, J.-Y. (2010). Mooring line fatigue: A risk analysis for an spm cage system. *Aquacultural engineering*, 42(1):8–16.

Infantes, E., Orfila, A., Bouma, T. J., Simarro, G., and Terrados, J. (2011). *Posidonia oceanica* and *Cymodocea nodosa* seedling tolerance to wave exposure. *Limnology and Oceanography*, 56(6):2223–2232.

IPCC (2019). *IPCC special report on the ocean and cryosphere in a changing climate [H.-O. Pörtner, D.C. Roberts, V. Masson-Delmotte, P. Zhai, M. Tignor, E. Poloczanska, K. Mintenbeck, A. Alegría, M. Nicolai, A. Okem, J. Petzold, B. Rama, N.M. Weyer (eds.)].* Cambridge University Press, Cambridge, UK and New York, NY, USA, 755 pp., Geneva, Switzerland.

Irving, A. D., Tanner, J. E., and Collings, G. J. (2014). Rehabilitating seagrass by facilitating recruitment: improving chances for success. *Restoration ecology*, 22(2):134–141.

Irving, A. D., Tanner, J. E., Seddon, S., Miller, D., Collings, G. J., Wear, R. J., Hoare, S. L., and Theil, M. J. (2010). Testing alternate ecological approaches to seagrass rehabilitation: links to life-history traits. *Journal of Applied Ecology*, 47(5):1119–1127.

Ismail, H. (2003). Valued-added shore protection structures for enhancement of the marine ecosystem services. In *Proceeding of the 2003 Technical Seminar on Shoreline Management, Malaysia.*

Jacobsen, N. G. (2016). Wave-averaged properties in a submerged canopy: Energy density, energy flux, radiation stresses and stokes drift. *Coastal Engineering*, 117:57–69.

Jacobsen, N. G., Bakker, W., Uijttewaal, W. S., and Uittenbogaard, R. (2019). Experimental investigation of the wave-induced motion of and force distribution along a flexible stem. *Journal of Fluid Mechanics*, 880:1036–1069.

James, R. K., Silva, R., Van Tussenbroek, B. I., Escudero-Castillo, M., Mariño-Tapia, I., Dijkstra, H. A., Van Westen, R. M., Pietrzak, J. D., Candy, A. S., Katsman, C. A., et al. (2019). Maintaining tropical beaches with seagrass and algae: a promising alternative to engineering solutions. *BioScience*, 69(2):136–142.

Jones, B. N., Hillier, T. S., Partridge, D. J., and Fagan, L. (2006). Artificial frond system for seabed scour control at wind farm platforms in nantucket sound, massachusetts. In *Civil Engineering in the Oceans VI*, pages 246–254. ASCE.

Kerpen, N. B., Schlurmann, T., Schendel, A., Gundlach, J., Marquard, D., and Hüpgen, M. (2020). Wave-induced distribution of microplastic in the surf zone. *Frontiers in Marine Science*, 7:590565.

KFKI (2020). *Die Küste, 88 EAK 2002, 3. korrigierte Ausgabe.* Number 88 in Die Küste. Archiv für Forschung und Technik an der Nord- und Ostsee. Kuratorium für Forschung im Küsteningenieurwesen. Bundesanstalt für Wasserbau, Karlsruhe.

Kidder, G. W., White, S., Miller, M. F., Norden, W. S., Taylor, T., and Disney, J. E. (2015). Biodegradable grids: an effective method for eelgrass (*Zostera marina*) restoration in maine. *Journal of Coastal Research*, 31(4):900–906.

Kobayashi, N., Raichle, A. W., and Asano, T. (1993). Wave attenuation by vegetation. *Journal of waterway, port, coastal, and ocean engineering*, 119(1):30–48.

Koch, E. W. (2001). Beyond light: physical, geological, and geochemical parameters as possible submersed aquatic vegetation habitat requirements. *Estuaries*, 24:1–17.

Koch, E. W., Ailstock, M. S., Booth, D. M., Shafer, D. J., and Magoun, A. D. (2010). The role of currents and waves in the dispersal of submersed angiosperm seeds and seedlings. *Restoration ecology*, 18(4):584–595.

Koch, E. W., Sanford, L. P., Chen, S.-N., Shafer, D. J., and Smith, J. M. (2006). Waves in seagrass systems: review and technical recommendations. Technical report, ERDC Vicksburg Coastal and hydraulics lab.

Koken, M. and Constantinescu, G. (2023). Influence of submergence ratio on flow and drag forces generated by a long rectangular array of rigid cylinders at the sidewall of an open channel. *Journal of fluid mechanics*, 966:A5.

Landmann, J., Fröhling, L., Gieschen, R., Buck, B. H., Heasman, K., Scott, N., Smeaton, M., Goseberg, N., and Hildebrandt, A. (2021). New system design for the cultivation of extractive species at exposed sites-part 2: Experimental modelling in waves and currents. *Applied Ocean Research*, 113:102749.

Lara, J. L., Maza, M., Ondiviela, B., Trinogga, J., Losada, I. J., Bouma, T. J., and Gordejuela, N. (2016). Large-scale 3-d experiments of wave and current interaction with real vegetation. part 1: Guidelines for physical modeling. *Coastal Engineering*, 107:70–83.

Lara, M., Peralta, G., Alonso, J., Morris, E. P., González-Ortiz, V., Rueda-Márquez, J., and Pérez-Lloréns, J. L. (2012). Effects of intertidal seagrass habitat fragmentation on turbulent diffusion and retention time of solutes. *Marine Pollution Bulletin*, 64(11):2471–2479.

Larkum, A. W., Orth, R. J., and Duarte, C. M. (2006). Seagrasses: biology, ecology and conservation. *Phycologia*, 45(5):5.

Lee, K.-S. and Park, J.-I. (2008). An effective transplanting technique using shells for restoration of *Zostera marina* habitats. *Marine Pollution Bulletin*, 56(5):1015–1021.

Lefebvre, A., Thompson, C., and Amos, C. (2010). Influence of *Zostera marina* canopies on unidirectional flow, hydraulic roughness and sediment movement. *Continental Shelf Research*, 30(16):1783–1794.

Lei, J. and Nepf, H. (2019a). Blade dynamics in combined waves and current. *Journal of Fluids and Structures*, 87:137–149.

Lei, J. and Nepf, H. (2019b). Wave damping by flexible vegetation: Connecting individual blade dynamics to the meadow scale. *Coastal Engineering*, 147:138–148.

Lei, J., Schaefer, R., Colarusso, P., Novak, A., Simpson, J. C., Masqué, P., and Nepf, H. (2023). Spatial heterogeneity in sediment and carbon accretion rates within a seagrass meadow correlated with the hydrodynamic intensity. *Science of the total environment*, 854:158685.

Leschen, A. S., Ford, K. H., and Evans, N. T. (2010). Successful eelgrass (*Zostera marina*) restoration in a formerly eutrophic estuary (boston harbor) supports the use of a multifaceted watershed approach to mitigating eelgrass loss. *Estuaries and coasts*, 33(6):1340–1354.

Lima, S. Q., Neves, C. F., and Rosauro, N. (2007). Damping of gravity waves by fields of flexible vegetation. In *Coastal Engineering 2006*.

Litsi-Mizan, V., Efthymiadis, P. T., Gerakaris, V., Serrano, O., Tsapakis, M., and Apostolaki, E. T. (2023). Decline of seagrass (*Posidonia oceanica*) production over two decades in the face of warming of the eastern mediterranean sea. *New Phytologist*.

Longuet-Higgins, M. S. (1953). Mass transport in water waves. *Philosophical Transactions of the Royal Society of London. Series A, Mathematical and Physical Sciences*, 245(903):535–581.

Lopez-Arias, F., Maza, M., Lara, J. L., and Losada, I. J. (2023). A new predictive tool for modeling wave attenuation produced by saltmarshes in swan based on standing biomass. *Coastal Engineering*, page 104380.

Losada, I. J., Maza, M., and Lara, J. L. (2016). A new formulation for vegetation-induced damping under combined waves and currents. *Coastal Engineering*, 107:1–13.

Lotze, H. K., Lenihan, H. S., Bourque, B. J., Bradbury, R. H., Cooke, R. G., Kay, M. C., Kidwell, S. M., Kirby, M. X., Peterson, C. H., and Jackson, J. B. (2006). Depletion, degradation, and recovery potential of estuaries and coastal seas. *Science*, 312(5781):1806–1809.

Lowe, R. J., Falter, J. L., Koseff, J. R., Monismith, S. G., and Atkinson, M. J. (2007). Spectral wave flow attenuation within submerged canopies: Implications for wave energy dissipation. *Journal of Geophysical Research: Oceans*, 112(C5).

Lowe, R. J., Koseff, J. R., and Monismith, S. G. (2005a). Oscillatory flow through submerged canopies: 1. velocity structure. *Journal of Geophysical Research: Oceans*, 110(C10).

Lowe, R. J., Koseff, J. R., Monismith, S. G., and Falter, J. L. (2005b). Oscillatory flow through submerged canopies: 2. canopy mass transfer. *Journal of Geophysical Research: Oceans*, 110(C10).

Luhar, M., Coutu, S., Infantes, E., Fox, S., and Nepf, H. (2010). Wave-induced velocities inside a model seagrass bed. *Journal of Geophysical Research: Oceans*, 115(C12).

Luhar, M., Infantes, E., and Nepf, H. (2017). Seagrass blade motion under waves and its impact on wave decay. *Journal of Geophysical Research: Oceans*, 122(5):3736–3752.

Luhar, M. and Nepf, H. (2016). Wave-induced dynamics of flexible blades. *Journal of Fluids and Structures*, 61:20–41.

Luhar, M. and Nepf, H. M. (2011). Flow-induced reconfiguration of buoyant and flexible aquatic vegetation. *Limnology and Oceanography*, 56(6):2003–2017.

Madsen, J. D., Chambers, P. A., James, W. F., Koch, E. W., and Westlake, D. F. (2001). The interaction between water movement, sediment dynamics and submersed macrophytes. *Hydrobiologia*, 444:71–84.

Mallée, R. and Eligehausen, R. (2013). *Design of fastenings for use in concrete: the CEN/TS 1992-4 provisions*. John Wiley & Sons.

Manca, E., Cáceres, I., Alsina, J., Stratigaki, V., Townend, I., and Amos, C. (2012). Wave energy and wave-induced flow reduction by full-scale model posidonia oceanica seagrass. *Continental Shelf Research*, 50:100–116.

Marques, A. R., de Oliveira Patrício, P. S., dos Santos, F. S., Monteiro, M. L., de Carvalho Urashima, D., and de Souza Rodrigues, C. (2014). Effects of the climatic conditions of the southeastern brazil on degradation the fibers of coir-geotextile: Evaluation of mechanical and structural properties. *Geotextiles and Geomembranes*, 42(1):76–82.

Marriott, M. and Jayaratne, R. (2010). Hydraulic roughness–links between manning's coefficient, nikuradse's equivalent sand roughness and bed grain size. *Advances in Computing and Technology 2010*, pages 27–32.

Matheson, F., Reed, J., Dos Santos, V., Mackay, G., and Cummings, V. (2017). Seagrass rehabilitation: successful transplants and evaluation of methods at different spatial scales. *New Zealand journal of marine and freshwater research*, 51(1):96–109.

Matsumura, K., Nakayama, K., and Matsumoto, H. (2022). Influence of patch size on hydrodynamic flow in submerged aquatic vegetation. *Frontiers in Marine Science*, 9:1001295.

Maxwell, P. S., Eklöf, J. S., van Katwijk, M. M., O'Brien, K. R., de la Torre-Castro, M., Boström, C., Bouma, T. J., Krause-Jensen, D., Unsworth, R. K., van Tussenbroek, B. I., et al. (2017). The fundamental role of ecological feedback mechanisms for the adaptive management of seagrass ecosystems–a review. *Biological Reviews*, 92(3):1521–1538.

Maza, M., Lara, J., Losada, I., Ondiviela, B., Trinogga, J., and Bouma, T. (2015). Large-scale 3-d experiments of wave and current interaction with real vegetation. part 2: Experimental analysis. *Coastal Engineering*, 106:73–86.

Maza, M., Lara, J. L., Ondiviela, B., and Losada, I. J. (2012). Wave attenuation modelling by submerged vegetation: ecological and engineering analysis. *Coastal Eng Proc*, 1(1):2.

McGlathery, K. J., Sundbäck, K., and Anderson, I. C. (2007). Eutrophication in shallow coastal bays and lagoons: the role of plants in the coastal filter. *Marine Ecology Progress Series*, 348:1–18.

McMahon, K., van Dijk, K.-j., Ruiz-Montoya, L., Kendrick, G. A., Krauss, S. L., Waycott, M., Verduin, J., Lowe, R., Statton, J., Brown, E., et al. (2014). The movement ecology of seagrasses. *Proceedings of the Royal Society B: Biological Sciences*, 281(1795):20140878.

Mendez, F. J. and Losada, I. J. (2004). An empirical model to estimate the propagation of random breaking and nonbreaking waves over vegetation fields. *Coastal Engineering*, 51(2):103–118.

Méndez, F. J., Losada, I. J., and Losada, M. A. (1999). Hydrodynamics induced by wind waves in a vegetation field. *Journal of Geophysical Research: Oceans*, 104(C8):18383–18396.

Merkens, J.-L., Reimann, L., Hinkel, J., and Vafeidis, A. T. (2016). Gridded population projections for the coastal zone under the shared socioeconomic pathways. *Global and Planetary Change*, 145:57–66.

Miller, D. E., Hoitsma, T. R., and White, D. J. (1998). Degradation rates of woven coir fabric under field conditions. In *Engineering Approaches to Ecosystem Restoration*, pages 266–271. ASCE.

Moksnes, P.-O., Gipperth, L., Eriander, L., Laas, K., Cole, S., and Infantes, E. (2016). Handbok för restaurering av ålgräs i Sverige: Vägledning.

Molin, J. M., Groth-Andersen, W. E., Hansen, P. J., Kühl, M., and Brodersen, K. E. (2023). Microplastic pollution associated with reduced respiration in seagrass (*Zostera marina L.*) and associated epiphytes. *Frontiers in Marine Science*.

Möller, I., Kudella, M., Rupprecht, F., Spencer, T., Paul, M., Van Wesenbeeck, B. K., Wolters, G., Jensen, K., Bouma, T. J., Miranda-Lange, M., et al. (2014). Wave attenuation over coastal salt marshes under storm surge conditions. *Nature Geoscience*, 7(10):727–731.

Morison, J., Johnson, J. W., and Schaaf, S. A. (1950). The force exerted by surface waves on piles. *Journal of Petroleum Technology*, 2(05):149–154.

Munkes, B. (2005). Eutrophication, phase shift, the delay and the potential return in the greifswalder bodden, baltic sea. *Aquatic Sciences*, 67(3):372–381.

Narancic, T., Verstichel, S., Reddy Chaganti, S., Morales-Gamez, L., Kenny, S. T., De Wilde, B., Babu Padamati, R., and O'Connor, K. E. (2018). Biodegradable plastic blends create new possibilities for end-of-life management of plastics but they are not a panacea for plastic pollution. *Environmental science & technology*, 52(18):10441–10452.

Nature Conservancy, T. (2021). The blue guide to coastal resilience. protecting coastal communities through nature-based solutions. a handbook for practitioners of disaster risk reduction. Technical report, The Nature Conservancy. Arlington, VA, USA.

Nepf, H. M. (1999). Drag, turbulence, and diffusion in flow through emergent vegetation. *Water resources research*, 35(2):479–489.

Nepf, H. M. (2012a). Flow and transport in regions with aquatic vegetation. *Annual review of fluid mechanics*, 44:123–142.

Nepf, H. M. (2012b). Hydrodynamics of vegetated channels. *Journal of Hydraulic Research*, 50(3):262–279.

Nepf, H. M. and Vivoni, E. (2000). Flow structure in depth-limited, vegetated flow. *Journal of Geophysical Research: Oceans*, 105(C12):28547–28557.

Neumeier, U. and Ciavola, P. (2004). Flow resistance and associated sedimentary processes in a spartina maritima salt-marsh. *Journal of coastal research*, 20(2):435–447.

Niklas, K. J. (1992). *Plant biomechanics: an engineering approach to plant form and function*. University of Chicago press.

Nikora, N., Nikora, V., and O'Donoghue, T. (2013). Velocity profiles in vegetated open-channel flows: combined effects of multiple mechanisms. *Journal of Hydraulic Engineering*, 139(10):1021–1032.

Okamoto, T., Nezu, I., and Sanjou, M. (2016). Flow–vegetation interactions: length-scale of the "monami" phenomenon. *Journal of Hydraulic Research*, 54(3):251–262.

Ondiviela, B., Losada, I. J., Lara, J. L., Maza, M., Galván, C., Bouma, T. J., and van Belzen, J. (2014). The role of seagrasses in coastal protection in a changing climate. *Coastal Engineering*, 87:158–168.

Orth, R. J., Carruthers, T. J., Dennison, W. C., Duarte, C. M., Fourqurean, J. W., Heck, K. L., Hughes, A. R., Kendrick, G. A., Kenworthy, W. J., Olyarnik, S., et al. (2006a). A global crisis for seagrass ecosystems. *Bioscience*, 56(12):987–996.

Orth, R. J., Lefcheck, J. S., McGlathery, K. S., Aoki, L., Luckenbach, M. W., Moore, K. A., Oreska, M. P, Snyder, R., Wilcox, D. J., and Lusk, B. (2020). Restoration of seagrass habitat leads to rapid recovery of coastal ecosystem services. *Science Advances*, 6(41):eabc6434.

Orth, R. J., Luckenbach, M., and Moore, K. A. (1994). Seed dispersal in a marine macrophyte: implications for colonization and restoration. *Ecology*, 75(7):1927–1939.

Orth, R. J., Luckenbach, M. L., Marion, S. R., Moore, K. A., and Wilcox, D. J. (2006b). Seagrass recovery in the delmarva coastal bays, usa. *Aquatic Botany*, 84(1):26–36.

Ozeren, Y., Wren, D., and Wu, W. (2014). Experimental investigation of wave attenuation through model and live vegetation. *Journal of Waterway, Port, Coastal, and Ocean Engineering*, 140(5):04014019.

Paling, E., Fonseca, M., Van Katwijk, M., and Van Keulen, M. (2009). Seagrass restoration, coastal wetlands –an integrated ecosystem approach.

Park, J.-I. and Lee, K.-S. (2007). Site-specific success of three transplanting methods and the effect of planting time on the establishment of *Zostera marina* transplants. *Marine Pollution Bulletin*, 54(8):1238–1248.

Park, J.-I. and Lee, K.-S. (2010). Development of transplantation method for the restoration of surfgrass, phyllospadix japonicus, in an exposed rocky shore using an artificial underwater structure. *Ecological Engineering*, 36(4):450–456.

Pascolo, S., Petti, M., and Bosa, S. (2018). On the wave bottom shear stress in shallow depths: the role of wave period and bed roughness. *Water*, 10(10):1348.

Patterson, M. R., Harwell, M. C., Orth, L. M., and Orth, R. J. (2001). Biomechanical properties of the reproductive shoots of eelgrass. *Aquatic Botany*, 69(1):27–40.

Paul, M. (2018). The protection of sandy shores–can we afford to ignore the contribution of seagrass? *Marine Pollution Bulletin*, 134:152–159.

Paul, M. and Amos, C. (2011). Spatial and seasonal variation in wave attenuation over *Zostera noltii*. *Journal of Geophysical Research: Oceans*, 116(C8).

Paul, M., Bouma, T. J., and Amos, C. L. (2012). Wave attenuation by submerged vegetation: combining the effect of organism traits and tidal current. *Marine Ecology Progress Series*, 444:31–41.

Paul, M. and de los Santos, C. B. (2019). Variation in flexural, morphological, and biochemical leaf properties of eelgrass (zostera marina) along the european atlantic climate regions. *Marine Biology*, 166:1–12.

Paul, M. and Gillis, L. G. (2015). Let it flow: how does an underlying current affect wave propagation over a natural seagrass meadow? *Marine Ecology Progress Series*, 523:57–70.

Paul, M., Henry, P.-Y., and Thomas, R. (2014). Geometrical and mechanical properties of four species of northern european brown macroalgae. *Coastal engineering*, 84:73–80.

Paul, M., Rupprecht, F., Möller, I., Bouma, T. J., Spencer, T., Kudella, M., Wolters, G., van Wesenbeeck, B. K., Jensen, K., Miranda-Lange, M., et al. (2016). Plant stiffness and biomass as drivers for drag forces under extreme wave loading: a flume study on mimics. *Coastal Engineering*, 117:70–78.

Peña, E., Ferreras, J., and Sanchez-Tembleque, F. (2011). Experimental study on wave transmission coefficient, mooring lines and module connector forces with different designs of floating breakwaters. *Ocean Engineering*, 38(10):1150–1160.

Pervez, R., Lai, Y., Song, Y., Li, X., and Lai, Z. (2023). Impact of microplastic pollution on coastal ecosystems using comprehensive beach quality indices. *Marine Pollution Bulletin*, 194:115304.

Poggi, D., Porporato, A., Ridolfi, L., Albertson, J., and Katul, G. (2004). The effect of vegetation density on canopy sub-layer turbulence. *Boundary-Layer Meteorology*, 111:565–587.

Polak, O. and Shashar, N. (2013). Economic value of biological attributes of artificial coral reefs. *ICES Journal of Marine Science*, 70(4):904–912.

Pujol, D., Serra, T., Colomer, J., and Casamitjana, X. (2013). Flow structure in canopy models dominated by progressive waves. *Journal of hydrology*, 486:281–292.

Reimann, L., Vafeidis, A. T., and Honsel, L. E. (2023). Population development as a driver of coastal risk: current trends and future pathways. *Cambridge Prisms: Coastal Futures*, 1:e14.

Reynolds, L. K., Waycott, M., McGlathery, K. J., and Orth, R. J. (2016). Ecosystem services returned through seagrass restoration. *Restoration Ecology*, 24(5):583–588.

Rickson, R. (2006). Controlling sediment at source: an evaluation of erosion control geotextiles. *Earth Surface Processes and Landforms: The Journal of the British Geomorphological Research Group*, 31(5):550–560.

Rifai, H., Quevedo, J. M. D., Lukman, K. M., Sondak, C. F., Risandi, J., Hernawan, U. E., Uchiyama, Y., Ambo-Rappe, R., and Kohsaka, R. (2022). Potential of seagrass habitat restorations as nature-based solutions: Practical and scientific implications in indonesia. *Ambio*, pages 1–10.

Rominger, J. T. and Nepf, H. M. (2011). Flow adjustment and interior flow associated with a rectangular porous obstruction. *Journal of Fluid Mechanics*, 680:636–659.

Savio, M., Vettori, D., Biggs, H., Zampiron, A., Cameron, S. M., Stewart, M., Soulsby, C., and Nikora, V. (2023). Hydraulic resistance of artificial vegetation patches in aligned and staggered configurations. *Journal of Hydraulic Research*, 61(2):220–232.

Schaefer, R. B. and Nepf, H. (2022). Wave damping by seagrass meadows in combined wave-current conditions. *Limnology and Oceanography*, 67(7):1554–1565.

Scheffer, M., Bascompte, J., Brock, W. A., Brovkin, V., Carpenter, S. R., Dakos, V., Held, H., Van Nes, E. H., Rietkerk, M., and Sugihara, G. (2009). Early-warning signals for critical transitions. *Nature*, 461(7260):53–59.

Scheffer, M., Carpenter, S., Foley, J. A., Folke, C., and Walker, B. (2001). Catastrophic shifts in ecosystems. *Nature*, 413(6856):591–596.

Schendel, A., Goseberg, N., and Schlurmann, T. (2016). Erosion stability of wide-graded quarry-stone material under unidirectional current. *Journal of Waterway, Port, Coastal, and Ocean Engineering*, 142(3):04015023.

Schoonees, T., Gijón Mancheño, A., Scheres, B., Bouma, T., Silva, R., Schlurmann, T., and Schüttrumpf, H. (2019). Hard structures for coastal protection, towards greener designs. *Estuaries and Coasts*, 42:1709–1729.

Seddon, N., Daniels, E., Davis, R., Chausson, A., Harris, R., Hou-Jones, X., Huq, S., Kapos, V., Mace, G. M., Rizvi, A. R., et al. (2020). Global recognition of the importance of nature-based solutions to the impacts of climate change. *Global Sustainability*, 3:e15.

Seonghun, K., Pyungkwan, K., Seongjae, J., and Kyounghoon, L. (2020). Assessment of the physical characteristics and fishing performance of gillnets using biodegradable resin (pbs/pbat and pbsat) to reduce ghost fishing. *Aquatic Conservation: Marine and Freshwater Ecosystems*, 30(10):1868–1884.

Serrano, O., Inostroza, K., Hyndes, G. A., Friedlander, A. M., Serrano, E., Rae, C., and Ballesteros, E. (2023). Seagrass *Posidonia* escarpments support high diversity and biomass of rocky reef fishes. *Ecosphere*, 14(6):e4599.

Short, F., Carruthers, T., Dennison, W., and Waycott, M. (2007). Global seagrass distribution and diversity: a bioregional model. *Journal of experimental marine biology and ecology*, 350(1-2):3–20.

Short, F. T., Kopp, B. S., Gaeckle, J., and TAMAKI, H. (2002). Seagrass ecology and estuarine mitigation: a low-cost method for eelgrass restoration. *Fisheries science*, 68(sup2):1759–1762.

Short, F. T., Polidoro, B., Livingstone, S. R., Carpenter, K. E., Bandeira, S., Bujang, J. S., Calumpong, H. P., Carruthers, T. J., Coles, R. G., Dennison, W. C., et al. (2011). Extinction risk assessment of the world's seagrass species. *Biological Conservation*, 144(7):1961–1971.

Soulsby, R. (1997). Dynamics of marine sands: a manual for practical applications. *Oceanographic Literature Review*, 9(44):947.

Statton, J., Montoya, L. R., Orth, R. J., Dixon, K. W., and Kendrick, G. A. (2017). Identifying critical recruitment bottlenecks limiting seedling establishment in a degraded seagrass ecosystem. *Scientific reports*, 7(1):14786.

Stratigaki, V., Manca, E., Prinos, P., Losada, I. J., Lara, J. L., Sclavo, M., Amos, C. L., Cáceres, I., and Sánchez-Arcilla, A. (2011). Large-scale experiments on wave propagation over *Posidonia oceanica*. *Journal of Hydraulic Research*, 49(sup1):31–43.

Subaida, E., Chandrakaran, S., and Sankar, N. (2008). Experimental investigations on tensile and pullout behaviour of woven coir geotextiles. *Geotextiles and Geomembranes*, 26(5):384–392.

Sulaiman, M., Sinnakaudan, S., and Shukor, M. (2013). Near bed turbulence measurement with acoustic doppler velocimeter (adv). *KSCE Journal of Civil Engineering*, 17:1515–1528.

Talbot, F. F., Wilkinson, C. C., et al. (2001). *Coral reefs, mangroves and seagrasses: A sourcebook for managers*. Australian Institute of Marine Science (AIMS).

Tanino, Y. and Nepf, H. M. (2008). Laboratory investigation of mean drag in a random array of rigid, emergent cylinders. *Journal of Hydraulic Engineering*, 134(1):34–41.

Tanner, J. E., McSkimming, C., Russell, B. D., and Connell, S. D. (2021). Rapid restoration of belowground structure and fauna of a seagrass habitat. *Restoration Ecology*, 29(1):e13289.

Taphorn, M., Villanueva, R., Paul, M., Visscher, J., and Schlurmann, T. (2021). Flow field and wake structure characteristics imposed by single seagrass blade surrogates. *Journal of Ecohydraulics*, 7(1):58–70.

Taylor-Burns, R., Nederhoff, K., Lacy, J. R., and Barnard, P. L. (2023). The influence of vegetated marshes on wave transformation in sheltered estuaries. *Coastal Engineering*, 184:104346.

Temmerman, S., Meire, P., Bouma, T. J., Herman, P. M., Ysebaert, T., and De Vriend, H. J. (2013). Ecosystem-based coastal defence in the face of global change. *Nature*, 504(7478):79–83.

Thomas, F. I. and Cornelisen, C. D. (2003). Ammonium uptake by seagrass communities: effects of oscillatory versus unidirectional flow. *Marine Ecology Progress Series*, 247:51–57.

Tran, P. D., Pham, T., Nguyen, L., Tran, H., and Nguyen, K. (2019). Artificial coral reefs restore coastal natural resources. *International Journal of Fisheries and Aquatic Studies*, 7(3):128–133.

Tuya, F., Vila, F., Bergasa, O., Zarranz, M., Espino, F., and Robaina, R. R. (2017). Artificial seagrass leaves shield transplanted seagrass seedlings and increase their survivorship. *Aquatic Botany*, 136:31–34.

UN (2022). UN world population prospects 2022. [https://population.un.org/wpp/Download/Standard/MostUsed/](https://population.un.org/wpp/Download/Standard/MostUsed/). Accessed: 2023-09-10.

UNFCCC (2016). The Paris Agreement.

UNISDR (2015). Sendai Framework for Disaster Risk Reduction 2015–2030.

Unsworth, R. K., Collier, C. J., Waycott, M., Mckenzie, L. J., and Cullen-Unsworth, L. C. (2015). A framework for the resilience of seagrass ecosystems. *Marine pollution bulletin*, 100(1):34–46.

Unsworth, R. K., McKenzie, L. J., Collier, C. J., Cullen-Unsworth, L. C., Duarte, C. M., Eklöf, J. S., Jarvis, J. C., Jones, B. L., and Nordlund, L. M. (2019). Global challenges for seagrass conservation. *Ambio*, 48:801–815.

van der Heide, T., van Nes, E. H., Geerling, G. W., Smolders, A. J., Bouma, T. J., and van Katwijk, M. M. (2007). Positive feedbacks in seagrass ecosystems: implications for success in conservation and restoration. *Ecosystems*, 10:1311–1322.

van der Heide, T., van Nes, E. H., van Katwijk, M. M., Olff, H., and Smolders, A. J. (2011). Positive feedbacks in seagrass ecosystems–evidence from large-scale empirical data. *PloS one*, 6(1):e16504.

van Eekelen, E. and Bouw, M. (2021). *Building with nature: creating, implementing, and upscaling nature-based solutions*. nai010 publishers.

Van Katwijk, M., Bos, A., De Jonge, V., Hanssen, L., Hermus, D., and De Jong, D. (2009). Guidelines for seagrass restoration: importance of habitat selection and donor population, spreading of risks, and ecosystem engineering effects. *Marine pollution bulletin*, 58(2):179–188.

van Katwijk, M., Hermus, D., De Jong, D., Asmus, R., and De Jonge, V. (2000). Habitat suitability of the wadden sea for restoration of *Zostera marina* beds. *Helgoland Marine Research*, 54:117–128.

van Katwijk, M. M., Thorhaug, A., Marbà, N., Orth, R. J., Duarte, C. M., Kendrick, G. A., Althuizen, I. H., Balestri, E., Bernard, G., Cambridge, M. L., et al. (2016). Global analysis of seagrass restoration: the importance of large-scale planting. *Journal of Applied Ecology*, 53(2):567–578.

Van Keulen, M., Paling, E. I., and Walker, C. (2003). Effect of planting unit size and sediment stabilization on seagrass transplants in western australia. *Restoration Ecology*, 11(1):50–55.

van Rooijen, A., Lowe, R., Rijnsdorp, D. P., Ghisalberti, M., Jacobsen, N. G., and McCall, R. (2020). Wave-driven mean flow dynamics in submerged canopies. *Journal of Geophysical Research: Oceans*, 125(3):e2019JC015935.

van Veelen, T. J., Fairchild, T. P., Reeve, D. E., and Karunarathna, H. (2020). Experimental study on vegetation flexibility as control parameter for wave damping and velocity structure. *Coastal Engineering*, 157:103648.

van Veelen, T. J., Karunarathna, H., and Reeve, D. E. (2021). Modelling wave attenuation by quasi-flexible coastal vegetation. *Coastal Engineering*, 164:103820.

van Zanten, B. T., Gutierrez Goizueta, G., Brander, L. M., Gonzalez Reguero, B., Griffin, R., Macleod, K. K., Alves Beloqui, A. I., Midgley, A., Herrera Garcia, L. D., and Jongman, B. (2023). Assessing the benefits and costs of nature-based solutions for climate resilience: A guideline for project developers.

Vettori, D. and Nikora, V. (2018). Flow–seaweed interactions: a laboratory study using blade models. *Environmental Fluid Mechanics*, 18:611–636.

Vettori, D. and Nikora, V. (2020). Hydrodynamic performance of vegetation surrogates in hydraulic studies: a comparative analysis of seaweed blades and their physical models. *Journal of Hydraulic Research*, 58(2):248–261.

Villanueva, R., Paul, M., and Schlurmann, T. (2022). Anchor forces on coir-based artificial seagrass mats: Dependence on wave dynamics and their potential use in seagrass restoration. *Frontiers in Marine Science*, page 345.

Villanueva, R., Paul, M., and Schlurmann, T. (2023). Wave dynamics alteration by discontinuous flexible mats of artificial seagrass can support seagrass restoration efforts. *Scientific Reports*, 13:19418.

Villanueva, R., Paul, M., Vogt, M., and Schlurmann, T. (2017). Vertical biomass distribution drives flow through aquatic vegetation. *SCACR 2017*.

Villanueva, R., Thom, M., Visscher, J., Paul, M., and Schlurmann, T. (2021). Wake length of an artificial seagrass meadow: a study of shelter and its feasibility for restoration. *Journal of Ecohydraulics*, 7(1):77–91.

Vitousek, P. M., Aber, J. D., Howarth, R. W., Likens, G. E., Matson, P. A., Schindler, D. W., Schlesinger, W. H., and Tilman, D. G. (1997). Human alteration of the global nitrogen cycle: sources and consequences. *Ecological applications*, 7(3):737–750.

Vogel, S. (2020). *Life in moving fluids: the physical biology of flow-revised and expanded second edition*. Princeton University Press.

Waycott, M., Duarte, C. M., Carruthers, T. J., Orth, R. J., Dennison, W. C., Olyarnik, S., Calladine, A., Fourqurean, J. W., Heck Jr, K. L., Hughes, A. R., et al. (2009). Accelerating loss of seagrasses across the globe threatens coastal ecosystems. *Proceedings of the national academy of sciences*, 106(30):12377–12381.

Wear, R. J., Tanner, J. E., and Hoare, S. L. (2010). Facilitating recruitment of amphibolis as a novel approach to seagrass rehabilitation in hydrodynamically active waters. *Marine and Freshwater Research*, 61(10):1123–1133.

Webber, J. J. and Huppert, H. E. (2021). Stokes drift through corals. *Environmental Fluid Mechanics*, 21(5):1119–1135.

White, B. L. and Nepf, H. M. (2007). Shear instability and coherent structures in shallow flow adjacent to a porous layer. *Journal of Fluid Mechanics*, 593:1–32.

Wilson, J. B. and Agnew, A. D. (1992). Positive-feedback switches in plant communities. In *Advances in ecological research*, volume 23, pages 263–336. Elsevier.

Wright, S. L., Thompson, R. C., and Galloway, T. S. (2013). The physical impacts of microplastics on marine organisms: a review. *Environmental pollution*, 178:483–492.

Xu, J. and Guo, B.-H. (2010). Microbial succinic acid, its polymer poly (butylene succinate), and applications. *Plastics from bacteria: Natural functions and applications*, pages 347–388.

Xu, T.-J., Zhao, Y.-P., Dong, G.-H., and Bi, C.-W. (2014). Fatigue analysis of mooring system for net cage under random loads. *Aquacultural engineering*, 58:59–68.

Zhang, X., Lin, P., and Nepf, H. (2021). A simple-wave damping model for flexible marsh plants. *Limnology and Oceanography*, 66(12):4182–4196.

Zhang, Y., Tang, C., and Nepf, H. (2018). Turbulent kinetic energy in submerged model canopies under oscillatory flow. *Water Resources Research*, 54(3):1734–1750.

Zhou, Y., Liu, P., Liu, B., Liu, X., Zhang, X., Wang, F., and Yang, H. (2014). Restoring eelgrass (*Zostera marina L.*) habitats using a simple and effective transplanting technique. *PLoS One*, 9(4):e92982.

Zong, L. and Nepf, H. (2012). Vortex development behind a finite porous obstruction in a channel. *Journal of Fluid Mechanics*, 691:368–391.

# Curriculum Vitae

| | |
|---|---|
| **Name:** | Raúl Armando Villanueva Granados |
| **Born in:** | Tegucigalpa M.D.C., Honduras |
| **Date of birth:** | June 28, 1990 |
| **Nationality:** | Honduran/German |
| **Website:** | www.linkedin.com/in/raulvillanueva7 |

PROFESSIONAL EXPERIENCE

| | |
|---|---|
| **2023–present** | **Chief Operations Officer (COO)** |
| | Collaborative Research Center (CRC) 1464 TerraQ |
| | Institute of Geodesy |
| | Leibniz University Hannover, Germany |
| **2015–2020** | **Lecturer, Research Associate** |
| | Ludwig Franzius Institute of Hydraulic, Estuarine and Coastal Engineering |
| | Leibniz University Hannover, Germany |
| **2014** | **PhD Assistant** |
| | Institute for Hydrology and Water Resources (WAWI) |
| | Leibniz University Hannover, Hanover, Germany |
| **2013** | **Resident Project Engineer** |
| | Grupo ITM |
| | Tegucigalpa, Honduras |
| **2011–2012** | **Supervising Field Engineer** |
| | Saybe y Asociados S de R.L. |
| | Tegucigalpa, Honduras |

EDUCATION

| | |
|---|---|
| **2016–2023** | **PhD Candidate** |
| | Ecohydraulics and ecosystem coastal engineering |
| | Leibniz University Hannover (Germany) |
| **2021–2022** | **Training** |
| | Python, Matlab and Simulink, ArcGIS Pro, Machine and Deep Learning |
| | AlfaTraining GmbH |
| | (virtual) Germany |

| 2013–2015 | **Master of Science (M.Sc.)** |
| | WATENV - Water Resources and Environmental Management |
| | Specialization: Water Resources and Environmental |
| | Hydraulics |
| | Leibniz University Hannover, Hanover, Germany |
| 2007–2011 | **Bachelor of Engineering (B.Eng)** |
| | Civil Engineering |
| | Universidad Tecnológica Centroamericana, Tegucigalpa, |
| | Honduras |
| 2002–2007 | **High school education** |
| | Elvel School |
| | Tegucigalpa, Honduras |

## a) peer-reviewed publications

1. Arboleda Chavez, C. E., Stratigaki, V., Wu, M., Troch, P., Schendel, A., Welzel, M., **Villanueva, R.**, ... Todd, D. (2019). Large-scale experiments to improve monopile scour protection design adapted to climate change – The PROTEUS Project. *Energies*, 12(9), 1709. DOI: 10.3390/en12091709

2. Carus, J., Arndt, C., Schröder, B., Thom, M., **Villanueva, R.**, and Paul, M. (2021). Using artificial seagrass for promoting positive feedback mechanisms in seagrass restoration. *Frontiers in Marine Science*, page 993. DOI: 10.3389/fmars.2021.546661

3. **Villanueva, R.**, Thom, M., Visscher, J., Paul, M., and Schlurmann, T. (2021). Wake length of an artificial seagrass meadow: a study of shelter and its feasibility for restoration. *Journal of Ecohydraulics*, 7(1):77–91. DOI: 10.1080/24705357.2021.1938256

4. Taphorn, M., **Villanueva, R.**, Paul, M., Visscher, J., and Schlurmann, T. (2021). Flow field and wake structure characteristics imposed by single seagrass blade surrogates. *Journal of Ecohydraulics*, 7(1):58–70. DOI: 10.1080/24705357.2021.1938253

5. **Villanueva, R.**, Paul, M., and Schlurmann, T. (2022). Anchor forces on coir-based artificial seagrass mats: Dependence on wave dynamics and their potential use in seagrass restoration. *Frontiers in Marine Science*, page 345. DOI: 10.3389/fmars.2022.802343

6. **Villanueva, R.**, Paul, M., and Schlurmann, T. (2023). Wave dynamics alteration by discontinuous flexible mats of artificial seagrass can support seagrass restoration efforts. *Scientific Reports*, 13:19418. DOI: 10.1038/s41598-023-46612-z

## b) other publications

1. **Villanueva, R.**, Paul, M., Vogt, M., and Schlurmann, T. (2017). Vertical biomass distribution drives flow through aquatic vegetation. *Proceedings of the Short Conference on Applied Coastal Research SCACR 2017*. DOI: 10.15488/13254